FEUP FACULDADE DE ENGENHARIA
UNIVERSIDADE DO PORTO



AN INVESTIGATION OF STRESS WAVE PROPAGATION THROUGH ROCK JOINTS AND ROCK MASSES

José Ricardo Pontes Resende

Dissertação elaborada no Laboratório Nacional de Engenharia Civil para obtenção do grau de Doutor em Engenharia Civil pela Faculdade de Engenharia da Universidade do Porto, no âmbito do protocolo de cooperação entre a FEUP e o LNEC

Tese realizada sob a orientação de:

Orientador: Doutor Rui Artur Bártolo Calçada
Co-orientador: Doutor Luís Manuel Nolasco Lamas
Co-orientador: Doutor José Antero Senra Vieira de Lemos

Porto, Maio de 2010

Para a Mariana

Acknowledgments

This work was developed at the Portuguese National Laboratory for Civil Engineering (LNEC). I thank LNEC for the excellent working conditions and trust that have been deposited in me. I particularly thank Senior Researcher Carlos Pina, who invited me to work at LNEC and that, sometimes closer by, sometimes from a distance, never ceased to keep track of my progression.

I wish to acknowledge the support of the Foundation for Science and Technology through project grant POCTI/ECM/57495/2004 and PhD grant SFRH/BD/36212/2007.

For the support for allowing the utilization of the data in chapter six I thank APDL–Administração dos Portos do Douro e Leixões. I particularly wish to thank and Engineer Luís Adão from Etermar SA and Engineer João Neves from APDL.

For the support in the blast tests and for allowing the utilization of the data in chapter five I thank EDP–Energias de Portugal.

I had the best of luck with my supervisors Principal Researcher Luís Nolasco Lamas and Senior Researcher José Vieira de Lemos. They supported my better ideas and helped me to get rid of the bad ones. I learned from them in every aspect. I also thank Professor Rui Calçada for accepting to supervise my work and for his encouraging advice.

To Professor Jian Zhao, head of the Rock Mechanics Laboratory of the École Polytechnique Fédérale de Lausanne I thank for welcoming me to his laboratory and for the helpful discussions.

To the Seismic Engineering and Structural Dynamics group I wish to thank for lending the vibration monitoring equipment used both in the seismic monitoring of the Leixões Harbour and in the blast tests at Bemposta underground complex. In particular I wish to thank Principal Researcher Alfredo Campos Costa for his advice and my colleague Luis André Marcos Mendes and technicians Artur dos Santos and Anabela Martins.

For their help in the Leixões vibration monitoring and the Bemposta blast tests I thank the Researcher Pereira Gomes, technicians João Rijo Nunes Magro, Hélder Vitória, Carlos Resende, Jorge Gião and Ricardo Duro.

I also thank my research colleagues and technicians at the Underground Works and Foundations Group (NFOS) for their everyday support and for welcoming this young engineer at NFOS some years ago. I thank in particular Senior Researcher Nuno Grossmann and Principal Researcher José Muralha.

To NFOS and DBB administrative staff Lucília Marmeleira and Maria de São José I thank for their prompt assistance to get me out of the bureaucratic dead-ends I sometimes got myself into.

To my colleagues at LNEC, some already with their PhDs behind, others now pursuing it, Luísa Braga Farinha, Bruno Figueiredo, Juan Mata, Nuno Azevedo, Ricardo Santos and others. Thank you for your friendship and to Luísa in particular for the final review of the manuscript.

To Miguel Curado, I thank his friendship and for delivering my classes at ISCTE during my leavings.

To Francisco Contreiras, Francisco Vasconcelos, Estrella Rodriguez, Luís Mesquita, Manuel Martins, Núria Frau, Tiago Nolasco and the whole Verbum Dei community, for the profound friendship and for being the closer companions en route to God.

To the management of the Windsurf café and Muchaxo restaurant at Carcavelos and Guincho beaches, I thank for the long afternoons working there.

To my family, who defies me to do better and with whom I am at home. My mother Teresa and father Antero. My father and mother-in-law João Paulo and Ana Maria. My brothers and sisters Catarina, Madalena, Inês, Filipe, Teresa, Samuel, Michael and Hugo. My nephews Francisco, Afonso, Margarida, Sofia, Luísa, Clara, Charlotte and Manel.

To aunts Tété and Edite for being so often the family's backup when I could not be there.

To my wife Mariana, to whom this thesis is dedicated. I thank her unconditional love in these thirteen years and in these last three in particular. To you and to our daughters Maria and Leonor I thank for your love and joy and apologise for not being with you during the work periods.

To our friends who shared these years with my family.

It takes a lot of people to make a thesis! To those missing in these lines I apologize. To all I am immensely grateful.

Abstract

Rock blasting is employed in underground excavation of tunnels, adits and caverns and also in surface rock removal and quarrying. Ground vibration is an unavoidable side-effect and one of the main environmental impacts. Stress waves disturb populations, are transmitted to structures and induce stresses that may damage sensitive equipments, compromise serviceability of constructions or, in extreme cases, cause structural damage.

In order to control and manage their impacts, a more profound knowledge of how stress waves propagate in fractured rock masses is needed and traditional methods of prediction of vibration propagation must be improved and complemented with numerical models that can cope with blast and ground variability in ways other than through empirical equations whose inputs are explosive weight and distance.

This thesis contributes to these goals through several means. The first is the development of a dynamic micromechanical numerical model that simulates propagation of stress waves in rock and through rock joints. This innovative model is based on the particle discrete element method. The dynamic properties of a non-structured assembly of circular particles are studied, and a new joint contact model is developed allowing the simulation of rock joints with realistic roughness, contact creation and erosion. This model performs well in static and dynamic normal tests, adjusting to the Displacement Discontinuity Theory for rock joints seismic behaviour.

In a second study, a blast test in a network of adits excavated in rock at a depth of a few hundred metres clarifies how vibrations travel and arrive at different locations in the complex. Two and three-dimensional simulation of blasting stress wave propagation is generically studied, which is followed by the modelling the test using two and three dimensional numerical models. The general performance of these models is assessed, while different modelling options are evaluated. This study delivers important conclusions on how to simulate stress wave generation, propagation and measurement on numerical models.

In a third study the object of attention is an even larger underwater blasting operation. Statistical, artificial intelligence and numerical modelling techniques suited for the low level of information on the blasting and the ground are used and developed to study peak particle

velocity dispersion. Simple three-dimensional numerical models were built to test the influence of hypothetical ground singularities on the peak particle velocity attenuation. These models are a great improvement of the means usually employed to study wave propagation, showing how dykes, softer ground and blast characteristics influence vibration levels.

Resumo

A vibração do terreno é um efeito colateral e inevitável da utilização de explosivos na escavação túneis, galerias e cavernas, e igualmente em pedreiras e desmontes à superfície. As vibrações podem incomodar as populações, danificar equipamentos sensíveis e são transmitidas às estruturas pondo em causa a sua conservação e, em casos extremos, causando danos estruturais.

Por forma a controlar e minimizar os impactos das vibrações, é necessário um conhecimento mais aprofundado da forma como se propagam nos maciços rochosos. São igualmente precisos novos métodos que complementem e expandam os métodos tradicionais da previsão dos níveis de vibração, nomeadamente através de modelos numéricos que possam lidar com variações na fonte e no meio de propagação.

Esta tese contribui para estes objectivos de diversas formas. A primeira consiste no desenvolvimento de um modelo numérico micromecânico, dinâmico, que simula a propagação de ondas de tensão em maciços rochosos fracturados. Este modelo inovador é baseado no método dos elementos discretos de partículas. São estudadas as propriedades dinâmicas de assembleias não-estruturadas de partículas circulares. Um novo modelo de contacto é desenvolvido e é simulada uma descontinuidade rochosa com rugosidade, sendo reproduzida a criação e erosão dos contactos entre as paredes da descontinuidade. Este modelo simula correctamente o comportamento de um provete com uma junta sob compressão estática e dinâmica, mostrando concordância com a Teoria do Deslocamento Descontínuo.

Num segundo estudo foi efectuado um teste que envolveu diversas explosões e a medição das vibrações por ela geradas numa rede de galerias escavadas em rocha a uma profundidade de poucas centenas de metros. As medições mostram como as vibrações são transmitidas e recebidas em diferentes locais do complexo subterrâneo e também mostram a influência das cavidades na sua progressão. Através de simulações uni, bi e tridimensionais é estudada genericamente a propagação de ondas de tensão recorrendo a diversas simplificações geométricas, sendo depois uma parte do teste modelada utilizando modelos bi e tridimensionais. Discute-se o desempenho geral destes modelos e avaliam-se diversas opções para a geração, propagação e a

recepção de ondas de tensão, chegando-se a conclusões importantes sobre as melhores práticas para a modelação deste tipo de fenómeno.

Num terceiro estudo o objecto da atenção é uma empreitada de desmonte subaquático de rocha de grandes dimensões. Para interpretar o comportamento identificando as causas da dispersão dos valores máximos de vibração, são desenvolvidos modelos empíricos estatísticos e de inteligência artificial assim como modelos numéricos adequados ao baixo nível de informação disponível sobre as operações de desmonte e as características do terreno. Os modelos numéricos tridimensionais são utilizados para compreender a transmissão de vibrações e testar a influência da fonte de vibração e de heterogeneidades no terreno. Estes modelos constituem um salto quantitativo importante em relação aos meios normalmente utilizados para estudar a propagação de vibrações, mostrando ainda como as falhas, as zonas de terreno de baixa qualidade ou as alterações nas características dos desmontes influenciam os valores máximos de vibração.

Resumé

Les vibrations du terrain sont un effet collatéral et inévitable de l'utilisation des explosifs pour creuser des tunnels, galeries et cavernes, et également dans les carrières et les excavations en surface. Les vibrations peuvent gêner les personnes, abîmer des équipements sensibles, et sont transmises aux structures menaçant leur conservation et, à l'extrême, endommagent la structure elle-même.

Pour contrôler et minimiser les impacts des vibrations, il est nécessaire d´avoir une connaissance plus approfondie de la forme de leur propagation dans les massifs rocheux. Il faut aussi des méthodes nouvelles qui puissent compléter et augmenter les méthodes traditionnelles de prévision des niveaux de vibration, notamment au moyen de modèles numériques qui puissent représenter les variations à la source et dans le milieu de propagation.

Cette thèse-ci contribue à ces buts de plusieurs façons. La première est le développement d'un modèle numérique micromécanique dynamique qui simule la propagation des ondes de tension dans la roche et ses discontinuités. Ce modèle innovateur est basé sur la méthode des éléments discrets de particules. Les propriétés dynamiques d'un ensemble non-structuré de particules circulaires sont étudiées, et un nouveau modèle constitutif de contact est développé qui permet la simulation des discontinuités de la roche ayant une rugosité, une création des contacts et une érosion réalistes. Ce modèle fonctionne bien pour les essais de compression statiques et dynamiques, et fournit des résultats semblables à ceux de la Théorie du Déplacement Discontinu pour le comportement séismique des joints rocheux.

Dans la deuxième étude, des explosions on été faites dans un réseau de galeries creusés dans une roche à une profondeur de quelques centaines de mètres, et on a mesuré les vibrations produites. Les mesures montrent comme les vibrations ont été transmises et reçues en différents endroits du complexe souterrain, et montrent aussi l´influence des cavités dans leur progression. La propagation des ondes de tension a été étudiée en général, au moyen des simulations à une, deux et trois dimensions. L'accomplissement général de ces modèles est discuté et on évalue les options pour la génération, la propagation et la réception des ondes de tension. On a obtenu des conclusions importantes sur les meilleures pratiques pour la modulation de ce type

de phénomène.

Dans une troisième étude, l'objet est un ouvrage de creusement subaquatique de grande dimension. Pour interpréter le comportement et identifier les causes des valeurs maximales de vibration, on a développé des modèles empiriques statistiques et d'intelligence artificielle, et aussi des modèles numériques adaptés au bas niveau d'information existant sur les opérations d´excavation et les caractéristiques du terrain. Les modèles numériques tridimensionnels sont utilisés pour comprendre la transmission des vibrations et essayer l´influence de la source de la vibration et de l´hétérogénéité du sol. Ces modèles constituent un important développement quand on les compare avec les autres moyens utilisés en général pour étudier la propagation des vibrations. Ils montrent comme les failles, les zones du sol de mauvaise qualité ou les changements des caractéristiques des excavations influencent les valeurs de la vibration.

Symbols

α, β	Parameters of Duvall's blast load function
δt	Calculation timestep
δ	Kronecker tensor
λ	Wavelength
μ	Contact friction coefficient
ν	Poisson's ratio
ω	Angular frequency
ϕ_1	Angle of the incident and reflected shear waves
ϕ_2	Angle of the transmitted shear waves
π	Pi (3.14159)
ρ	Density (general)
ρ_{disk}	Disk density
ρ_{solid}	Continuous solid density
ρ_{sphere}	Sphere density
σ	Stress tensor
σ_n	Joint normal stress
σ_s	Joint shear stress
θ_1	Angle of the incident and reflected compressive waves
θ_2	Angle of the transmitted compressive waves
θ_T	Phase shift of the reflected and transmitted waves
ε	Strain tensor
A	Harmonic wave amplitude
A_{ball}	Particle transversal area (general)
A_{disk}	Cylindrical particle transversal area
A_{sphere}	Spherical particle transversal area
bf_{depth}	Boundary depth correction factor

c	Propagation velocity of stress waves (general)
c_p	Propagation velocity of compressive waves
c_s	Propagation velocity of shear waves
d_{kf}	Final contact stiffness (joint contact constitutive model)
d_{ki}	Initial contact stiffness (joint contact constitutive model)
d_{radius}	Percentage of ball radius that triggers hardening (joint contact constitutive model)
dt_{gR}	Reflected wave group time delay
dt_{gT}	Transmitted wave group time delay
E	Young modulus
En	Wave energy
f	Frequency
F, F_{ball}	Force at particle
F_n	Contact normal force
F_s	Contact shear force
g	Acceleration of gravity (9.801 m/s^2)
G	Shear modulus, or Lamé's second constant
i	Imaginary number ($\sqrt{-1}$)
I	Incident wave amplitude
k	Wavenumber ($k = 2\pi/\lambda$)
K	Bulk modulus
k, m, n	Parameters of attenuation equation
$K_{n,R}^{dyn}$	Dynamic joint normal stiffness (from reflected wave)
$K_{n,T}^{dyn}$	Dynamic joint normal stiffness (from transmitted wave)
k_n	Contact normal stiffness
K_n^{dyn}	Dynamic joint normal stiffness (general)
K_n^{static}	Static joint normal stiffness
k_s	Contact shear stiffness
K_s^{dyn}	Dynamic joint shear stiffness
K_s^{static}	Static joint shear stiffness
L	Lamé's first constant
l_{bound}	Length of boundary in particle model
l_z	Finite-difference zone length
m	Particle mass (generic)
m_{disk}	Disk particle mass

m_{sphere}	Sphere particle mass
nb_{bound}	Number of balls in boundary
$p(t)$	Pressure blast load function
p_0	Peak amplitude of blast load function
PPV	Peak Particle Velocity ($PPV = max\sqrt{v_x^2 + v_y^2 + v_z^2}$)
r	Particle radius
R	Distance from blast to measurement point
r_{mean}	Average particle radius
R_{SH}	Reflected horizontal shear wave amplitude
R_{SV}	Reflected vertical shear wave amplitude
R_P	Reflected compressive wave amplitude
R_S	Reflected shear wave amplitude
S	Shear wave
S_H	Horizontally polarized shear wave
S_V	Vertically polarized shear wave
T	Time description term of harmonic wave
t	Particle thickness
t	Time
t_{peak}	Peak time of blast load function
T_{SH}	Transmitted horizontal shear wave amplitude
T_{SV}	Transmitted vertical shear wave amplitude
T_P	Transmitted compressive wave amplitude
T_S	Transmitted shear wave amplitude
u	Particle displacement
v	Particle velocity
W	Mass of instantaneous blast charge
X	Spacial description term of harmonic wave

Acronyms

3DEC	Three-dimensional Discrete Element Code
ANFO	Ammonium Nitrate Fuel Oil
APDL	Administração dos Portos do Douro e Leixões
BEM	Boundary Element Method
BPM	Bonded Particle Model
DEM	Discrete Element Method
DLL	Dynamic Linked Library
EDZ	Excavation Damaged Zone
FDM	Finite Difference Method
FEM	Finite Element Method
FFT	Fast Fourier transform
FLAC	Fast Lagrangian Analysis of Continua
IFFT	Inverse Fast Fourier Transform
ISO	International Organization for Standardization
ISRM	International Society for Rock Mechanics
ITA	International Tunnelling and Underground Space Association
LNEC	Laboratório Nacional de Engenharia Civil
MLP	Multilayer Perceptron Neural Networks
PDEM	Particle Discrete Element Method
PFC	Particle Flow Code
RMR	Rock Mass Rating
RQD	Rock Quality Designation
TNT	Trinitrotoluene
UDEC	Universal Discrete Element Code
UDM	User Defined Model

Contents

Chapter 1 – **Introduction** **1**

1.1 Background 1
1.2 Thesis objectives and lines of action 4
1.3 Thesis outline 6

Chapter 2 – **Stress Wave Generation and Propagation** **9**

2.1 Introduction 9
2.2 Stress Wave Generation 10
2.2.1 Rock blasting 11
2.2.2 Rail and road circulation 16
2.2.3 Earthquakes 18
2.3 Stress wave propagation in elastic and non-elastic media 19
2.3.1 Rock material wave attenuation 19
2.3.2 Geometrical wave attenuation 20
2.3.3 Plane wave equation 22
2.4 Stress waves in rock masses 26
2.5 Stress wave interaction with rock joints 27
2.5.1 Interfaces between solids with different properties 29
2.5.2 Rock joints 30
2.5.3 Displacement Discontinuity Theory 33
2.5.4 Fluid-filled discontinuities 36
2.6 Discussion 38

Chapter 3 – **Vibration Impact Assessment Tools** **41**

3.1 Introduction 41
3.2 Wave propagation models 42
3.2.1 Attenuation laws, statistical and probabilistic analysis 43
3.2.2 Peak particle vibration attenuation laws 43
3.2.3 Artificial intelligence methods: Neural networks 46
3.2.4 Numerical modelling of wave propagation in the ground 47
3.3 Impacts on human beings, structures and equipment 50

3.4 Monitoring strategies . . . 51
3.5 International regulations on blast-induced vibrations . . . 55
3.5.1 ISO regulation . . . 56
3.5.2 German regulation . . . 57
3.5.3 Portuguese regulation . . . 58
3.5.4 USA regulation . . . 58
3.5.5 Swiss regulation . . . 60
3.5.6 British regulation . . . 60
3.5.7 Regulation comparison . . . 61
3.6 Discussion . . . 63

CHAPTER 4 – **Micromechanical Modelling of Dynamic Rock and Joint Behaviour 65**
4.1 Introduction . . . 65
4.2 The Discrete Element Method . . . 68
4.2.1 The calculation cycle . . . 69
4.2.2 Contact management . . . 69
4.2.3 Solution of motion equations . . . 71
4.3 Micromechanical modelling of rock with particle models . . . 74
4.3.1 Contact models . . . 77
4.3.2 Generation of Bonded Particle Models . . . 80
4.3.3 Macroscopic properties . . . 81
4.4 Rock joints static normal behaviour . . . 85
4.4.1 Mechanics of joint compression . . . 86
4.4.2 Empirical models . . . 88
4.4.3 Predictive models . . . 89
4.4.4 Simulation of joint behaviour with particle models . . . 91
4.4.5 Jointed synthetic rock specimen behaviour . . . 92
4.5 Modelling wave propagation in rock masses with Particle Models . . . 100
4.5.1 Dynamic properties of rectangular packings . . . 102
4.5.2 Dynamic properties of hexagonal packings . . . 104
4.5.3 Dynamic properties of unorganized packings . . . 106
4.5.4 Modelling wave propagation in Bonded Particle Models . . . 106
4.5.5 Quality of wave propagation . . . 113
4.5.6 Discussion on wave propagation in BPM . . . 126
4.6 Propagation of compressive stress waves across fractures . . . 126
4.6.1 Test description . . . 127

4.6.2 Results discussion . . . 128
4.7 Discussion and future developments . . . 136

CHAPTER 5 – **Stress Wave Propagation Test at the Bemposta Hydroelectric Complex** **139**
5.1 Introduction . . . 139
5.2 Bemposta dam and underground hydroelectric scheme . . . 140
5.2.1 Site characterization . . . 142
5.2.2 Geotechnical characterization of the test adits . . . 146
5.3 Vibration propagation test . . . 149
5.3.1 Description of the test site . . . 150
5.3.2 Blast description . . . 154
5.3.3 Vibration measurement system . . . 154
5.3.4 Digital signal processing . . . 161
5.3.5 Baseline situation . . . 162
5.4 Results of the vibration propagation test . . . 162
5.4.1 Blast set 1 . . . 163
5.4.2 Blast set 2 . . . 166
5.4.3 Blast set 3 . . . 170
5.4.4 Blast set 4 . . . 172
5.5 Numerical modelling . . . 177
5.5.1 Dynamic modelling using finite difference models . . . 178
5.5.2 Blast representation in numerical models . . . 179
5.5.3 Two and three dimensional modelling of stress wave propagation . . . 186
5.5.4 Modelling of the Bemposta test . . . 192
5.6 Discussion and future developments . . . 217
5.6.1 Contributions . . . 217
5.6.2 Future developments . . . 219

CHAPTER 6 – **Vibration Monitoring, Control and Analysis in Large Scale** **221**
6.1 Introduction . . . 221
6.1.1 Background . . . 221
6.1.2 Vibration monitoring in urban areas . . . 222
6.2 Description of the deepening works of the Leixões Harbour . . . 223
6.2.1 The harbour and surrounding urban area . . . 223
6.2.2 Blasting description . . . 224

6.2.3 Monitoring 224
6.2.4 Recorded data, digital time-series processing and PPV scattering 228
6.3 Determination of PPV attenuation laws 230
6.4 Multilayer Perceptron Neural Networks applied to PPV attenuation 233
6.4.1 Network architecture 233
6.4.2 Results and discussion 235
6.5 Finite difference numerical modelling 238
6.5.1 Introduction 238
6.5.2 Model description 239
6.5.3 Reference model and influence of distance 240
6.5.4 Influence of blast load location and application 241
6.5.5 Influence of dyke filled with soft material 245
6.5.6 Influence of ditch in vibration path 245
6.5.7 Influence of filling material in the quay walls 246
6.6 Discussion and future developments 248

CHAPTER 7 – **Conclusions** **253**
7.1 General 253
7.2 Conclusions and contributions 254
7.3 Future developments 259

List of References **263**

APPENDIX I – **Photographs of the Bemposta Test Site** **275**

APPENDIX II – **Plots of the Bemposta Test Results** **285**

List of Figures

Chapter 1 – **Introduction** **1**

1.1 Evolution of physical scale, scope and level of detail along the thesis core applications 5

Chapter 2 – **Stress Wave Generation and Propagation** **9**

2.1 Early mechanical pumping of a bulk explosive 12

2.2 Electronic detonator 13

2.3 Partition of explosives' energy when blasting in rock. 14

2.4 Detonation reaction in a borehole and corresponding radial pressure 15

2.5 Charge detonating in plexiglas 15

2.6 Effect of blasting in rock around the borehole 16

2.7 Car-suspension-rail system 17

2.8 Schematic representation of earthquake generation and corresponding stress waves 18

2.9 Schematic representation of spherical and cylindrical wave propagation 21

2.10 Divergent and plane wave propagation 22

2.11 Compressive, Rayleigh, shear and Love waves 26

2.12 Transmission and reflection of compression, vertical shear and horizontal shear waves at discontinuities 29

2.13 Compressive waves propagated parallel and across well-defined jointing 31

2.14 P-wave spectra after crossing intact and fractured rock samples 32

2.15 Magnitude of transmission and reflection ratios for P and S waves normally incident to a discontinuity 36

2.16 Measured and DDT predicted wave spectra 37

Chapter 3 – **Vibration Impact Assessment Tools** **41**

3.1 Scatter of PPV as a function of cube and square root scalling. 44

3.2 Variation of peak particle velocities and attenuation laws for 46

3.3 Monitoring, Modelling and Regulations as a system to assess vibration impacts. . 64

Chapter 4 – **Micromechanical Modelling of Dynamic Rock and Joint Behaviour** **65**

4.1 DEM calculation cycle. 70

4.2 Resolution of contacts in 3D solids and in 2D balls 70
4.3 Representation of contact forces in two dimensional disc assembly 76
4.4 UDEC polygonal model of rock core and disk and sphere clumps 77
4.5 Contact between two balls. 78
4.6 Force-displacement normal and shear behaviour for point contact 79
4.7 Generation of a bonded assembly 82
4.8 Three dimensional bounded assembly 83
4.9 Periodic brick 83
4.10 Elastic constants of synthetic material *vs* microscopic contact parameters 84
4.11 Normal stress *vs* deformation curves in intact and fractured rock joints 87
4.12 Roughness of a natural rock fracture 88
4.13 Sketch of a rough profiles in contact 90
4.14 Micromechanical modelling of rock joint in shear 91
4.15 30x30 m^2 rock mass model with three joint sets in PFC^{2D} 92
4.16 Vertical stress *vs* vertical strain and Young's modulus 94
4.17 Particles defining the model's top and lateral boundaries 96
4.18 Generation of joint surface in BPM model 97
4.19 Ball-to-ball repulsion 98
4.20 Joint contact force-displacement law. 98
4.21 Vertical stress *vs* joint closure and tangent joint normal stiffness 99
4.22 Evolution of joint model throughout the joint compression test 101
4.23 Equivalent continuous solid dimensions of a particle string composed of spheres and disks 103
4.24 Hexagonal packing and assembly geometric relations 105
4.25 Snapshots of the velocity field of a model "at rest" 108
4.26 Wave created by a force and by a displacement load 109
4.27 Wave impact at a clamped, a free and an absorbing boundary 111
4.28 Ricker wavelet 113
4.29 Rough and fine discretization of sinusoidal wave 114
4.30 Wave dispersion in a discrete hexagonal arrangement 115
4.31 Sections of velocity probing 117
4.32 Compressive wave propagation velocity along the model 119
4.33 Relative variation of compressive wave velocity with peak frequency. 120
4.34 Relative variation of peak wave amplitude along the model 122
4.35 Velocity waveforms and frequency content of waves of growing frequency at the bottom and top of the BPM assembly 123

4.36 Relative variation of peak wave velocity measured at the bottom and top of the model . . . 124
4.37 Vertical stress *vs* joint closure curve . . . 127
4.38 Ball velocity vectors of wave passing across fracture . . . 128
4.39 Reflected and Transmitted waves from fracture submitted to normal stress . . . 130
4.40 Fourier transform of the Reflected and Transmitted waves from fracture submitted to normal stress . . . 131
4.41 Reflected frequency amplitudes for the different normal stress tests . . . 132
4.42 Transmitted frequency amplitudes for the different normal stress tests . . . 133
4.43 Reflection and transmission coefficients and energy balance . . . 134
4.44 Evolution of the dynamic and static tangent stiffness with normal stress . . . 135

Chapter 5 – **Stress Wave Propagation Test at the Bemposta Hydroelectric Complex** **139**
5.1 Location, in Portugal, of the Bemposta dam . . . 141
5.2 Map of the dam site with existing and planned underground excavations . . . 141
5.3 Views of the dam and the valley . . . 143
5.4 Surface geotechnical characterization map . . . 145
5.5 Gneissic granite and heterogeneous migmatite . . . 146
5.6 Test site discontinuity survey . . . 146
5.7 Right bank fault survey . . . 147
5.8 Geotechnical and geomechanical survey of the test adits . . . 148
5.9 Stress state in the area of the underground complex . . . 149
5.10 Map of the surface, hydraulic circuit, powerhouse and auxiliary adits . . . 151
5.11 Test adits topographic survey . . . 152
5.12 Three-dimensional representation of the underground complex . . . 153
5.13 Explosive preparation and loading . . . 155
5.14 Blasts and monitoring devices location . . . 156
5.15 GSR-16 Geosig and S-6 Peak Vibration Monitor seismometers . . . 157
5.16 Detailed representation of accelerometer bases installation. . . . 158
5.17 Data acquisition system and triaxial base installed in the wall of a adit . . . 159
5.18 Plot of the four sets' peak particle velocity *vs* scaled distance. . . . 163
5.19 Plot of direct and indirect peak particle velocity *vs* scaled distance. . . . 164
5.20 Location of blasts and measurement points of the first blast set. . . . 165
5.21 Plot of peak particle velocity *vs* scaled distance of the first blast set. . . . 166
5.22 Plot of peak particle velocity *vs* scaled distance for blast 16 (Set 1). . . . 167

5.23 Location of blasts and measurement points of the second blast set. 168
5.24 Plot of peak particle velocity *vs* scaled distance of the second blast set. 169
5.25 Plot of peak particle velocity *vs* scaled distance for blast 15 (Set 2). 169
5.26 Plot of peak particle velocity *vs* scaled distance for blast 14 (Set 2). 170
5.27 Location of blasts and measurement points of the third blast set. 171
5.28 Plot of peak particle velocity *vs* scaled distance of the third blast set. 172
5.29 Plot of peak particle velocity *vs* scaled distance for blast 6 (Set 3). 173
5.30 Location of blasts and measurement points of the fourth blast set. 174
5.31 Plot of peak particle velocity *vs* scaled distance of the fourth blast set. 175
5.32 Plot of peak particle velocity *vs* scaled distance for blast 20 (Set 4). 175
5.33 Plot of peak particle velocity *vs* scaled distance for blast 21 (Set 4). 176
5.34 Duvall double exponential blast pressure function 182
5.35 Exponential blast pressure function. 183
5.36 Triangular and linear-exponential blast pressure functions 183
5.37 Blast wave generated by hydrodynamical code 184
5.38 Three methods of application of the blast load in a finite-difference mesh 185
5.39 One dimensional plane strain model for plane wave propagation. 187
5.40 Two dimensional plane strain model for cylindrical wave propagation. 188
5.41 Finite difference model assessment of 2D and 3D wave propagation. 188
5.42 Cylindrical wave propagation in axisymmetric 1D finite difference model. 189
5.43 Absolute velocity amplitude plot of cylindrical wave propagation on a 3D plane strain model 190
5.44 Two dimensional axisymmetric model. 190
5.45 Non-dimensional peak amplitude plot of numerical models' and analytical's cylindrical and spherical wave attenuation. 192
5.46 Underground complex showing cross-section represented in 2D model 197
5.47 Finite-difference two-dimensional model of blast B15 198
5.48 Adit's real cross section and finite-difference model representation 198
5.49 Velocity time-histories recorded at the Surface tunnel caused by stress and velocity blast loading in the Outlet adit 199
5.50 PPV from the test blast and from 2D numerical model 199
5.51 Representation of the underground complex showing the 3D model bounding box. 200
5.52 3D model of the Surface and Outlet adits 201
5.53 3D model of the Surface and Outlet adits 201
5.54 Surface and Outlet adit's real and 3D model's cross sections 202
5.55 Detail of the "negative" of the Outlet and Surface adits 202

5.56 "Negative" of the adits with blasts' and accelerometer location 203
5.57 Plan view and perspective of the Surface adit showing the velocity measurement points 203
5.58 Location of blast loading, in Outlet adit 204
5.59 Plot of the blast load function 205
5.60 Comparison of the PPV from the test blast and the 3D numerical model 206
5.61 Plan view of the Surface adit interior showing the exact and alternative measurement points 207
5.62 Plan view and perspective of the Surface adit showing the exact and alternative measurement points 207
5.63 PPV evolution when place of velocity probing is changed in the Surface adit's wall and floor 208
5.64 PPV evolution when velocity is recorded in the rock mass interior 209
5.65 Location of blast loading to study the effect of load position 210
5.66 PPV evolution when place of blast is changed 211
5.67 PPV evolution due to changes in the adits length 212
5.68 Seismic velocity variation as a function of radius in a blast-excavated pressure tunnel 213
5.69 EDZ simulation on Outlet adit 213
5.70 PPV evolution due to EDZ 214
5.71 Realistic geometrical representation of the Surface adit's concrete plug and base P1. 215
5.72 PPV evolution with realistic geometrical representation of the Surface adit's concrete plug and base P1 216

Chapter 6 – **Vibration Monitoring, Control and Analysis in Large Scale** **221**

6.1 Leixões harbour aerial view 223
6.2 Barges in drilling and rock loading operation 225
6.3 Barges in rock loading operation and in repair 225
6.4 Monitoring points location 226
6.5 Reinforced concrete building and house in Leça, North of the harbour 227
6.6 Small rise buildings in Matosinhos, South of the harbour and cereal silos located Northeast of the harbour 227
6.7 Installation of Geosig's GSR-16 macro seismometer 228
6.8 Histograms of instantaneous blast charge and distance 229

6.9 Acceleration and corresponding frequency component record of a typical vibration record . . . 229
6.10 Velocity and frequency components of a typical vibration record . . . 231
6.11 Norm of the velocity time series plotted in figure 6.10 and histogram of the peak particle velocities . . . 231
6.12 PPV scattering and 50% and 95% percentile attenuation laws. . . . 232
6.13 Neural network unit cell. . . . 233
6.14 Multilayer Perceptron network structure . . . 234
6.15 Cross-validation criteria and optimum training point . . . 234
6.16 Variation of peak velocities as a function of distance and charge weight . . . 236
6.17 Iso-velocity lines calculated using the average regression equation and the Multilayer Perceptron Neural Network . . . 237
6.18 Reference finite difference model grid. . . . 239
6.19 Detail of the harbour channel showing the removed element in which walls the blast load is applied. . . . 240
6.20 Location of vibration velocity recording points . . . 241
6.21 Plots of horizontal *vs* vertical displacement along the monitoring line . . . 242
6.22 Plot of PPV *vs* distance to channel axis for the reference numerical model and the attenuation law . . . 243
6.23 Detail of the channel with modelling options for the blast loading . . . 244
6.24 Plot of PPV *vs* distance to channel axis for the reference numerical model and for the variations in load application. . . . 244
6.25 Models with 3 m and 9 m wide dykes . . . 245
6.26 Plot of PPV *vs* distance to channel axis for the reference numerical model and the models with varying dyke materials. . . . 246
6.27 Plot of PPV *vs* distance to channel axis for the reference numerical model and the models with varying dyke widths. . . . 247
6.28 Model with 3 m wide, 3 m deep ditch excavated 60 m away from quay wall. . . . 247
6.29 Plot of PPV *vs* distance to channel axis for the reference numerical model and the models with 3 and 6 m deep ditch. . . . 248
6.30 Detail of the filling material in the channel quay . . . 249
6.31 Plot of PPV *vs* distance to channel axis for the reference numerical model and the models with softer material in the quay interior. . . . 249

List of References **263**

Appendix I – **Photographs of the Bemposta Test Site** **275**

I.1 Concrete plug at the end of Surface adit seen from the inside. 276
I.2 Concrete plug at the end of Surface adit seen from the outside. 277
I.3 Base P1 in the floor of the concrete plug at the end of Surface adit. 277
I.4 Surface adit photographed from the concrete plug 278
I.5 Base P2, in the Surface adit. 278
I.6 Base P3, in the Surface adit 279
I.7 Base P4, in the Surface adit. 279
I.8 Base P5, in the Surface adit. 280
I.9 Concrete plug at the beginning of the Outlet adit 280
I.10 Detail view of base P6, in the Outlet adit. 281
I.11 Access adit and bases P7 and P19 281
I.12 Base P7, in the Access adit. 282
I.13 Base P19, in the Access adit. 282
I.14 Base P11, in the elevator and stairs shaft. 283
I.15 Base P18, in the cable adit. 283
I.16 Cable adit taking cables from the powerhouse cavern to the shaft 284

Appendix II – **Plots of the Bemposta Test Results** **285**

II.1 Plot of peak particle velocity *vs* scalled distance for blast B1. 285
II.2 Plot of peak particle velocity *vs* scalled distance for blast B2. 286
II.3 Plot of peak particle velocity *vs* scalled distance for blast B3. 286
II.4 Plot of peak particle velocity *vs* scalled distance for blast B4. 287
II.5 Plot of peak particle velocity *vs* scalled distance for blast B5. 287
II.6 Plot of peak particle velocity *vs* scalled distance for blast B6. 288
II.7 Plot of peak particle velocity *vs* scalled distance for blast B7. 288
II.8 Plot of peak particle velocity *vs* scalled distance for blast B8. 289
II.9 Plot of peak particle velocity *vs* scalled distance for blast B9. 289
II.10 Plot of peak particle velocity *vs* scalled distance for blast B10. 290
II.11 Plot of peak particle velocity *vs* scalled distance for blast B11. 290
II.12 Plot of peak particle velocity *vs* scalled distance for blast B12. 291
II.13 Plot of peak particle velocity *vs* scalled distance for blast B13. 291
II.14 Plot of peak particle velocity *vs* scalled distance for blast B14. 292
II.15 Plot of peak particle velocity *vs* scalled distance for blast B15. 292

II.16 Plot of peak particle velocity *vs* scalled distance for blast B16. 293
II.17 Plot of peak particle velocity *vs* scalled distance for blast B17. 293
II.18 Plot of peak particle velocity *vs* scalled distance for blast B18. 294
II.19 Plot of peak particle velocity *vs* scalled distance for blast B19. 294
II.20 Plot of peak particle velocity *vs* scalled distance for blast B20. 295
II.21 Plot of peak particle velocity *vs* scalled distance for blast B21. 295

List of Tables

Chapter 1 – **Introduction** **1**

Chapter 2 – **Stress Wave Generation and Propagation** **9**

Chapter 3 – **Vibration Impact Assessment Tools** **41**

3.1 Reference PPV values of the German DIN 4150 standard for blasting vibrations . 57

3.2 Reference PPV values of the Portuguese NP 2074 standard for blasting vibrations 58

3.3 Reference PPV values of the United States Bureau of Mines RI 8507 standard for blasting vibrations 59

3.4 Reference PPV values of the Swiss SN 640312a standard for blasting vibrations . 60

3.5 Reference PPV values of the British BS 7385-2 standard for blasting vibrations . 61

Chapter 4 – **Micromechanical Modelling of Dynamic Rock and Joint Behaviour** **65**

4.1 Data points of the stress-joint displacement curve and calculated joint tangent stiffness. 100

4.2 Ball and contact properties in the four modelled packings. 118

4.3 Wavelength of the Ricker waves in the four packings 121

4.4 Wave amplitude loss in the BPM model 124

4.5 Wave amplitude loss in the Rectangular model 125

4.6 Wave amplitude loss in the Hexa$_{kn=ks}$ model 125

4.7 Wave amplitude loss in the Hexa$_{kn=2.5ks}$ model 125

Chapter 5 – **Stress Wave Propagation Test at the Bemposta Hydroelectric Complex** **139**

5.1 Statistical parameters and characterization of the discontinuity sets surveyed in the test site 144

5.2 Characterization of the faulting in the right bank 147

5.3 Mechanical properties of the laboratory tested rock cores 150

5.4 Blast characteristics. 155

5.5 Location of vibration sensors. 160

Chapter 6 – **Vibration Monitoring, Control and Analysis in Large Scale** **221**
6.1 Empirical models' performance 235

Chapter 7 – **Conclusions** **253**

List of References **263**

Appendix I – **Photographs of the Bemposta Test Site** **275**

Appendix II – **Plots of the Bemposta Test Results** **285**

Chapter 1

Introduction

1.1 Background

Motivated by the optimization of space for circulation and permanent activities, use of the underground space is steadily increasing worldwide. Utilisation of tunnels and caverns for road, rail and subway circulation, distribution of electricity, gas, water and telecommunication, sewage treatment, storage, emplacement and disposal of goods and human activities presents many advantages, being in some occasions the only feasible option. Underground activities reduce surface noise, pollution and congestion; help preserve archaeological sites, historical cultural areas, towns and cities, free prime-valued surface space and preserve the environment (ITA, 2010). In large cities, even the underground space is becoming crowded. Underground lines are, in some cases, excavated deeper below existing tunnels, basements and buildings' foundations.

Underground excavation is becoming increasingly competitive due to greater demand but also because of the increasing sophistication and reliability of underground design, excavation and observation methods. Properly used, the Design–Construction–Observation triangle mitigates mishaps usually associated with underground excavations. It is therefore necessary to continue development in all these fronts and to educate the public perception of the risk associated with underground excavations.

Portugal faces two important movements regarding underground construction in rock. The first is the return to the construction of new large hydroelectric power schemes which was halted for many years mainly due to environmental constraints. Recent rise in oil price and concern with CO_2 emissions has made this kind of energy production attractive again. Not only several large dams but also upgrade of existing schemes are in the design phase or already under construction. The upgrades have two purposes. In some cases just to increase direct power production through installation of new turbines. In other cases turbine-pump systems

are installed to allow storage of energy during periods where electricity production due to other sources (especially wind-farms) exceeds demand. Most of these schemes involve excavation of long tunnels and large caverns in rock. The National Programme for Dams with High Hydroelectric Energy Potential (INAG, 2009) includes the construction of several new dams, currently in the design phase. Some of them will have with long underground hydraulic circuits reaching a total tunnel length of almost 24 km. Two other dams, currently under construction, involve excavation of shaft powerhouses and 0.3 and 0.6 km long hydraulic circuits. Power upgrade of six existing hydroelectric schemes (half of them under construction) involves excavation of five new shaft and cavern powerhouses and more than 20 km of underground hydraulic circuits.

The second movement is the integration on the European High-Speed Railway Network. High-speed rail connections with Spain and an internal Lisbon-Oporto line will be built, linking most large cities, industrial areas and harbours in the Iberian Peninsula. More than 40 km of tunnels are planned for these lines.

Finally, subway lines in Lisbon and Oporto, the two major cities in Portugal, are in constant expansion and digging of more than 4 km of urban tunnels and several stations are planned for the next few years.

There is an increase in mechanized excavation in all kinds of ground, from very soft soils to hard rock. Tunnel boring machines design and operation has seen great advancements and, in areas where minimization of environmental impacts is crucial, they are usually preferred. This thesis is not about the pros and cons of blasting, but there is a number of reasons why blasting is, and probably will continue to be, unavoidable in tunnelling, even when the tunnel or cavern in construction is near cities or villages. One of the greatest strengths of blasting, and maybe the greatest advantage over tunnel boring machines, is its versatility. Blasting is effortlessly adaptable to virtually any excavation geometry, the initial cost is small in comparison to mechanized means and blasting can usually start quickly in several fronts, when necessary.

Among most relevant sources of ground vibration–blasting, road and rail (especially high-speed) circulation or construction activities such as pile driving–earthquakes are the most dangerous. Causing numerous victims each year, most due to structural collapse of buildings and bridges, earthquake-generated ground vibrations and dynamic structural behaviour is the object of considerable attention, especially in seismic regions, as is the case of Portugal and some other Mediterranean countries. There are some areas of superposition, but also considerable offset, between the methods of geotechnical earthquake engineering and those necessary to successfully address blast wave propagation in rock masses. Earthquake and blast vibrations differ in frequency–blasting vibrations being higher–and amplitude–blasting vibrations being smaller. Earthquake engineering focuses on the non-linear effects that take place in the ground and structures. In blasting, non-linear effects are usually confined to the vicinity of the blast

(military and very large civil blasts being the exception). Civil blasting for rock excavation in surface and underground construction and quarrying is the major source of the vibrations considered in this thesis.

Public awareness and intolerance to annoyances related to construction activities has grown steadily in the last decades. The impacts of the underground construction in cities, though less important than surface construction's, are evident, especially when rock has to be excavated by blasting. To the effective impacts adds the populations' mistrust regarding underground excavations. The major environmental consequence of rock blasting are stress wave generation, noise, which in extreme cases may form hazardous shock waves, dust and rock projection. Ground vibration, which is one of the most hazardous and also most difficult to mitigate, induces discomfort in people that fell the vibrations, be it directly through the ground or via buildings or other structures. Vibration also damages or disrupts operation of equipment and causes aesthetic and, in extreme cases, structural damage.

New dams and associated circuits are usually built far from inhabited places and thus their impact on populations is usually small. Even then, blast vibrations may hamper construction activities by delaying, for example, application of fresh concrete which may be damaged during curing. Excavation of dam's foundations, hydraulic circuits or caverns in the vicinity of working dams and powerhouses requires great precaution since vibrations can damage electronic control devices or sensitive mechanical equipment such as turbines.

The most significant feature of rock masses is their discontinuity. Rock masses are stricken by fractures and faults of different origins. Jointing plays an important role in the way most rock masses bear loads, deform and fail. Fluid flow is also mainly determined by the joint network.

Stress waves' interaction with discontinuities through reflection, refraction and absorption mechanisms is the major cause of attenuation. Though it is not easy to investigate the internal structure of joints under dynamic loads, the stress wave–rock discontinuity interaction has been subject to experimental and analytical investigations. The resulting Displacement Discontinuity Theory adequately explains rock joints' basic dynamic behaviour, but questions still remain unanswered.

There is, thus, a need for tools that evaluate the way in which vibrations are generated, propagate across the ground and damage structures or equipment and disturb people. Traditionally, the problem has been addressed by means of empirical attenuation laws parametrized from *in situ* measurements. This methodology not only yields results that can be directly compared with regulatory limits but is also expedite and economical. Since in these laws the variables are the blast energy and the distance to the blast, other important factors that are not easily characterized by a scalar variable cannot be considered. These include preferential

directions of vibration emission at the source, ground excavations blocking the vibrations or ground heterogeneity that either attenuate or guide vibrations.

Numerical models are nowadays used across all engineering areas. In geotechnical engineering they have become an essential tool in all kinds of situations, from displacement predictions to safety calculations and also on the investigation of the internal mechanics of rock material. Models that represent the geometry and properties of the rock mass and structures therein can incorporate many of their characteristics and influence on the stress wave propagation, rendering possible the simulation of real and hypothetical scenarios.

This thesis comprises three core applications, each addressed in an independent chapter. The first is micromechanical simulation of stress wave propagation in intact rock and across rock joints. The second is a blast test in an underground complex and corresponding numerical simulation. The third is the monitoring of a large underwater blasting in an urban area, which is complemented by statistical and numerical simulation.

Along each of the three applications there is a discontinuous increase on the scale of the problem in three different levels. Fractures studied in the first application are some centimetres long and are modelled by a model with elements with about one millimetre. As such, the level of characterization (geometric and mechanical) of the problem must be very high, almost grain-size. On the underground blast test there is a huge jump in geometric scale, which goes up to dimensions in the order of one hundred metres. The level of information of the rock mass goes down accordingly. Finally, in the underwater blast monitoring the working area is more than two kilometres long and there is almost no information on the ground characteristics. The methods used and developed across these situations range from pure phenomenological exploratory micromechanical models to widely used and established attenuation laws. Thus, this thesis aims to contribute to knowledge advancement and tools development and amelioration for a wide array of situations. Figure 1.1 illustrates this evolution graphically.

1.2 Thesis objectives and lines of action

Three important needs were identified in the domain of stress wave propagation in rock masses, and three corresponding lines of action, which do not correspond directly to the three applications enumerated in the end of the previous section, were devised to contribute to these needs.

The first is the simulation and understanding of stress wave interaction with real rock joints. Stress waves–rock fracture interaction is a fundamental investigation that is mainly conducted by laboratory testing of small size samples and is now moving to larger *in situ* studies. Particle micromechanical models, which have seen advancements in recent years, are a particular class of

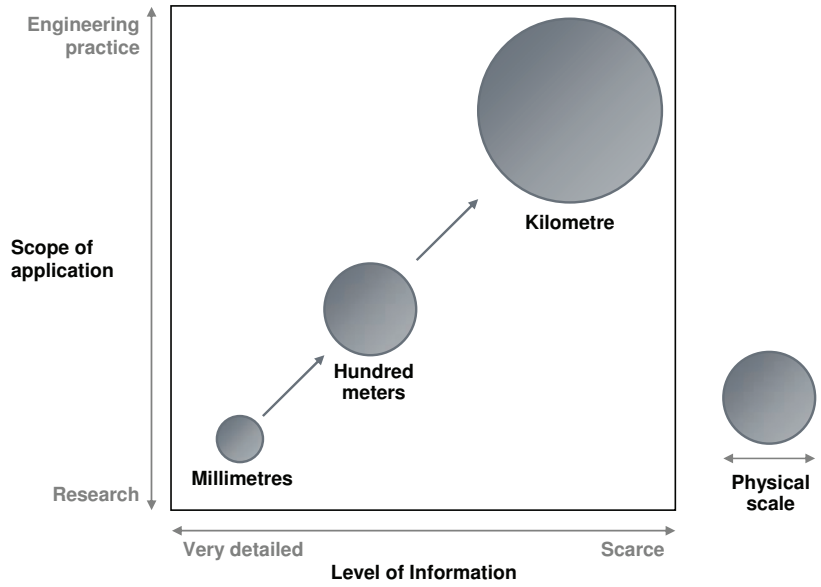


Figure 1.1: Evolution of physical scale, scope and level of detail along the thesis core applications. Smaller circle represents the micromechanical simulation, the middle circle the underground blast test and the largest circle the underwater blasting monitoring.

models in the sense that they replicate the microstructure of rock and its internal mechanisms of deformation and failure, but their application to the simulation of stress wave propagation in rock is, at best, incipient. It is possible, and desirable, to complement laboratory and theoretical study of stress wave–rock fracture interaction with numerical models that interpret and simulate this interaction at micromechanical level.

The purpose of this line of investigation is twofold. First, to establish the soundness of micromechanical models in simulation of stress wave propagation in rock masses. This will allow a deeper understanding of the details of stress wave interaction with intact rock and set a base for the micromechanical simulation of stress wave interaction with rock joints. Although several theoretical approaches explain the dynamical behaviour of rock joints, the Displacement Discontinuity Theory being the more prominent, they all involve some degree of simplification, especially on what concerns fracture geometry. Using particle modelling, this line of action aims at simulating the wave-fracture interaction of real joint geometries requiring the least possible simplifications.

The second line of action, nearer to the realm of the practice of underground engineering, aims to answer to a need for greater insight on how stress waves propagate in rock masses with presence of excavations and other singularities. A more profound perception and knowledge will lead to better blasting plans, especially near vulnerable targets and also to more efficient vibration monitoring.

Two different large dimension real cases in which the author has been involved provide the basis for analysis. The first case comprises an *in situ* blast test in the Bemposta hydroelectric underground complex. The test preceded the excavation of a new hydraulic circuit and powerhouse while keeping the existing ones in operation and involved blasting and vibration measurements along a network of adits excavated in rock at a depth of a few hundred metres. In the second case, the vibration monitoring of a large underwater blasting operation in the Leixões Harbour is described. Its results are compiled and analysed with the help of statistical tools. Important insights in the evolution of stress waves in rock masses are drawn from the field tests results.

The third line of action is the development and improvement of numerical models to simulate vibration propagation in rock masses at several scales and levels of information of the rock mass properties. There is a clear need for increased modelling of the propagation of stress waves in rock masses through more advanced numerical models that permit not only reproduction and understanding of observed stress waves in complex realistic sites, but also qualitatively forecast vibration propagation in hypothetical scenarios. Dynamic simulations of blasting still lacks concrete methodologies and well founded guidelines.

For this purpose, two and three-dimensional numerical models were used to simulate the blast test on the underground hydroelectric complex and the harbour underwater blasting works and to test a number of hypothetical conditions of the blasts and the ground. The development of these modelling activities provide guidance on best practices for the efficient simulation of blast loading, quality of wave propagation, vibration extraction and treatment, contributing to establishing guidelines for the dynamical simulation of blast vibration propagation and impact in rock masses.

The simulations contribute indirectly to the previous line of action, since models' results expand, enhance or confirm both sites' observations of stress wave propagation.

1.3 Thesis outline

In face of the objectives presented in the previous section, the thesis was structured in seven chapters, of which this introduction is the first.

The two introductory chapters, coming after this introduction, present a state of the art on blast stress wave generation and propagation phenomenology and on the instruments currently available to understand, control and simulate it.

Chapter 2, Stress Wave Generation and Propagation, provides the necessary background on stress wave generation and propagation in rock masses with an emphasis on interaction with rock fractures.

Chapter 3, Vibration Impact Assessment Tools: Modelling, Monitoring and Regulations, starts by describing the tools available to assess vibration levels: analytical solutions, statistical models and numerical simulation. It then mentions the most important impacts of vibrations on structures, equipment and people and describes some of the more relevant vibration control regulations.

The three following chapters constitute the thesis' core and develop the main lines of action, harbouring the original developments of the thesis. Each chapter focuses on a different perspective of stress wave interaction with rock fractures and rock masses.

Chapter 4, Micromechanical Modelling of Dynamic Rock and Fracture Behaviour, presents particle discrete element method models that simulate rock at the grain-level. Models of hard rock cores are generated and their static elastic properties tested. The core is then submitted to dynamic excitation and the models' dynamic properties are established. A new contact constitutive model for rock fractures wall-to-wall contact is introduced and the normal static and dynamic properties of a realistic discontinuity representation are determined and compared with available theoretical models.

Chapter 5, Stress Wave Propagation Test at the Bemposta Hydroelectric Complex, describes low intensity vibration tests performed in the underground complex of the Bemposta dam. The rock mass and adits where the blasts were performed are first described. Then the test results are thoroughly analysed and first conclusions on how vibrations travel and arrive at different locations in the complex are drawn. Two and three-dimensional simulation of blasting stress wave propagation is generically tested and then a part of the test is modelled, also using two and three dimensional numerical models. The results of the numerical models are compared with those obtained during testing and improvements of the models are tried and evaluated.

Chapter 6, Vibration Monitoring, Control and Analysis in Large Scale – Deepening of the Leixões Harbour, refers to a much larger underwater blasting operation on the Leixões international harbour, near Oporto. The scale increase from the previous chapter is tenfold, but the level of detail of the ground parameters and of the blasts is much lower, resulting in a dispersion of vibration maxima whose cause cannot be easily attributed. Vibration attenuation laws and artificial intelligence techniques are calibrated and their performance analysed. Finally, the results of simple numerical models testing the influence of hypothetical ground's natural and artificial singularities are reported.

In the last chapter the more relevant and innovative conclusions are summarized and suggestions for future developments of the work are suggested.

Chapter 2

Stress Wave Generation and Propagation

2.1 Introduction

The treatment of mechanical problems as static phenomena is always a simplification of reality, although frequently a very reasonable one. All loadings upon solid bodies, be they transient or permanent in time, stress releases or imposed deformations, take a finite amount of time to propagate from their place of origin. When a permanent load is applied to a body it will be out of balance for a short period of time. This interval lapses from the instant the load is applied to the instant when reactions at the supports are mobilized and equilibrium is reached again. Usually, this dynamic effect leaves no permanent effect and the time lapse during which the structure is out of balance is negligible. Under these conditions, if the structure behaves elastically and the load is non-permanent, the initial and final equilibrium states are equivalent.

In nature, some wave propagation phenomena are visible to the naked eye. The classical example is the rock thrown into a pond, producing circular waves that travel from the impact point, taking several seconds to reach the shore. In the ocean, at a larger space and time scale, waves generated by a storm may travel for several days before reaching shore. On the same space scale, waves generated by an earthquake travel around the globe in some minutes, allowing the localization of the source of the earthquake, by comparison of arrival times at three or more synchronized seismometers. Similarly, vibrations caused by a blast in the ground will propagate from the blast point to reach structures, equipment or people.

In all these situations, different kinds of waves (surface and bulk waves) and materials (water and solids) are present, but there are common features. First, all the waves carry energy transmitted to the medium by an exterior perturbation. Second, the propagation of the energy

is done without permanent displacement of the particles, since the passage of the wave causes them to move around an equilibrium position. Third, if we look at the wave as a carrier of information, the medium can be divided in two regions: one is aware of the perturbation, the other is not. In the first example (pond), the first region is a circle limited by the wave front. The velocity at which the wave front advances depends on the material's stiffness and density, which define the capacity of the medium to store and transfer potential and kinetic energy.

In solids, wave passage causes deformation of the medium that is associated to the stress variation. For this reason waves in solids are also called stress waves. Several excellent text books (Achenbach (1973); Kolsky (1953); Bedford and Drumheller (1994)) display the deduction of the wave equations in solids, starting with simpler examples like waves on strings, and then advancing to the three dimension general equation. To arrive at the general law, several paths are possible, either through energy balance or continuum mechanics laws. As propagation of stress waves in rock and their interaction with fractures are the main themes of this thesis, a short presentation of the laws governing wave propagation in elastic linear solids is due. This is presented in the following sections of the chapter.

To anyone familiar with rock mechanics, it is clear that practical problems rarely come in simple geometric settings, rock masses are rarely continuous and rock does not follow ideal linear reversible paths. As a consequence, propagation of waves in rock masses is especially complicated, involving phenomena such as velocity dispersion and frequency-selective attenuation due to the rock material, and also wave reflection, conversion and refraction at fractures. Real-life problems must be simplified and then handled by means of analytical solutions, empirical strategies or numerical simulations. These methods will be presented in chapter 3.

This chapter continues by introducing the mechanisms of wave generation in the situations that are most common and cause greater impacts: earthquakes, rock blasting and road and rail circulation. The formulation of the laws governing wave propagation in linear elastic media is presented and the state of knowledge on wave propagation in rock masses is detailed. The influence of both small scale heterogeneities such as voids and cracks embedded in the rock matrix and macroscopic discontinuities such as fractures and interfaces is highlighted and the current theories applicable to their dynamic behaviour laid out.

2.2 Stress Wave Generation

The most important sources of stress waves in the ground are earthquakes, rock blasting, industrial or construction machinery, rail and road traffic. Less frequent, at least in most places on Earth, are mine induced seismicity, rockbursts, nuclear or other kind of military blasts, earth and rock slides. The sources most relevant to the Portuguese reality and to the scope of this

thesis - rock masses - will be addressed in this chapter. They will be discussed in the aspects and with the detail necessary for the development of the work.

2.2.1 Rock blasting

There is excellent literature on every aspect of rock blasting, covering explosives properties down to the molecular level, rock fragmentation and projection (*e.g.* Persson *et al.* (2001), Roy (2005) or the Blasters' Handbook (Hopler, 1998)). Some technological aspects of rock blasting that are relevant to the generation of vibrations will be briefly described.

Explosives used in rock blasting

History of explosives is interwoven with humanity's best and worse traits: construction and war. Black powder discovery is attributed to the Chinese who are said to have used it in fireworks as early as the 10th century but it was the monk and scientist Roger Bacon who in 1242 published its formula.

Black powder was used from the Middle Ages until the modern time in mining and construction, in bombs and as a propellant in ammunition. During the construction of the first railway lines in the XIX century, millions of tons were used every year, with consumption reaching its peak and then declining fast in the beginning of the 20th century, after World War I.

In 1846 Ascanio Sobrero, a professor in Turin, Italy, synthesised Nitroglycerin. Having many times the explosive power of black powder, nitroglycerin almost completely replaced it in a few decades. This tendency was accelerated by the accidental discovery of dynamite by Alfred Nobel in 1861. Dynamite, which is no more than sawdust or kieselguhr (a naturally occurring, soft, siliceous sedimentary rock that is easily crumbled into a fine powder) imbibed in nitroglycerin, solved, for the time, the greatest problem associated with nitroglycerin fabrication and use: its instability. An enormous advance at the time, dynamite ruled explosives industry for a large part of the XX century. Today it is considered dangerous and its use is residual. History of explosives is not only stained by their use in military activities but also, in a much smaller scale, by large accidents in their manufacture and use.

Advances in nitroglycerin-based explosives alleviated problems such as toxic fume production and water sensitivity, but after the middle of last century new civil explosives were discovered that overcome nitroglycerin in every aspect but explosive power.

Ammonium nitrate was initially used as an ingredient in dynamite but its potential as an explosive by itself was rapidly evident: it is safer to use and fabricate. Subsequent progresses promoted the fast replacement of dynamite by ammonium nitrate-based explosives. One of these is the mixture of ammonium nitrate and fuel oil, ANFO, discovered in 1960. It became

extremely popular due to the fact that it is hard to ignite accidentally and can be pumped into boreholes (similarly to the slurry in figure 2.1). Its major weakness is the sensitivity to water. Until the invention of water based explosive gels the only solution was to package it in water resistant containers, when needed.



Figure 2.1: Early mechanical pumping of a bulk explosive. Taken from Persson *et al.* (2001).

In water gel explosives, the explosive agent (and other substances such as oxidisers) are mixed in an emulsion that is water resistant and can therefore be used in the presence of ground water or in underwater blasting.

Cost of explosive application must be calculated taking into account not only its nominal price but also its transportation, loading, initiation and the resulting rock fragmentation output. For this reason, borehole excavation technology is closely tied with the evolution of explosives and initiation systems.

Initiation systems

The devices employed to start the detonation of the main explosive charges are very briefly presented in this section. In what concerns vibration production, the initiation system plays an important role, as it determines how and when each charge will detonate. Each explosive

sensitivity to detonation varies widely and the methods of initiation have evolved to deliver ever-growing reliability.

There are two main parts in an initiation system. The first is the electric wiring or pyrotechnic chord that transmits the signal from the device starting the blast to the detonator. The second part is the detonator itself. Early pyrotechnic detonators were no more than a small container with black powder or other explosive placed inside the explosive mass. Pyrotechnic detonators are still in use today and though more sophisticated, the principle is the same. The composition and length of the pyrotechnic fuse determine the time delay.

Studies by several authors (e.g. Dowding (1996)) indicate that with precise time-delays better fragmentation of rock and smaller vibration levels can be attained, as they allow the frequency content of the vibrations to be manipulated. Time delays as small as a few milliseconds can be attained with pyrotechnic detonators.

Electronic circuits housed in the detonator replace the pyrotechnic fuse with several advantages. Timing precision is about ten times that of pyrotechnic detonators. Moreover, microchips can be mass-produced at reduced costs, do not deteriorate with time, are insensitive to shock and heat and contain smaller quantities of hazardous elements. Figure 2.2 shows a schematic diagram of the internals of an electronic detonator.

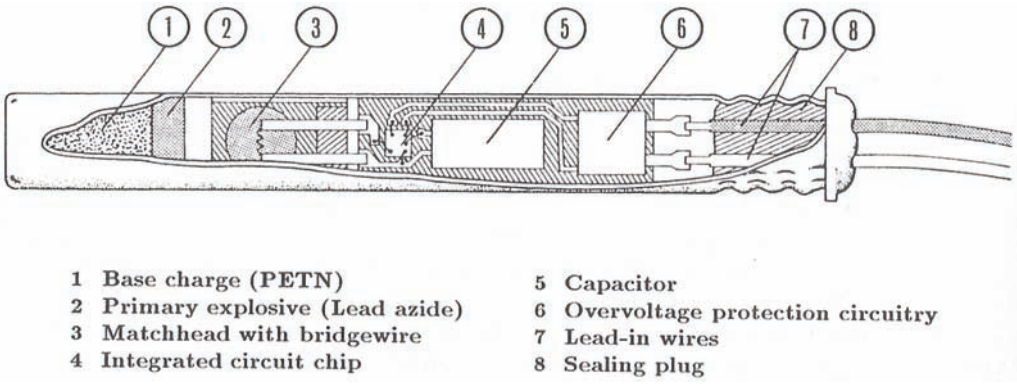


Figure 2.2: Electronic detonator. Taken from Persson *et al.* (2001).

Stress wave generation

When the first railroads were built across North America and England in the XIX century, rock blasting's only purpose was to move rock out of the way as fast as possible with no regard for vibration or quality of fragmentation.

Today the situation is very different in every aspect and a deeper knowledge of the processes that take place in and around the detonation is essential to comprehend how the rock is fractured

and stress waves irradiate. Fragmentation and vibration production are interdependent because vibrations are an unintended side-effect of fragmentation. In an ideal explosion all energy would be spent breaking rock and no vibration would be produced. Figure 2.3 displays the partitioning of the explosives energy in an explosion.

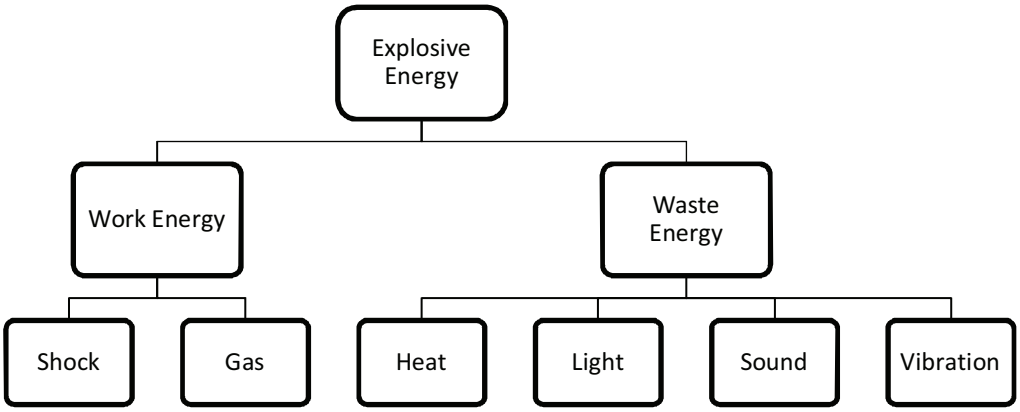


Figure 2.3: Partition of explosives' energy when blasting in rock.

Not intending to look too deeply into the complex phenomena that take place during the explosion, a brief description of the process is indispensable. The detonation of an explosive is a reaction started by means of heat, shock, friction or a combination of these factors. The products of explosive's detonation are a high intensity shock wave followed by a mixture of gases under high pressure and temperature.

An explosion in a borehole can be divided in two phases. Firstly, the reaction of detonation propagates through the explosive generating a violent shock wave that travels to the surrounding rock. The speed of propagation of the reaction is called detonation speed and is a characteristic of the explosive. In a second phase, that advances behind the detonation reaction, the produced gases' volume increases inside the borehole and they exert pressure, smaller than the shock wave but lasting longer, and eventually escaping through fractures. Figure 2.4 schematically presents the described mechanism while figure 2.5 illustrates a laboratory detonation test in plexiglas.

The development of the explosion process depends mainly on the properties of the explosive, shape and diameter of the borehole, mechanical characteristics and state of tension of the rock. Due to the high speed of deformation, stress in rock attains very high levels of tension (2,000 to 10,000 MPa) and of temperatures (1,500 to 4,000º C). Under such conditions, rock behaves as a fluid under pressure. In the ring immediately around the borehole (see figure 2.6) the rock material is subjected to high pressures caused by the initial shock wave and is pulverized. The shock pulse continues to propagate beyond this region causing strong radial fracturing. The

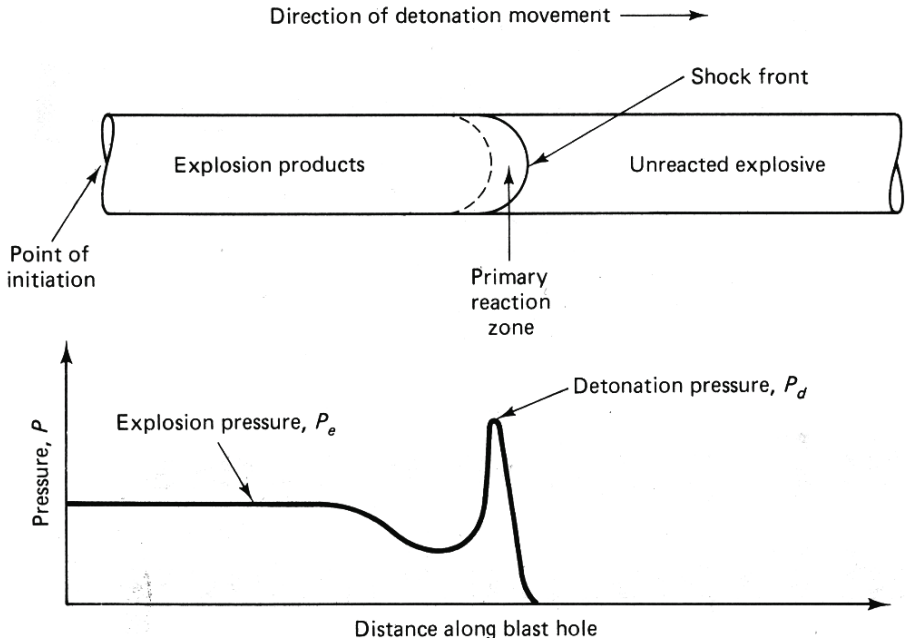


Figure 2.4: Detonation reaction in a borehole (top) and corresponding radial pressure (bottom). Taken from Dowding (1996).

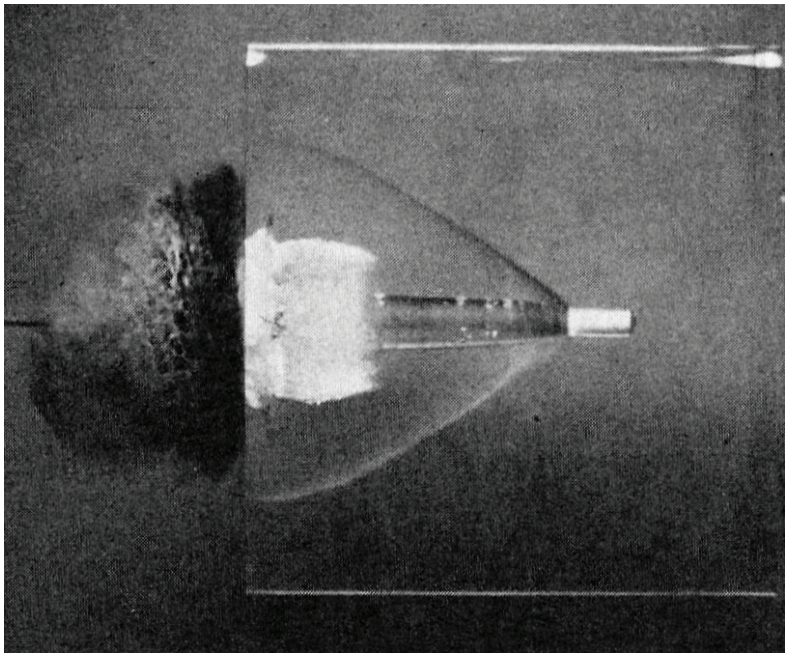


Figure 2.5: Charge detonating in a 5.2 mm borehole in plexiglas. Notice the shock wave and gas release, similar to figure 2.4. Taken from Persson *et al.* (2001).

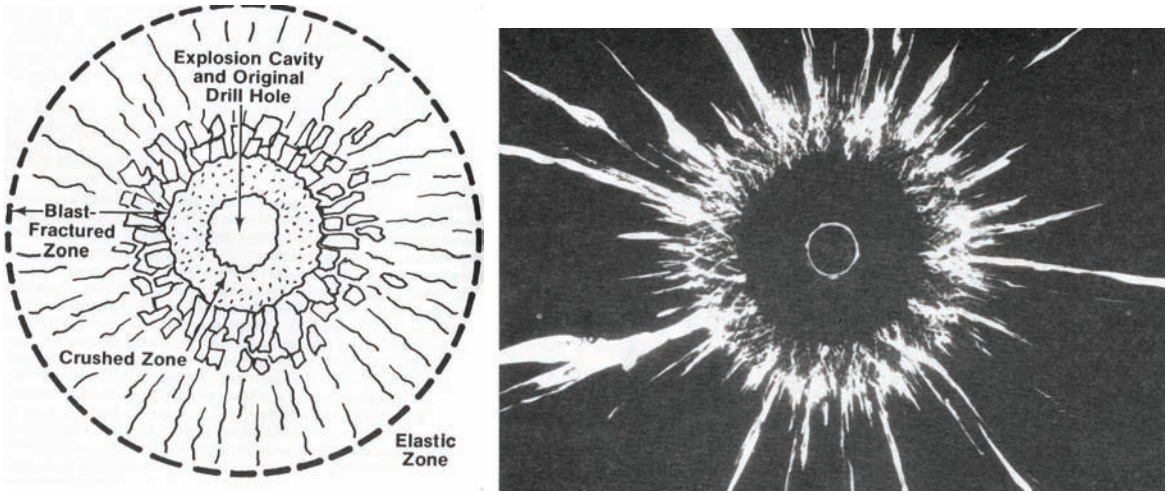


Figure 2.6: Effect of blasting in rock around the borehole (left, taken from Hopler (1998)). Crack pattern in plexiglas around a charge detonated in a 3 mm diameter borehole (right, taken from Persson *et al.* (2001)).

energy absorbed in these zones depends on the deformability and strength of the rock and it is usually assumed to vary from one third to one tenth of the explosive energy.

The expansion of the gases produced by the decomposition of the explosives lasts much longer than the detonation and exerts pressure in the explosion chamber walls. The borehole diameter increases and gas escapes through the cracks increasing their extension and width. At a certain distance from the explosion the stress level decreases and no longer exceeds the resistance of the rock. From there on the shock wave spreads elastically, that is, the particles return to their initial position.

In recent years some hydro-dynamic computer codes include the equation-of-state of the explosive, mechanical response of rock including plasticization and fracturing under extreme thermal and mechanical conditions and even gas circulation in the generated and existing fractures. These codes now complement laboratory studies and help in the testing of hypothesis, avoiding testing programmes which may be too expensive or hard to realize (*e.g.* Zhu *et al.* (2007)).

2.2.2 Rail and road circulation

The ground and aerial vibrations are among the most important environmental impacts of the exploration of railway and, in a smaller scale, of roads.

While in some cases cities have developed around roads and railway lines, in other cases the expansion preceded planning and construction of adequate communication lines. The first case is typical of the outskirts of large cities (in Lisbon, Sintra or Cascais rail lines are a per-

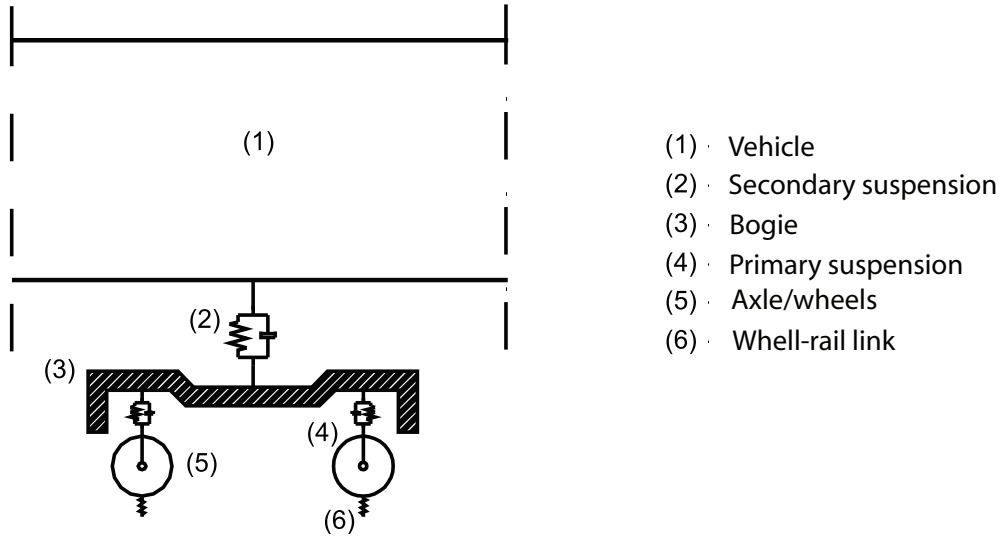


Figure 2.7: Car-suspension-rail system. Adapted from Ribeiro (2004).

fect example) where buildings have been built linearly along rail and roads. The inhabitants suffer their negative impacts during all the working time. In the second case, usual in densely constructed urban centres, surface or subterranean metropolitan lines are built in difficult conditions (the recent Oporto metro being a perfect example). In this case the construction and exploration of the lines disturbs inhabitants, as tunnels may in some cases be a few metres away from buildings' foundations.

Characteristics of the vibration generated by a railroad circulation depend on the type of vehicle, speed and the support and load transmission infrastructure. Vibration due to road traffic is generally less important but the generation mechanism is similar. Because the process is far simpler and easier to observe and reproduce than explosions, there are analytical models that reproduce it with some accuracy. However, since each vehicle/track pair has a "specific signature", *in situ* measurements are the only way to determine the emitted vibrations.

A vehicle can be described as a mass connected to a suspension system that circulates on a track with a more or less irregular profile, as displayed in figure 2.7. Equations of motion for this system can be easily written and solved. In circulation at surface the support structures between the rail and the foundation are traditionally composed of pre-stressed concrete or wood sleepers that rest on a crushed stone ballast bed. Under the ballast, one or more layers of soil mixture, called the subgrade, further degrades the load before it reaches the foundation. In ballastless tracks the rails are either embedded in a concrete slab or supported by sleepers.

The vibration generated at the wheel-rail contact is transmitted to the supporting structure and from there to the ground, so the whole system, including ground characteristics, has to be considered when calculating vibration levels. In the case of underground circulation, the tunnel

geometry and materials must also be taken into account.

It is usually at the level of the rail-sleeper-ballast link that intervention to reduce vibration starts by placement of isolation pads between the several elements.

Finally, high speed circulation brings new problems beyond the expected speed scale effect. When train speed becomes higher than the velocity of propagation of stress waves in the ground, supersonic phenomena of high potential destructive power take place. This is, however, not an issue in rock masses but only in very soft ground.

2.2.3 Earthquakes

Vibrations produced by earthquakes and by blasts differ in their frequency contents, duration and intensity. While blasts release a small amount of energy close to the targets (structures), earthquakes' epicentres (figure 2.8) are usually at least tens of kilometres away, and the amount of energy released is of a completely different scale. This said, many of the tools that are developed for one discipline can be adapted to the other, since the underlying phenomenon is the same. For this reason, a short mention is included to the impact of earthquake induced vibration on rock masses and on the structures on them.

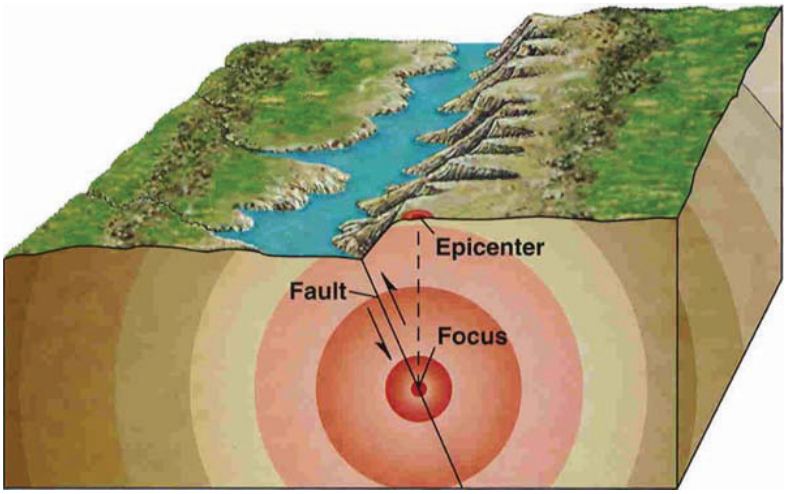


Figure 2.8: Schematic representation of earthquake generation and corresponding stress waves. Taken from http://www.stevekluge.com.

Seismic risk is generally disregarded in the design of underground structures, even when they are in regions with known seismic activity. It is considered that underground structures response is satisfactory due to the fact that they follow the movement of the ground with very small inertia effects and irradiate all received energy to the surrounding medium, unlike buildings that have much smaller interface area with the ground. The other cause for not

considering the seismic action on underground structures is that understanding of ground's behaviour under dynamic actions and of the tools for assessing that behaviour are not widely disseminated. Nevertheless, underground structures have suffered damage and in some cases, severe failures during earthquakes.

2.3 Stress wave propagation in elastic and non-elastic media

Vibrations due to blasting are generated by the extreme stresses, gas pressures and associated temperatures produced by the detonation of the explosive that pulverize and break the rock around the borehole, while earthquake-generated stress waves are released when the resistance of the contacts between tectonic plates is exceeded releasing violent bursts of energy. Given these different origins for stress waves, the use of linear elastic theory must be conveniently justified. It is true that in the vicinity of the boreholes where explosive detonates highly non-linear phenomena take place. But heating, breaking and plastification of surrounding rock spends a large portion of this energy lowering the stress levels significantly, and after a relatively short distance, usually 6 to 10 borehole diameters, stress and strain amplitudes become much smaller than the level necessary to cause permanent deformation and it can be assumed, with a small margin of error, that the propagation regime is elastic.

The amplitude of these elastic (the term is employed to distinguish waves that do not alter the properties of the material from those that cause fracturing, plastification or other damage) waves decreases rapidly, due to the material damping and to geometric effects. The first cause is related to dissipation of energy due to rock material characteristics, while the second is provoked by the increase of the wavefront surface with the distance from the source. Both causes of vibration decay will be addressed here.

2.3.1 Rock material wave attenuation

No material in nature is ideal, that is, there is no such thing as a conservative medium, and much less in geological materials. Thermodynamics' laws tell us that every time movement occurs, large or small amplitude, cyclic or not, energy is dissipated. When an elastic wave travels across a material, particles move around an equilibrium point to which they return. During this hysteretic looping, energy is lost in overcoming several kinds of resistance namely friction between grains, opening and closing of cracks, fluid squirting, heating.

Johnston (1978) lists the following mechanisms as being responsible for the attenuation of seismic waves in rock and rock masses:

- Matrix anelasticity.

- Frictional dissipation due to relative motions at grain boundaries and across crack surfaces.
- Fluid flow causing relaxation due to shear motions at pore-fluid boundaries.
- Relative motion of the matrix frame with respect to fluid inclusions in the case of fully saturated rock,
- Squirt phenomena in unsaturated pores,
- Gas pockets squeezing when only partial saturated,
- Geometrical effects due to small pores, larger irregularities, thin beds (major discontinuities, faults, rock boundaries, dikes are included here).

An important characteristic of hysteretic damping is that it is not proportional to the distance travelled by the wave but to the number of performed cycles. This means, for example, that if two plane monochromatic waves with the same amplitude and propagation velocity but different frequency travel the same distance the one with higher frequency will be more attenuated, since it has completed more cycles. The same line of thought applies to the different frequencies that are found on a broad-band wave. As the wave travels higher frequencies are more attenuated. With distance higher frequencies disappear and lower frequencies become predominant. Earthquakes that travel a large number of kilometres are a especially acute case.

Wave dispersion should not be mistaken with hysteretic damping since it is also caused by the way in which different frequencies interact with the medium. In geological materials higher frequencies travel faster than low frequencies. The consequence is that a broad-frequency wave tends to spread and even distinct waves may form.

A thorough discussion of these mechanisms would be out of place. An excellent revision of work published so far is given in Barton (2007). Chapters 4 to 6 address aspects of material attenuation that are relevant to the modelling of vibration propagation in different scales.

2.3.2 Geometrical wave attenuation

Geometrical spreading is a simpler mechanism than material damping and can be modelled analytically. When a wave travels away from a point or a spherical volume source in an unbounded media, its wavefront spreads along an increasingly larger spherical surface. If the wave source is an infinite line or cylinder, the wavefront will occupy cylindrical surfaces centred in the source, as shown in figure 2.9.

In blasts, waves are generally generated in a region which is small when compared to the volume where the stress waves spread. Exceptions exist, of course: large blasts on surface mines can be several dozens of metres long, or sometimes the object of interest is very close to the blast, as in twin tunnels. Although the phenomenon is the same, different idealizations of the propagation can be employed. In earthquakes fault rupture zones may be many kilometres long

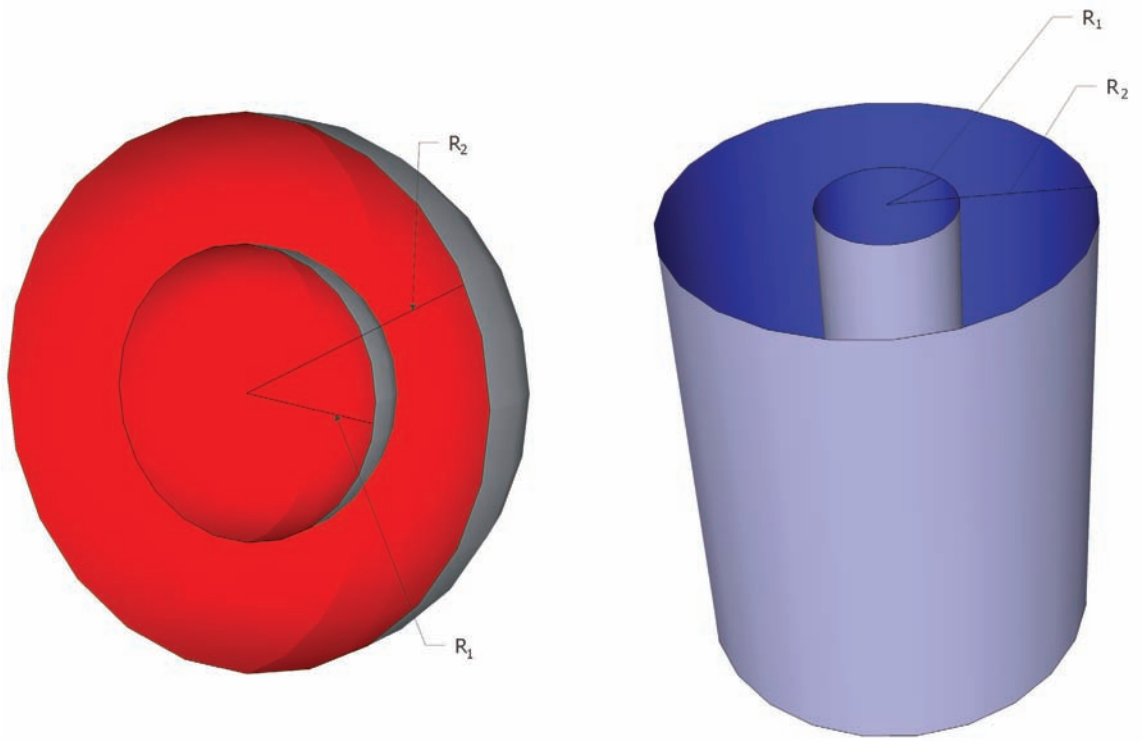


Figure 2.9: Schematic representation of spherical (left) and cylindrical (right) wave propagation.

and waves propagate for thousands of kilometres from that area. In some situations the source size is of the same order of magnitude as the distance travelled until the wave hits a structure, other times it is much smaller.

If only the geometrical spreading is considered, there is energy conservation and the attenuation of the vibration can be represented by a decay law. Particle velocities v_1 and v_2 are taken at two instants t_1 and t_2, when the wavefront is at distances R_1 and R_2 from the source, respectively. Wave energy En is proportional to the square of the vibration velocity and the total energy of the wave is proportional to the integral of the square of that peak velocity, integrated across the wavefront surface:

$$En\ \alpha \int v^2 dS. \tag{2.1}$$

Considering that the wave energy is the same in surfaces S_1 and S_2:

$$En_1 = En_2 \Leftrightarrow \int v_1^2 dS_1 = \int v_2^2 dS_2. \tag{2.2}$$

In the case of a spherical wavefront, the surface area will be $4\pi R^2$ and equation 2.2 becomes

$$v_1^2 \left(4\pi R_1^2\right) = v_2^2 \left(4\pi R_2^2\right) \tag{2.3}$$

and thus:

$$v_2 = v_1 \frac{R_1}{R_2} \tag{2.4}$$

In the case of a cylindric wavefront, the surface area will be $2\pi R$ (considering a cylinder height of 1) and equation 2.2 becomes

$$v_1^2 (2\pi R_1) = v_2^2 (2\pi R_2) \tag{2.5}$$

which can be worked to give:

$$v_2 = v_1 \sqrt{\frac{R_1}{R_2}} \tag{2.6}$$

The further away from the source both R_1 and R_2 are, the closer to one their quotient is, and the smaller the attenuation will be. Also, the directions of propagation will be increasingly parallel. For practical effects the wavefront may, then, be considered to have a plane wavefront, *i.e.* a plane wave. The point where this approximation becomes reasonable depends on the size of a real or hypothetical object that is hit by the wave (figure 2.10).

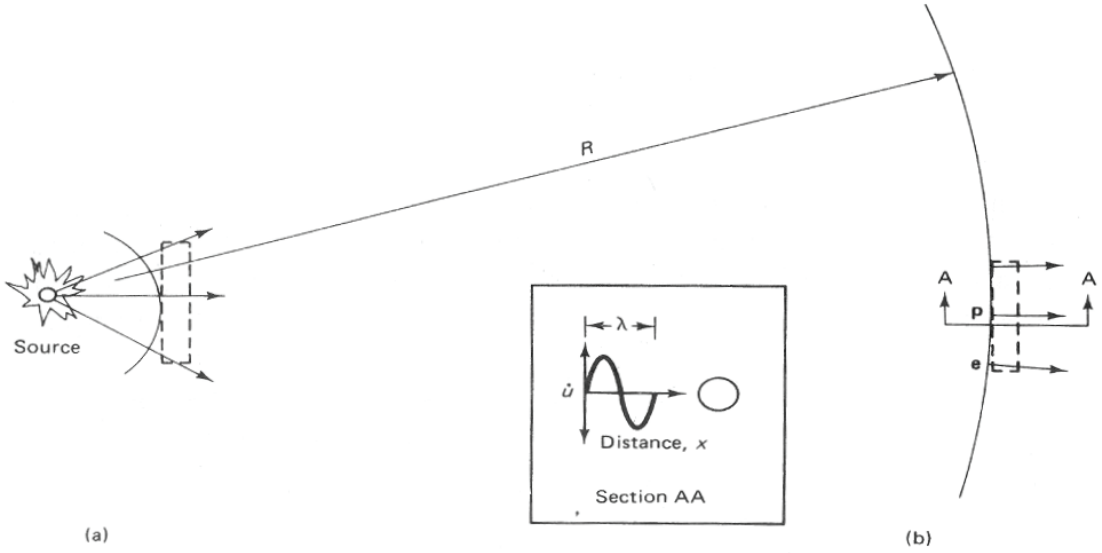


Figure 2.10: In region (a) particle motion associated with spherical or cylindrical expansion is strongly divergent, while in (b) there is plane wave expansion and particle motion is almost parallel. Taken from Dowding (1996).

2.3.3 Plane wave equation

The one dimensional, linear elastic equation of wave propagation in solids, describing the relation between particle acceleration and spacial curvature, is:

$$\frac{\partial^2 u}{\partial t^2} = \alpha \frac{\partial^2 u}{\partial x^2} \tag{2.7}$$

where u denotes displacement, x the position, t time and α is a constant value dependent on the medium of propagation. In an infinite isotropic elastic solid, equation 2.7 has two solutions,

each one corresponding to a particular way in which energy can propagate. There are the compressive waves, when particle motion occurs in the same direction as the wave propagation, and shear waves, when particle motion occurs in the plane perpendicular to the propagation direction. When a perturbation travels along the surface of a solid medium it takes the form of surface waves, which can be of two kinds: Rayleigh and Love waves. In rock mechanics, seismology and earthquake engineering, these are the most important waves. There are other solutions that correspond to waves that travel along fractures and interfaces between two media with different properties, but usually they can be ignored.

The solution for the wave equation, of which 2.7 is a particular case, can be arrived at from diverse paths, some more intuitive than others. For the sake of brevity, the demonstration from the classical book by Achenbach (1973) is followed. Some restrictions must be satisfied to ensure the validity of the elastic wave equation: the solid must be homogeneous and linear elastic, deformations due to the wave must be small and the process must be adiabatic (no heatwave energy can exit the system or be converted in heat, sound or other energy form).

Hooke's law relates stress and strain in a homogeneous linear elastic isotropic solid. In an infinitesimal volume it is expressed by (Indicial notation with $i = 1, 2, 3$ and Einstein's index summation rule are used):

$$\sigma_{ij} = L\varepsilon_{kk}\delta_{ij} + 2G\varepsilon_{ij}, \tag{2.8}$$

where L and G are Lame's first and second constants, ε_{ij} is the strain tensor, ε_{kk} is the volumetric fraction of the strain and δ_{ij} is the Kronecker tensor. Assuming that the small-strain hypothesis is valid the strain tensor is obtained by the well known displacement-deformation relation:

$$\varepsilon_{ij} = \frac{1}{2}(u_{i,j} + u_{j,i}). \tag{2.9}$$

If the self-weight parcel is disregarded, the linear momentum conservation law of an infinitesimal volume is:

$$\sigma_{ij,i} = \rho\frac{\partial^2 u_i}{\partial t^2}. \tag{2.10}$$

If the right hand side of equation 2.8 is derived and then inserted in the left hand side of 2.10 one obtains the plane wave partial differential equation:

$$Gu_{i,jj} + (L + G)u_{j,ij} = \rho\frac{\partial^2 u_i}{\partial t^2}. \tag{2.11}$$

The displacement solution u_i of a plane wave, *i.e.*, a wave with linear wavefront that travels with velocity c and is perpendicular to the propagation direction, defined by a vector p_i, is expressed mathematically by the function:

$$u_i = f(x_i p_i - ct)d_i, \tag{2.12}$$

where unit vector d_i indicates the direction in which the particle at the position x_i is moving. Replacing this generic solution in the differential equation 2.11 results in:

$$(G - \rho c^2)d_i + (L + G)(p_i d_i)p_i = 0. \tag{2.13}$$

This condition is satisfied when $p_i = \pm d_i$ or when $p_i d_i = 0$. In the first case, vectors d_i and p_i are collinear, that is, particles move in the direction of wave propagation. This is called compressive or longitudinal wave, as it induces compression and tension in the direction in which it is progressing. As $p_i = \pm d_i$, the rotational of the vectorial displacement field associated to this mode of energy propagation is null–this wave is then called irrotational wave. Because this wave progression causes change of volume in the solid, it is also named volumetric and bulk wave. Equation 2.13 yields the expression for the compressive waves' propagation velocity c_p:

$$c_p = \sqrt{\frac{L + 2G}{\rho}}. \tag{2.14}$$

The second case, $p_i d_i = 0$ implies the vectors p_i and d_i to be perpendicular, meaning particles' movement will take place in a direction normal to the direction of propagation. This is the shear or distortion wave. The divergence of the vectorial displacement field is null, as propagation happens without change of volume, so that another name for shear waves is rotational or equivoluminal waves. By introducing the condition $p_i d_i = 0$ in equation 2.13, the propagation velocity of shear waves c_s, lower than c_p (expression 2.14) is obtained:

$$c_s = \sqrt{\frac{G}{\rho}}. \tag{2.15}$$

Equations 2.14 and 2.15 can be rewritten in terms of other equivalent elastic constants:

$$c_p = \sqrt{\frac{K + 4/3G}{\rho}} = \sqrt{E\frac{1 - \nu}{(1 + \nu)(1 - 2\nu)\rho}} \tag{2.16}$$

and

$$c_s = \sqrt{\frac{E}{2(1 + \nu)\rho}}, \tag{2.17}$$

where K is the bulk modulus, G is the shear modulus (equal to Lamé's second constant), E is Young's modulus and ν is Poisson's ratio.

From the previous equations, it is evident that the dynamic behaviour of a material is governed by its stiffness and mass density. The product of a material's wave velocities and mass density, called compressive and shear impedance are:

$$Z_p = \rho c_p \tag{2.18}$$

and

$$Z_s = \rho c_s. \tag{2.19}$$

In seismology, compressive waves are also called primary or P waves and shear waves, secondary or S waves. The reason is that in a typical earthquake record, compressive waves are the first to arrive, followed by shear waves and then surface waves. This is the base of many geophysical methods and provides a very convenient way of indirectly probing a rock core or a rock mass for its mechanical characteristics.

Deformability of a rock mass, however, is not so easily defined. It depends on the strain rate, meaning an uniaxial compression test of a rock core at a high load rate yields higher stiffness than a standard test, and even higher than a creep test. The stiffness obtained from a wave propagation velocity test is even higher.

Scale also affects stiffness and strength. A test on a rock core will also yield bulk and shear modulus higher than a field dilatometer, plate or flat jack test, since these sample a larger volume of the rock mass, increasing the probability of existing imperfections influencing the result. The same applies to shear and compressive wave velocities measured *in situ* and in cores. Field and laboratory, or static and dynamic parameters are not easily matched, and relationships for one location or a specific rock type cannot be applied directly in a different environment. For an in-depth review, including an up to date and thorough enumeration of static and dynamic parameters' relationships found in the literature, consult "Rock Quality, Seismic Velocity Attenuation and Anisotropy" (Barton, 2007) .

Other means of energy propagation arise when the medium is not infinite: propagation of perturbations at the surface of a solid takes place by means of surface Rayleigh and Love waves. The most important–Rayleigh waves–propagate with particle movement in the plane defined by the normal to the surface and the direction of propagation. Rayleigh wave particle movement is elliptic in the direction contrary to the advancement of the wave and decaying exponentially with depth. Love waves appear when there is a surface layer with different characteristics. Love wave causes particles to move as in a kind of surface shear wave. As surface waves are not particularly relevant to this thesis their analytical expressions (that can be found in, Kolsky (1953)) are not presented. Figure 2.11 represents the four kinds of volume and surface waves.

Finally, analytical solutions for wave transmission in transverse isotropic media are available (e.g. Sheriff and Geldart, 1995). This solution is very useful in geophysics, where shear wave polarization is an indicator of the characteristics of the terrain. The direct integration of equation 2.11 is, in most real cases, very difficult or even impossible, as all but very specific loadings cause different kinds of waves to propagate, with the resulting wave field being a superposition of the original P and S waves with distinct velocities being reflected, converted

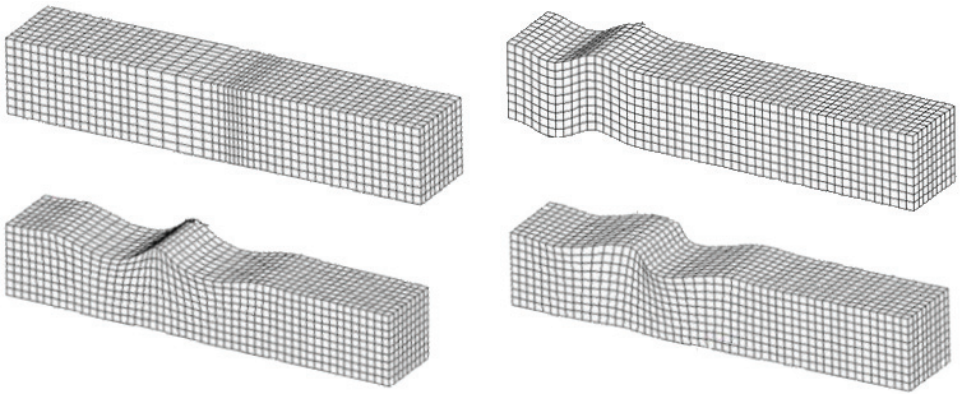


Figure 2.11: Clockwise from top left corner: compressive, Rayleigh, shear and Love waves. Adapted from http://www.geo.mtu.edu/UPSeis/waves.html.

into surface and interface waves by obstacles and the borders. In this case, the use of numerical techniques is imperative.

2.4 Stress waves in rock masses

Rock masses present several kinds of flaws differing in size, shape, filling and origin, from microscopic voids and cracks to faults. This thesis focuses on the role of rock joints in wave propagation. How can a rock joint be defined? Though the distinction between a rock joint and the voids and cracks dispersed in the rock material is clear to any practising engineer, a clarification is desirable at this stage. A rock joints is here assumed to be an extensive, approximately planar feature that interrupts rock continuity, locally defining two separate domains. Joint aperture, defined as the average distance between walls, must be small, tending to zero when compared with the other two dimensions of the joint and the wavelength of the stress waves. Joint walls touch in non-welded points of contact, and the space in between may be filled with air, water, oil or other fluids, but also soil and deposited or intruded minerals. Response to static and dynamic actions is sensitive to this filling, to the rock wall properties and to the spatial distribution of contacts. Frequently, joint walls present weaker mechanical properties due to weathering. Weathering is caused by wall-to-wall compression and shearing and by contact with physically or chemically aggressive filling materials. This description excludes rock pores, microcracks (even if these may be incipient rock fractures) and faults, since the latter have large wall-to-wall distance.

Vibrations propagating in a rock mass are affected by the macroscopic joints, by microscopic voids and cracks and by the rock material itself. When waves interact with an heterogeneity they can be transmitted across, reflected back, converted and possibly converted into heat or sound, if the discontinuity behaves anelastically. Rock behaviour is frequently assumed to be

linear and elastic, concentrating non-linearities and damage in joints.

Three general classes of models have been proposed so far to describe the propagation of stress waves in rock masses. The first are the equivalent continuum models, which consider the ensemble of the rock material and any voids, impurities, micro cracks and imperfections on the rock matrix, but are also frequently used to include the effect of joint sets. The rock material and the heterogeneities are modelled together in a homogeneous continuous material, with such properties that are a balance between the intact solid matrix characteristics and the imperfections, with propagation velocity resulting from equivalent elastic parameters. Loss of amplitude can be introduced through hysteretic damping included in the constitutive model or damping in the equation of motion.

Wave scattering models make an intermediate class. In these models, the waves progressing through the solid are considered to be scattered by cracks much shorter than the wavelength and far apart from each other so that no interaction between individual cracks is possible. Cracks are represented as collections of disc shaped voids, filled with a fluid (whose bulk and viscosity moduli can be set up to represent air). Various authors worked on this method (*e.g.* Hudson 1981, 1986 and 1988) and provided a mean to integrate scattering effects in an equivalent material which is able to simulate the frequency dependent attenuation. Laboratory tests on intact and on heat or load damaged samples showed the good performance of these models. The frailty of these models is evident when cracks have large dimensions, *i.e.*, in the case of rock joints.

Finally, an adequate theory for treating wave interaction with macroscopic fractures is the Displacement Discontinuity Theory–DDT (Schoenberg, 1980). DDT does not refer explicitly to the microstructure of rock and fractures. Fractures are treated individually as non-welded discontinuities with stress continuity and displacement discontinuity, thus providing a simple theoretical formulation for the individual wave-joint interaction. The Displacement-Discontinuity model, as presented by Pyrak-Nolte *et al.* (1990), considers the effect of different materials in both sides of the fracture, wave incidence from all angles and the presence of viscous fluids, modelled through Kelvin or Maxwell's models, in fracture internal voids. A brief description of the wave interaction with discontinuities and of the DDT model formulation follows in the next sections. An excellent in-depth review of these classes of models can be found in Cai (2001).

2.5 Stress wave interaction with rock joints

Being the main obstacle to stress waves, rock joints decrease what can be called the dynamic "quality" of the rock mass, in the same way as they decrease global stiffness in static conditions. Joints, in general, interact with stress waves by diminishing peak particle velocity, delaying wave

propagation and by filtering selective frequency ranges. Nevertheless, the influence of joints in the dynamic response has received far less attention than the voids and micro cracks present in the rock matrix, to a point that joints have been treated as collections of co-planar cracks (Myer, 2000). In the author's opinion, this can be attributed to two reasons. The first is that most of rock dynamics' research has been the responsibility of geophysics and petroleum researchers. Since they tend to look at rock masses at a larger scale than rock mechanics researchers do, the dimension of the conceptual models is usually much larger than the joint spacing, leading to idealize rock masses in terms of distributed features and properties. Not independent from the first, the second reason is that up to some years ago investigation methods and hardware capacity did not allow realistic discrete joint sets representation, something that starts to happen today.

Employ of different methods to address macro and micro features is advantageous, and both are available and can be considered. In particular, in chapter 4 we will try to show how the Particle Discrete Element Method can be used to build models that integrate micro and macro features. In the next section, the main characteristics of macroscopic discontinuities are presented.

The evolution of the theories that explain wave-discontinuity interaction will be presented hereafter. Since the final stage of this evolution incorporates previous steps (interface, joint, free and restrained borders) as particular cases, the intermediate solutions will not be presented.

A plane harmonic wave is a particular case of a plane wave (equation 2.12) that can be expressed as the product of a constant denoting the amplitude A and two harmonic independent terms: X containing the spacial description of the wave and T the time description.

$$u(x_i, t) = AX(x_i)T(t). \tag{2.20}$$

Complex number notation provides a very compact way of expressing this solution, in which k represents the wavenumber ($k = 2\pi/\lambda$) and ω the angular frequency:

$$u(x_i, t) = X(x_i)T(t) = Ae^{kx_i}e^{-i\omega t} = Ae^{kx_i - i\omega t}. \tag{2.21}$$

The advantage of restraining to plane harmonic waves is that their analytical formulation allows finding theoretical solutions while still keeping the possibility of modelling more elaborate waveforms, given that a sufficient number of Fourier series terms is used, *e.g.* Bendat and Piersol (1986).

What happens when a plane harmonic stress wave, be it compressive or shear, hits a discontinuity at an arbitrary angle? As it will be demonstrated ahead, depending on the kind of incident wave and of the angle of incidence, the resulting wave field can be composed of up to four waves that originate from the point of impact, as shown in figure 2.12.

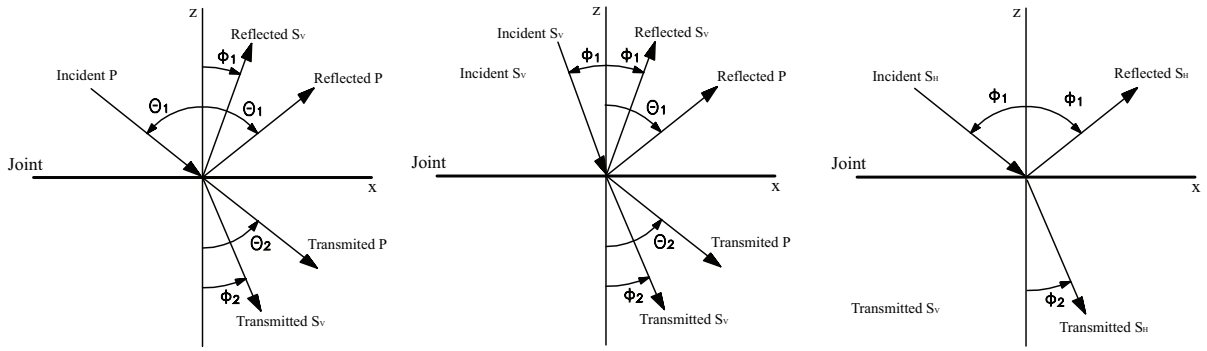


Figure 2.12: Transmission and reflection of waves at discontinuities: compression wave (left), vertical shear wave (centre) and horizontal shear wave (left).

Horizontal shear waves S_H (waves with particle motion in the plane of the discontinuity, that do not propagate "into" the discontinuity) generate two horizontal shear waves only. One is a reflected and the other is transmitted. Compressive waves P and vertical shear waves S_V can generate two, if the angle of incidence is null, or four waves otherwise. The incident and, therefore, each of the four resultant waves can be expressed in a form similar to equation 2.21:

$$\begin{aligned} u_I(x_i,t) &= I\ e^{kx_i}\ e^{-i\omega t} \\ u_{R,P}(x_i,t) &= R_P\ e^{kx_i}\ e^{-i\omega t} \\ u_{R,S}(x_i,t) &= R_S\ e^{kx_i}\ e^{-i\omega t} \\ u_{T,P}(x_i,t) &= T_P\ e^{kx_i}\ e^{-i\omega t} \\ u_{T,P}(x_i,t) &= T_S\ e^{kx_i}\ e^{-i\omega t} \end{aligned} \tag{2.22}$$

where I, R_P, R_S, T_P and T_S, are the amplitudes of the incident waves, the reflected compressive wave, the reflected shear wave, the transmitted compressive wave and the transmitted shear wave, respectively. It is through the imposition of appropriate boundary conditions to equations 2.22 that the solutions (amplitude and direction) for each of the resulting waves are deducted.

2.5.1 Interfaces between solids with different properties

The first discontinuity that was studied was the interface between two solid media with different properties. The behaviour of stress waves in solids is similar to light or electromagnetic waves, which were first studied in Optics. Kolsky (1953) presents the conditions and solutions for wave propagation across the border of two solids in which stress waves travel at different speed. This discontinuity has no properties in itself, as it is just the contact plane between two solids. It is called a welded interface or slip-free surface, as both displacements and stresses are continuous across the contact plane.

The directions of propagation of each of the four outgoing waves (as defined in figure 2.12)

will be defined by an angle that is a function of the incident wave direction and of the propagation velocities of P and S waves in both sides of the interface. These relations are known as Snell's Law, and are expressed by the following relation, which is valid for incident P and S waves:

$$\frac{\sin\theta_1}{c_{p1}} = \frac{\sin\phi_1}{c_{s1}} = \frac{\sin\theta_2}{c_{p2}} = \frac{\sin\phi_2}{c_{s2}} \tag{2.23}$$

where, following the interface/discontinuity $x-y$ orientation of figure 2.12, θ and ϕ are the angles of incidence and emergence of transmitted and reflected P and S waves, and the indices 1 and 2 indicate the domains in each side of the interface.

The displacement and stress compatibility conditions at the interface, for plane P or S waves, are:

$$\begin{array}{cc} \text{Displacement Conditions} & \text{Stress Conditions} \\ u_{x1} = u_{x2} & \sigma_{zz1} = \sigma_{zz2} \\ u_{y1} = u_{x2} & \sigma_{zx1} = \sigma_{zx2} \\ u_{z1} = u_{x2} & \sigma_{zy1} = \sigma_{zy2} \end{array} \tag{2.24}$$

The application of the above conditions to the wave equation 2.22 will yield the amplitudes of the reflected and transmitted waves, with their directions given by Snell's sine law (equation 2.23).

2.5.2 Rock joints

King et al. (1986) performed a field test that revealed the role of rock joints in wave propagation, separating it clearly from the effect of rock material. They blasted a charge in a vertical basalt columnar formation while measuring the waveforms of the seismic waves in the same column and in neighbour ones, so that it was possible to measure waves that travelled the similar distances in directions parallel and perpendicularly to the predominant jointing. Three different facts were observed when comparing the time-histories (see figure 2.13) corresponding to direct waves and to waves that crossed the joints: taking in consideration their distance to the blast, the later were delayed, their amplitude was much lower and their major frequencies shifted down.

Figure 2.14 shows the amplitude spectra of compressive waves after they cross three rock intact and fractured rock samples under varying compression. Wave amplitude in intact samples is similar in all three samples. Higher compression causes the emitting and measuring devices to couple better with the rock core leading to higher spectra amplitude. The first effect that can be observed is that in well mated fractures (mating is higher in sample E32 and lower in sample E35) makes the fracture almost insensitive to the effect of compression. In sample E30 it is possible to clearly see that when compression is low the wave does not go through the

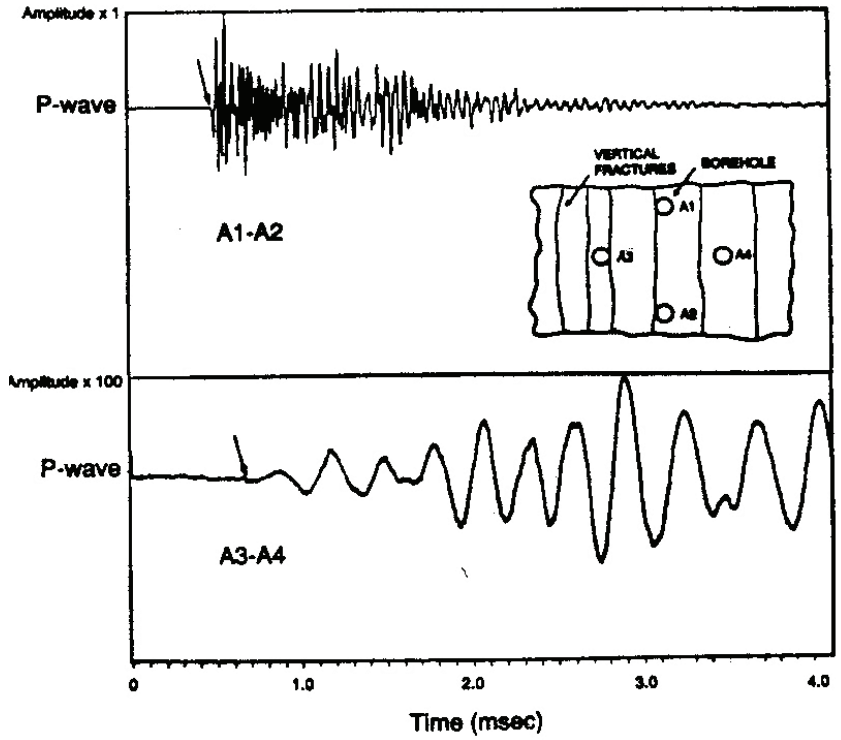


Figure 2.13: Comparison between compressive waves propagated parallel and across well-defined jointing. Taken from King *et al.* (1986).

fracture and when it increases the fracture becomes more compliant and transmits vibration better.

The questions to be answered are, then: how to quantify the influence of jointing in the amplitude, velocity of propagation and frequency of transmitted waves? Can a model correctly cover all aspects? What features of the joints are capital to their dynamic behaviour: roughness, mating, normal stress, shear stress, opening, filling?

Jones and Whitter (1967) formulated that while stresses must be continuous across the joints, displacements are not, idealizing the joint as an intercalation of elastic material in the rock. This intercalated material is defined by its thickness (b), Young's modulus (E) and shear modulus (G). Disregarding wave interference in the passage from rock to the elastic filling and vice-versa, border conditions 2.24 can be rewritten as:

$$\begin{array}{ll} \text{Displacement Conditions} & \text{Stress Conditions} \\ u_{x1} - u_{x2} = \frac{\sigma_{zx} b}{G} & \sigma_{zz1} = \sigma_{zz2} \\ u_{y1} - u_{y2} = \frac{\sigma_{zy} b}{G} & \sigma_{zx1} = \sigma_{zx2} \\ u_{z1} - u_{z2} = \frac{\sigma_{zz} b}{E} & \sigma_{zy1} = \sigma_{zy2} \end{array} \tag{2.25}$$

Kendall and Tabor (1971) recognized that the amplitude and phase delay of the transmitted

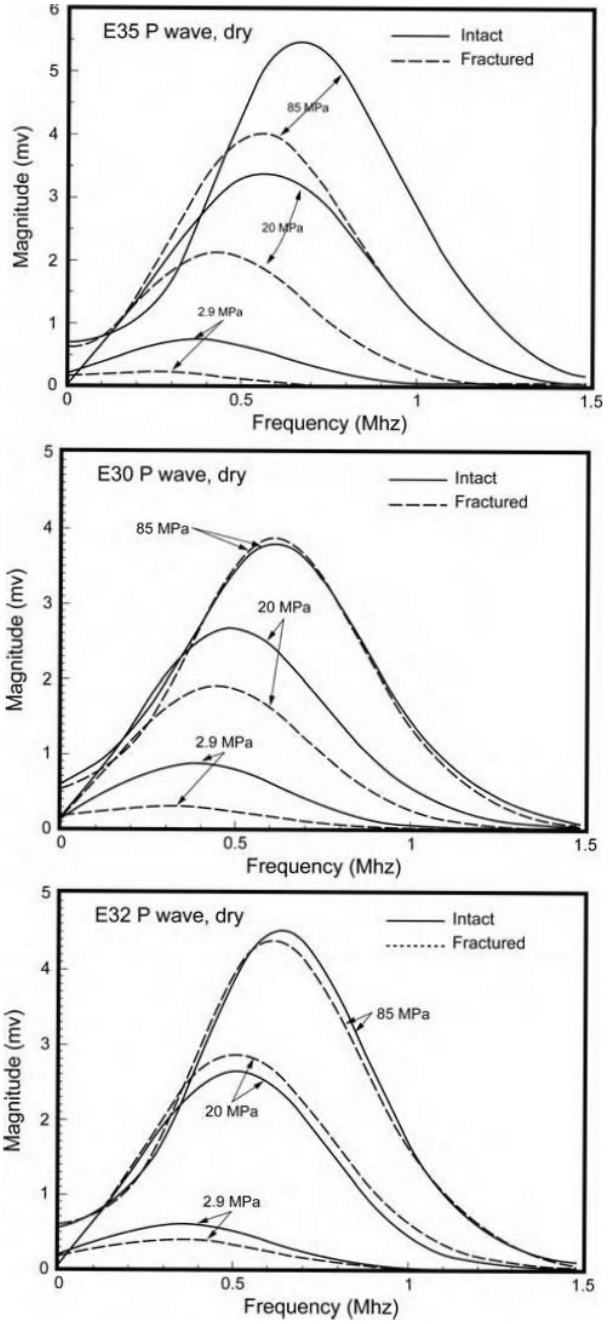


Figure 2.14: *P*-wave amplitude spectra after crossing intact and fractured rock samples. Joint mating increases from top (sample E35) to bottom (sample (E32). Taken from Pyrak-Nolte *et al.* (1990).

and reflected waves originated by a compression wave travelling normal to the joint depend on the relation of the joint normal stiffness, the impedance of the rock material and the frequency of the incident wave. By expressing the joint displacement as a function of normal dynamic stiffness K_n^{dyn} (units are pressure/length), it is included as a boundary condition in the wave equation of a normal P wave. They were then able to match the results of tests of artificial joints, fabricated by placing spacers between the two surfaces of two steel blocks.

Finally, Schoenberg (1980) expressed the joint dynamic response through its compliance, the inverse of stiffness. He managed to integrate the wave equation of P and S waves of arbitrary angles of incidence. Later, Pyrak-Nolte *et al.* (1987) expanded Schoenberg's solution to the case of discontinuities filled with viscous fluids (Kelvin and Maxwell models). In Pyrak-Nolte's formulation joint dynamic response was expressed again by means of normal and shear stiffness and also fluid's (where present) viscosity and compressibility. It is this formulation that is used in the following text.

2.5.3 Displacement Discontinuity Theory

Here, the solutions for the amplitudes of reflected and transmitted waves generated by the impact of a P or S wave on a discontinuity characterized by tangential and normal stiffness are presented (roughly following 1996's Pyrak-Nolte's and Cook's 1992 review papers).

The displacement and stress boundary conditions to be applied to the wave equations (equations 2.22) are:

$$\begin{array}{ll} \text{Displacement Conditions} & \text{Stress Conditions} \\ u_{x1} - u_{x2} = \frac{\sigma_{zx}}{K_s^{dyn}} & \sigma_{zz1} = \sigma_{zz2} \\ u_{y1} - u_{y2} = \frac{\sigma_{zy}}{K_s^{dyn}} & \sigma_{zx1} = \sigma_{zx2} \\ u_{z1} - u_{z2} = \frac{\sigma_{zz}}{K_n^{dyn}} & \sigma_{zy1} = \sigma_{zy2} \end{array} \tag{2.26}$$

The solution for the amplitudes depends on the dynamic joint specific stiffness, which is defined by the ratio of the joint normal or tangent dynamic stiffness to the medium impedance to compressive or shear waves (K_n^{dyn}/Z_p and K_s^{dyn}/Z_s):

The solution for the problem consists then on solving the system of equations posed by the application of conditions 2.26 to wave equations 2.22. In the case of horizontal shear waves, S_H, the system contains two equations only, since there is no wave conversion (production of reflected and transmitted waves of different type):

$$\begin{bmatrix} K_s^{dyn} & K_s^{dyn} - iZ_{s2}\omega\cos\phi_2 \\ Z_{s1}\cos\phi_1 & Z_{s2}\cos\phi_2 \end{bmatrix} \begin{bmatrix} R_S \\ T_S \end{bmatrix} = \begin{bmatrix} K_s^{dyn} \\ Z_{s1}\cos\phi_1 \end{bmatrix} \tag{2.27}$$

A larger, 4×4, system must be solved for P waves:

$$\begin{bmatrix} K_n^{dyn}\cos\theta_1 & K_n^{dyn}\sin\phi_1 & -K_n^{dyn}\cos\theta_2 + i\omega Z_{p2}\cos 2\phi_2 & K_n^{dyn}\sin\phi_2 - i\omega Z_{s2}\sin 2\phi_2 \\ -K_s^{dyn}\sin\theta_1 & -K_s^{dyn}\cos\phi_1 & K_s^{dyn}\sin\theta_2 - i\omega\frac{Z_{s2}^2}{/Z_{p2}}\sin 2\theta_2 & K_s^{dyn}\cos\phi_2 - i\omega Z_{s2}\cos 2\phi_2 \\ -Z_{p1}\cos 2\phi_1 & Z_{s1}\sin 2\phi_1 & Z_{p2}\cos 2\phi_2 & -Z_{s2}\sin 2\phi_2 \\ \frac{Z_{s1}^2}{Z_{p1}}\sin 2\theta_1 & Z_{s1}\cos 2\phi_1 & \frac{Z_{s2}^2}{Z_{p2}}\sin 2\theta_2 & Z_{s2}\cos 2\phi_2 \end{bmatrix}$$

$$\begin{bmatrix} R_P \\ R_{SV} \\ T_P \\ T_{SV} \end{bmatrix} = \begin{bmatrix} -K_n^{dyn}\cos\theta_1 \\ K_s^{dyn}\sin\theta_1 \\ Z_{p1}\cos 2\phi_1 \\ \frac{Z_{s1}^2}{Z_{p1}}\sin 2\theta_1 \end{bmatrix} \tag{2.28}$$

For S_V waves, the matrix is the same and only the product vector is different:

$$\begin{bmatrix} K_n^{dyn}\cos\theta_1 & K_n^{dyn}\sin\phi_1 & -K_n^{dyn}\cos\theta_2 + i\omega Z_{p2}\cos 2\phi_2 & K_n^{dyn}\sin\phi_2 - i\omega Z_{s2}\sin 2\phi_2 \\ -K_s^{dyn}\sin\theta_1 & -K_s^{dyn}\cos\phi_1 & K_s^{dyn}\sin\theta_2 - i\omega\frac{Z_{s2}^2}{/Z_{p2}}\sin 2\theta_2 & K_s^{dyn}\cos\phi_2 - i\omega Z_{s2}\cos 2\phi_2 \\ -Z_{p1}\cos 2\phi_1 & Z_{s1}\sin 2\phi_1 & Z_{p2}\cos 2\phi_2 & -Z_{s2}\sin 2\phi_2 \\ \frac{Z_{s1}^2}{Z_{p1}}\sin 2\theta_1 & Z_{s1}\cos 2\phi_1 & \frac{Z_{s2}^2}{Z_{p2}}\sin 2\theta_2 & Z_{s2}\cos 2\phi_2 \end{bmatrix}$$

$$\begin{bmatrix} R_P \\ R_{SV} \\ T_P \\ T_{SV} \end{bmatrix} = \begin{bmatrix} K_n^{dyn}\sin\phi_1 \\ K_s^{dyn}\cos\phi_1 \\ -Z_{s1}\sin 2\phi_1 \\ Z_{s1}\cos 2\phi_1 \end{bmatrix} \tag{2.29}$$

When P and S_V waves hit the joint with null angle of incidence ($\theta_1 = 0$ or $\phi_1 = 0$ in equations 2.27, 2.28 or 2.29) only two waves, which are of the same kind of the incident wave, are generated. That is, an incident compressive wave will generate two compressive waves, and a shear wave will generate two shear waves. The formulae for reflected and transmitted waves' magnitude are similar for P, S_V and S_H waves, with the difference being the joint stiffness and medium impedance, which must be set to match the incident wave type. The following expressions result for the absolute values of the complex magnitudes:

$$|R(\omega)| = I(\omega)\left[\frac{4\left(\frac{\omega Z_x}{K_x}\right)^2}{4\left(\frac{\omega Z_x}{K_x}\right)^2 + 1}\right]^{1/2} \tag{2.30}$$

and

$$|T(\omega)| = I(\omega)\left[\frac{1}{4\left(\frac{\omega Z_x}{K_x}\right)^2 + 1}\right]^{1/2}, \tag{2.31}$$

where the subscript x represents either compressive wave or shear wave impedance or joint stiffness: $K_x = K_n^{dyn}$ or K_s^{dyn}, $Z_x = Z_p$ or Z_s.

Since the system is assumed to behave elastically, there is no loss of energy associated to the wave reflection and transmission. This condition can be shown to correspond to

$$|R|^2 + |T|^2 = |I|^2. \tag{2.32}$$

The change of amplitude of the wave causes it to suffer a phase shift and, consequently, a time delay. The phase shift of the transmitted wave θ_T is the inverse tangent of the imaginary part divided by the real part of the transmitted wave (again with subscript x set to represent either normal or shear fracture stiffness and compressive or shear medium impedance):

$$\theta_T = \tan^{-1}\left(\frac{Z_x\omega}{2K_x}\right). \tag{2.33}$$

The wave group time delay[1] that corresponds to the phase shift (dt_{gT}) is given by

$$dt_{gT} = \frac{d\theta_T}{d\omega} = dt_{gR} = \frac{\frac{2K_x}{Z_x\omega}\frac{1}{\omega}}{\left(\frac{2K_x}{Z_x\omega}\right)^2 + 1}. \tag{2.34}$$

Figure 2.15 plots equations 2.30 and 2.31. When frequency is low relative to the specific stiffness (K_n^{dyn}/Z_p or K_s^{dyn}/Z_s), there is no reflection. Accordingly, the wave is completely transmitted, with no time delay, as this corresponds to a static loading which is equivalent to a wave with null frequency. On the other hand, when the frequency is high, again compared with the specific stiffness, the wave is completely reflected.

The Displacement Discontinuity Theory (DDT) has been thoroughly verified at the laboratory by means of measurement of transmitted ultrasonic waves across natural rock, cement and steel joints.

Figure 2.16 shows the DDT applied to the transmitted waves shown in figure 2.14. Here only the waves transmitted across the fractures are shown, since intact waves are equivalent to passage through a joint with infinite stiffness. The DDT predicted waves were obtained by finding a joint stiffness K_n^{dyn} that generates a transmission function that, multiplied by the incident wave results in a transmitted wave that fits the wave recorded in the test. Each joint will, then, have several values of dynamic joint stiffness K_n^{dyn}. These grow with the normal stress applied to the joint, as with static joint stiffness. It can be observed in the figure that theoretical and laboratory curves match is not always perfect, especially at high frequencies. It is thought that this happens because dynamic stiffness is not really frequency independent. More on the limits of DDT is discussed in the next paragraphs.

[1]The velocity of the waveform envelope is called group velocity, while the velocity of each wave with a particular frequency is called phase velocity. This lag in wave velocities, which also occurs in geomaterials, is called wave dispersion (e.g. Achenbach, 1973).

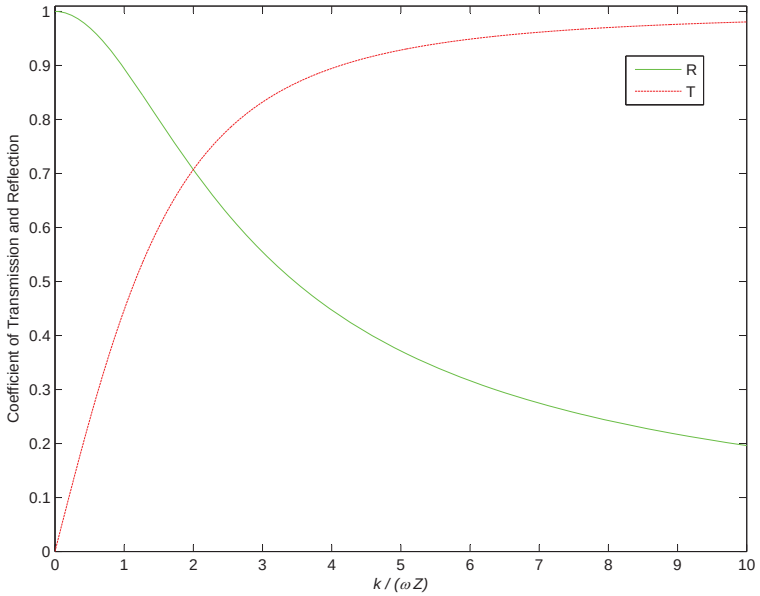


Figure 2.15: Magnitude of transmission and reflection ratios as a function of non-dimensional frequency for P and S waves normally incident to an elastic discontinuity.

In tests on artificial samples,*e.g.* Cai (2001), the stiffness of the joints was modified through alteration of the joint contact area. This alteration of joint contact area was attained by artificially changing joint geometry on fabricated joints, by compression of the specimen, or both. In these cases, the alteration in joint stiffness led to the modification of the transmitted wave amplitude and frequency that were consistent with predictions made by the DDT.

The limits of validity of DDT, which are associated to the relationship between wavelength and joint internal dimensions, were also studied. Nolte *et al.* (2000) determined that for the DDT to be valid the following conditions must be met: (i) fracture extension must be much larger than wavelength; (ii) fracture aperture must be much smaller than wavelength; (iii) asperity spacing must be much smaller than wavelength and (iv) distribution of contacts must be approximately uniform across fracture length.

The first and second conditions more or less define what a fracture is, dynamically speaking. If its length is of the same order of size or smaller than the wavelength, the wave will "sense" it as a small crack. Also if the crack opening is not much smaller than the wavelength, the wave will loose all its features when crossing it. The two last conditions must be met to avoid the occurrence of resonance scattering at the voids between the contacts of the two walls.

2.5.4 Fluid-filled discontinuities

As indicated above, Pyrak-Nolte conducted wave transmission tests on natural and artificial fractures and expanded the DDT to include viscous effects. Rock fractures are frequently filled

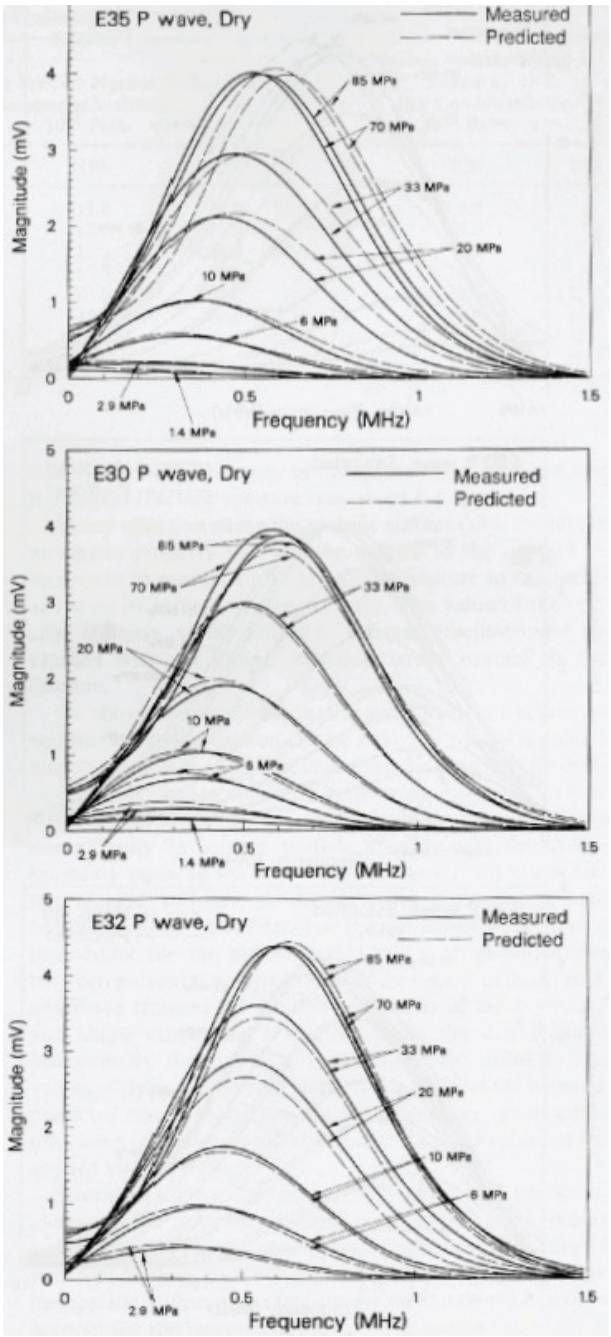


Figure 2.16: Measured and DDT predicted wave spectra from fracture samples shown in figure 2.14. Taken from Pyrak-Nolte *et al.* (1990).

with fluids that change dynamic joint behaviour in two ways. If the fluid is incompressible it will boost normal and shear joint stiffness. Under seismic loading the joint movement is expected to be too fast to allow the fluid to release applied pressure by flowing in the fracture. Fluid viscosity, if present, may introduce viscous coupling between fracture walls.

Pyrak-Nolte (1996) assumed perfect Kelvin (spring and a dashpot in parallel) and Maxwell (spring and a dashpot in series) models for the fluids, inserting velocity (and therefore dynamic stress) boundary conditions in the wave equations. Actually, most joints behave in a mixed elastic-viscous fashion, even when they are not filled. By integrating the elastic and viscous responses in the same system, this enhancement of DDT offers a comprehensive solution for most rock joint behaviours. Conservation of energy ceases to exist, *i.e.* equation 2.32 is no longer valid, as energy is converted into other forms such as heat, leading to an increase of temperature in the fluid. For a complete presentation of the solution refer to Pyrak-Nolte (1996).

2.6 Discussion

Although some questions remain unanswered the work described in the previous sections is considered to provide a satisfactory theoretical framework through which fracture interference in wave propagation in rock masses can be understood. However, there is still a gap between the laboratory experiments that verify Displacement Discontinuity Theory and the *in situ* practical cases. In the field, rock mechanics practitioners work not on small samples but on rock masses with extensive sets of rock joints with little known characteristics. Some of the questions, whose answers will contribute to fill this gap, are:

- Is there a simple relation between static and dynamic joint shear and normal stiffness?
- What are the properties that drive dynamic response of joints? Does dynamic stiffness depend on the same joint features as static stiffness, namely aperture or asperity distribution, rock wall hardness, filling? What is the relative weight of each feature?
- Is it possible to predict joint dynamic response by observation of the joint properties?
- Can a detailed rock joint numerical model (including asperity geometry and rock properties) simulate static and dynamic response?
- How can the dynamic effects of fractures be represented in a numerical model that, due to its dimension, cannot yet represent every fracture? Can dynamic properties be scaled to a smaller number of fractures or to a material model?

This chapter described the basic phenomenology of stress wave generation and propagation. These topics were only briefly introduced here since each one contains, in itself, potential for a lot more than can be presented here and there is high quality bibliography available. The

propagation of stress waves in rock masses and, in particular, in rock joints deserves a detailed analysis since it is the central matter of this thesis and is essential for the following chapters. In chapters 4, 5 and 6, different models for wave propagation in rock masses will try to address some of these questions.

Chapter 3

Vibration Impact Assessment Tools: Modelling, Monitoring and Regulations

3.1 Introduction

In the sequence of the previous chapter describing the phenomena involved in generation, propagation and impact of vibrations, this chapter focuses on the tools and methods used to assess and measure vibrations in order to control their impacts.

These tools (the term should be taken in a broad sense) are divided into three categories. Monitoring measures the vibrations in a necessarily limited number of locations. Regulations establish vibration limits at the targets, be them populations, structures or equipment. Propagation models have two different purposes: (i) to support the design of blast works and planning of monitoring and mitigation measures, and (ii), to fill the gaps in the frequently insufficient spatial distribution of monitoring devices. Although the second kind of utilization is more frequent, numerical models can also be useful as a support for blast design and vibration assessment and mitigation.

The first section in this chapter is dedicated to models based on more or less sophisticated and physically meaningful assumptions that simulate the process of wave propagation. Two kinds of models are presented. In the first one, analytical expressions or more sophisticated pattern recognition techniques are calibrated to adjust to previously gathered data. The second one comprises numerical models that explicitly model the phenomenon of stress wave generation, propagation and interaction with structures. Far more richer and complex than the previous class, they have the ability to simulate non-existing situations.

The second part describes how vibrations are monitored: the preparation of pre-blast survey of existing structures and of the test blast, the importance of well prepared and simultaneously flexible monitoring plans that protect existing structures and gather data that enables definition and calibration of wave propagation models.

The last section describes relevant international regulations on rock blasting vibrations with a particular focus on the Portuguese ones. As regulations are described, the structural characteristics that make constructions vulnerable to blast damage are highlighted.

3.2 Wave propagation models

There are two possible ways to treat the problem of vibration levels prediction. The first is the purely statistical way: mathematical functions or more sophisticated artificial intelligence techniques are calibrated to fit data gathered through monitoring. Most statistical methods have some physical relation to the phenomenon, as the variables involved have a real meaning, *e.g.* distance to blast or charge mass.

The second path corresponds to more or less sophisticated ways to emulate the chain of events: blasting, wave generation and propagation and structural impact. In this process a number of complex phenomena take place. A numerical simulation is a crude representation of reality and even the most sophisticated models focus into one stage of the problem at the time. Models that do include the whole process have to further simplify each stage.

It would be naive to think that this second method is deterministic. There are several levels of complexity that numerical models can aim to. More sophisticated analyses can, potentially, deliver more accurate results. But they have to rely on a larger number of assumptions, need more information and thus become more vulnerable to errors. All models should be simple at start and be completed as more information and confidence on the system are gained.

A numerical model may be built in several layers of complexity. Sophistication should pace with the level of information on the problem: geometry of the blast, ground properties and structures, explosion characteristics, etc. Also, the outcome must be regarded in accordance with the information the model was fed with and complexity. In rock blasting, the majority of models should be regarded more as guides on mechanisms and tendencies than providers of precise quantitative results. It must be reinforced that information, model complexity and outcome should all be aligned. An engineer used to traditional geotechnical static calculations is used to having its models fit field results with a precision that is better than what can be expected from vibration prediction. Errors in the order of five to tenfold may be a good result. Peak particle velocities are represented on logarithmic-scaled plots for some reason!

An advantage of numerical over statistical models is that the former can be used before

blasting works start, while the latter can be built only after a significant number of blasts have been measured. Clearly the results of numerical models must be regarded with great reserve until they are compared with field data. Each kind of model has its role and none should be expected to replace another. While curve-fitting is economical and fast but rigid, dynamic modelling is expensive but adjustable to real and also hypothetical situations. Both should be in the toolbox of the engineer in all phases of blasting works: from the preparation of the design to the after-blast period where complains may have to be addressed and judged.

3.2.1 Attenuation laws, statistical and probabilistic analysis

Study of wave propagation in rock masses envelops a large number of variables, most of which are hard to quantify in a single variable. This has led researchers and practitioners to develop simple empirical models that may be fitted to simulate monitoring results.

A recurrent "temptation" when working with real data is to classify as outliers points outside the main cloud. In blast vibration, these points' value can be one or more order of magnitude larger or smaller than the average and are more frequent in the direction of higher Peak particle velocities (PPV), heavily penalizing curve fitting results. It may seem, then, appropriate to dismiss them. Unusually heavy traffic, people or animals that bump into the monitors, equipment that work sporadically and numerous other causes may be responsible for extreme records. A careful analysis of the time of occurrence (which must be coherent with shot times), of velocity or acceleration time-history and of the frequency spectrum validates a genuine blasting record. If a data point is confirmed as being caused by a shot, it should never be ignored as an outlier. It is exactly the exceptionally high values which may be caused by particular features of a shot that have the capacity to cause damage and not the average points, no matter how predominate their number may be.

3.2.2 Peak particle vibration attenuation laws

The independent variables in wave propagation are the blast energy, the distance to the blast, the impedance of the ground (equal to the product of its mass density and seismic velocity of propagation) and time. Peak particle velocity is independent of time and, in rock masses, both ground density and seismic velocity rarely vary by more than a factor of two, while distance and energy variations are much higher than that. Therefore, distance and blast energy remain as the two most relevant parameters in the prediction of blast vibration effects. These two variables, which are usually included in attenuation equations, can be represented unequivocally by a scalar variable. Distance to the explosion is represented by R. Blast energy, taken as the maximum explosive mass per delay, is represented by W.

The role of distance to the source is instinctive. As laid out in chapter 2 vibration dissipates with distance due to two phenomena: geometrical spreading and intrinsic material damping.

Explosive's energy and mass are related through explosive energy density [Joule/kilogram] which is an explosive characteristic indicated by the manufacturer. It is not exactly the energy of the explosive in itself that is relevant to predict vibration but the parcel that, not being consumed in heat, vaporization and fragmentation of rock, is released to the ground (see figure 2.3). In practice, it is hard to define which part of the explosive's energy is spent in rock breakage and which part is released to the ground. Efficient blasting maximizes the former, minimizing explosive cost and perturbation to the environment. From site to site and even within the same site the rock breakage process may change due to variations in lithology, voids and fractures in rock and also variations, intentional or not, in the application and detonation. The ground where vibrations travels also changes radically their intensity. Attenuation laws aim to include the influence of these factors in the equations' parameters.

Dimensional analysis considerations have led to the use of the relation $W/R^{1/3}$ as the sole independent variable in most attenuation laws (Ambraseys and Hendron, 1968). Analyses of large numbers of blasts show a consistent relation between peak particle velocity and $W/R^{1/3}$.

Square root scaling, that is, $W/R^{1/2}$, has also been employed, despite not having a theoretical support as consistent as the cube root ratio. Justification for the square root scaling is related to the fact that charge mass in boreholes is proportional to the square of the borehole radius. Thus, $W/R^{1/2}$ can be taken as the ratio between the radius of the borehole and the distance R to the point of vibration measurement or estimation (Dowding, 1996). Square and

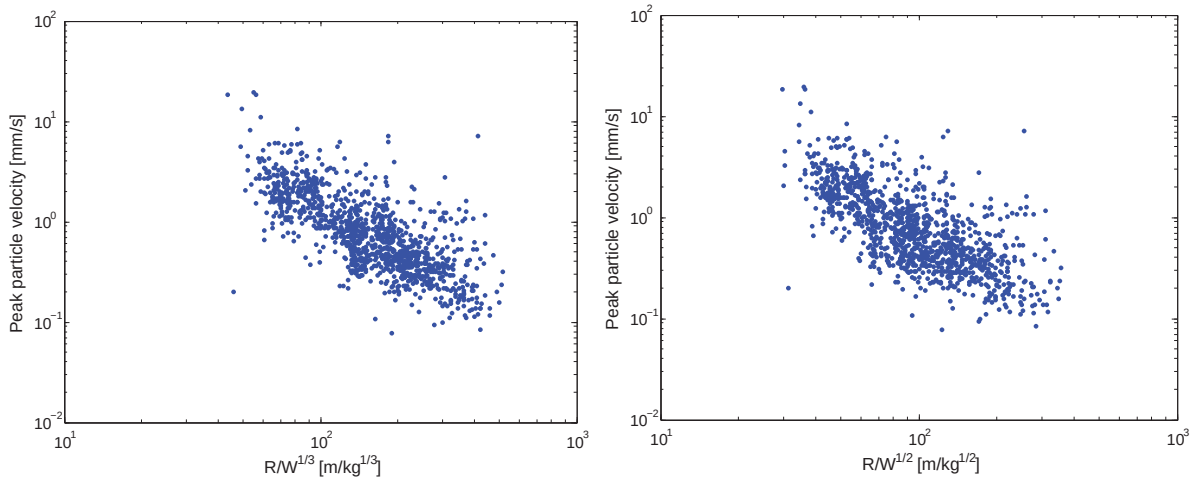


Figure 3.1: Scatter of PPV as a function of cube and square root scalling.

cube root PPV attenuation laws follow the general form:

$$PPV(R,W) = k\left(\frac{R}{W^{1/2}}\right)^m \tag{3.1}$$

and

$$PPV(R,W) = k\left(\frac{R}{W^{1/3}}\right)^m \tag{3.2}$$

with k and m being parameters that depend both on the characteristics of the blast and on the propagation path and are determined through curve fitting. If a logarithm is applied at both sides of the equation, the optimization problem is simplified, since it can be solved by linear regression.

In many cases the range of PPV variation is so large that the importance of this exponent is small, as figure 3.1 clearly demonstrates. The optimal value of the scaling exponent is usually between 1/3 and 1/2, and the choice of the optimal value can be left to a fitting algorithm.

In a more sophisticated approach, the exponent of the charge mass is not pre-determined, resulting in an equation like

$$PPV(R,W) = kR^mW^n \tag{3.3}$$

in which k, m and n are found by curve fitting. In this case, the curve fitting routine is not as straightforward as in the two previous equations but is still relatively simple.

The three parameters can be found through non-linear multi-variable regression, but it is the author's experience that better results are attained if logarithms are applied to both sides of the equation and then multi-variable linear regression is used.

Square or cube root scaling allows the graphic representation of results prior to the determination of law parameters. To visualize equation 3.3 a 3D plot must be used, which is in most situations inconvenient. An alternative is to fix one of the variables (*e.g.* mass) and plot the PPV *vs* the other variable (*e.g.* distance). This corresponds to showing a cross-section of the 3D plot.

Attenuation laws as presented above capture PPV trend evolution with distance and explosive mass by finding a curve that minimizes absolute distance to data points. But it is not the average but the extreme values of PPV that must be controlled, since they have the potential to trigger the most negative consequence. Damage in structures is cumulative, *i.e.*, cracks length grow with each blast that causes vibrations above a certain level. However, the responsible for new cracks, damaged equipment and frightened or annoyed populations are the events at the end of the distribution.

Dowding (1996) describes a simple and effective (in the author's experience) method to obtain attenuation laws that address this situation. It consists on determining a curve that is greater, not than 50% of the points (as the average curve is) but than 85 or 95%. Maintaining

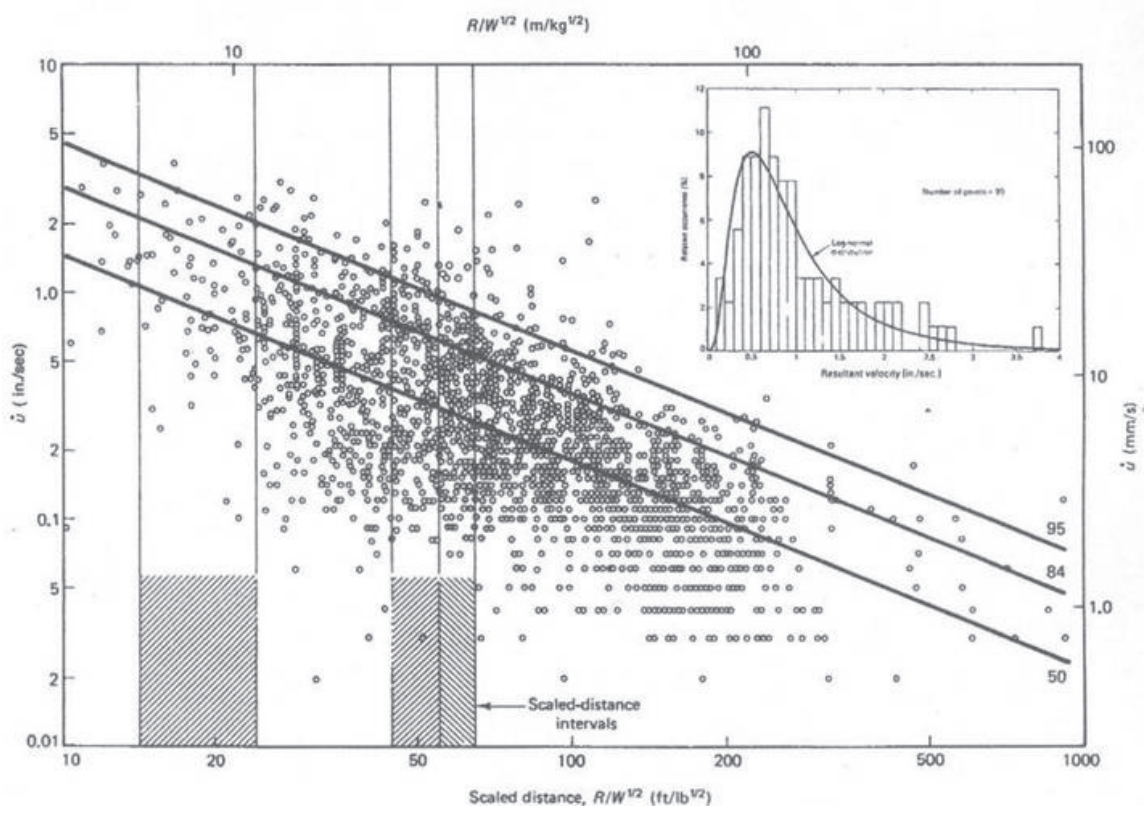


Figure 3.2: Variation of peak particle velocities for blasting in different circumstances and attenuation laws for several bounds. Taken from Dowding (1996).

other parameters constant, k is increased, corresponding to a vertical shift of the curve keeping its shape constant. While not bullet-proof in purely statistical terms, as additional hypothesis regarding the dispersion distribution accross the distance and charge range need to be checked, this method has shown to deliver good results in more than one situation. Figure 3.2 shows the application of the technique to a set of vibration measurements. In chapter 6 these techniques are applied to a large data set.

3.2.3 Artificial intelligence methods: Neural networks

One of the shortcomings of the attenuation laws presented in last section is the fact that the shape of the function is constrained and the number of variables limited. Distance and explosive mass are traditionally the chosen variables and follow exponential laws. Of course one can devise new laws by introducing other variables and trying other mathematical arrangements. There are, however, advanced pattern finding techniques, such as artificial neural networks that can be applied with better results.

Artificial neural networks are computational methods based on the efficiency of the brain

process (Patterson, 1998). They find patterns in the observations and calibrate themselves emphasizing the variables relevance through a set of weights. The interest for this area derives from the learning ability of these models, which relate the variables without imposing prior relationships among them.

The main disadvantages of these models are the fact that abundant data must exist in the domains where predictions are required. They are particularly inappropriate for extrapolation out of the range of the data used in the learning process. Chapter 6 describes an application of neural networks and compares the results with conventional attenuation laws.

3.2.4 Numerical modelling of wave propagation in the ground

Because this thesis proposes some innovations in modelling of dynamic phenomena in rock masses, it is considered that a short discussion on the nature, potential and shortcomings of modelling in geothecnical engineering is due. This section's major sources are the author's experience in diverse areas of modelling in addition to the following references: Lemos (2001), Oreskes *et al.* (1994) and Jing (2003).

Lemos (2001) discusses the different meanings of the term model in geomechanics. Model may mean "a purely conceptual description of a physical system in general terms" or it may refer to a numerical or physical model. Context is usually sufficient to clarify which one is being referred, but meanings can sometimes be confounded, also because typically a certain type of model (*e.g.* finite difference) is linked to a set of hypothesis (*e.g.* continuity of the domain).

Oreskes *et al.* (1994) demonstrate that truly verification of numerical models is impossible because natural systems are open and numerical models outputs are non-unique. While the arguments may seem obvious and the discussion sterile, practitioners frequently overlook the frailties of their models and become over-confident and dependent on their predictions. Recent discussions in the media about the political decisions based on climate models that later prove to be partially incorrect are a relevant example. Five arguments support Oreskes' point.

- Models' input parameters are incompletely known. An example is the description of rock jointing, which must resort to statistical distributions that aim to represent the variability of the joint sets.
- Representation of a system always incurs in loss of information. In rock masses, one of the most important losses occurs when a continuous formulation is used.
- Measurements of systems' properties are done on a scale that is, usually, not the one of the model. A fracture or a rock core tested in the laboratory have 100 to 200 mm. *In situ* tests are performed on samples that are around 1000 mm. A tunnel or cavern's dimensions are always 10 to 100 times greater.

- Observations and measurements are themselves laden with inferences and assumptions. Mechanical parameters such as Young's modulus or unconfined compressive strength are extracted from a stress-strain curve that is itself a simplification of the even richer behaviour when the core is inside the rock mass.
- Finally, a number of hypotheses are at the base of a working model. If the match with reality is not satisfactory, hypothesis and parameters are adjusted until a fit is achieved. In this process of calibration how can be known, for example, that two wrong hypotheses are not cancelling each other in the particular tested situation?

The fact that a model works well on a situation where it can be compared with an analytical solution or experimental data does not imply that it will perform in a prediction, where it is needed and useful. A leap of faith is always necessary and sometimes the solid ground is not there at the end. The way in which failures in the modelling process (which are always present) are handled is important. Are the lessons learned and incorporated in the "modelling culture" or dismissed and therefore forgotten?

These considerations label and organise the doubts and insecurities that every conscious engineer involved in modelling faces when using a model and even more when developing one.

Modelling of blast vibration propagation and impacts draws from two modelling "traditions": conventional (static) geotechnical modelling and earthquake engineering. This thesis remains below ground level, meaning all structures built above the surface are not directly considered. The final product of the propagation models referred to can be used as the input to structural models that represent above ground structures such as buildings. This may be not advantageous when the soil-structure interaction is relevant. In those cases the structural model may include a portion of the ground and the vibration time-history fed into that model's foundation.

One of the most important divisions in numerical models applied to rock mechanics is between continuous and discontinuous models. In the first group the rock mass is modelled by an equivalent continuum material that incorporates the deformability and strength contribution of the discontinuities. In the second group models explicitly represent the rock mass' blocky nature. Also in this class, particle models do not model blocky nature of rock but simulate the continuum behaviour of the rock throughout a large number of particles.

A hybrid class of models allows the internal discretization of blocks and even the internal damage of rock material, crack growth and block sub-division. The finite element method is the numerical modelling technique most widely used across all disciplines of engineering. One of the reasons is that it was formulated early on and was appropriate for the hardware configuration of early computers. As stated above, it divides the domain into elements (the finite elements)

where the differential equations of elasticity are solved. It supports constitutive models that simulate different characteristics of the rock material and joint elements.

Finite elements method condenses the system through the assembly of a global stiffness matrix where the contributions from each individual element is accounted. The matrix forms part of a system of equations that must be solved in each timestep, rendering dynamic calculations computationaly heavy. In finite-difference formulations the domain is discretized in a grid of points where the governing equations are solved. In initial formulations, anterior to the first finite-element models, only regular grids could be used. This limited the application of the method to very simple problems. Subsequent evolutions using integral difference techniques allowed more flexibility of use and resemble finite element formulations. What distinguishes the finite difference and finite-element traditional formulation is, above all, the explicit dynamic relaxation scheme and the large displacement capabilities of the former. Boundary element methods discretise the domain boundary based on fundamental solutions of the governing equations. Since only the boundary is represented boundary element methods are very economical but also limited in dealing with complex geometries in fractured rock masses. The discrete or distinct element method was proposed by Cundall (1971) for the study of jointed rock masses modelled as assemblies of rigid blocks. Any kind of movement and displacement of the blocks is allowed since equations of motion are integrated and contacts between blocks are resolved along the calculation.

Particle element methods rely on a large number of microscopic circular or spherical particles whose interaction is easier to solve to model the macroscopic behaviour of rock. It is applied not only to coherent solids but also to all sort of incoherent materials: soil, powder, masonry, etc.

The time-steeping integration technique and the fact that stiffness matrix needs not be built make discrete element and the finite difference methods particularly suited for linear and non-linear dynamic analyses.

Other formulations for the simulation of discontinuous blocky media were developed, the most important being Discontinuous Deformation Analysis (Shi and Goodman, 1988), in which a discontinuous material is modelled as a system of individually deformable blocks that move independently without interpenetration. It has a dynamic equilibrium formulation that considers the kinematics of each block resorting to the minimization of potential energy to calculate the progression of block movements with time.

3.3 Impacts on human beings, structures and equipment

It is not the objective of this work to study the way in which people or diverse types of structures and equipment are affected by ground vibrations, this being the domain of human physiology, structural dynamics and other scientific areas where abundant work is continuously published. It is, however, important to understand the interaction between the terrain where vibrations travel and the receiver structures. This allows the identification of the most important characteristics of vibrations and the quantification of the acceptable levels for each target type.

The assessment of consequence of vibrations in structures is a problem with a larger level of complexity. On top of ground vibration propagation comes the response of the structures, which is studied using completely different tools.

Most countries set strict limits on vibrations and noise due to construction, rail and road circulation and other sources. The human being, besides being more sensitive to vibrations than structures and equipment, is also extremely susceptible to blast aerial shock waves and noise in general.

The first research efforts in this field, described by Dowding (1996), were dedicated to continuous vibrations. A discomfort threshold of 2.5 mm/s for vibrations with a duration superior to 300 s was found. For shorter-duration vibrations the discomfort level is much more difficult to set up depending on the vibration frequency. 0.1 mm/s is the level at which most standing people notice vibrations with a frequency under 100 Hz.

Being a human phenomenon, the sensitivity to vibrations involves a large number of parameters of which the psychological ones are not the least important. The predictability and acceptance of the source of vibrations, the time of the day, the position, age and occupation of the person are some of the most important factors.

With the exception of rare extreme situations, vibrations from sources other than earthquakes do not pose structural safety problems. The most common situation are related to comfort conditions: fissuration or cracking in wall and ceiling plaster, excitation of structural and non-structural components, noise and discomfort of the users.

Much of the know-how and methodologies for seismic analysis of structures can be employed in the study of the response to blast vibrations, if significant differences in dominant frequencies, duration and intensity of vibrations are taken into account. Also worthy of note is the fact that methods of earthquake resistance assessment focus on damage levels that are much worse than the consequence of blast vibrations, usually much more subtle.

The response of conventional structures to dynamic actions is a whole field of structural engineering being off this thesis scope. In the last part of this chapter international regulations on blast vibrations are presented and the impact on structures is discussed in more detail.

Underground or near surface structures such as tunnels, caverns, ducts, retaining walls and slopes receive vibrations directly from the source and are surrounded by the medium that transmits these vibrations. Being, in general, less stiff than the surrounding ground, they conform to the displacements and deformations of the ground. Also, since rock masses' mechanical characteristics usually improve with depth, underground structures may be subject to higher intensity actions. In chapter 5 a site test at an underground complex built in hard rock is described and modelled and the interaction of tunnels and caverns with vibrations is discussed.

The vulnerability of fresh concrete to vibrations is frequently relevant as it may hamper the advancement of the construction work. According to Esteves, cited in Dowding (1996), two opposite tendencies are at stake. Both stiffness and strength of the concrete are null or very small after mixing and increase with curing time. Larger stiffness corresponds to greater vibration-induced stresses, but strength also augments and decreases the concrete vulnerability. Since the concrete properties, the form of application and vibration characteristics change from site to site, each case may need a specific experimental study.

It is not unusual for special industries to be housed in isolated installations, far from vibrations sources or structurally isolated. The sensitivity of industrial, electronic, information and healthcare equipment, among others, is extremely variable and is usually defined by the manufacturers. Hospitals and laboratories are among the most common types of installation that require small vibration levels in the ground.

3.4 Monitoring strategies

Some of the national regulations on blast vibrations (section 3.5) go further than setting limits on vibration and indicate how monitoring should be conducted. Anyhow, there is good literature on this matter. Dowding's (1996) "Construction Vibrations" is the most authoritative work only lacking a description of the most recent advances in vibration measuring devices which are significant, improving monitoring considerably. Persson's *et al* "Rock Blasting and Explosives Engineering" (2001) is a more general book on rock blasting and includes a chapter on ground vibration propagation and impact that covers most of the relevant issues.

The monitoring of vibrations due to blasting works should start before the first blast. Vibration control usually puts heavy constraints on the unfolding of blasting works so monitoring planning should be linked to the preparation of other, if existing, construction activities.

Vibration control is only one of the many issues that must be considered when blasting. Noise, dust and fly-rock control, quality of blasting results, safety of personnel, explosives' handling and storing rules, specific blasting insurance and attribution of blasting responsibilities

are some of the problems that are closely linked to vibration monitoring, but their discussion is out of the boundaries of this thesis. Bernardo's PhD thesis (Bernardo, 2004) is an authoritative source, covering impacts of blasting from flyrock to dust, sound and vibrations.

The remaining of this section describes a recommended procedure – adapted from Dowding (1996) – for the preparation and conduction of blasting works, in what regards vibration control. The first step of the preparation of a rock blasting work is the recognition of the area around the blasting zone. The size of this area varies with the characteristics of the blasts and the sensitivity of the constructions. Dowding (1996) recommends a radius of 120 m, or out to a distance where vibrations are expected to be smaller than 2 mm/s (in the case of Portuguese regulation the lowest possible limit is 1.75 mm/s). Such an area can be hard to define in advance if there is no previous experience of blasting in the zone.

The geologic and geotechnical characteristics of the area to be blasted are usually carefully studied for the blasting preparation. Ideally the remaining area (the medium where vibrations will travel until they reach constructions) should be characterized as regards bedrock lithology, bedding and main fracturing directions. If the excavation is underground and at considerable depth, *in situ* stress state influences fracture closure, so it should also be estimated. Soil cover's depth, water level and geomechanical characteristics should also be estimated or measured, especially when structures have their foundations on it.

In the majority of situations the available level of information is below the ideal. At least the foundation material of vulnerable constructions should be known as well as the velocity of propagation of sound in the ground. From this, it follows that geophysical surveying is more useful than logging or other localized investigation techniques.

If steep slopes, deposits of loose soil that can suffer densification or other geological accidents prone to disrupture from vibrations exist they should be surveyed and consolidation measures considered.

The constructions and equipment inside the perimeter of vibrations influence, be they built above or below ground, must be identified and their sensitivity must be established. Each construction should be analysed and a limit level of vibration assigned, according to the applicable regulation's standard: construction type, state of repair, foundation conditions, etc.

An independent survey of the constructions using photo and/or video previous to the start of the blasts will establish a baseline situation. This is demanded by some regulations as it is the only unequivocal way to distinguish if cracking or other damage were caused by blasting. The surveying and classification of the constructions can be made difficult due to lack of cooperation from home-owners and by the large number of constructions in densely constructed urban areas, so the "soft-skills" of public-relations work is essential. Some regulations detail the method of classification of buildings according to their sensitivity to vibrations, while others are vague in

their description.

A common difficulty is the definition of maximum vibration levels for sensitive targets: structures such as historical patrimony (in good or bad condition), dwellings of populations with special characteristics (very young, ageing or sick), equipment for which a limit vibration level is not known, hospitals, precision industries or laboratories. Work in these areas demands special care and restricted blasting schedules may be imposed. From the author's experience, maximum vibration levels on buildings of high historic or social value such as monuments are set very low even when they are able to withstand relatively high levels of vibration without damage.

All the available information about vulnerable targets should be compiled and presented on a drawing that serves as the basis for the design of the Vibration Monitoring Plan.

When no previous blasts have been performed, even if detailed information on the blasting area and on the blast programme is available, it is difficult if not impossible to forecast with confidence the level of vibrations that will be produced and how they will propagate and attenuate. Therefore, a test blast programme is almost always necessary.

The test blast starts with low intensity charges, which are increased as confidence on the produced vibration is acquired. Blast vibration monitoring devices are installed in one or more radial lines that cover the distance between the blast and the structures (above or below ground) needing protection. The first measuring device must be installed at a small distance from the blast, the second at approximately ten times that distance and so forth. This provides attenuation levels at logarithmic distances from the blast, allowing the calibration of exponential attenuation laws. Usually, more monitors are necessary at this stage than later during the course of the works. A sufficient number of blasts as similar as possible to those that will be performed during production should be measured, allowing an estimation of the attenuation, dispersion and frequency associated with ground peak velocities.

At the time of the Test Blast Programme conditions like blast confinement, geometry, depth and location may not be similar to those during production, and familiarity with the produced vibration and its attenuation is still incipient. This can penalize the emitted vibrations and should be taken into account.

It is desirable that the Test Blast Programme conclusions are used in the blasting design, but this may be hard to do if tests are performed at the start of the construction.

Prior to the start of any blasting, a Blast Production Plan including details of the drilling and firing patterns is usually written. If it is likely that vibration control will pose large constraints to the blast production, this plan is considered temporary until the first monitoring results are available. A feedback and update dynamic is necessary in blasting as in all geotechnical works.

The Blast Production Plan should indicate the planned schedule for blasting, which can

restrict it to workdays, daylight or other times, depending on the activities that take place on the site and around. The plan must also include procedures to follow in case of excessive vibration and official channels of communication between all actors.

With the information gathered from the pre-Construction Survey, the Test Blast Programme and the Blasting Production Plan a Monitoring Plan is established. The main piece of this Plan is a map that displays the blasting area and its geology, the constructions or equipment to protect and admissible vibration and the location of the vibration monitors. Since the blast area progresses and moves at surface and at depth the Monitoring Plan must also be dynamic and collocation of monitors be indicated for all phases.

The Monitoring Plan should also describe the equipment that will be used to measure vibrations. This description should cover the manufacturer and model of the monitor, what it measures (acceleration or velocity), number of transducers (uni or triaxial), sensitivity and range, which data are recorded and stored (complete time series or only the peaks), power (plugged to the electric grid or stand alone) and storage media.

The method used to retrieve the data should also be described: who has access to the monitors, frequency and method of data gathering (through a wireless network, modem or on site). Regarding the installation of the vibration monitors, the way in which they are fixed to the ground or structures must also be previewed, in particular for monitors placed nearer to the blast where large accelerations can be expected. If the applicable norm does not specify it, the digital treatment to be applied to the data records should be briefly described with special mention to how the peak particle velocities and associated frequencies are calculated.

The Monitoring Plan may also include structural monitoring of structures such as permanent displacement (translation, rotation or tilting) or crack movement. The kind of measurement (namely topographic methods, tilt-meters or crack-meters) must be described as well as the frequency and responsibility of readings and the pre-determined limits.

All gathered data and information must be archived for future reference. If more than one company is working on the site it should be agreed in advance who will maintain and keep the archive and in which form (digital, paper or both) and who can access it.

Similarly to the Blasting plan, the Monitoring Plan is updated as shots' local evolves and understanding of the site response is enhanced. The propagation models (statistical, numerical or probabilistic) built for the Test Blast Programme must be updated and their validity continuously checked. As a greater number of shots and resulting vibration becomes available, statistical models can be built.

Alert and danger vibration levels and procedures must be defined for when these levels are exceeded. Blasting and eventually, drilling may have to be interrupted in the case safe levels are reached and not resumed until the causes are identified and corrected.

Communication with the population should be established in order to transmit changes in the construction and receive feedback on the perception of eventual damage and discomfort. Local newspapers and radios, civic associations and clubs, websites and mailing lists are some of the most evident communication channels. Besides addressing complaints earlier, demonstrating that the entities in charge of the construction do care about the impact in people's lives and property go a long way in improving acceptance of the annoyance.

3.5 International regulations on blast-induced vibrations

The rise of public awareness of its civic rights and the environment conservation movement, both of which gained momentum in the second half of last century, led governments and government agencies to address the environmental consequence of industrial activities. Blasting was not an exception and the regulations setting limits on the noise, dust and vibrations have been gradually introduced.

Regulation of industrial activities seeks an equilibrium between economy of the process, environmental damage and population annoyance. In the case of blasting, looser regulation permitting higher vibration levels allows the use of more intense charges, leading to more economical and faster construction/exploitation. If blasting is due to construction activities which are transitory the equation may become more complicated, as a faster construction which is preferred by populations is associated to more intense vibrations. In addition, the review of a blasting methodology to lower vibration levels often ends in more efficient blasting, not only in terms of vibration levels but also quality of the excavation (overbreak, rock damage zone, fragmentation) and explosives consumption. It should not be forgotten that vibration and noise are the manifestation of explosive energy that is not used in rock fragmentation. All summed up the control of vibrations is a challenging task and not necessarily a win-lose situation.

The large scope of the intensity and frequency content of vibrations produced by what may seem identical situations is the first challenge. Variations greater than one order of magnitude due to changes in geology, explosion conditions, propagation paths or other causes that are not easily identified are frequent.

The other challenge lies on the other end of the system: the way in which vibration progresses from the ground into the target, be it an equipment, a structure or a human being. Vibration can arrive at a person directly from the ground or through a structure. In the latter, that structure transmits, amplifies or reduces frequency bands, depending on how close they are to its own resonance frequencies. The way a vibration is felt by the human body varies with its position (standing, sitting, lying down), occupation (working, resting, reading). The vibration can go unnoticed or be better tolerated if expected or if there is background noise or vibrations.

The response of structures to vibrations depends on the type of construction and construction material (*e.g.* concrete, masonry, wood or metallic) and interaction with the foundation, wall lining (*e.g.* plaster, gypsum or wood wallboard, wallpaper) and on the condition of the structure. The elements of the structure (walls, beams or slabs) or furniture (*e.g.* lamps, cupboards) have self-vibrating frequencies that are lower or higher than the structure, and therefore can be excited by different frequencies. Damage due to vibration can go from unnoticeable to complete ruin but in typical situations it is limited to creation or aggravation of cracks in walls and ceiling and fall of already loose parts of the lining.

It is difficult to determine if a crack has been created by a recent blast or if it results from air temperature and moisture variations, settlement at the foundation, door banging, excessive static loadings due to furniture or other common environmental causes. If a pre-construction survey is not done, a home-owner that starts looking at his ceilings and walls after a blast will eventually notice some cracking and most likely associate it with the blast. To judge effectively and fairly such situations is not an easy task.

Psychological aspects should not be underestimated. Populations are generally more tolerant to sources of annoyance when its product is advantageous. Vibrations from a quarry will most likely generate more complains than those from a railway line that serves that population. But, the same quarry will be better tolerated if it provides local jobs. Good public relations campaigns and regular meetings with the population always have positive impact.

It is in this complex scenario that practitioners supported by sound engineering analysis and guided by the available regulations must work. In the following sections, the most relevant regulations are presented. Their theoretical foundations, the empirical data that supports them is highlighted and there are some comments on the similarities and discrepancies. Finally, there is a more detailed analysis of the Portuguese regulation.

3.5.1 ISO regulation

The International Organization for Standardization (ISO) issued a standard (ISO 4866) concerning the effects of vibrations on structures. The version "Mechanical vibration and shock - Vibrations in buildings - Guidelines for the measurement of vibrations and evaluation of their effects on buildings" dates from 1990. This norm provides guidance on classification of vibrations according to source and duration (traffic, blasting, earthquake, wind, construction), building classification, influence of soil type, choice of transducers, signal conditioning and evaluation of measured data. It does not define vibration limits. Companion norm ISO 2041 (2009) defines vibration and shock terms in English and French while ISO 2631 (1997) addresses human exposure to vibrations.

3.5.2 German regulation

German blast vibration norm DIN 4150 "Structural vibration in buildings" (1999) is divided in three parts: "Principles, predetermination and measurement of vibration parameters", "Effects on humans in buildings" and "Effects on structures". It is this third part that sets the maximum allowable peak particle velocity.

The purpose of the norm is to avoid damage in terms of reduction of the utility value of the buildings. Examples of such impacts are provided: impairment of the stability of the structure (or parts of it), reduction of the load bearing capacity of the floors and crack formation or growth.

Two types of controls are set. One limits vibration at the structure's foundation and the other in the floor of the uppermost storey. The maximum allowable PPV in the ground is calculated by consideration of the type of structure and dominant frequency of the vibration. Vibration in the top floor depends only on the type of structure.

Three building classes are defined. They are, from most robust to most fragile: commercial and industrial buildings (class I), dwellings (class II) and structures particularly sensitive to vibration such as buildings under a preservation order (class III). Four frequency intervals are defined: 0 to 10 Hz, 10 to 50 Hz, 50 to 100 Hz and above 100 Hz. Allowed peak particle velocities grow with vibration frequency and are 3 to 10 mm/s in fragile constructions, 5 to 20 mm/s in residential buildings and 20 to 50 mm/s in industrial buildings.

By controlling the vibration at the top floor, the response of the structure is directly included. In the top floor, peak velocities are 8, 15 and 40 mm/s, for fragile, intermediate and sturdy constructions. Table 3.1 displays the reference values.

Table 3.1: Reference PPV values (in mm/s) of the German DIN 4150 standard for blasting vibrations. Taken from DIN (1999).

Type of Construction	Frequency range [Hz]				Top floor
	0 - 10	10 - 50	50 - 100	100 - ∞	All frequencies
I	20	20 - 40	40 - 50	50	40
II	5	5 - 15	15 - 20	20	15
III	3	3 - 8	8 - 10	10	8

DIN 4150 provides guidance as to how measured vibration, on the impacts on humans, calculation of dynamic stresses in structural elements and on the effects of continuous vibration.

3.5.3 Portuguese regulation

The Portuguese NP 2074 (1983) follows the general line of the 1975 (not the current) version of DIN 4150. The peak particle velocity limit is found through the following expression:

$$PPV_{max} = \alpha \cdot \beta \cdot \gamma \cdot 10^{-3}\ [mm/s]. \tag{3.4}$$

Coefficients α, β and γ take values that change with the kind of foundation material, type of construction and average number of blasts per day. α is 2 in rock and very stiff soil ground, 1 in stiff and average soils and 0.5 in loose soils. Indicative compressive wave propagation velocity for each kind of ground are provided. Ground with a compressive wave propagation velocity (c_p) above 2000 m/s falls on the first ground category, from 1000 to 2000 m/s in the second and softer soils have c_p smaller than 1000 m/s.

β is function of the type of construction and, again, three categories are defined. For reinforced constructions (class I) β is 3, for average constructions (class II) β is equal to 1 and when structures are especially sensitive to vibrations (class III) β is 0.5.

Finally γ is a function of the average number of vibration events per day: it is 0.7 if there are more than 3 blast/day and 1 if there are less.

Application of formula 3.4 results in a maximum particle velocity of 60 mm/s (reinforced construction on hard soil or rock, less than three blasts per day) and a minimum value of 1.75 mm/s (sensitive construction on soft soil and more than three blasts per day). Table 3.2 displays the reference vibration values in the case of less than three events (on average) per day.

Table 3.2: Reference PPV values (in mm/s) of the Portuguese NP 2074 standard for blasting vibration (PPV values are to be used when there is less than three events per day and must be multiplied by 0.7 otherwise). Taken from DGQ (1983).

Type of Construction	Soil type		
	Hard	Medium	Soft
I	60	30	15
II	20	10	5
III	10	5	2.5

3.5.4 USA regulation

The (now extinct) United States Bureau of Mines conducted a large (perhaps the largest ever) monitoring campaign of structural and cosmetic building response to blast vibration. The

studies and conclusions were released in a series of bulletins. The USBM 656 bulletin "Blasting Vibrations and their Effects on Structures" published in 1971 (USDI, 1971) proposed a peak particle velocity of 50 mm/s for civil constructions.

In 1980 the report RI 8507 "Structure Response and Damage Produced by Ground Vibration from Surface Mine Blasting" (USDI, 1980) was published. It clearly linked vibration frequency and damage and a new criterion, which depends on the type of structure and vibration frequency, was proposed.

The criterion aims at avoiding what is denominated as minor damage defined as "loosening and falling of plaster, cracks in masonry around openings near partitions; hairline to 3 mm cracks; fall of loose mortar". Two other levels of damage were defined: threshold damage, less serious, and major damage, more severe. Also two kinds of residential structures were defined. In modern homes with drywall interiors (class I) a 19 mm/s vibration is unlikely to cause minor damage if frequency is less than 40 Hz while above this frequency 50 mm/s is allowed. In older homes, with plaster on wood lath construction for interior walls (class II) 13 mm/s are allowed if frequency is lower than 40 Hz, and 50 mm/s if the frequency is higher. Table 3.3 displays the reference vibration values.

Table 3.3: Reference PPV values (in mm/s) of the United States Bureau of Mines RI 8507 standard for blasting vibrations. Taken from USDI (1980).

Type of Construction	Frequency range [Hz]	
	0 - 40	40 - ∞
I	19	50
II	13	50

After the publication of RI 8507 the mining industry complained that the limits were too severe and would impair the mining industry arguing that no damage was observed for vibrations below 20 mm/s and that the 13 mm/s limit was political and not scientific. To the knowledge of the author this was, however, the better supported study and the 13 mm/s level contains a necessary margin of safety.

One of the particularities of this regulation is the kind of building studied, typical of the United States rural areas. Other singularity is that the norm's document describes thoroughly the field studies that led to its conclusions presenting the original data in great detail.

3.5.5 Swiss regulation

Swiss regulation SN 640312a (VSS, 1992) details four different construction types. The first category (class I) includes reinforced concrete and steel constructions such as industrial buildings, earth supporting walls and bridges. Underground caverns tunnels and galleries with or without concrete lining and surface conducts are included in this class. The second category (class II) includes ordinary structures such as buildings with concrete foundations and also buried conducts. The third category (class III) includes buildings with concrete and masonry foundations and wood structures. The fourth category (class IV) includes constructions which deserve special protection and/or are particularly sensitive to vibrations.

In each class peak vibration levels are defined for blast and machine vibration. For each of these they are defined in two frequency intervals: 10 to 60 and 60 to 90 Hz. For vibrations below 10 Hz, special analysis must be performed to contemplate structural resonance. Table 3.4 displays the reference vibration values.

Interesting aspects of this norm are that it is one of the few that addresses buried structures and it sets different limits for blast and continuous vibrations. Finally, it demands detailed structural analysis of buildings to be performed in the situations where structural resonance is possible.

Table 3.4: Reference PPV values (in mm/s) of the Swiss SN 640312a standard for blasting vibrations. Taken from VSS (1992).

Type of Construction	Frequency range [Hz]		
	10 - 60	60 - 90	90 - ∞
I	30	30 - 40	40
II	18	18 - 25	25
III	12	12 - 18	18
IV	8	8 - 12	12

3.5.6 British regulation

An extensive body of regulations is in place in the United Kingdom. The British Standard BS 7385 “Evaluation and measurement for vibration in buildings” (BSI, 1992), is composed by two parts. Part 1 “Guide for Measurement of Vibrations and Evaluation of their Effects on Buildings” is identical to ISO 4866. Part 2 “Guide to Damage Levels from Ground Borne Vibration” discusses the parameters for protection of constructions. BS 5228 - Part 2 “Code of Practice for Noise and Vibration Control on Construction and Open Sites. Vibration” gives

recommendations for basic methods of vibration control relating to construction and open sites where work activities generate significant vibration levels. BS 6472 "Guide to Evaluation of Human Exposure to Vibration in Buildings" focuses on human response to vibration.

BS 7385-2 divides buildings in two kinds according to their construction and purpose. The first kind includes reinforced or framed structures used as industrial or heavy commercial buildings (class I). The second includes non-reinforced or light framed structures, residential or light commercial type buildings (class II). This classification is detailed in the first part of the norm.

Damage in structures is classified into three categories: cosmetic cracking, minor damage and major or structural damage. For structures in the second category (more vulnerable) the possibility of occurrence of cosmetic damage depends on frequency and peak particle velocity. Guide values for cosmetic cracking are 15 mm/s at 4 Hz, 20 mm/s at 15 Hz and 50 mm/s at frequencies over 40 Hz. For the first kind of structure (robust) a 50 mm/s limit is indicated for all frequencies above 4 Hz. If in any building class vibration frequency is lower than 4 Hz, a displacement criterion of 0.6 mm is used. Minor and structural damage are expected to occur at values twice and four times larger than those for cosmetic damage, respectively. The indicated vibration values are to be measured at the foundation level or as close as possible. Table 3.5 displays the reference vibration values.

Table 3.5: Reference PPV values (in mm/s) of the British BS 7385-2 standard for blasting vibrations. Taken from BSI (1992).

Type of Construction	Frequency range [Hz]		
	4 - 15	15 - 40	40 - ∞
I		50	
II	15 - 20	20 - 50	50

The British Standard defines several levels of impact in the constructions. Also very useful to practitioners is the careful definition of each class of building as it avoids conflicts over this matter. Similarly to the Swiss norm, it has a specific treatment of low frequency vibrations recognizing that the structural response to vibration is different in this case.

3.5.7 Regulation comparison

The described regulations are similar as to the general criteria for vibration control:

- Peak particle vibration of the ground, measured as near as possible to the structure's foundation level is the control parameter.
- Vibration limits are set according to frequency, with higher vibration levels allowed in the

higher frequencies.

- Structures are classified according to their vulnerability to vibrations.

In addition to the varying vibration limits, which will be briefly discussed hereafter, there are some differences between the regulations that are considered to be the most representative, and the Portuguese regulation.

In all the reported regulations particle velocity is the chosen control parameter. There is a generalised consensus about this for several decades as particle velocity correlates directly with strain and stress. The British and Swiss regulations go a little further and acknowledge that when the vibration frequency is very low specific analysis is necessary.

The definition of peak particle velocity is not unanimous. It is defined as the maximum value of the vector sum of the three directions of velocity, as the maximum of the three components or in some regulations, just the vertical component.

Given the impossibility of measuring vibrations in all structures affected by vibrations, especially in urban settings, and also the difficulty of defining where to measure in each structure, measurements are to be made at foundation level or as close as possible. Some regulations go further and also set limits to vibrations measured inside the structure, *e.g.* DIN4150 limits the vibration on the top floor. While some regulations like the British Standard provide indications on what kind of device should be used (seismometer, geophone), its frequency range, orientation of the sensors, the way it is installed (clamped or attached to the structure or ground, buried in the ground), signal treatment and data analysis, others such as the Portuguese NP2074 do not mention such treatment.

In all analysed regulations but the Portuguese, frequency is one of the parameters that controls the maximum allowed vibration. The determination of the dominant frequency is not straightforward. It can be taken as the frequency of the peak wave or of the maximum amplitude in the frequency spectrum. In the Portuguese regulation, frequency is not directly considered but its influence, however, is indirectly taken into account through the kind of ground where the structure is founded on. Three ground categories are defined, and higher vibration levels are allowed on structures set on stiffer ground. In a broad sense this makes sense as it is known that soft soils filter higher frequencies and this regulation dates from 1983 when digital signal analysis software or devices were not as readily available in the way they are today. This justification does not, however, wishes to hinder the fact that a revision of the Portuguese regulations is due. The PhD thesis of Bernardo (2004) thoroughly analyses this aspect of the Portuguese regulation and argues and supports the inclusion of vibration frequency as a parameter for the definition of the maximum admissible vibration.

In all the analysed regulations, vibration levels vary according to the structure under protection. Building categories are defined by their vulnerability and importance (social, historical, political). The classification changes from country to country, reflecting not only the construction traditions but also the kind of structures that were tested when the regulation was developed. Similarly to the classification of the ground type, some regulations carefully define how each structure should be classified, including special structures such as bridges, industrial structures or underground excavations, while others only provide vague descriptions.

Perhaps the discrepancy in regulations that is harder to justify is precisely the most important one: the limit vibration levels. Differences in the characteristics of buildings from country to country justify part, but not all the dispersion in the allowed peak particle velocity criteria. A possible justification is that less and less field studies with real buildings are being conducted and this leads to a decrease on legal vibration levels. Also, most regulations aim not only at preventing damage to structures but also at avoiding perception of the blasts, disturbance to people, complaints and litigation. The relative unpredictability of vibration levels and of their consequence and the low threshold level of human sensitivity have led to increasingly cautious peak vibration levels. On the other hand, everybody (population, public administration bodies, contractors and constructors) desires disturbing activities to be completed as fast and economically as possible. Some old and also new tools can help the practitioners to minimize the disturbance caused by blasting mainly by applying methods from other disciplines, such as earthquake and structural engineering, to a phenomenon that has been, for the most part, treated with simplified, purely empirical tools.

3.6 Discussion

This chapter looks at a triangle whose vertices are Monitoring, Modelling and Regulation, as represented in figure 3.3. The description of each of the three vertices has, necessarily, been superficial. Some particular aspects will be looked upon hereafter, such as finite-difference and discrete element models or monitoring and impact vibration on underground structures. Other topics such as structural models of buildings or the vibration induced cracking are not explored at all. The relations of dependence and influence between the vertices of the system are described in the following paragraphs. Attenuation laws and artificial intelligence techniques are calibrated with the results of Monitoring campaigns while numerical models are built using information from blast and site observation and then calibrated and improved also through comparison with Monitoring results (arrow C). On the other hand, numerical tools' results help understand blasting and wave propagation (arrow D).

Relation between Regulations and Monitoring is evident. Monitoring plans are designed

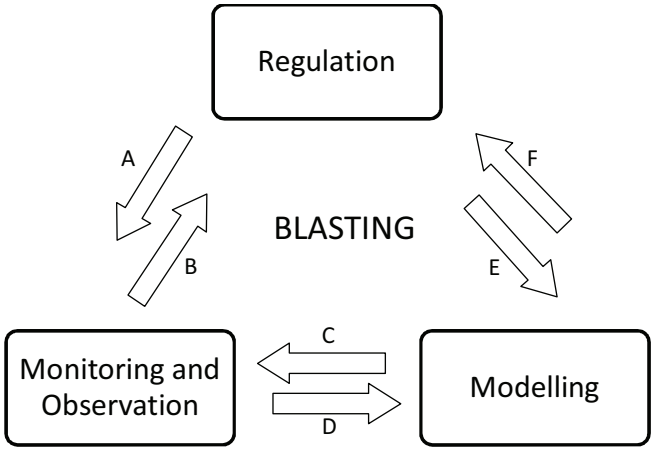


Figure 3.3: Monitoring, Modelling and Regulations as a system to assess vibration impacts.

by considering the vibration limits on structures indicated by the Regulations (arrow A). On the other hand, Regulations are written based mainly on the outcome of monitoring campaigns (arrow B).

Numerical models allow the application of Regulations' vibration limits in locations where measurements could not be made. In this aspect, Regulations determine the way models are built and the results that are extracted from them (arrow E). By helping to understand the phenomenon and permitting the study of a large number of situations that cannot be found in real scenarios, models may also be used to improve existing regulations (arrow F).

Acceptance and exploitation of these relations by all involved in blasting improves the mutual understanding of all involved in blasting: designers, authorities and blasters, leading to more efficient and safer blasting.

Chapter 4

Micromechanical Modelling of Dynamic Rock and Joint Behaviour

4.1 Introduction

The goal of micromechanics is to predict the mechanical response of materials by simulating the microscopic mechanisms of deformation and failure. The major benefit is that the behaviour of the material can be modelled without resorting to complicated constitutive models, which tend to be hard to calibrate and implement, mathematically complex and numerically problematic. If the fundamental hypotheses that drive the microscopic behaviour of the media are correct and efficiently implemented, the interaction of a few simple mechanisms should cover the response of the material under a broad range of situations: uni and multiaxial loading deformation, compressive and tensile strength, post-peak response, time effects, etc.

One of the first models for the modelling of materials at microscopic level was the lattice method. The material is described by a network of bar elements which transmit normal and, in some formulations, moments and shear forces that translate the macroscopic stress. The bars can be assigned breaking criteria that cause them to break. Lattice models have been used in and outside the rock mechanics community, and are elegant and computationally efficient. Among other authors, Schlangen and Van Mier (1994) tested different arrangements of lattice structures to model the response of sandstone.

The Particle Discrete Element Method (P-DEM) was proposed by Cundall and Strack in 1979 as a novel implementation of the Discrete Element Method, where polygonal blocks were replaced by plane circular particles. Initially built for the analysis of granular soils, as soon as computational power became available, it's use expanded into many other applications, one of which is the simulation of cohesive materials such as hard rock and concrete. It was generalised

to 3D, and various codes are available today. The P-DEM code PFC, acronym for Particle Flow Code, was developed by Itasca and is today available in both two and three dimensions (PFC^{2D} and PFC^{3D}) (Itasca (2004) and Itasca (2005)). It is one of the most complete and used particle codes. In general mechanics, a particle is an entity with null radius, but in P-DEM, a particle refers to a surface or volume with finite dimensions. In PFC^{2D}, particles are either disks or spheres, to which properties, such as mass, contact stiffness and strength, can be assigned. In PFC^{2D} circular particles have three degrees of freedom: two dimensional translation and spin in the disk's plane, while in PFC^{3D} particles possess the complete six degrees of freedom. Contacts between particles are easily resolved, as they are characterized by their centre coordinates and radius. In the initial implementation, contact consisted in a normal and a shear force, proportional to distance between particles. Later, more complex interaction contact models, such as Hertzian contact[1] were included. PFC users can add contact constitutive models by writing C^{++} routines that can be included in the code as DLL files (Dynamic Linked Libraries).

Rock static behaviour can be simulated by assemblies of a large number of particles with finite radius, bonded by ball-ball contacts. The relation between the models' properties (assembly arrangement, particles' radius and contact characteristics) and rock properties such as compressive strength or Young's modulus is not direct as there is no complete theoretical framework to relate micro and macroscopic properties (Potyondy *et al.* (1996) and Potyondy and Cundall (2004)).

Not much attention, however, has been dedicated to the modelling of rock dynamic behaviour using particle models. In the field of geophysics, some authors have used particle codes to model wave propagation in large scale, from hundreds of metres to tens of kilometres (Toomey (2001), Abe *et al.* (2004)). However, the model in question employed regular assemblies of particles, and this does not simulate with realism rock's more complex behaviour. Matsuoka *et al.* (2003) also used a regular arrangement of disks to model a Hopkinson bar test of rock, capturing some of the main features of the experiment, namely the detachment of a piece of the bar's extremity, separated and ejected due to the reflected tension wave. Hentz *et al.* (2004) employed a 3D particle model to investigate the effect of strain rate in the compressive and tensile strength of rock. Several authors have used particle models to model blasting in several aspects. Kim *et al.* (1997) and Donzé *et al.* (1997) modelled the crack generation caused by a blast charge in a cylindrical borehole, Donzé and Bernasconi (2004) modelled a shaft sinking blast in three dimensions, obtaining patterns of rock damage around the shaft. Kim *et al.* (2006) investigated the influence of joint direction and spacing at a tunnel contour blasting. These works employ particle methods on blasting and rock dynamic applications, managing

[1] In Hertz's contact theory (e.g. Johnson, 1985) the stiffness of a contact is related to the contact area and hence increases non-linearly with applied stress).

to qualitatively capture the major phenomena at stake, namely fracture creation and propagation, rock fragmentation, movement of the blasted rock and damage due to high dynamic stress. However, the propagation of elastic stress waves outside the zone of rock fragmentation is not a relevant issue in these cases and has not been addressed so far.

Hazzard and Young (2004) used PFC^{3D} to reproduce the anisotropic damage inflicted to a sandstone sample by triaxial deviatoric loading. The damage in the PFC^{3D} synthetic specimen is translated by broken bonds that lower the static stiffness and P and S-wave velocity in preferential directions. This is the only work, to the knowledge of the author, that investigates some of the characteristics of the propagation of stress waves in unorganized particle models of rock.

Interaction of the stress waves with rock fractures has been explicitly modelled in block DEM codes. The works of Lemos (1987) and later Cai (2001) apply the two dimensional DEM program UDEC to the propagation of plane waves normally incident on fractures. The fractures have linear elastic stiffness, and the model is able to reproduce the frequency dependence of the transmission and reflection ratio. The fracture is represented as contacts between blocks with shear and normal stiffness. This characterization is, however, far from reality. Fractures are irregular, present normal and shear non-linear response and show different stiffness values according to the intensity and velocity of the loading. More sophisticated block-to-block contact models have been developed, including some of these effects (Zhao and Cai, 2001), but the response is always represented by a constitutive model that does not include explicitly the real cause of the fracture's behaviour namely: asperity distribution, deformation and degradation with normal and shear load.

Some researchers (Kabeya (1999), Cundall (2000) and Kusumi *et al.* (2005)) have reported on the application of particle models to reproduce static shear behaviour of rock joints and faults. In these models, joint roughness is explicitly represented, the interaction between the walls of the joint is commanded by the geometry and by the properties of the rock material. The peak strength and dilatation dependency on normal stress are correctly modelled, as well as asperity damage by cracking. No work on the characterization of rock joints under normal loading by particle models has been found in the literature. It is natural that the shear response has been subject to more attention, given that failure in shear and tension are involved in most rock mass failure mechanisms, while joint normal behaviour has a relevant effect on rock mass deformability, permeability and stress wave propagation.

This chapter is dedicated to the application of P-DEM to the modelling of wave propagation in rock masses. The purpose is to investigate the capabilities of this thriving and versatile numerical method on modelling wave propagation in rock masses and rock fractures at the microscopic level. When stress waves cross rock masses they are altered in several ways, and

the main cause is, usually, interference with fractures. Research on the mechanics of this interaction at the level of asperity has been pursued, but the small scale of the phenomena and the complexity in controlling emitted waves' shape and measuring accurately these waves poses several difficulties. Micromechanical models simulate the deformation of asperities and allow the observation in close detail of the passage of the waves across fractures. In this thesis, the focus is on the simplest case, *i.e.*, propagation of low amplitude high frequency plane compressive waves normally incident on fractures that are loaded with growing compressive stress. Compression closes the joint and the area of contact increases, changing the transmissivity of the joint. For this reason, a particle contact model for the joint was developed. This model reproduces a generic rock joint under normal stress, and emulates the increase in contact area and corresponding growing stiffness with applied stress. Then, compressive waves are generated and propagate towards the rock joint, under growing normal stress loads, and the transmitted and reflected waves are analysed.

Since the mechanics and fundamental aspects of particle and block methods are similar, a generic exposition of the DEM is given. Then, follows the specific aspects of modelling static rock behaviour with PFC^{2D}. Afterwards, the application of P-DEM to modelling normal joint static and dynamic behaviour is presented. Finally, conclusions are presented, as well as future paths of development in this field.

4.2 The Discrete Element Method

The observation of typical rock masses and their modes of failure, particularly of those near surface, asks for models that represent rock joints and movement along them. One of the responses to this was the inclusion of joint models into the already existing Finite Element Method.

In 1971, a numerical method totally based on the assumption that rock mass behaviour is dictated by movement at the level of rock joints was developed (Cundall, 1971). It was called the Distinct/Discrete Element Method (DEM) or Block Method. The rock mass is simulated by an assembly of plane rigid blocks of polygonal shape. As blocks are rigid, and able to move freely, all deformability in the model is due to movement–opening, closure and shear displacement–of the joints. The calculation of the blocks' motion at each instant of the calculation is performed in two steps. In the first, the forces and moments acting in each block are added and applied to its mass centre. This stage includes resolving forces that arise at the contact between blocks. In the second stage, the equation of motion of each block is solved independently.

Later, an internal triangular finite element mesh has been introduced in each block, allowing the deformability of rock to be taken into account improving the response of the model,

especially in occasions where the relation between stress and rock strength is high. A scheme that allows blocks to crack and split according to a given strength criterion was also introduced. The program UDEC (Cundall, 1980), put together all these possibilities.

In 1988, the code 3DEC brought the expansion of DEM to three dimensions (Cundall (1988), Hart *et al.* (1988)). The three dimensional blocks have polyhedral convex form, with planar faces, and can be rigid or deformable, by means of internal division in tetrahedral finite-strain finite elements.

A lot of improvements and new capabilities have been introduced in the block and particle element methods, and some of the most important are enumerated. The inclusion of linear and shell structural elements allows for the representation of reinforcing cables, piles, beams and tunnel lining. The introduction of thermal and hydraulic calculation allows the conduction of fully coupled thermo-hydro-mechanical calculations. Finally, higher order parabolic finite-elements can be employed as the internal mesh in cubic blocks in the three dimensional code 3DEC, a valuable tool when the lower-order discretization does not provide sufficient accuracy.

4.2.1 The calculation cycle

Discrete element method simulates the interaction and motion of bodies whose shape is limited only by the capacity of the model to manage their interactions: polygons, balls or spheres. DEM does this by performing the time marching calculation of the movement of the bodies under the influence of loading and contact forces. The two main phases of a calculation cycle are: calculation of the forces at play, which includes managing the interaction between the bodies, and solving the equations of motion. Each cycle, as depicted in figure 4.1, is associated to a timestep Δt, whose significance and determination method are explained later on.

Although most DEM codes, namely Itasca's UDEC and 3DEC were initially designed to model rock masses and geomaterials, the flexibility and connection with reality make them suitable for other uses.

4.2.2 Contact management

Being a cyclic time steeping method, any part of the cycle (figure 4.1) is equally a good place to start the description of the calculation. This section describes the computation of forces acting on the bodies, with special emphasis on the most complex part: contact management and resolution of contact forces.

The aim of contact management is to find pairs of bodies in contact and to calculate the forces between them. Theoretically, finding which bodies are touching is a simple task, the problem lies on the calculation volume. Using a direct method, the number of operations grows

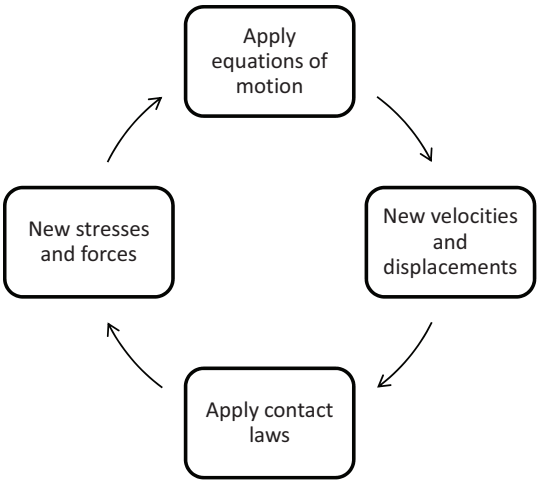


Figure 4.1: DEM calculation cycle.

with the square of the bodies. Itasca's codes employ a strategy in which the domain is mapped into cells, and contact is searched only inside them. To increase efficiency, bodies at rest are not checked against each other and contact updating may not be done on every.

Different body types can touch in different ways. 3D polygonal shapes, for example, can interact in a variety of ways: vertex to face, face to face, edge to face, edge to edge, etc. Strategies to represent different contact types were developed reducing all contacts to basic contact types, independent of the type of body in question. Edge-face contacts, for example, are represented by two point-point contacts, face to face contacts by three or more point contacts (figure 4.2).

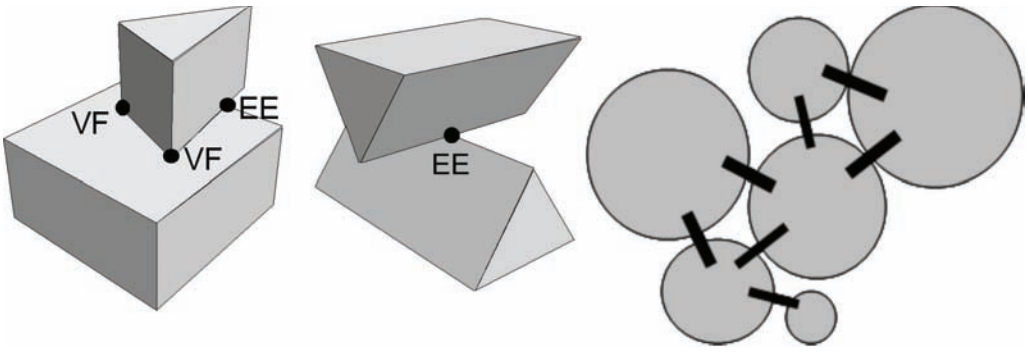


Figure 4.2: Resolution of contacts in 3D solids and in 2D balls. Taken from Lemos (2001).

Contact between circular or spherical particles is much simpler. Each contact is characterized by a contact law, which may have any desired formulation. The simplest contact law is a

linear elastic model:

$$F = ku. \tag{4.1}$$

In this equation u is the accumulated displacement, so k is a ball contact stiffness[2]. The law may be defined in incremental fashion, that is, the force in instant *j+1* is a function of the previous timestep *j*. Then, k represents a tangent stiffness and incremental displacement Δu and force ΔF are used:

$$\Delta F = k\Delta u, \tag{4.2}$$

and

$$F_{j+1} = F_j + \Delta F. \tag{4.3}$$

Either way, the stiffness of the contact has always dimensions $[Newton/metre]$, and absolute or incremental displacement of the contact are easily calculated from the updated body position and geometry.

In order to model contact failure in tension or shear, adequate strength criteria, of which the Mohr-Coulomb is the most popular, can be used. When rock joints are modelled as the contact between the faces of two blocks, stiffness and strength values can be taken from laboratory or *in situ* tests and attributed to the face to face contacts, eventually scaled to take into account size effects. On the other hand, in micromechanical modelling, contact parameters are not directly linked to measurable properties of rock or rock mass. Micro properties must be calibrated via indirect methods, resorting to empirical strategies.

After the contact and other forces (external loads, forces in block boundaries, gravity loads) are calculated, they are transferred to the centre of mass of the body (polygon or ball).

4.2.3 Solution of motion equations

This section deals with the part of the cycle when new positions of the blocks/particles are determined. In the previous part, forces acting at the centres of mass were determined. These forces, acting on bodies of known linear and angular inertia, will cause acceleration, increasing or decreasing their speed and spin velocity, according to Newton' second law of motion:

$$F_i = m\ddot{u}_i, \tag{4.4}$$

where i denotes the three directions and m the mass.

Most DEM models employ explicit timestepping techniques to integrate the second-order differential equations of motion. In implicit techniques, ensemble equilibrium of the model

[2]Since in the text "microscopic" particle contact stiffness and "macroscopic" rock joint stiffness values are widely used, the former are represented by a lowercase k and the latter by a uppercase K.

is attained at the end of the calculation cycle, which has to be performed just once. This calculation is expensive in terms of memory and CPU time, as it involves assembling and solving a global matrix of the model. In order to run a calculation in the time domain, or one with several steps (e.g., due to incremental loading, physical or material non-linearity or phased construction), the model matricial representation has to be assembled and solved in each stage or timestep.

Explicit techniques are well suited for dynamic analyses, incremental calculations and non-linear systems involving large displacements, as changes in the model are transported into the next step with no need to modify a global variable or matrix that stores the state of the whole system. The resolution of static problems is done by letting the model find its own equilibrium state under static and kinematic boundary conditions, dissipating excess of energy through damping.

In DEM, integration of motion equations is done through the finite-difference algorithm. The scheme is stable if the timestep is limited to the smallest period of the system, which is associated to the highest mode of vibration. However, as calculation of the model's eigenvalues is lengthy and presupposes that a stiffness matrix is available, alternative methods, which obligatorily lead to higher smaller timesteps than the exact value, are generally used (Belytschko, 1983).

Central difference scheme

The translation of a body obeys Newton's second law, equation 4.4, written now in terms of acceleration (body rotation follows the equivalent Euler's law and therefore the equations are not included here):

$$\ddot{u}_i = \frac{F_i}{m}, \tag{4.5}$$

where u_i is the displacement vector of the block's centroid, F_i represent forces acting at the centre of mass and m is the body mass. The central-difference scheme calculates velocity at the start of each new calculation cycle, to which a time t and a timestep value Δt are associated, from the motion values at the middle of cycle. The velocity of a particle is taken as the average of the velocities in the middle of the previous and following timestep:

$$\dot{u}_i(t) = \frac{\dot{u}_i\left(t - \frac{\Delta t}{2}\right) + \dot{u}_i\left(t + \frac{\Delta t}{2}\right)}{2}. \tag{4.6}$$

Acceleration at instant t is, similarly:

$$\ddot{u}_i(t) = \frac{\dot{u}_i\left(t + \frac{\Delta t}{2}\right) - \dot{u}_i\left(t - \frac{\Delta t}{2}\right)}{\Delta t}. \tag{4.7}$$

Inserting equations 4.6 and 4.7 in Newton's equation 4.5, it is possible to obtain the velocity ahead of the current timestep, $\dot{u}_i(t + \Delta t/2)$, because $\dot{u}_i(t - \Delta t/2)$ is known from previous

timestep and the applied force and moment are known for the instant t:

$$\dot{u}_i\left(t+\frac{\Delta t}{2}\right)=\dot{u}_i\left(t-\frac{\Delta t}{2}\right)+\frac{F_i(t)}{m}\Delta t. \tag{4.8}$$

Displacement at the next timestep $(t+\Delta t)$ is:

$$u_i(t+\Delta t)=u_i(t)+\dot{u}_i\left(t+\frac{\Delta t}{2}\right)\Delta t. \tag{4.9}$$

One of the advantages of this integration algorithm is its versatility. It can be applied to linear or non-linear static or dynamic problems. In non-linear dynamic analysis, and contrary to iterative schemes, equilibrium need not be attained at every timestep. The algorithm is also independent of the structural element and of the constitutive models at contacts.

Numerical stability

In an elastic linear system, the convergence of the explicit integration algorithm depends on the timestep, which is linked to the highest vibration mode of the system, as previously written. Calculation of the model's eigenvalues is very time consuming, demanding the assembly and inversion of a stiffness matrix, which is not needed for other purposes.

An overly conservative but efficient way to calculate an upper value of the model's highest frequency of vibration is to consider each particle as an isolated, one degree of freedom structure, characterized by its mass and rotational inertia, attached to a spring that sums the contributions of all the contacts' springs that link to that particle. The particle's translation period will then be:

$$P=2\pi\sqrt{\frac{m}{\sum k}}. \tag{4.10}$$

The rotation period is calculated in a similar manner, with the particle's inertia angular moment and rotational stiffness replacing mass and translational stiffness. Each particle is assigned a critical timestep for translational and rotational motion. The model's timestep will be the minimum of all timesteps, translational or rotational, and is recalculated periodically, in order to accommodate changes in the model's characteristics, such as new or vanishing contacts.

Mass scaling and mechanical damping

In static calculations, the transitory state of the calculation is irrelevant, only the final, steady-state solution is of interest. As such, it is convenient to use the highest stable timestep, which is a function of the contacts' stiffness and of the balls' mass (equation 4.10), in order to speed up the calculation as much as possible. Since the mass m of the motion equation 4.8 has no real physical meaning, the particles' mass (but not their self-weight) may be altered at will.

This procedure, called mass or density scaling, aims to arrive at an unitary critical timestep. Each balls' mass is scaled so that the ratio inside the square root in equation 4.10 approaches one. The calculation time also has no real meaning.

In DEM, mechanical damping may pursue two distinct goals. In dynamic calculations, damping mimics the material stress wave attenuation, due to inter-particle friction, scattering at voids and microcracks and interaction with fractures, with the associated loss of energy that occurs in all real structures and materials. In static calculations, damping is employed to take away energy from the system until it arrives at a final steady state. When no damping is included in the motion equations, the model will vibrate endlessly, never reaching a steady state solution. Since, in static calculations, dynamic transient states are not relevant and damping is not attached to the physical problem, it is treated as a numerical artefact.

In PFC, three different kinds of damping are available: local, combined and viscous damping. Local damping consists on the addition of a force, contrary to the particle velocity, that is summed to other forces (contact loads, gravity loads, etc.) that act upon the particle. It intervenes at the level of the equations of motion. This has some advantages, namely that only particles that are moving are affected, it is independent of frequency and very simple to calibrate. In cases where there is significant rigid-body motion of parts of the model, combined damping, which is a combination of local damping and a force that is proportional to the rate of change of the force applied to the particle, may provide a more efficient method of achieving the solution. Just like local damping, combined damping acts at the level of the motion equation. Viscous damping acts not on the particles' movement equation, but at contact level. A viscous dashpot is added in parallel to each contact's spring. By altering the contact response, viscous damping alters the critical timestep, which must be reduced for sake of stability (Belytschko, 1983). Finally, in hysteretic damping, energy is dissipated in each cycle, and therefore is introduced via the contacts' constitutive model.

4.3 Micromechanical modelling of rock with particle models

So far, the description of DEM has broadly covered common aspects of the method, without focusing on block, disks, rigid or deformable models. However, particle discrete element models, and the uses they are put to, have certain particularities. In some cases, the implementation of particle models is far simpler (*e.g.* contact search), in others, more complex (*e.g.* particle assembly generation or particle clustering).

Particle models are employed in quite diverse fields: mechanics of incoherent soils, fracture of concrete and rock, mining, nuclear reservoir stability, slope stability, avalanche study, grain storage in cereal silos (Itasca, 2008a). The development of a basic Particle DEM code is not

excessively hard, and several have been developed (Donzé (2002), Azevedo and Lemos (2005), Sena and Silveira (2007) or Toomey (2001)).

In the next section of this chapter, the fundamentals of modelling of hard rock and hard rock fractures, under static and dynamic conditions are described. Some of the particulars of DEM that are specific to micromechanical simulation are depicted here. The code employed in all the modelling on this chapter is Itasca's 2D Particle Flow Code–PFC^{2D}, version 3.1, with the C^{++}/UDM option, which allows the user to add external contact constitutive models. For a comprehensive description of Particle-DEM modelling refer to Itasca (2004), Potyondy *et al.* (1996) and (2004).

The mechanical phenomena that take place at the level of the rock's grain are difficult to understand and reproduce faithfully in the framework of the continuum theory. Rock response to mechanical loadings, even in the linear, reversible domain is the ensemble of a multitude of interactions, between rock grains of similar or different minerals, cement, microscopic voids and flaws.

It is in this medium, by no means homogeneous, but that initially presents a response that is similar to that of an ideal homogeneous material, that crack growth, generation and coalescence takes place. When this process, caused by mechanical or thermal loading, begins, the continuum model has difficulty accompanying the response. Elasto-plasticity (Vermeer and de Borst, 1992, e.g.) and continuum damage theory (Krajcinovic, 1995, e.g.) provide tools, or extensions that help continuum theory to explain and reproduce this behaviour, but none of these models relates to what really happens in the core of the rock: localized crack growth, grain interlocking, stress location, etc.

In steel, for example, cracking starts in the imperfections in the atomic structure. The scale of these phenomena in rock is not really microscopic, but in the order of 10^{-4} to 10^{-3} metres. This makes the use of models that replicate the grain possible, although models with larger particles can also replicate well the behaviour of rock.

Micromechanical models of rock initial goal was helping to understand phenomena, test theories and provide input for continuum constitutive models, but they are now taking the leap to full scale applications, as processing power, memory availability and codes that run in several processors, converge and open the door to models with hundreds of thousands to millions of particles.

The mechanical behaviour of rock is simulated by a collection of rigid disks or spheres with non-uniform size distribution. The disks or spheres have a finite mass and are bonded at their contact points. These contacts are governed by contact laws that, for the simulation of rock materials must include shear and tensile strength limits. Though particles are treated as rigid, they can overlap, originating strong repulsive forces which force the superposition to be small.

This causes the contact area of two particles to be small in relation to the particles' dimensions.

This set of assumptions leads to the formation of a tightly packed set of particles (see figure 4.3), where deformation comes from change in interparticle space. Since the particle's arrangement has a degree of randomness, the irregularities are the natural starting point of cracking and damage, as in rocks. Also similarly to real rock samples, a measurement taken at the balls' scale is not representative of the general state of the specimen or even the region around the ball. So, contrary to continuum models, stress, deformation and damage cannot be locally defined, and must be averaged over an area or volume that captures a sufficient number of particles and contacts.

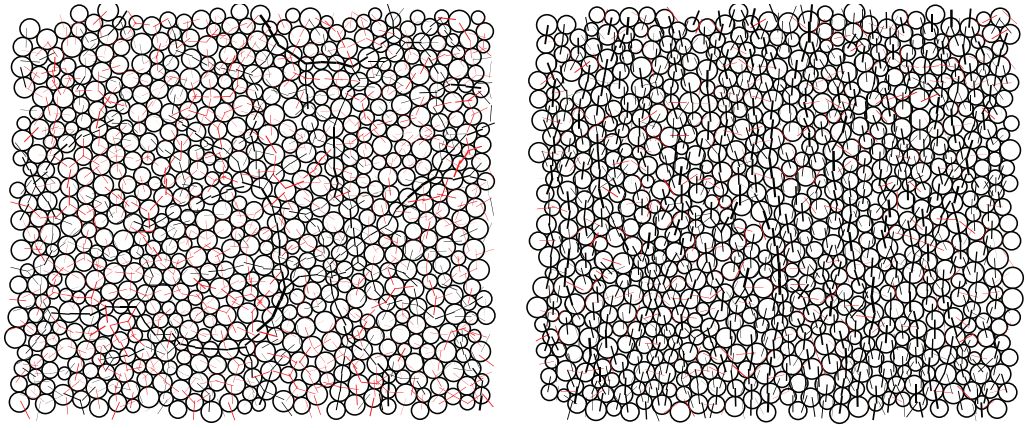


Figure 4.3: Representation of contact forces (line thickness is proportional to force, black is compression and red is tension) in two dimensional disc assembly: isotropic stress state (left) and vertical stress state (right).

In PFC^{2D}, balls represent either a cross section of a disk, whose length can be defined by the user, or a mid cross-section of a sphere, with radius equal to the ball radius. The only consequence of choosing either mode lies in the calculation of the ball's mass, as all other properties and behaviour are equivalent. In the case of disks of radius r and height t, a particles' mass is a function of both dimensions and mass density ρ:

$$m_{disk} = \pi r^2 t \rho_{disk}. \tag{4.11}$$

In the case of a sphere of radius r:

$$m_{sphere} = \frac{4}{3}\pi r^3 \rho_{sphere}. \tag{4.12}$$

In static calculations, ball mass is relevant only when determining self-weight loads, as the mass is scaled to attain optimal timesteps and thus speed up the calculation process. On dynamic

simulations, mass plays an important role, as ball translational and rotational inertia intervene in the movement equation. The choice between disks and spheres is justified in section 4.5. In the continuation of the text, the terms ball and particle are used to refer indiscriminately to either disks or spheres.

Representation of rock as an assembly of small particles can be done with more elaborate shapes, such as ellipses or polygons, which allows for a richer behaviour (figure 4.4). The main disadvantage of these more complex shapes is that the contact search and resolution is much more complicated and lengthy. Circular and spherical particles can be clumped together to form higher-order shapes, but this also implies an increase in computation time. An interesting study is to investigate when the computational expense of clumps composed of simple particles starts to exceed the use of more complicated elements, like polygonal shapes.

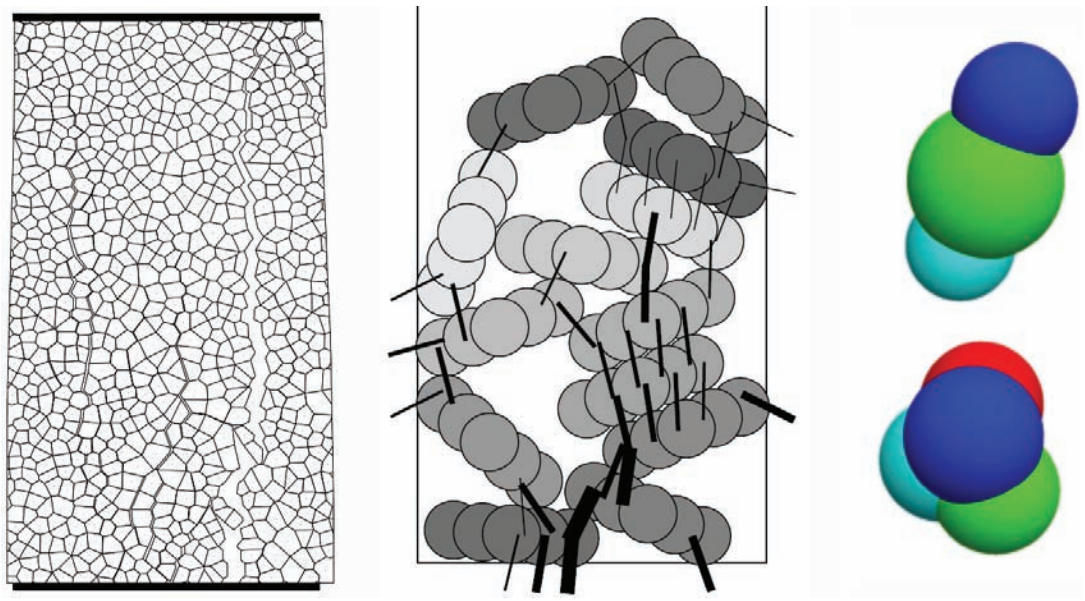


Figure 4.4: UDEC polygonal model of rock core after compression test (Kazerani and Zhao, 2008) (left); two dimensional clumps in equilibrium, notice contact forces only exist between clumps, not inside them (Itasca, 2004) (centre); three dimensional particle clumps (right).

In the following paragraphs, the creation of two-dimensional compact assemblies, contact laws and calibration of synthetic models of rock are described.

4.3.1 Contact models

A specimen is defined by the particle arrangement and by the properties of the contacts. It should once again be noted that properties at the level of the contacts are not directly propor-

tional to macroscopic properties, although general tendencies can be drawn.

Whenever two particles overlap, a new contact, located in the line that connects the two particle centres, is formed. A contact comprises two forces, both in the plane of the particles: a normal force, acting along the line that connects the centres, and a shear force, acting perpendicular to the normal force (vectors $\vec{n}$ and $\vec{s}$ in figure 4.5).

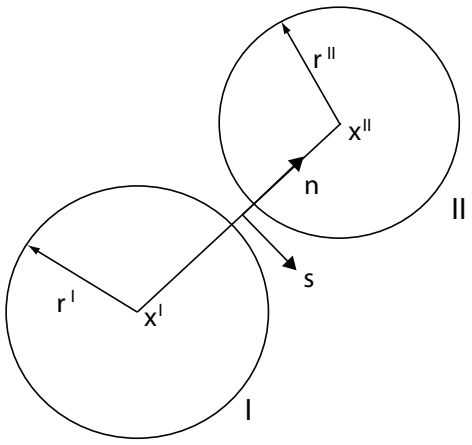


Figure 4.5: Contact between two balls.

The default contact model in PFC is constituted by three separate models: a stiffness model, a bond model and a slip model. The stiffness model controls the deformation of the contact through linear force-displacement relations. Each contact is assigned a shear and a normal stiffness, k_s and k_n, respectively. The stiffness values are derived from the properties of the two particles in contact (k_n^I, k_n^{II}, k_s^I and k_s^{II}). Each ball contributes with a spring and the contact stiffness is calculated by equations:

$$k_n = \frac{k_n^I k_n^{II}}{k_n^I + k_n^{II}}, \tag{4.13}$$

and

$$k_s = \frac{k_s^I k_s^{II}}{k_s^I + k_s^{II}}. \tag{4.14}$$

From equations 4.13 and 4.14 it is evident that the contact between two balls with similar stiffness will have half of the stiffness assigned to the balls. Contact stiffness in this model has no regard for the ball dimensions: if two balls of different sizes and the same stiffness are in contact, each ball will contribute equally to the contact stiffness. Other stiffness models, like the Hertz model, take ball's dimensions into account.

In PFC, the normal stiffness is a secant stiffness, meaning that the normal force's absolute value is calculated directly from the accumulated displacement, as in equation 4.1. The shear stiffness is a tangent value, *i.e.*, in each timestep an increment of the force is calculated and

added to the shear force from the previous timestep, as in equation 4.2 and 4.3. This incremental implementation facilitates the use of elasto-plastic models in shear Itasca (2004).

The bond model (figure 4.6) is a strength criterion that limits the amount of shear and tension a contact can withstand, by definition of shear and tension forces in each contact. These bonds act on a vanishingly small area, thus carrying forces but not moments. The parallel bond, more sophisticated, does have the possibility of opposing to particle rotation by transmission of moments between two balls. An area of contact, that is a function of the balls' radius, is associated to the parallel bond. Parallel bonds are so called because they act in parallel with contact bonds, so that the interaction between two balls can be composed of contact bonds, parallel bonds, or both. In this study it was found that for the purpose of modelling wave transmission in elastic conditions, as performed in this chapter, parallel bonds are not required and add complexity to the calibration of the model and to the interpretation of results, so only contact bonds were used.

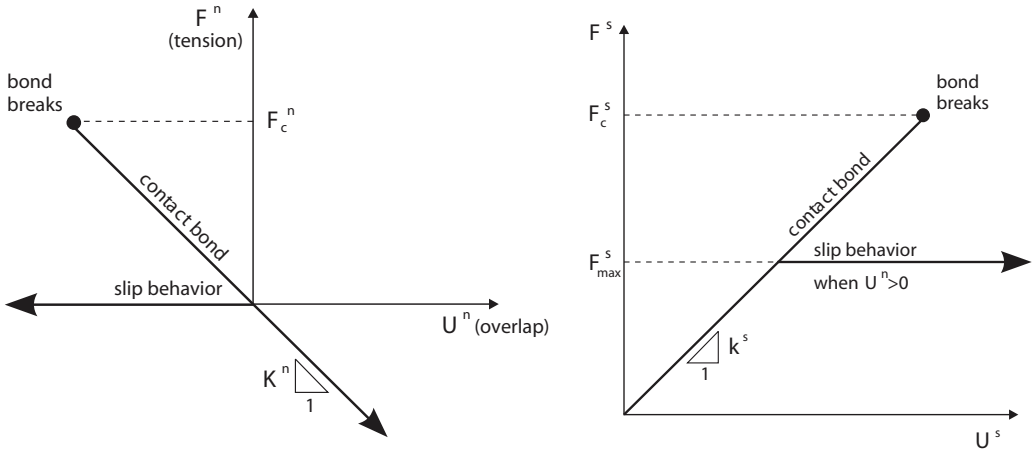


Figure 4.6: Force-displacement behaviour for point contact. Normal (right) and shear (left) component of contact force. Adapted from Itasca (2004).

When the magnitude of the tensile normal contact force exceeds the tension bond contact strength, the bond will disappear and all forces in the contact are set to zero. This makes sense: if the tension strength is exceeded, balls are no longer in contact. On the other hand, if the shear bond strength is exceeded, the bond will disappear but contact forces remain, and the slip model takes the place of the contact bond.

The slip model starts to act as soon as the contact bond fails in shear. The slip model is a friction criterion, that defines a maximum allowed shear force F_s^{max}:

$$F_s^{max} = \mu \left| F_n \right| , \tag{4.15}$$

where F_n is the normal force acting on the contact and the friction coefficient of the contact, μ is the smallest value assigned to each of the two balls. In the widely used Mohr-Coulomb strength criterion, friction and cohesion act simultaneously, and initially it can be a source of confusion that in the basic PFC contact model the friction is accounted only after the shear bond failure. It should be noted that the ball-ball contact does not aim to replicate directly the response of rock that is usually well represented by the Mohr-Coulomb model. While the ball contact models act in small scale, the Mohr-Coulomb criterion models a behaviour, that is a macroscopic consequence of the collective response of the particle contacts.

4.3.2 Generation of Bonded Particle Models

Bonded Particle Models (BPM) are assemblies of particles that have such packing characteristics and contact models and parameters such that they replicate hard rock response. These models must meet two conditions: particles must be well connected (each particle should be in contact with three or more other particles) and the assembly must be able to withstand isotropic locked-in stresses. As will be seen ahead, regular rectangular or hexagonal arrangements do no meet the second condition.

Several methods can be employed in creating an initial packing. PFC^{2D} and PFC^{3D} include an external programming language called FISH that allows the user complete control of the input to the program, provides conditional and cyclic structures and gives direct access to the data structures of the code. A large set of pre-built functions, called FISHTANK, is included with the program. FISHTANK is a complete environment of FISH functions that allows the creation of ball assemblies to model cohesive and non-cohesive materials. The procedure used for the creation of hard rock samples consists on five sequential steps (Itasca, 2004). The data entered by the user is divided in two groups, one corresponding to the geometry of the packing and the other corresponding to the microscopic properties of the balls. The geometry of the packing is defined by specimen width and height and minimum and maximum radius of the balls (the maximum over minimum radius relation should not be far from 1.6, to generate a void ratio of approximately 16%). The steps are:

1. A domain with the intended dimensions is limited by planar walls and filled with particles whose radii follow an uniform distribution bounded by the upper and lower values inserted by the user. The number of particles is calculated in order to achieve a porosity of around 16%. Initially the balls are generated with half of their final radius. After insertion of all particles, their radius is expanded while they are allowed to accommodate to their neighbours.
2. The average stress in the specimen is measured and the radii of the balls are gradually

reduced until the desired locked-in stress is achieved.

3. All particles with less than 3 contacts, called floaters, are expanded, so that a dense network of well connected balls is achieved.
4. Bonds, corresponding to connections with shear and tensile strength are installed between all particles that are either touching or very near.
5. The walls that confine the specimen are deleted and the packing is allowed to expand, relaxing until the repulsive forces due to particle interpenetration and the bonds balance each other. When the final equilibrium is achieved, a set of locked-in forces is in place. These forces should be much smaller (around 1%) than the resistance of the bonds, in order for the full strength of the material to be available. The locked-in forces replicate the inter-granular self-balanced residual stress that exists in every rock. The packing has a certain amount of stored energy that can be liberated when cracking occurs.

Figure 4.7 presents the result of each of the five steps of a two dimensional model, while figure 4.8 displays the final state of a three dimensional model.

This procedure presents two problems: it does not work well when the specimen is very slender, and it is time consuming when particle number grows above several tens of thousands particles.

A workaround to both problems is provided by the "Periodic Brick" scheme. In this scheme, a rectangular assembly with self-similar border geometry that permits a perfect match with periodic borders is created, following the same five steps described above. The periodic borders allow the assembly of bricks in all directions, as illustrated in figure 4.9. The user must be cautious when choosing the initial dimensions of the brick, as each brick should be large enough to be representative of the rock material.

4.3.3 Macroscopic properties

Once a compact, well connected packing is assembled, the properties of the ball's contacts must be assigned. In reality, mechanical properties are defined and set during the assemblage of the packing, but the processes can be considered as independent, for greater clarity and easier understanding.

The properties of a synthetic rock sample that are usually used as goals for the calibration are the elastic Young's modulus and Poisson's ratio, the unconfined compressive strength, the crack initiation stress, defined as the stress at which dilation just begins on a plot of volumetric strain (Martin, 1993), and the tensile strength. It is not possible to predict the properties of a sample with a given distribution of micromechanical properties, so empirical relationships between micro and macroscopic properties based on dimensional analysis and optimization strategies

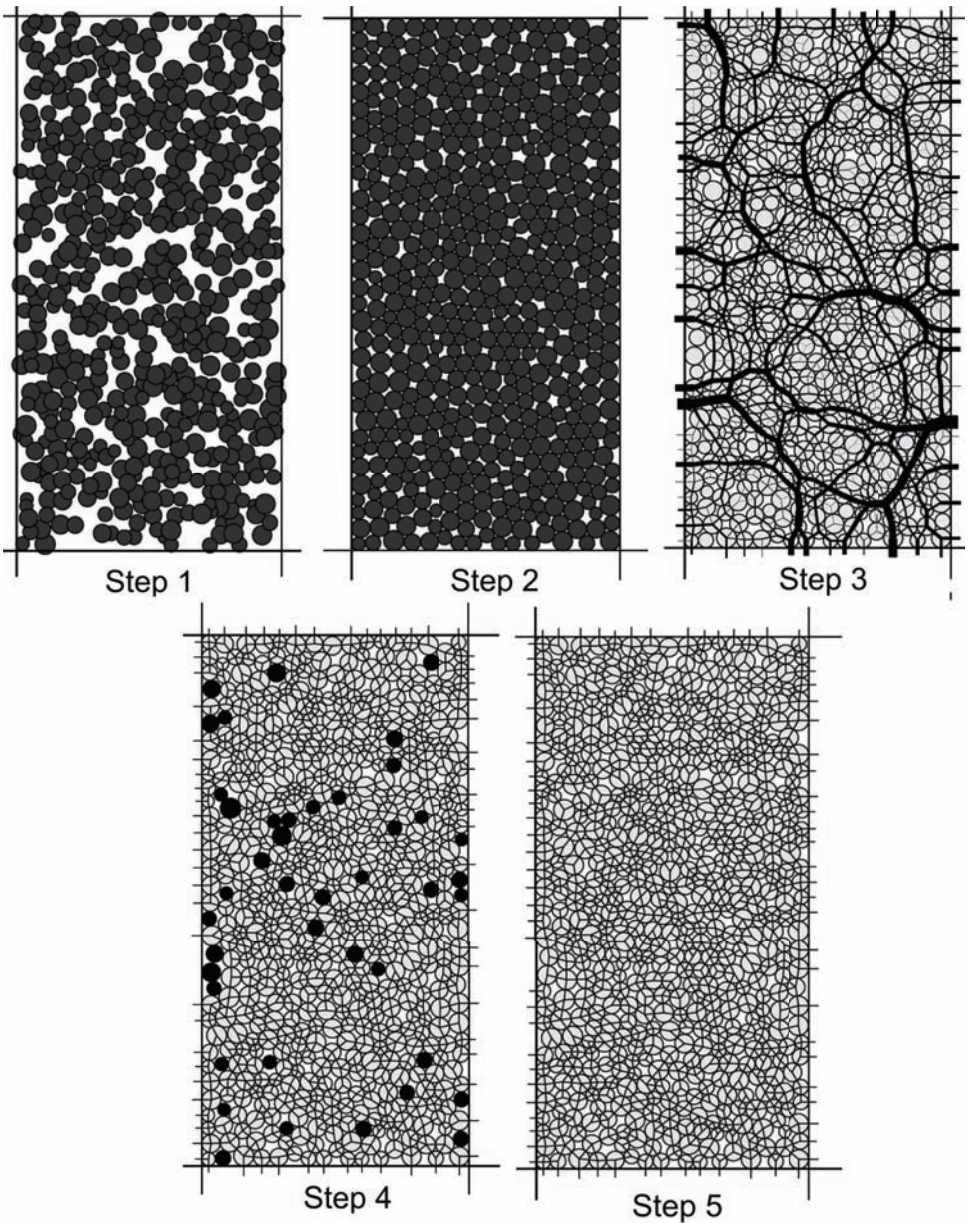


Figure 4.7: Generation of a bonded assembly: model at the end of each of the five steps. Taken from Itasca (2004)).

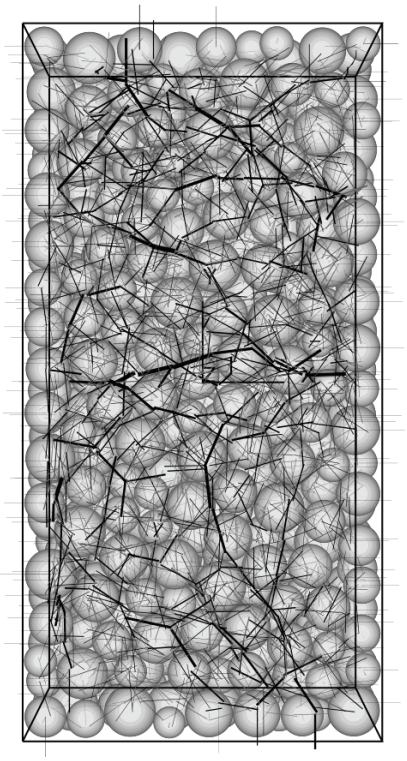


Figure 4.8: Three dimensional bounded assembly showing locked-in forces. Taken from Itasca (2005).

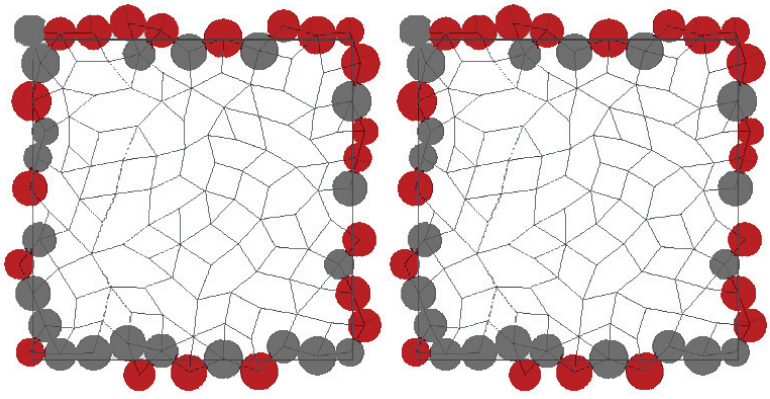


Figure 4.9: Periodic brick. Red balls will take the place of grey balls ensuring a perfect fit in all directions. Adapted from Itasca (2004).

have been developed (*e.g.* Huang *et al.* (1999), Yoon (2007) and Fakhimi and Villegas (2007)). Figure 4.10 shows empirical curves that relate contact shear and normal contact stiffness, which are microscopic parameters, and the macroscopic response of the model, materialized in Young's modulus and Poisson's ratio.

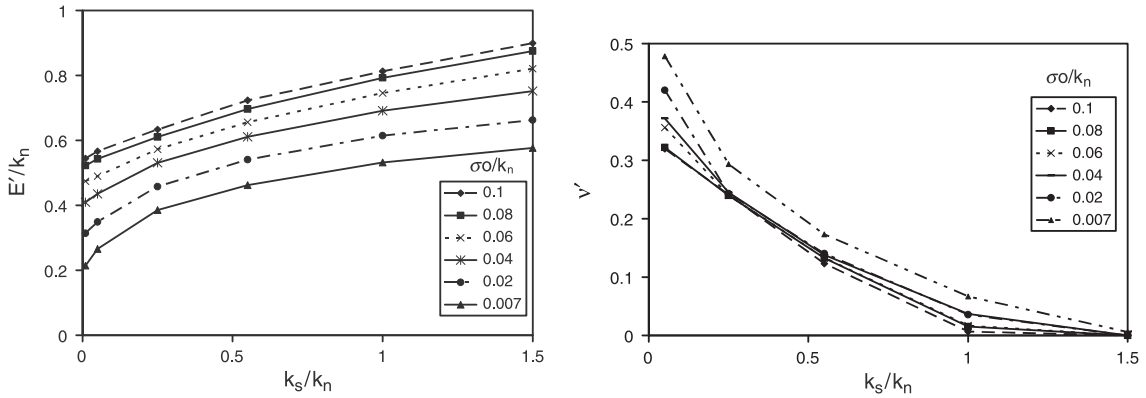


Figure 4.10: Elastic constants of synthetic material *vs* k_n/k_s for different genesis stress-normal stiffness ratios. Normalized apparent Young's modulus (left), Poisson's ratio (right). Taken from Fakhimi and Villegas (2007).

A discussion of a five step sequential procedure to calibrate BPM microproperties can be found in Potyondy and Cundall (2004). It has been thoroughly tested and provides an economical and reliable way of generating good quality specimens. The parameters that define the short-term static response of a specimen are: contact normal and shear stiffness, contact bond and shear strength and contact friction coefficient. Bond strengths can be set as constant or follow a normal distribution, defined by its mean and standard deviation. Ball density must also be set, as it is used in self-weight load calculation. In dynamic calculations, density influences the material impedance. The procedure follows these steps:

1. The bond strengths are set to a very high value, so that no contact ruptures occur during the calibration of the elastic constants. The Young's modulus is set by varying the contact normal stiffness, while keeping the ratio of the normal and the shear stiffness constant. Once an acceptable value of the Young's modulus has been attained, normal stiffness is held constant while the shear stiffness is adjusted until the target Poisson's ratio is attained. It may be necessary to readjust the normal stiffness if the initial ratio changes too much. This ends the calibration of the elastic response.
2. The unconfined compressive strength is set by varying the shear and tension bond strengths, while keeping the standard deviation null. To lower the number of parameters to calibrate,

the ratio of the tension to shear bond strength can be held constant.

3. Then, the crack-initiation stress is set by gradually increasing the standard deviation of the bond strengths. This step may alter the peak strength, so iterating with the previous step to fine-tune may be necessary.
4. Post-peak behaviour (from brittle to softening response) can be set by varying the particle friction coefficient;
5. Finally, the strength envelope can be determined by performing biaxial tests at different confinements. The tensile strength can also be found by cutting a circular domain of the specimen and performing a Brazilian test. It should be noted that, at the current state of knowledge of P-DEM modelling of rock, there is no way of matching both the strength envelope and the tensile strength of a specimen.

Two synthetic samples generated using exactly the same sequence of commands will have slightly different properties, as there is a certain degree of randomness in the ball generation and microproperties distribution. The difference from one synthetic sample to another due to assembly randomness is smaller than what can be expected between rock cores taken from a homogeneous rock mass. Particle radius has little influence on the static properties, provided that the particles' dimensions remain much smaller than the specimens' smaller dimension (Potyondy and Cundall, 2004).

In this thesis, the goal is to investigate the dynamic properties of rock material and rock fractures. As there is no pre-established procedure to calibrate dynamic properties of a specimen, it was decided to build one with well defined static properties, then measure compressive wave propagation velocity, and back adjust normal contact stiffness as necessary to match the desired value. The specimens were, therefore, generated using just the first step of the calibration process. As all non-linearity is to reside in the rock macroscopic fracture that is to be generated in the specimen, bond strengths in the intact material are set to very high values, so that the rock behaves elastically no mater how high the stresses imposed on the model.

4.4 Rock joints static normal behaviour

This chapter describes the work of modelling the wave - fracture interference at the microscopic level in two dimensions. Laboratory sized rock specimens are assembled, then fractures are generated and these are tested under normal loading. Afterwards, plane waves are sent against these fractures and the transmitted reflected waves are measured. On a 2.2 GHz dual-core processor with 2GB of RAM the whole process is quick: some hours to run the complete compression test of the fracture and then some minutes to run each wave propagation test.

With codes adapted to multi-processor machines large particle models incorporating sets of natural discontinuities can be run.

Here, the first step is taken, starting with the simplest problem in wave-fracture interference: two dimensional plane P waves hitting a fracture under various normal stresses. The next steps are the expansion of the model to three dimensions, oblique and mixed waves and the study of wave attenuation on intact rock by simulating flaws and voids in rock material.

Prior to the dynamic test, a rock sample is generated, following the procedures presented in the preceding sections. Then, a rock fracture is generated and tested under increasing normal stress. Finally, a wave is generated at the bottom of the model, and allowed to propagate across the fracture. The waves that are reflected and transmitted are measured and compared with analytical solutions.

4.4.1 Mechanics of joint compression

When approaching the problem of analysing, understanding and simulating the effects of rock joints in the behaviour of rock masses, there are two diverging paths that can be taken: in the first, the effect of the joints is indirectly taken into account when choosing the model and the parameters of the rock mass, which is thus considered as an equivalent continuum. In the second, rock joints (and possibly, voids, bedding planes, etc.) are taken and modelled individually. In this second path, which is followed in this chapter, the behaviour of individual joints must be especially well understood.

Rock joints' behaviour under normal loading has been the object of less attention than shear behaviour. The main reason is that rock masses under low to medium stress fail mainly due to joint tangential movement. Shear response does depend on the associated normal load, but it is not necessary to know the normal behaviour in detail in order to predict shear failure. Continuous rock joints (without filling) under tension loading behave, generally, in a very predictable way, opening with very little or no resistance. The behaviour under compression is not as simple, but models that are generally satisfactory have been developed years ago.

It is in seismic and hydraulic scenarios that joint deformation under normal loads is particularly important, as joint aperture commands both wave transmissivity and hydraulic conductivity. The need for models that realistically incorporate the normal behaviour of joints increases as dynamic and mechanical-hydraulic coupled analysis becomes more frequent and important, driven by the modelling of hydrocarbon reserves, thermal energy production and storage of CO_2 and radioactive waste.

Rock joint compression test can in principle be performed *in situ* but are almost always done at the laboratory. Since the procedure that allows the experimental determination of

shear strength envelopes (to fit, for example, a Mohr-Coulomb strength model) involves several shear tests under varying normal stress, compression test are generally performed in conjunction with these (ISRM, 1974).

The stress-displacement curve of compression tests, with a distinct hyperbolic shape, characterize the normal response, as shown in figure 4.11. The curve has initial low slope, stepping up as joint closure increases. The final slope is stronger in well matched joints and smaller in those where there is no adjustment between the peaks and valleys in both walls. In some tests, the displacement is measured between the ends of the sample and includes the deformation of the rock and the closure of the joint. Usually, the latter parcel is much larger but nevertheless the displacement corresponding to the rock deformation has to be calculated and subtracted to the curve, that then reflects the response of the joint only.

Figure 4.11 presents intact rock and rock joint closure curves. The interpretation of the shape of the joint closure curves is the following: prior to the beginning of the test, when the top part of the specimen is placed over the lower part, the area of contact between both halves may be very small: the joint needs only three points of contact. The load that is applied to the top half is transmitted through these few contact points, which are under huge local stresses. They deform significantly and/or are partially or totally crushed, depending on their strength to stiffness ratio. The increase in displacement that corresponds to each load increment is large in this initial part of the curve, leading to an almost flat curve. Figure 4.12 displays real and 2 and 3D characterizations of joint profiles.

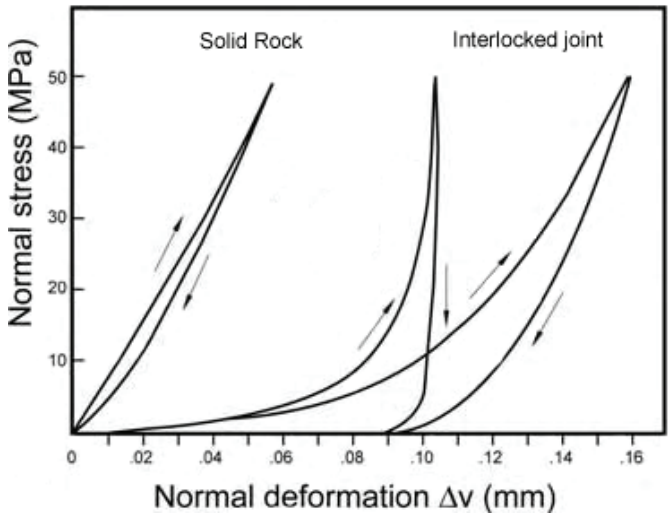


Figure 4.11: Normal stress *vs* deformation curves in intact and fractured rock joints. Taken from Bandis *et al.* (1983).

As joint compression goes up, walls distance shortens, more asperities from both sides come in contact, the load gets distributed over a larger area and the stress in each contact zone diminishes. The deformation of an asperity also increases its own area but this effect contributes much less than new contacts to the global increase in contact area and therefore to stiffness. As the load is supported by more and more contacts, the resistance grows and the stress-displacement curve gets steeper. The rock material that supports the asperities also deforms which makes it harder to distinguish where the effect of the rock joint deformation ends and that of the rock material starts.

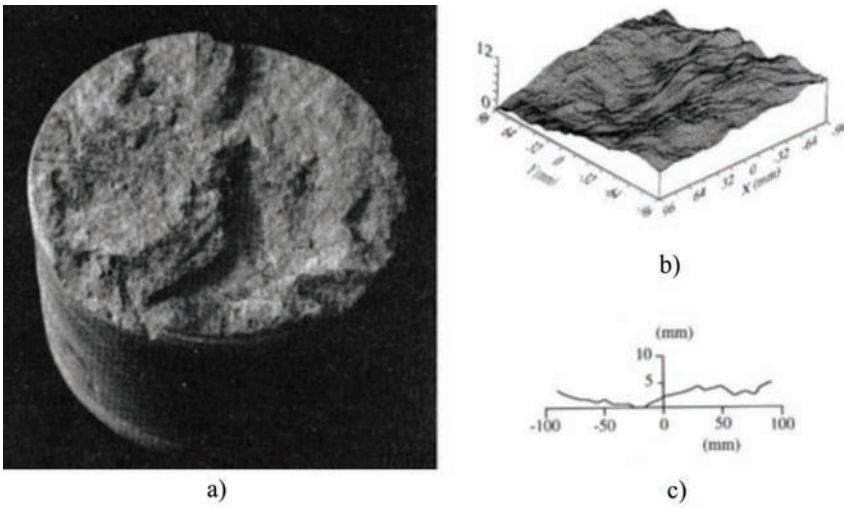


Figure 4.12: Roughness of a natural rock fracture (a); 3D and 2D characterization of joint surface (b) and (c). Adapted from Plesha (1995).

In this explanation of the mechanics of joint closure, the role of each of the factors that influence the behaviour is evident. The three-dimensional wall roughness (difficult to characterize) commands the initial distribution of the asperities, which is related to the contact area at the beginning of the test. The filling material (if present), the amplitude, strength and deformability of the asperities and of the joint walls control the way in which the fracture will deform, leading to more or less stiff behaviour.

4.4.2 Empirical models

Several analytical expressions have been used to fit the typical stress-displacement curve. Muralha (1995) reviews almost all of the known curves and compares their fit with numerous tests of fractures from dam sites in Portugal. The two most popular expressions are due to Goodman

et al. (1968) and to Bandis *et al.* (1983). Goodman proposed the following function:

$$\frac{\sigma_n - \sigma_0}{\sigma_0} = B \left(\frac{d_n}{d_{n,max} - d_n} \right)^b, \tag{4.16}$$

where σ_n stands for the current normal stress, σ_0 for an initial, usually low, normal stress, d_n is the closure that corresponds to the current normal stress, $d_{n,max}$ is the maximum joint closure and b and B are parameters to be determined experimentally. Goodman's formula adjusts well to test data, but presents numerical singularities that difficult its inclusion in numerical codes (Lamas, 1993).

Bandis proposes the hyperbolic function:

$$\sigma_n = \frac{d_n}{a - bd_n}, \tag{4.17}$$

where parameter a is the inverse of the initial stiffness and a/b is the maximum joint closure. Normal stiffness K_n^{static}, written with a capital K because it refers to the stiffness of a macroscopic joint, is defined for any stress level by:

$$K_n^{static} = \left(\frac{1}{a\left(1 - \frac{b}{a}u_n\right)} \right). \tag{4.18}$$

These expressions provide simple, easy to understand and use methods, which depend on meaningful parameters (closure at infinite stress, initial stiffness) that can be calculated from experimental curves. However, the intrinsic mechanics of joint closure is not expressed by the functions.

Several works have attempted to predict the mechanics of joint closure directly based on statistical characterizations of the asperities height, on more sophisticated spectral and fractal analyses of the asperities height, or directly on the surface topography. Since the micromechanical model that will be presented later in this chapter is, in a way, under this class, a short review of existing predictive models follows.

4.4.3 Predictive models

Predictive models, instead of fitting empiric mathematical expressions to the force-displacement curve of the joints, consider the topography of both joint surfaces and the mechanical characteristics of the material (stiffness and strength). From this characterization, it is, in theory, possible to predict the joint response.

Tsang and Witherspoon (1981) developed a model that considers a joint as a collection of aligned voids. Under compression, as the voids deform, the top and lower walls start touching and contact area increases. If the aperture distribution of the joint is known and laws governing

the voids' deformation are used, the increase in contact area is calculated and the stress-displacement curve is estimated.

Swan (1983) and Greenwood and Williamson (1966) worked on the statistical distribution of asperity peaks, having determined that peak heights of asperities fitted a Gaussian distribution and that the upper quartile of this distribution (the part that is thought to influence more the joint closure) is well approximated by an exponential distribution. They derived expressions for the stiffness of the contact between a rough and a smooth surface.

Brown *et al.* (1986) stated that by summing the heights of the asperities of the two walls, an equivalent surface that contains the uncorrelated component of the two surfaces is obtained, as indicated in figure 4.13. By employing Hertzian contact theory to calculate the deformation of asperities of the walls they developed equations that relate average stress to joint aperture.

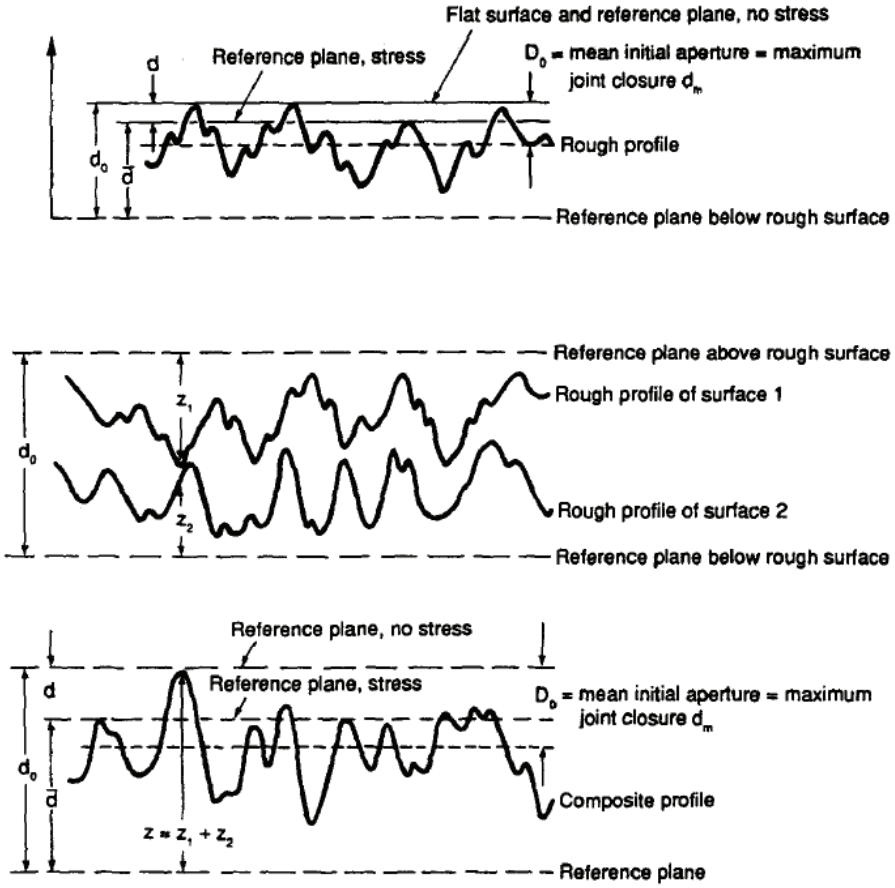


Figure 4.13: Sketch of a single rough profile in contact with a smooth surface showing reference planes and definitions of quantities describing joint closure (top); sketch of the profiles of two rough surfaces (centre); sketch of a composite profile, the sum of the ordinates of the two profiles in the central sketch (bottom). Taken from Brown *et al.* (1986).

Billaux (1990) proposed an interesting model in which the joint is represented by a toothed surface, with teeth of varying heights, pressed against a flat surface. The teeth are assumed to behave elastically but can fail, according to the Hoek-Brown strength criterion.

Grasselli (2006), after high quality measurement of joints surface, described how the roughness influences the size and distribution of contact areas during shearing, arriving at the conclusion that the variation in the contact area can be expressed as a function of the local dip inclination of the surface, measured along the shear direction. Then, based on these results, he proposed a constitutive model which is able to describe experimental shear tests.

4.4.4 Simulation of joint behaviour with particle models

Particle models have been used to model the static behaviour of rough undulating rock joints in shear (Cundall (2000), Kusumi *et al.* (2005) and Kabeya (1999)) but not in compression. Gutierrez and Barton (1994) used the two-dimensional DEM code UDEC to represent a shear test of a rock joint. The joint topography is described by a continuous, irregular line that mimics typical JRC profiles (Bandis *et al.* (1983)). The model allowed the investigation of the micromechanics of the shear failure of these joints and also the evolution of hydraulic aperture. Final stages of the calculation are shown in figure 4.14.

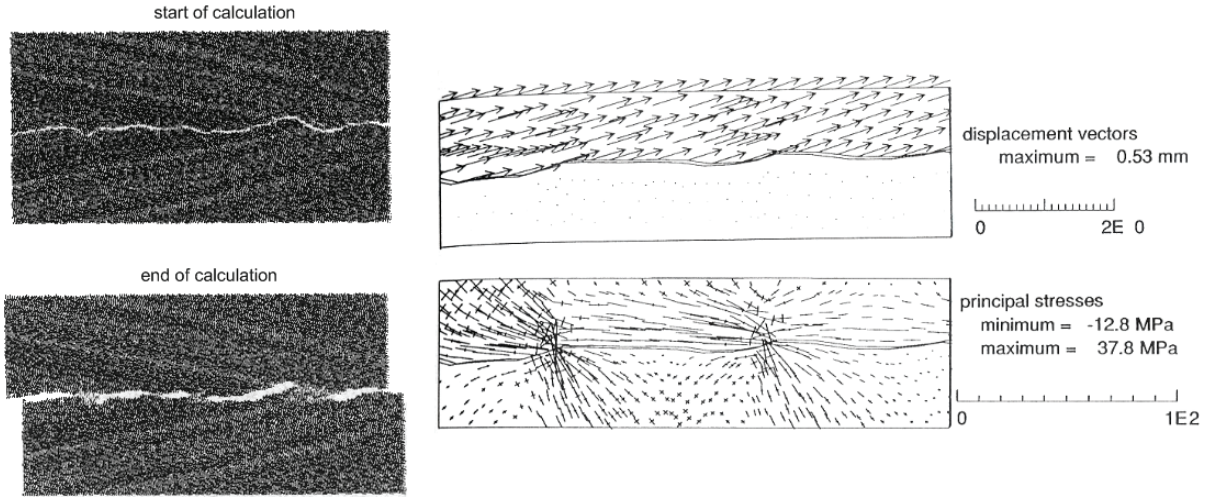


Figure 4.14: Micromechanical modelling of rock joint in shear. Particle DEM representation (left, Kusumi *et al.* (2005)). Block DEM (UDEC) representation (right, (Gutierrez and Barton, 1994)).

Recently Park and Song (2008) used the 3D code PFC^{3D} to model the behaviour of rough rock joints during shear displacement. It is the first study, to the author's knowledge, to model rock joints three-dimensionally. Karami and Stead (2008) used the hybrid FEM/DEM code

ELFEN to model the shear behaviour of several JRC profiles under varying normal stresses. This hybrid code is capable of generating tensile fractures in continuous media, by forcing fracture to progress through existing element boundaries. The degradation and failure of rock joints under combined compression and shear is well captured, as well as the generation of smaller fractures due to damage of asperities in tension and shear. Kerstiëns (1999) employed discrete element software UDEC to model rough joints in shear.

Other authors employed both block discrete element (*e.g.* Min *et al.* (2005)) and particle models at a larger scale to represent volumes of rock as large as some dozens of metres explicitly including joint sets. The topography of discontinuities walls is not represented because joints are defined by assigning lower contact strengths and/or stiffness to particles that lay upon or in the vicinity of the line (in 2D) or plane (in 3D) that define the joint (Toomey (2001) and Park *et al.* (2004), show in figure 4.15). Nevertheless, macroscopic influence of joint sets in rock mass properties is evident.

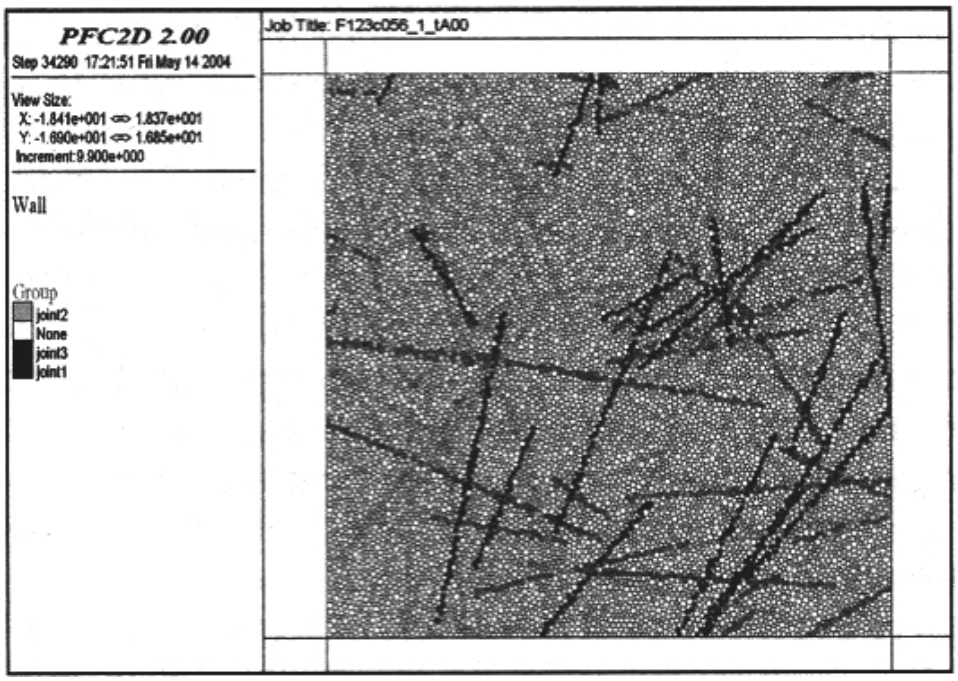


Figure 4.15: 30x30 m^2 rock mass model with three joint sets in PFC^{2D}. Taken from Park *et al.* (2004).

4.4.5 Jointed synthetic rock specimen behaviour

The modelling of rock joint closure using particle models is attempted here, not with the ultimate purpose of replicating with detail the static normal behaviour, but as a step to the

simulation of rock joints interaction with stress waves.

Micromechanical models can be used to emulate the geometry of joints to a degree of detail that is limited by the means to characterize their geometry and the hardware capacity. If particles with a mean radius of 0.25 mm are employed (granite typical grain size is greater than 0.5 mm), a $100 \times 100 mm^2$ 2D sample can be modelled by approximately 50,000 particles. It has been found that a model with this level of detail is appropriate to represent the basic features of a joint under static and dynamic loadings being manageable by a standard personal computer.

It was decided to model joint closure and then wave passage across a synthetic rock sample representing a granite rock core of the size of laboratory samples. The first step is the creation of an assembly with properties that resemble those of a typical granite: Young's modulus of about 40 GPa and Poisson's ratio of 0.2.

To simulate a real test, both the stress-displacement curve and a detailed surface characterization of both joint surfaces that can be reproduced by the particles assembly are necessary. As these are not available, a generic rock joint geometry is generated and tested.

Another limitation of this simulation is that it is performed in two dimensions, grossly simplifying the real problem. The reasons for this choice are connected with the computational cost. Three dimensional runs are many times more time-consuming than two dimensional runs, resulting too long for the time scale of this thesis. It is considered by the author that 2D joint profiles can represent most of the mechanics that happen in the joint surfaces, although with a poorer grade of detail.

Model generation

The BPM model described here is used in both static and dynamic tests, with and without a fracture at mid-height. It measures 90×600 mm^2 (the reason for this high specimen length is related to the correct extraction of long wavelength waveforms, explained in section 4.6). It is composed by 34,773 particles with radii that vary uniformly between 0.50 and 0.83 mm, with an average radius of 0.665 mm (maximum radius is 1.66 times minimum radius). The model is generated by stacking 9 periodic bricks (see section 4.3.2) measuring 90×66.67 mm^2. Brick's width is set equal to the models's, so that there is no pattern repetition in the fracture profile.

Particles are set as disks (as opposed to spheres, explanation of the choice is given in section 4.5). Ball density is set to 3150 kg/m^3. Given that the porosity of the packing is aproximatly 14%, continuum-equivalent porosity is 2700 kg/m^3 (as explained in section 4.5.4 ahead). This value is relevant only in the dynamic part of the study, as self-weight is not considered in the static calculation. Contacts are of contact bond type. In PFC, two kinds of ball-ball

contact are available: contact bond and parallel bond (see section 4.3.1). Parallel bonds allow the transmission of moments between balls, and therefore, parallel bonded assemblies show a wider, richer behaviour range. As there is very little experience with wave propagation in granular assemblies, it is decided to employ contact bonds, which, having simpler individual response, result in a more predictable macroscopic model.

Contacts are set with normal stiffness of 6.20×10^{10} N/m, 2.5 times the shear stiffness, which is then 2.48×10^{10} N/m, these values have been found by trial and error to result on the intended properties. An unconfined compression test of the assembly (figure 4.16) shows that the resulting Young's modulus is fairly constant in the range of compressive stresses of interest (0 to 120 MPa) with an average value of 43.5 GPa and a standard deviation of only 0.54 MPa. Poisson's ratio is approximately 0.2 and remains constant during the compressive test. These are properties of a typical granite.

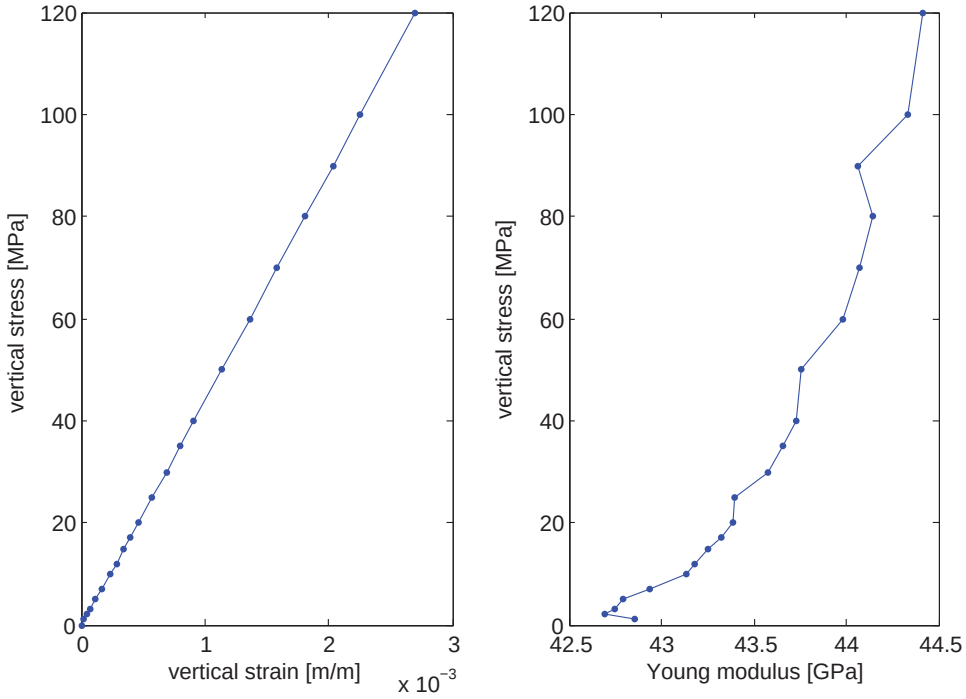


Figure 4.16: Vertical stress *vs* vertical strain (left) and Young modulus (right).

The slight increase in the Young's modulus with normal stress is a consequence of creation of new contacts. Since the goal of this simulation is in a first stage to isolate the influence of the BPM fabric in the wave progression, and afterwards to focus on the phenomena that occur at the joint, contacts are not allowed to fail which is achieved by setting their bond strength to very high values. This decision is not free from criticism. In a joint compression test it is the

failure at asperity level that after a certain amount of compression causes non-linearity, but this is dealt with in another way, as will be shown ahead. Also, microfracturating or plastic damage can occur in the rock material that supports the asperities which means that it is difficult to define exactly where the material in the rock core ends and the joint begins.

Boundary conditions

PFC presents three ways of defining force or displacement boundary conditions. The first is the application of forces and moments to balls' centres. In the second method, translational or rotational velocities can be assigned to balls. The last and more complex one involves walls, which are linear entities defined arbitrarily by the user, that interact with balls via normal and shear springs. Having no mass, their motion is completely defined by the user (Itasca, 2004).

Since the tests of joint compression are load controlled, it is more advantageous to set loading forces directly to balls at the boundary, as prescription of balls or wall motion involves the construction of a loop mechanism routine that monitors reaction forces and adjusts movement accordingly. A strip of balls is defined at the top, sides and bottom of the sample, as shown in figure 4.17. The width of the strip is defined with enough depth to leave no part of the model unbounded, since the boundary geometry is not regular.

Balls at the lateral boundary can rotate and move in all directions. A null-velocity condition is applied to the bottom boundary balls. Balls at the top boundary are not allowed to rotate and move in the horizontal direction. A vertical downwards force is applied to impose the normal stresses at the joint.

Since stress is a concept valid only in continuous media it must be translated into forces that are applied to the balls' centres (similarly to, in FEM, passage of stress in an element face to nodal forces). If a stress value σ is to be applied at a cylindrical particle with unitary height ($t = 1$), the equivalent force F_{ball} must take into account the transversal area of the particle (A_{ball}), as defined in figure 4.23:

$$F_{ball} = \sigma \cdot A_{ball} \Leftrightarrow F_{ball} = \sigma \cdot 2 \cdot r_{ball}. \tag{4.19}$$

The passage from stress at the boundary to forces applied to the balls must also take into account the border's depth (measured in terms of balls). In regular rectangular packings, the boundary may be easily set to be one ball deep, and no correction is necessary (it is equal to one). In other packings, with thicker boundaries, the boundary depth correction factor bf_{depth} is:

$$bf_{depth} = \frac{l_{bound}}{2 \cdot r_{mean}} \cdot \frac{1}{nb_{bound}}, \tag{4.20}$$

where l_{bound} is the boundary length and nb_{bound} is the number of balls in that boundary. The

force in each particle is given by the product of equations 4.20 and 4.19:

$$F_{ball} = bf_{depth} \cdot \sigma \cdot A_{ball}. \tag{4.21}$$

The model width is 90 mm the average ball radius being 0.665 mm. One average row has, thus, $90/(0.665 * 2) \approx 69$ balls. The top boundary, for example, has 164 balls (figure 4.17), so the force in each particle becomes:

$$F_{ball} = \frac{69}{164} \cdot \sigma \cdot 2 \cdot r_{ball}. \tag{4.22}$$

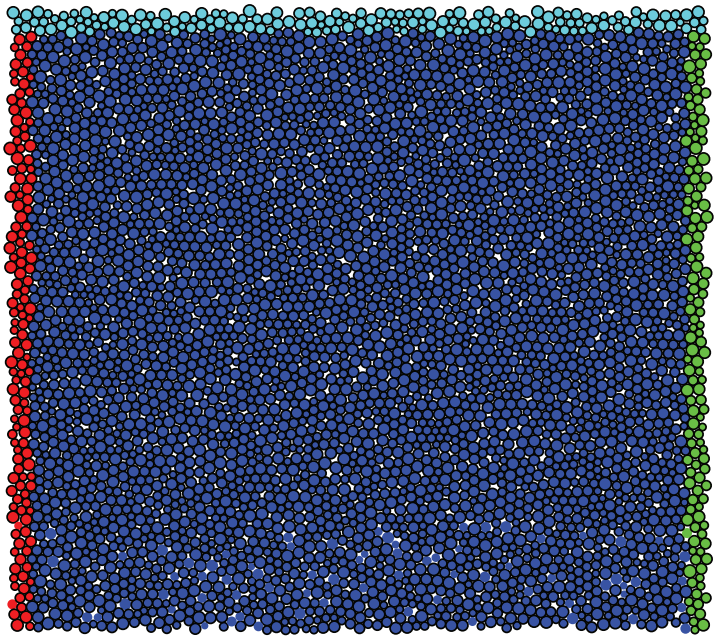


Figure 4.17: Particles defining the model's top (cyan) and lateral (red and green) boundaries.

Rock joint generation and contact behaviour

Previous utilizations of BPM to model rock joint shear tests used various strategies to generate fractures. Cundall's (2000) approach to generate the surfaces for the shear test of a rough joint was to use a sum of varying wavelength sine waves, thus replicating the several orders of roughness. Kusumi *et al.* (2005) reproduced different JRC profiles by erasing particles from a rock model, and they were able to reproduce experimental damage patterns in the joint surface.

Another method is to create a realistic fracture surface by submitting a notched rock core to a tensile load (possibly in combination with shear) until complete separation of the two halves. The employed method, which is also the most straightforward one, is to simply delete enough balls in the middle of the synthetic specimen until there is no contact between the two

halves. The resulting joint surfaces are potentially less rich, but have the advantage of being very predictable, planar and with small irregularities (figure 4.18).

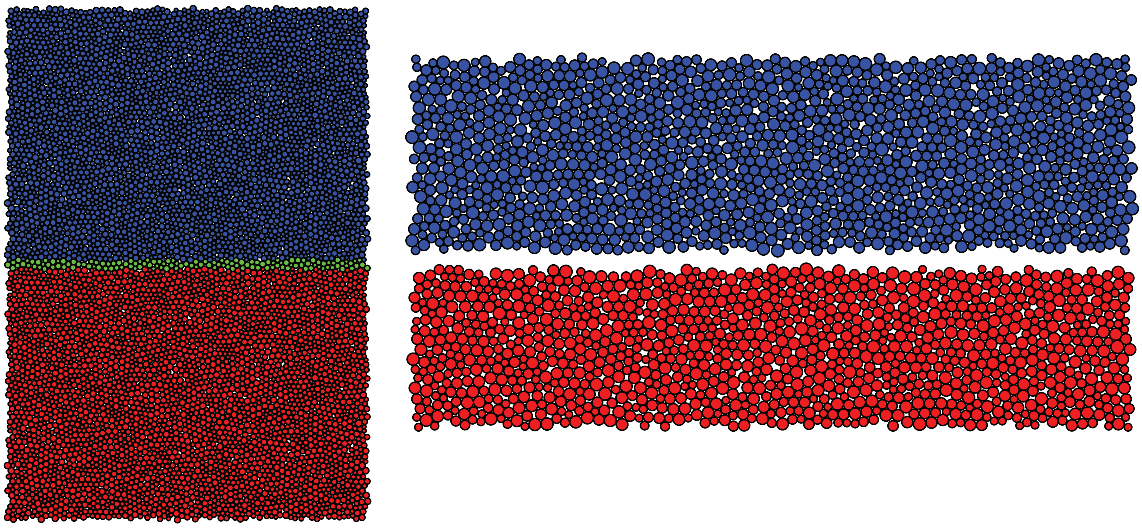


Figure 4.18: Generation of joint surface with balls in green marked for removal (left) and detail of the final surface (right).

As stated above, in section 4.3.3, particle contact microproperties drives the macroscopic behaviour of synthetic rock samples. Microproperties are not related to measurable properties like Young's modulus or Poisson's ratio through analytical laws, but by empirical relations that have been established through experience.

When it comes to the properties of joint wall to wall contacts, no previous experience is available. The displacement in rock joints under compression is mostly caused by elastic deformation of the asperities, followed by their partial or total crushing, together with deformation of the rock that supports the asperities. It is then postulated that, after suffering a certain amount of deformation and crushing, the contact area of each asperity increases, and consequently the same happens to the contact stiffness.

In the current representation of the rock surface (figure 4.18), each peak is represented by a small number of particles (see right side of figure 4.18), thus keeping the number of balls in the model manageable through the whole static and dynamic calculations. Peak deformation, crushing and hardening must then happen at each ball. To simulate this, a new contact constitutive model was developed and compiled, resulting in a C^{++} dynamic link library that can be integrated in PFC^{2D} and PFC^{3D}.

It was found that, if the rock material's contact properties are used at the contact between balls in each joint wall, the first balls to come in contact are compressed, withstanding very

high values of contact force and do not deform enough to allow new contacts to be created. On the other hand, if low contact stiffness is employed inter-penetration of balls in opposing faces is such that their centres cross each other and the direction of repulsive forces reverses, pushing the sample halves against each other, as represented in figure 4.19.

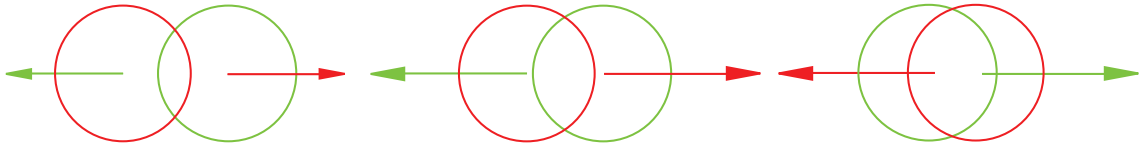


Figure 4.19: Green arrow denotes repulsion exerted by green ball on red ball and vice-versa. As balls' centres pass through each other, direction of repulsion is inverted.

The developed constitutive model is bi-linear in shear and compression, with no tensile strength and a Mohr-Coulomb strength criterion in shear. Its force-ball overlap curve is shown in figure 4.20.

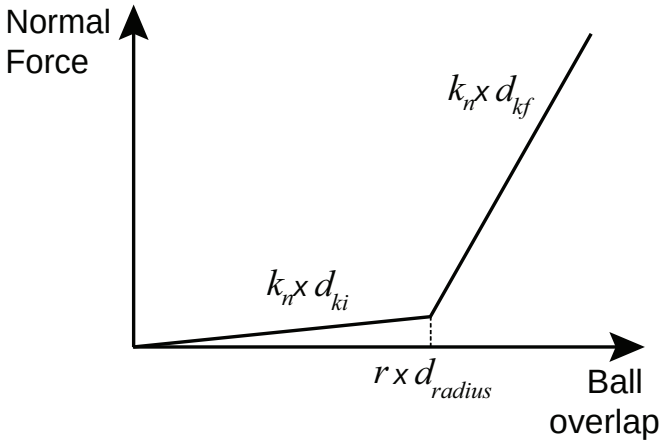


Figure 4.20: Joint contact force-displacement law.

The initial d_{ki} and final d_{kf} stiffnesses are set as a percentage of the stiffness of the contacts in the rock material k_n. The point where stiffness value increases, simulating a fast increase of contact area in the contact, is defined as a percentage of the radius of the smaller ball of the pair.

To maintain the model's calibration as simple as possible, shear and compressive stiffness evolve in parallel and the final stiffness is equal to the rock matrix stiffnesses, which corresponds to $d_{kf} = 1$. The behaviour is then defined by only two parameters: initial percentage of the rock stiffness d_{ki} and percentage of the radius of the smaller ball in contact that triggers hardening

d_{radius}.

Strategies to represent asperity degradation, such as ball radius decrease, ball deletion or ball breakage were either inadequate or more difficult to implement.

The normal stress *vs* joint normal displacement curve for the BPM model with contact model parameters $d_{ki} = 1\%$ and $d_{radius} = 10\%$ is depicted in figure 4.21 and the data points are in table 4.1. The stress-displacement curve shows the main characteristics of rock joint normal tests. Initial low stiffness due to a small number of contacts followed by a gradual increase in the slope, typical of a mismatched joint. This reflects the creation of new contacts and the increase in stiffness in existing ones. Joint stiffness is represented in the same figure. Its evolution is also according to the experimental results. The abrupt variations, also observed in real tests, are due to the high sensibility of the stiffness to very small features on the joint surface. Figure 4.22 illustrates the evolution of contact forces across the joint with normal stress. The visualization of how contact forces pass from one side of the model to the other through the active contacts is a very good tool to understand the mechanics of joint closure in the model and in real joints, if the model is accurate.

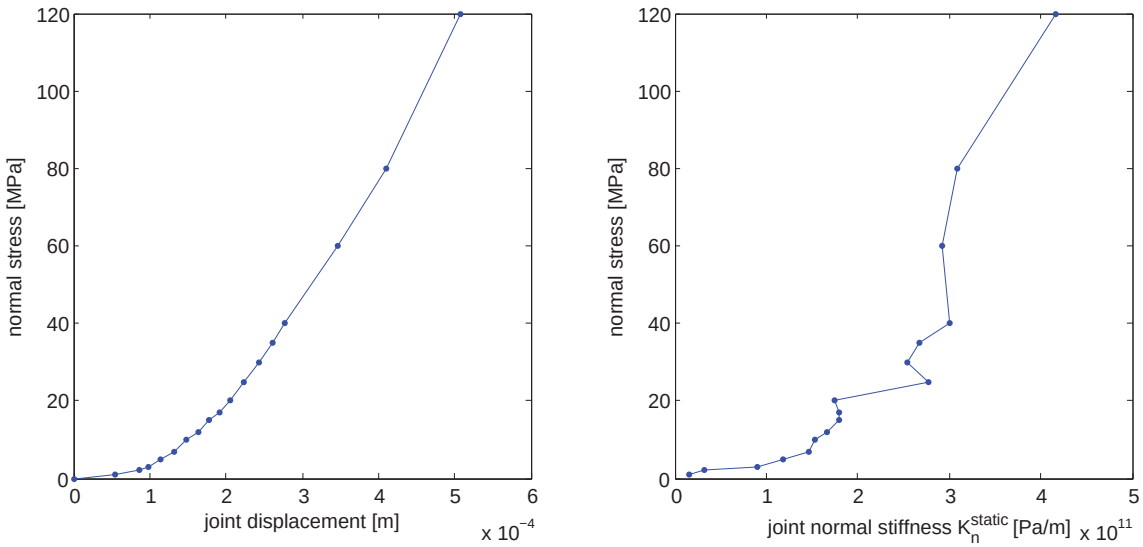


Figure 4.21: Vertical stress *vs* joint closure (left) and tangent joint normal stiffness (right). Joint closure is measured between joint walls.

At the end of this modelling step, the following considerations can be made:

- Though very simple, the method of joint generation resulted in a two dimensional representation of the rock joint planar low roughness joint.
- The main mechanisms of joint normal behaviour are correctly represented.

Table 4.1: Data points of the stress-joint displacement curve and calculated joint tangent stiffness.

Vertical stress [MPa]	Joint closure [mm]	K_n^{static} [MPa/mm]
0	0.000	-
1	0.009	114
2.0	0.010	625
5.0	0.013	1 250
7.5	0.015	1 136
10.0	0.016	3 125
12.5	0.016	5 000
15.0	0.017	6 250
17.5	0.017	25 000
20.0	0.017	12 500
25.0	0.017	16 667
30.0	0.018	25 000
35.0	0.018	25 000
40.0	0.018	25 000
60.0	0.019	22 222
80.0	0.019	40 000
120.0	0.021	33 333

- Major shortcomings of the method are: complete closure of the joint is attained for very high normal stress, parametric control over the behaviour is difficult (trial and error), real asperities have longer wavelengths and characteristic of undulating fractures are not represented.
- 3D modelling can be attempted only with particle codes that run on parallel computers, due to the long calculation times.

The presented way of modelling joint closure can still be improved, but it provides a simple method to model joint closure and its main features.

4.5 Modelling wave propagation in rock masses with Particle Models

The focus of this chapter is on the influence of fractures on wave propagation. Before reaching the fractures, stress waves cross the irregular BPM representation of rock material, so it is necessary to understand how waves propagate and are changed while crossing the dense, non-organized bonded particle assemblies that are used to simulate rock. Work on this area has been scarce, and some new findings and methods are presented.

The study of the mechanics of particulate media has been object of research for some

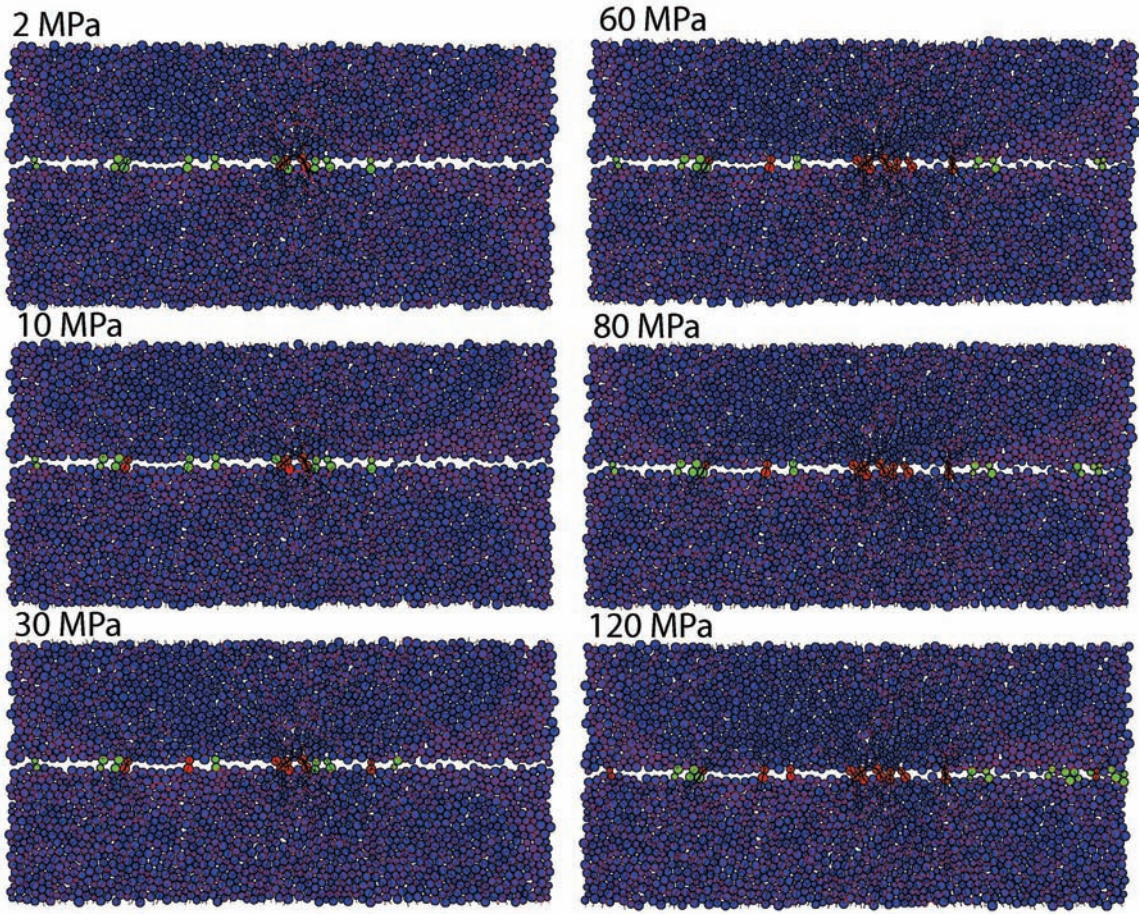


Figure 4.22: Evolution of joint model throughout the joint compression test. Black lines denote compression and red lines tension forces at contacts. Green and red balls are in contact. Green balls are in the first branch of the force-displacement law (figure 4.20) while red balls are on the second branch.

decades. Contributions come from diverse fields: geomechanical engineers studying granular soils or rocks of crystalline structure, to physicists researching the properties of atomic crystalline lattices. Difficulties are numerous: the structure of the packings may be chaotic, contact stiffness may not be constant and may increase with particle penetration; shear and normal stiffnesses are different; slip can occur under certain contact conditions; previous loadings and the stress state influence response; real particles are not perfectly round and have varying diameters.

Mindlin (1954) summarizes some of the first works on a mathematical theory of small deformation of compact granular media. Several other authors contributed to the derivation of stress-strain relations for planar and spacial organized arrangements of disks or spheres. Analytical stress-strain relations, and consequently wave velocities for simple particle organization schemes (rectangular, hexagonal and cubic) have been derived (Duffy (1959), Hoover

et al. (1974)) and are helpful in pointing the way in more complex cases and in assessing the performance of particle codes.

When it comes to unstructured assemblies, with non-uniform diameters, there is no available theory, and an unequivocal characterization of models properties is not possible, due to the variability and randomness. It is only possible to statistically characterize the particle fabric through such quantities as the particle size distribution, particle's density or porosity, coordination number (average number of contacts per particle) and branch vector (an indicator of preferential contact orientation) (*e.g.* Tai and Sadd, 1997).

Thanks to efficient particle codes and hardware evolution, it is now possible to simulate wave propagation in all kinds of organized, chaotic or semi-organized particle arrangements, including non-linear contact laws and varying stress states.

4.5.1 Dynamic properties of rectangular packings

Analytical solutions are available and are easily deducted for the simplest organized modes of circular particle organizations.

In a rectangular packing of constant radius undeformable disks or spheres, each particle is in contact with four other particles, whose centres are initially at a distance of one diameter. In this kind of packing, there is no particle imbrication, so Poisson's ratio is null and bulk modulus is equal to one third of Young's modulus. If a wave is generated in a linear boundary of the packing, all strings will behave exactly in the same way, so one single string is representative of the behaviour of the packing.

The case of a compressive wave in an array of particles with normal elastic linear contacts of stiffness k_n is presented (a shear wave in a string with shear contacts of stiffness k_s has equivalent solution). The string is composed of spheres of radius r, or disks with radius r and thickness t. A portion of a sphere and a disk string, and equivalent continuous solid bars, are represented in figure 4.23.

The transversal area of the equivalent continuous bars in the string direction is, for a string of spheres a cylinder and, for a string of disks, a rectangular prism:

$$A_{sphere} = \pi r^2 \tag{4.23}$$

$$A_{disk} = 2rt. \tag{4.24}$$

The secant Young's modulus (E) of the equivalent continuous bar can be written in terms of the particles properties:

$$E = \frac{\sigma}{\varepsilon} = \frac{F/A}{\Delta u/u} = \frac{F}{A} \cdot \frac{2r}{F/k_n} = \frac{2k_n r}{A}, \tag{4.25}$$

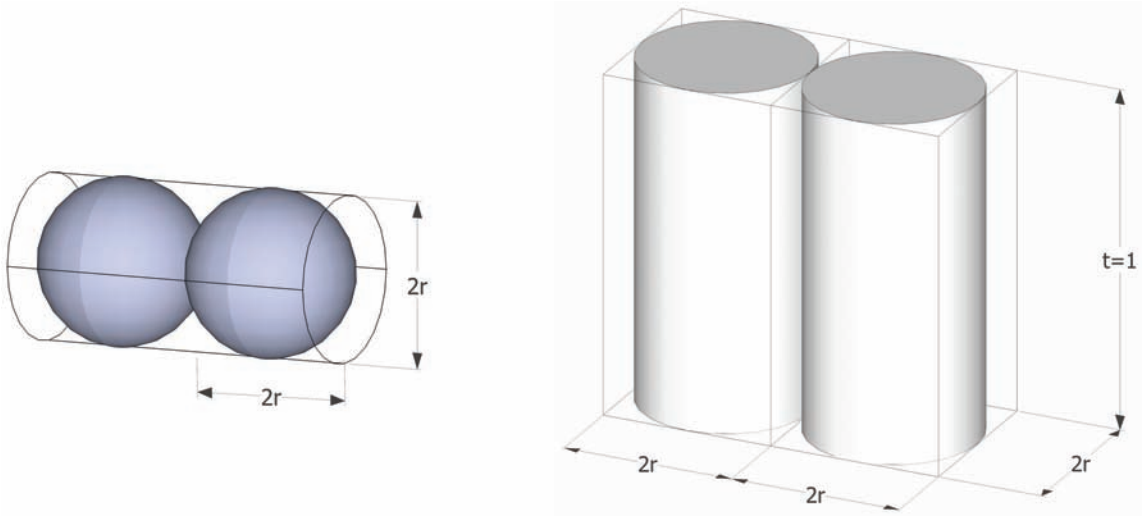


Figure 4.23: Equivalent continuous solid dimensions of a particle string composed of spheres (left) and disks (right).

with $2r$ being the distance between the centre of consecutive disks/spheres and F/k_n the relative displacement between the particles when force F is imposed upon them. As stated in section 4.3.1, k_n refers to the stiffness of the contact, not the ball. Introducing equation 4.24 in 4.25, results Young's modulus, for a string of spheres:

$$E_{sphere} = \frac{2k_n}{\pi r}, \tag{4.26}$$

and doing the same with equation 4.23, results Young's modulus for a string of disks:

$$E_{disk} = \frac{k_n}{t}. \tag{4.27}$$

To achieve equivalence between the discrete model and a continuum material, porosity must be taken into account. Each ball's density must be scaled up so that there is equivalence in mass between the packing and the solid bar.

$$m = m_{sphere} \Leftrightarrow 2r\pi r^2\rho = \frac{4}{3}\pi r^3\rho_{sphere} \Leftrightarrow \rho_{sphere} = \frac{3}{2}\rho \tag{4.28}$$

$$m = m_{disk} \Leftrightarrow 2r2rt\rho = \pi r^2 t\rho_{disk} \Leftrightarrow \rho_{disk} = \frac{4}{\pi}\rho. \tag{4.29}$$

This is equivalent to a porosity of:

$$1 - 2/3 \approx 33.3\% \tag{4.30}$$

for an arrangement of spheres and, for an arrangement of disks,

$$1 - \pi/4 \approx 21.5\%. \tag{4.31}$$

Compressive wave velocity in an unbounded elastic solid is given by:

$$c_p = \sqrt{\frac{E}{\rho}}. \tag{4.32}$$

The same compressive wave velocity is obtained when Poisson's ratio of the material is null. By replacing eq. (4.26) and (4.28) in (4.32), results:

$$c_{p,sphere} = \sqrt{\frac{3k_n}{\pi r \rho_{sphere}}}. \tag{4.33}$$

And by using eq. (4.27) and (4.29) in (4.32), results:

$$c_{p,disk} = \sqrt{\frac{4k_n}{\pi \rho_{disk}}}. \tag{4.34}$$

At this stage, the choice of whether to use disks or spheres can be made. The only difference in the numerical code, lies in the calculation of sphere/disk mass, as all other properties and behaviour are equivalent. In static calculations, ball mass is used to calculate self-weight loads, as the particles' mass is scaled down to attain optimal timesteps, speeding up the calculation. But, in dynamic simulations, mass plays an important role, as ball translational and rotational inertia intervene in the movement equation, so correct density values must be used. Equally correct wave velocities can be attained using either disks or spheres, given one uses correct expressions for each case. However, when comparing equations 4.33 and 4.34, it is clear that dynamic properties become independent of particle radius, which is convenient.

Even though this conclusion derives from analysis of a regular packing, it is also approximately valid in packings with non-uniform spatial distribution and particles of variable radius.

4.5.2 Dynamic properties of hexagonal packings

The strategy to arrive at a correspondence between micro-properties and propagation velocity in a hexagonal packing is different from the one for rectangular arrangements, although one still has to start by calculating equivalence between disk and solid material densities. The solution for a packing with no shear interaction ($k_s = 0$) and elastic linear normal contact of stiffness k_n is given.

From geometric considerations (figure 4.24) we find that the mass of an assembly of N rows and M columns of disks with radius r and thickness t (as the demonstration is similar for spheric particles, only the disk case, used later, is presented) is:

$$m = (M2r)\left(N2r\frac{\sqrt{3}}{2}\right)t\rho. \tag{4.35}$$

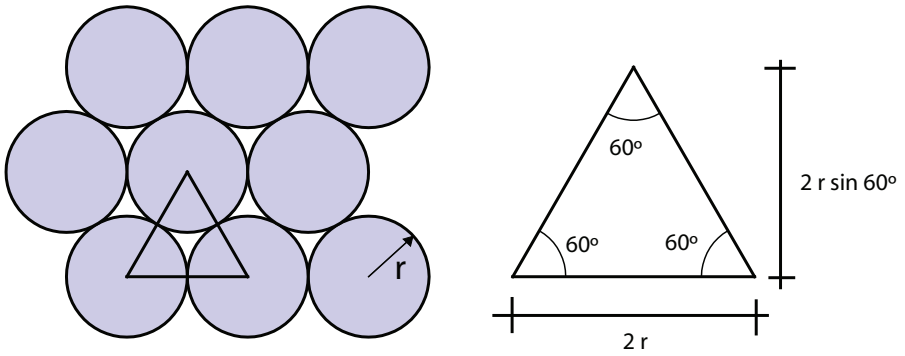


Figure 4.24: Hexagonal packing (left) and assembly geometric relations (right).

The total mass of the disks in the assembly is:

$$m_{disk} = MN\pi r^2 t\rho_{disk}. \tag{4.36}$$

To arrive to an equivalent mass in the granular assembly and in the solid, ball's densities must be scaled up:

$$m = m_{disk} \Leftrightarrow \rho_{disk} = \frac{2\sqrt{3}}{\pi}\rho. \tag{4.37}$$

From this condition we can calculate the porosity of this kind of packing, which is the minimum attainable in a packing of disks of equal radius:

$$1 - \frac{\pi}{2\sqrt{3}} = 9.31\%. \tag{4.38}$$

In his 1974 paper, Hoover *et al.* arrive at an equivalent result, by stating that the volume per atom in an atomic crystal network with this kind of packing is $V = \sqrt{3/4}D^2$. The deduction of elastic constants and propagation velocity's values is not as straightforward as in rectangular arrangements. In the same paper, Hoover, following energy balance considerations, calculates the correspondence between Lamé's elastic constants and normal stiffness k_n, which in his case represents spring-like attraction or repulsion force between atoms in a regular atomic lattice.

$$L = \mu = \frac{\sqrt{3}}{4}k_n. \tag{4.39}$$

Compressive and shear wave propagation velocity in an isotropic solid can be expressed in terms of Lamé's constants:

$$c_p = \sqrt{\frac{L + 2\mu}{\rho}} \tag{4.40}$$

$$c_s = \sqrt{\frac{\mu}{\rho}}. \tag{4.41}$$

Substituting the Lamé's constants and disk density (equations 4.39 and 4.37) in equations 4.40 and 4.41, we arrive at the expressions relating microscopic parameters and macroscopic properties:

$$c_{p,disk} = \sqrt{\frac{9k_n}{2\pi\rho_{disk}}} \tag{4.42}$$

$$c_{s,disk} = \sqrt{\frac{3k_n}{2\pi\rho_{disk}}}. \tag{4.43}$$

This solution is limited as it will not handle packings with shear interaction between particles, and the Poisson's ratio of a hexagonal packing with no shear interaction is fixed at 0.25 (easily verified by considering the ratio of the shear and compressive wave velocities).

4.5.3 Dynamic properties of unorganized packings

If the particle arrangement is not organized, due to particle disposition, irregular size and/or properties distribution, no exact solution is available. Wave velocity must be calculated for each assembly by running a stress wave across the model and measuring its velocity. Winkler (1983) derived the following expressions for the propagation velocities of a random pack of spheres with constant radii.

$$c_p = \sqrt{\frac{3C}{20\pi r\rho}\left(k_n + \frac{2}{3}k_s\right)} \tag{4.44}$$

$$c_s = \sqrt{\frac{3C}{20\pi r\rho}\left(k_n + \frac{3}{2}k_s\right)}. \tag{4.45}$$

In Winkler's equations, C stands for the coordination number, the average number of contacts per particle.

4.5.4 Modelling wave propagation in Bonded Particle Models

From static to dynamic calculation

Frequently, dynamic analyses are preceded by static calculations, where, for example, a stress state is installed in the model. In the present study, the analysis of stress waves passage across compressed fractures is also performed in two steps. In the first one, a fracture is generated at mid-height of the synthetic rock sample, and the top half of the model is loaded against the bottom half, compressing the fracture with a pre-determined stress, as described in section 4.4.4. This static calculation was described in the previous section of the chapter. The second step consists of injecting a velocity time-history at the base of the bottom half of the model, while the model is kept under the stress of the previous step.

In the first static step, which in reality is a quasi-static calculation, as it is performed by the dynamic relaxation method (Belytschko, 1983), density scaling is used to keep the run-times at a minimum. After the static equilibrium is reached, but before the start of the dynamic calculation, density scaling must be switched off and the correct dynamic damping must be set. Density (or mass) scaling, as explained in section 4.2.3, scales the mass of each of the particles so that the critical timestep of the model, which is the minimum of the timesteps calculated in each particle, becomes one (see equation 4.10). When the static calculation ends, the particles are almost at rest, and unbalanced forces are small, when compared with the repulsion forces between particles. As density scaling is turned off, masses return to their real value that is usually several orders of magnitude lower and the same happens to the timestep, which also decreases several orders of magnitude, but proportionally to the square root of the particles mass change. As a consequence, the acceleration of the particles will increase in the same proportion as the mass, generating abnormal particle velocities. These take a long time to dissipate and can compromise the attained equilibrium.

A strategy to overcome this problem in BPM, which had never been referenced, was designed with the advice of Dr. David Potyondy from Itasca. After static equilibrium is attained, static boundaries are replaced by velocity boundaries (that is, external forces are deleted and balls are fixed). The dynamic timestep is determined, and, still in mass scaling mode, the timestep is lowered one order of magnitude and the model runs until excessive velocities dissipate. This is repeated until the timestep is near the dynamic value. Then, mass scaling is switched off and local damping is turned on, as the model is run again until velocity values become at least one order of magnitude lower than the dynamic waveforms that will be used. Before resuming to full dynamic loading, damping must be set to the desired model and value (in this case, zero damping is used).

The amplitude of the waves that will be injected into the model cannot be chosen arbitrarily. Stress waves must be at least two to three orders of magnitude larger than the level of "noise" in the model, represented in figure 4.25.

Particulate *vs* continuum media density

When simulating wave propagation on a particulate model that aims to emulate a continuous medium, the high porosity of the model must be taken into account. The global density of the model will be lower than the density assigned to each particle, and dynamic properties reflect this difference. After generation of the model, the model's real density must be calculated, and every ball's density should be multiplied by the following corrective factor:

$$\frac{\text{real density}}{\text{model density}} = \frac{1}{1 - \text{Porosity}}. \tag{4.46}$$

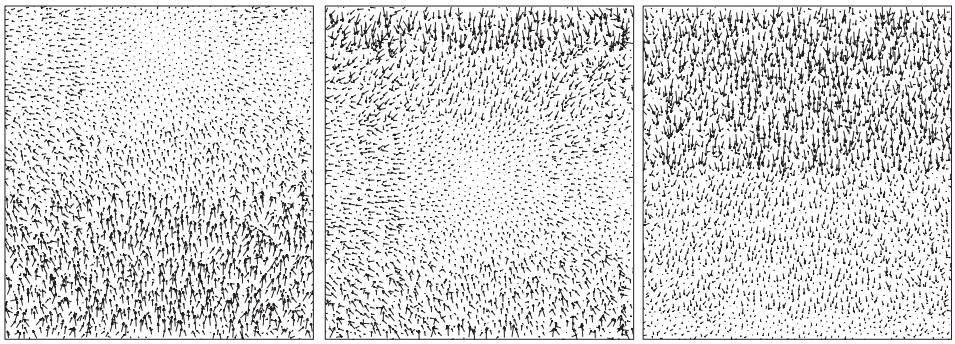


Figure 4.25: Three snapshots, taken 1000 steps apart, of the velocity field of a model "at rest". Maximum ball velocities are in the order of 10^{-10}m/s.

Compact bonded contact models generated through the method of section 4.3.2, with maximum ball radius about 1.6 times the minimum radius, have porosities between 14 and 16%.

Dynamic loadings and boundary conditions

Mechanical loadings or, more generally, boundary conditions applied directly to balls (which excludes usage of walls), can be kinematic, static, or mixed. Kinematic loadings are materialized by prescription of particle movement (translational and rotational displacement or velocity), while static loadings correspond to application of forces and/or moments. In real cases, some loadings are truly force loadings (*e.g.*, a falling object that hits the ground), while others correspond to an imposed displacement, velocity or acceleration history being prescribed in a boundary or in the interior or the ground (*e.g.* earthquake, blast). In numerical modelling of elastic materials, the distinction between both loading types is less important, as an equivalence can be established.

Tests with both velocity and force loadings in PFC^{2D} (figure 4.26) showed that the methods produce practically equivalent waves. Force loading occurs with a lag of one timestep, as the force load is integrated in the motion equation one timestep after introduction, while an imposed displacement produces its effect immediately.

When the velocity of a particle is constrained (all or just some of its degrees of freedom) the corresponding equations of motion of that particle are not solved. Static boundary conditions cannot be applied to that particle, because the corresponding equation of motion (equation 4.8) is no longer solved. Also, as the movement at the boundary is constrained, it will reflect and invert any incoming wave, which may be inconvenient. A possible way around is to release the boundary balls as soon as the injection of the dynamic load ends. However, waves coming from other sources or reflected in the interior of the model, may arrive at the border before the end of the loading. Fan *et al.* (2004) paper discusses in detail the implications of these options.

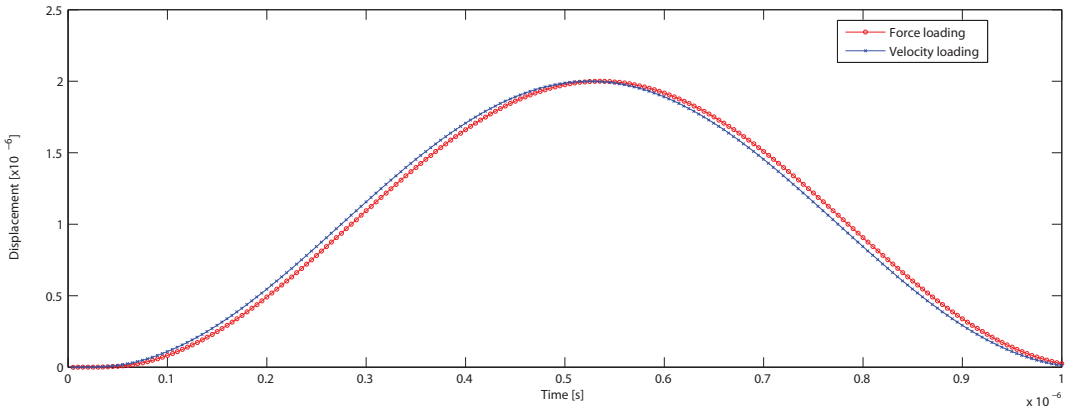


Figure 4.26: Wave created by a force (red) and by a displacement (blue) load on a "balls' boundary". Horizontal lag between curves corresponds to one timestep ($\Delta t = 10^{-6}$ s).

When a force loading is applied to a particle, that force is added to other acting forces (contact, gravity, inertia, damping, etc.) and is included in the particle's equation of motion (equation 4.8). To all effects, the boundary is still free from any restriction, and incoming waves will be reflected unaltered. More important, this allows the simultaneous application of loading and absorbing boundary conditions in the same particles. The correspondence between velocity and stress in continuous media is direct (as deducted in chapter 2):

$$\sigma = \rho \cdot c \cdot \dot{u}_{load}. \tag{4.47}$$

Absorbing, or silent boundaries are used whenever it is desirable that waves vanish and are not reflected back into the model when they hit a boundary. Absorbing boundaries simulate the dynamic continuation of the domain without representing it. In the current case, reflected waves difficult the extraction of other waves. There are several different strategies to implement silent boundaries. Belytschko (1983) lists some of the most relevant and also the theoretical requirements for efficient absorbing boundaries. Their response must be independent of the frequency, they must collect information about the model in their vicinity (in order to accommodate non-linear behaviour), and it is desirable that the behaviour is simple to understand and implement. Viscous (*i.e.* particle velocity dependent) boundaries, as proposed by Lysmer and Kuhlemeyer (1969), are one of the most widely used strategies. They have been implemented in the source code of all Itasca programs, except PFC^{2D} and PFC^{3D}, and also on several popular FEM codes, such as ABAQUS. When a wave hits a viscous boundary, the boundary generates a symmetric wave that cancels the incoming wave (Belytschko, 1983). This symmetric wave is materialized by imposition of equivalent forces, as in the velocity-stress equation 4.47, but with a minus sign and $\dot{u}_{ball}$ standing for the velocity in the interior of the model:

$$\sigma = -\rho \cdot c \cdot \dot{u}_{ball}. \tag{4.48}$$

Forces calculated through this equation are added to other forces, constant or time-varying, acting at that border in that moment.

The density of the boundary particles must be set to half of its real value, in order to simulate the continuation of the domain (as only half of the particle is represented, the other half of the mass belongs to the absent particle). Also, if a dynamic load is to be introduced simultaneously, and in the same place of an absorbing boundary, it must be set as a force loading, and, as half of the load will be absorbed by the viscous boundary (it is as if the loading is imposed in the middle of the material, not at its limit), the load magnitude must be doubled. In the case of both force loading and absorbing boundary being applied in the same local, both forces will be added to the same particle, one should not replace the other.

To translate dynamic stress into particle forces, particle dimensions and boundary depth must be taken into account via the boundary depth correction factor bf_{depth} (equation 4.20).

$$F_{ball} = bf_{depth} \cdot \sigma \cdot A_{ball} = \frac{l_{bound}}{2 \cdot r_{mean} \cdot nb_{bound}} \cdot \rho \cdot c \cdot \dot{u}_{ball} \cdot 2 \cdot r_{ball}. \tag{4.49}$$

In the current model, it results in:

$$F_{ball} = \frac{69}{164} \cdot \rho \cdot c \cdot \dot{u}_{load} \cdot 2 \cdot r_{ball} \tag{4.50}$$

for dynamic loads and

$$F_{ball} = -\frac{69}{164} \cdot \rho \cdot c \cdot \dot{u}_{ball} \cdot 2 \cdot r_{ball} \tag{4.51}$$

for viscous boundaries.

Another particularity in the application of viscous boundaries to unorganized particulate media is that wave velocity is not available prior to the calculation as there is no way to guess the static and dynamic properties of a synthetic rock model. The propagation velocity must be measured in a previous run and the value then used in the calibration of the absorbing boundary.

This method was implemented in PFC^{2D} and tested by the author with pure shear and compressive waves hitting linear boundaries at normal angles, and presented an efficiency (defined as the ratio between reflected and incoming wave amplitude) larger than 99%. Figure 4.27 shows the velocity time history recorded in the middle of a rectangular bar. A Ricker wave is produced in the bottom of the model, passes through the middle of the bar and hits the top boundary. At that boundary, three different conditions were tested. In the top graph, the displacements at the boundary are restrained through a null velocity condition, and therefore the wave is reflected back with symmetric velocity. The middle graph corresponds to the situation where the top boundary is free. When it hits the top boundary, it is reflected back with the same signal. In the third graph, an absorbing boundary condition is implemented in the top boundary and the wave is almost completely absorbed.

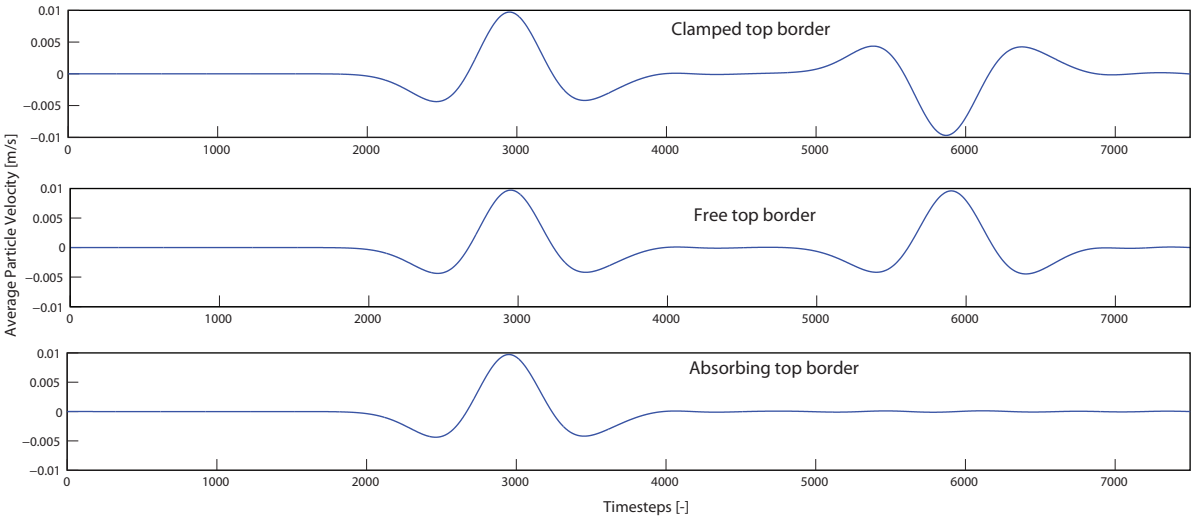


Figure 4.27: Wave velocity at the centre of the model showing upwards moving compressive wave (first peak) and returning wave after reflection at the top border (second peak). Top border is clamped–fixed vertical displacement (top plot), free–no restriction to movement (middle plot) and viscous absorbing boundary (bottom plot).

It is well known (*e.g.* Belytschko, 1983) that viscous absorbing boundaries loose efficiency as the angle of incidence decreases. Further tests are necessary to investigate these limits in particulate media. We must take into consideration that the response of the absorbing boundaries under mixed shear and compressive waves has not been verified. This step is also essential because both kinds of waves are present in most real cases. Visualization methods indicated in Marques (2007) may help to the efficiency of the absorbing boundaries when waves are not normal.

A strategy to prevent unwanted reflections that is alternative to the absorbing boundaries is the utilization of hybrid discrete element-finite difference models. The philosophy behind this strategy is to employ particles in the regions of the model where non-linearity occurs and finite-difference zones in the rest of the domain. The transition between the regions is essential for the good response of the model, and efficient strategies have been devised for static cases (*e.g.* Azevedo and Lemos (2005) or Cai *et al.* (2007)). This has not been tried in wave propagation problems, so the question on how well waves cross the division between the discrete and the continuum still has to be dealt with.

Absorbing viscous boundaries have been implemented in PFC^{2D} through the FISH language. An implementation of the method through a C^{++} external DLL, or in the source code is desirable, as FISH routines are computationally inefficient, when compared to C^{++}.

Load waveform

When studying generic dynamic properties of a model, not a specific case like an earthquake or a blast, one has to pick a wave-function that better suits the objective of the study, as any kind of waveform can be fed into the model. The ultimate goal of this study is to simulate the passage of dynamic compressive waves across fractures. The main characteristics to seek in such a wave-function are, therefore, the following: beginning and end should have null slope, so that the frequency content does not present high frequency components and the introduction of the wave in the model does not produce large unbalanced forces; the final displacement should be zero; the frequency content of the wave-form should be similar to that presented in laboratory studies of wave-fracture interaction (*e.g.* Pyrak-Nolte *et al.* (1990), Zhao *et al.* (2006)).

The Ricker wavelet, often called "Mexican Hat" wave, is a null phase function frequently employed in geophysics to model seismic waves. It is the normalized second derivative of a Gaussian function, and a special case of the family of continuous wavelets known as Hermitian wavelets. It is composed of one positive central peak surrounded by two symmetric lateral lobes, as represented in figure 4.28.

The mathematical expression of a Ricker wavelet is:

$$v(t) = \left(1 - 2\pi^2 f^2 t^2\right) e^{-2\pi^2 f^2 t^2}, \tag{4.52}$$

where f is the central frequency (the only parameter of the wave equation) and t is time. This formula generates a wave centred in zero; time variable t can be shifted to start the wave at a positive or negative time and scaled up or down to make the wave longer or shorter.

The function shows no high frequency corners that aggravate wave dispersion and the first frequency component is zero so the integral of the function is zero. The plot of the absolute value of the Fourier transform is not symmetric and vanishes when frequency approaches zero and when the maximum frequency, which is approximately three times the central frequency, is reached (30,000 Hz in figure 4.28).

A monochromatic (pure sinusoidal) wave's wavelength is equal to the quotient of the wave frequency and the medium propagation speed. As the Ricker wave is not a narrow band process, that is, its Fourier transform is not a single peak, it is not evident which frequency should be used to define it's wavelength. If the peak frequency of the wave is used, a wrong, shorter wavelength will result. In the definition of the conditions for good wave transmission in the model, it is the wavelength measured between the peaks of the negative lateral lobes, equivalent to a time lapse of $\sqrt{6}/\pi/f$ that is used. The complete duration of a Ricker wave corresponds to an average frequency that is about 2/3 the peak frequency expressed in the wave function (6,667 Hz in figure 4.28).

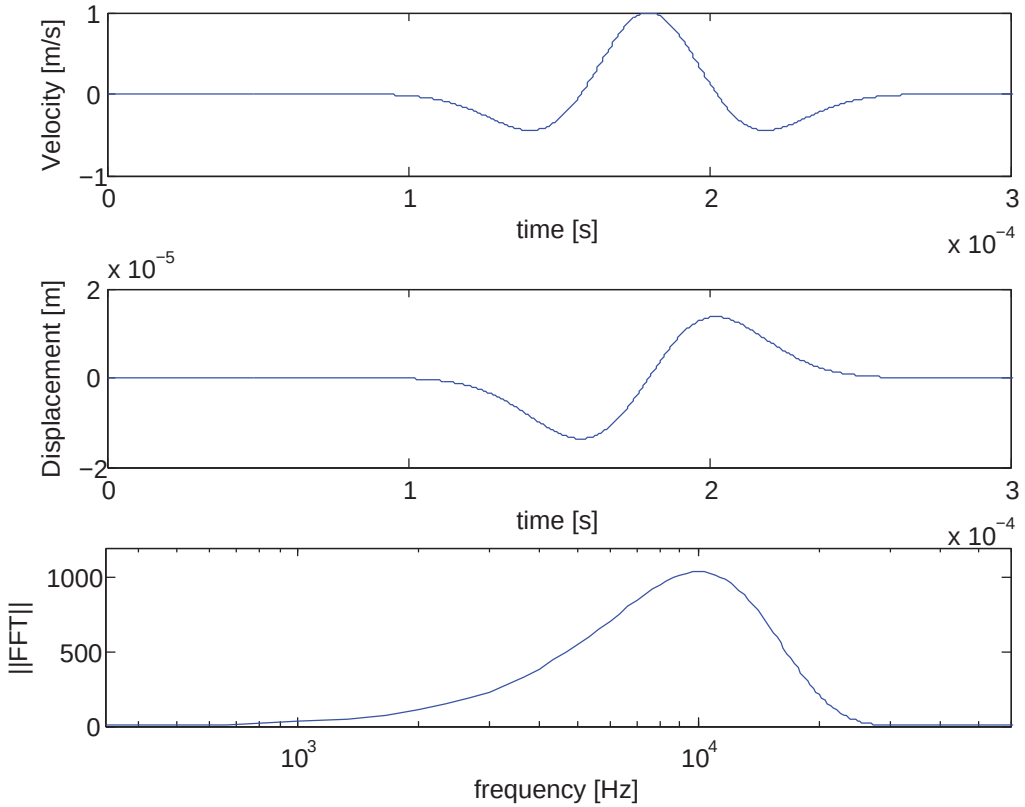


Figure 4.28: Ricker wavelet with central frequency 10^4 Hz and unitary amplitude shifted to the positive time domain. Velocity plot (top), displacement plot (center) and FFT amplitude of the velocity (bottom).

4.5.5 Quality of wave propagation

Waves propagating in a numerical model have their characteristics changed in several ways. This happens because the numerical representation of the wave never represents with complete detail the original, and this is more pronounced in higher frequencies, whose discretization is always of poorer quality. In numerical models, waves of different frequencies travel with distinct velocities, causing the alteration of the waveform envelope of any finite bandwidth wave[3].

The dispersion of the waveform builds as the distance travelled by the wave increases, so the degradation should be measured in terms, not of physical distance, but of wavelengths, or number of oscillations. This concept finds parallel in the rock quality factor Q, that translates the percentage of dissipated energy (defined in relation to total vibration energy) in each vibration cycle.

[3]The velocity off the waveform envelope is called group velocity, while the velocity of each wave with a particular frequency is called phase velocity. This lag in wave velocities which occurs in geomaterials is called wave dispersion (*e.g.* Achenbach, 1973) (repeated from chapter 2).

In each particular modelling situation, the requirements of wave quality must be defined. Firstly, the distribution of energy across the frequency range must be identified. In some cases, the higher frequencies that do not carry appreciable energy can be filtered. Also, the goal of the simulation must be defined. If only wave arrivals will be recorded, more degradation can be allowed, but if peak amplitude, or the entire waveform is needed, quality requirements increase. Finally, because degradation accumulates with the distance that the waves will travel, the locations where waves must have good quality should be defined in advance.

The principle behind wave transmission quality in numerical models is that the shortest wavelength (highest frequency) of interest must be correctly represented (as illustrated in figure 4.29). In finite-difference and finite-element codes especially written for wave transmission problems, higher-order elements are employed (*e.g.* Hildyard, 2001), so that a lower element density is necessary. This comes with an associated cost: higher order elements demand more computational power and their formulation is more complex.

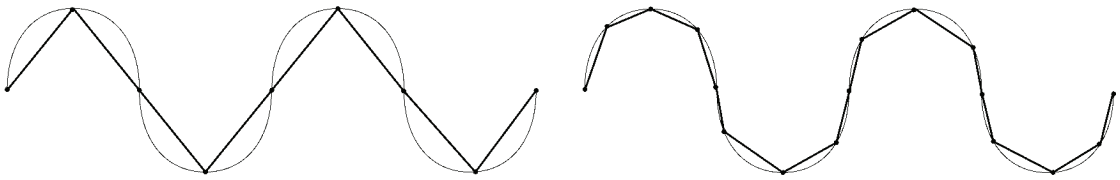


Figure 4.29: Rough (left) and fine (right) discretization of sinusoidal wave.

From observation of figure 4.29 it becomes clear that, no matter how high the relative number of balls/elements per wavelength, loss of quality is inevitable. But, adjusting ball's radius to maintain the desirable wave quality across the model can result in excessively large models. One or a conjugation of the following strategies may be used: the quality of the wave transmission must be partially sacrificed taking into account the minimum necessary degree of precision, the size of the model reduced (employing absorbing boundaries, for example) or the frequency of the signals scaled down or filtered eliminating higher frequencies with low energy content.

Some work has been done on the study of wave propagation in numerical representations of particle assemblies, but all using regular rectangular or hexagonal arrangements, which are quite limited in the scope of behaviours they provide for rock. Toomey (2001) derived dispersion

laws for hexagonal (hence, constant radius) packings of spheres, which is expressed in figure 4.30. An equivalent expression can easily be deducted for disk packings, but it is still of limited value when working with BPM unorganized packings.

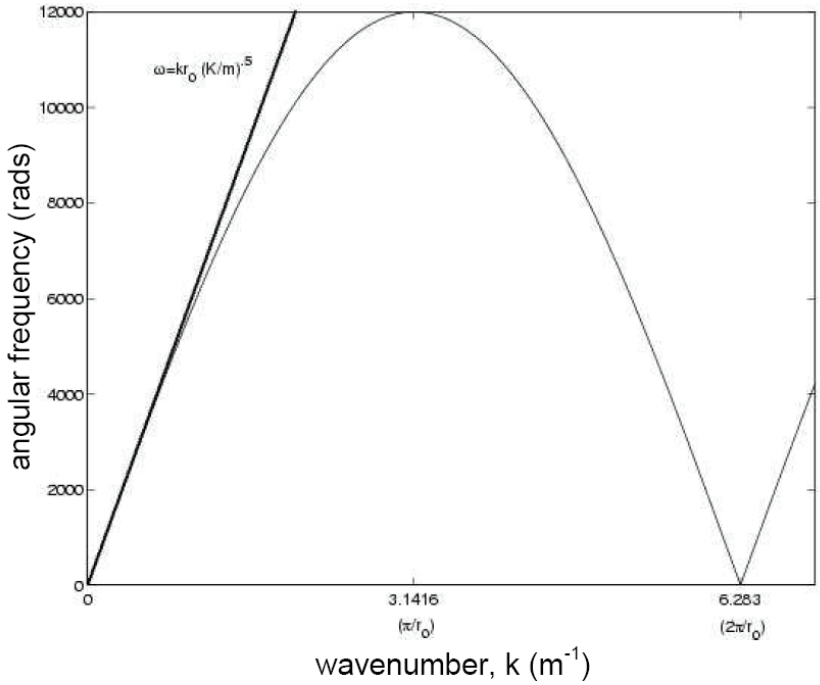


Figure 4.30: In a discrete hexagonal arrangement, different frequencies propagate at different velocities. For waves with longer wavelengths (small wavenumbers), the curve is approximately linear and all frequencies propagate at approximately the same velocity (Toomey, 2001).

In regular difference-finite or finite element meshes, the quotient of the smallest wavelength and the maximum element dimension is used as an indicator of the mesh quality. This adimensional parameter represents the minimum number of elements that discretize with good quality the highest-frequency waves. In dense, non-structured particle assemblies, such as those used here to model rock, the quality controlling parameter was taken as the quotient of the average ball diameter and the smallest wavelength, which corresponds to the number of particles per wavelength. No previous work has been found on this problem.

Hazzard and Young (2004) studied the effect of thermal and mechanically induced cracking in the seismic velocity in brittle rock. They managed to show that the phenomena of rock degradation can be simulated in BPM models, and how this degradation influences not only static but also dynamic properties. Since they were interested in measuring wave arrival times, they did not focus on the preservation of wave characteristics across the model and used the frequency-particle size relations for hexagonal arrangements expressed in figure 4.30.

In this thesis, however, not only the wave arrival times but also the whole wave is to be acurately known in order to investigate in detail how the fractures change the wave. It is then desirable that the influence of the "continuum" part of the model is as small as possible, to isolate the effect of the fracture.

To investigate the effect of the number of particles per wavelength, it is possible to keep the wave frequency constant and vary the balls' size, but that introduces a new variable in play: each new packing will have its own arrangement. According to the tests performed by the author and on Itasca (2004), packings generated with the same set of parameters have similar static and dynamic elastic properties, given that the particles' radius is sufficiently small when compared with models' size, but, anyway, it is more practical and correct to change the frequency of the load than to generate a new packing. Another possibility would be to change the contact stiffness, in order to change wave velocity and, consequently, wavelength, as $\lambda = c/f$ (c being wave velocity and f wave frequency). However, this complicates the analysis even further, as it forces a new wave velocity measurement in each test, and invalidates the comparison of propagation velocities for different frequencies.

To determine the minimum number of particles per wavelength in BPM packing, Ricker waves with central frequencies from 5 to 200 kHz, which have maximum frequency content that is three times the central frequency, are sent in the specimen generated for joint closure tests, already presented in section 4.4.4, without the joint. Dimensions of the model are 90×600 mm^2 and it is composed of 34,773 particles with radii that vary uniformly between 0.5 and 0.83 mm (average diameter is 1.33 mm).

Figure 4.31 presents the model and the sections where waves are probed, located at 10, 30, 50, 70 and 90% of the model's height, which corresponds to a distance of 6, 180, 300, 420 and 450 mm from the bottom.

Contrary to continuous codes with uniform properties distribution, it can be misleading to extract a waveform from one particle. The velocity and contact forces of a single particle are hardly representative of the local behaviour: it can be less or more connected than average, be outside of the local path of passage of waves, or be at the extremes of radius distribution. To minimize errors, a sufficient number of particles must be probed and have their response statistically analysed. This is especially true after a singularity such as a discontinuity or a void. Five particles distributed along the cross-section of the model are probed in each section and their arithmetic average is used in the analyses.

The repeatability of the dynamic properties of several models generated with *FISHTANK* using the same seed parameters was tested and it was confirmed that the variation in properties is small. The same conclusion applies to models generated using the conventional *FISHTANK* routines and the Periodic Brick scheme (Itasca, 2004). Other methods of generation of compact

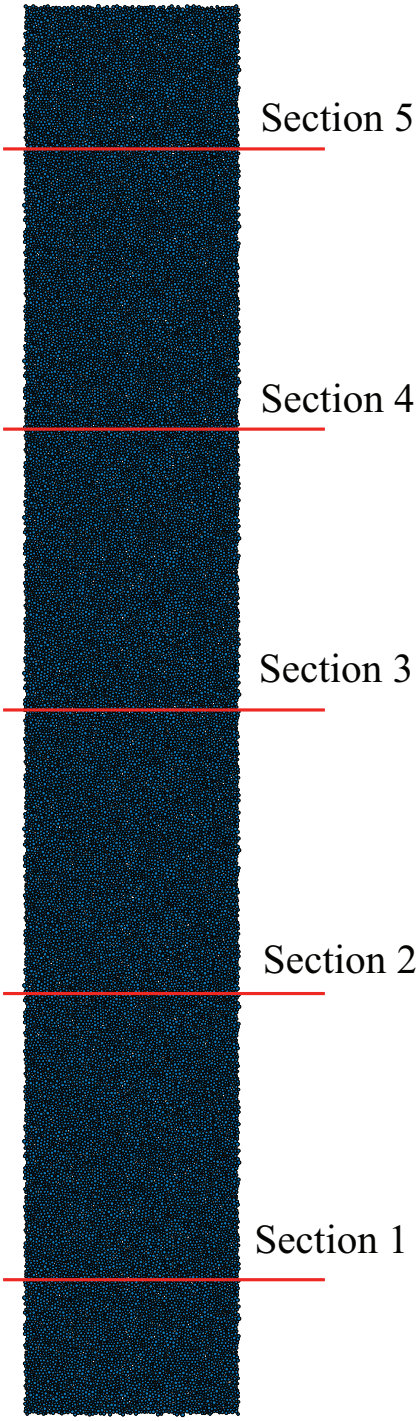


Figure 4.31: Sections of velocity probing.

packings result in somewhat different particle organization and wave propagation on those packings may be slightly different. However, if the radii distribution, porosity and contact type are similar this study's conclusions should hold valid.

In order to compare and frame the dynamic response of the BPM, three other assembly types, with the same external dimensions, balls' radius equal to the average radius of the rock model (0.665 mm) and similar microproperties where generated and tested. Ball density plays an important role in the definition of dynamic properties and thus it is set to a value so that all assemblies have an equivalent continuum density of 2700 kg/m^3 after each packing porosity is taken into account. Ball and contact properties are displayed in table 4.2.

Table 4.2: Ball and contact properties in the four modelled packings.

	Radius [mm]	k_n [GN/m]	k_s [GN/m]	ρ_{ball} [kg/m^3]	Porosity [%]	ρ [kg/m^3]
BPM	0.5 to 0.83	62.0	24.8	3150	14.3%	2700
Rectangular	0.665	62.0	–	3438	21.5%	2700
Hexag$_{kn=ks}$	0.665	62.0	62.0	2977	9.31%	2700
Hexag$_{kn=2.5ks}$	0.665	62.0	24.8	2977	9.31%	2700

In the Rectangular model, contact normal stiffness is set equal to the normal stiffness in the BPM model. The same value is attributed to normal and shear contacts in the first hexagonal assembly model (Hexag$_{kn=ks}$), while in the second hexagonal model (Hexag$_{kn=2.5ks}$) normal stiffness is 2.5 times the shear stiffness, as in the BPM.

Similar static and dynamic boundary conditions are applied in all models. Absorbing boundary conditions are applied to the top of the model and the waves are injected at the bottom by prescribing a velocity time-history. Movement in the direction normal to the wave propagation is restricted in lateral boundaries. This simulates a semi-infinite medium in this direction thus preventing the generation of surface waves that drain energy from the compressive wave.

Timestep is set to 5×10^{-8} s which is slightly smaller than the maximum stable timestep in all models. No damping is used because all alterations to the waveform must come from assembly-caused dispersion. Waves with central frequencies of 5, 10, 20, 30, 40, 80, 120, 150 and 200 kHz were tested in each of the four models.

Wave velocity

Wave propagation velocity is calculated using the time lapse between the passages of waves in the five chosen sections of the model shown in figure 4.31. The most direct method of measuring the wave arrival is to record the instants when the peak of the wave arrives at the different

sections and divide the distance by this time interval. However, when wave frequency is higher, waves loose part of their shape as they travel along the model, and the peak may suffer a shift. To prevent this from interfering, wave velocity is also calculated using wave arrival time. Results between the two methods are fairly consistent, showing that the translation of the peak is not relevant. Figure 4.32 displays the velocity of propagation measured in several sections, for all tested frequencies.

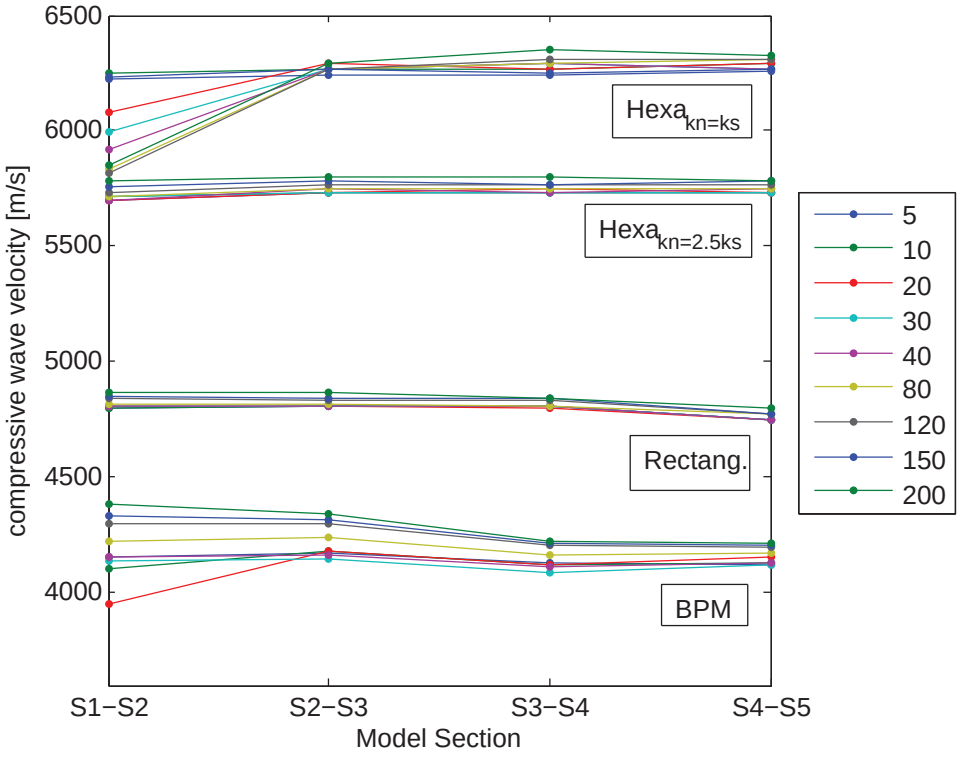


Figure 4.32: Compressive wave propagation velocity c_p along the model, for all tested frequencies (legend shows peak frequency of the waves in kHz).

Wave velocity is fairly constant in the central and final areas of the model, where the wave has stabilized its progression mode. At the bottom of the model, where the velocity loading is imposed, the wave has to adapt to the particulate medium, as it "chooses" local paths of progression. The effect is stronger in the unorganized packing and when the number of balls per wavelength is lower. Notwithstanding the variation in wave velocity in the initial zone in the BPM and Hexa$_{kn=ks}$, the velocity values measured in the middle sections S2 to S4 of each model are almost uniform. These are the propagation velocity values used in the subsequent analyses. Figure 4.33 displays the relative evolution of propagation velocity, when central wave frequency varies from 5 to 200 kHz. It can be seen that wave velocity is almost constant

across the frequency range and that higher frequencies travel at slightly higher velocities, as is characteristic of dispersive media. It should be noted that even in the higher frequencies when the waveform is almost completely destroyed waves maintain their velocities nearly constant, showing that wave velocity is independent of wave quality.

Due to the unorganized structure BPM is the most dispersive assembly: from 5 to 200 kHz, wave propagation velocity increases around 3%. The variation is smaller in the other assemblies, topping at about 1%. Given that c_p presents very small variation in the considered range, an average value is used in the subsequent studies. Compressive wave velocities are, then, 4191 m/s in the BPM, 4819 m/s in the Rectangular, 6279 m/s in the Hexa$_{kn=ks}$ and 5750 m/s in the Hexa$_{kn=2.5ks}$ assemblies. The wave velocity in the Rectangular and Hexa$_{kn=ks}$ assemblies match theoretical expressions, presented in sections 4.5.1 and 4.5.2. The lower wave velocity occurs in the BPM, which is logical given that it is the packing with the lowest degree of organization, and waves have to find and follow less direct paths to travel through the model. Between the two hexagonal packings, there is a significant difference in wave velocities: the packing with the same shear and compressive contact stiffnesses allows waves to travel almost 10% faster. The decrease in the shear stiffness in the Hexa$_{kn=2.5ks}$ model causes the decrease of wave velocity. Since waves travel with different velocities in the models, waves with equal frequencies will have distinct lengths, as represented in table 4.3.

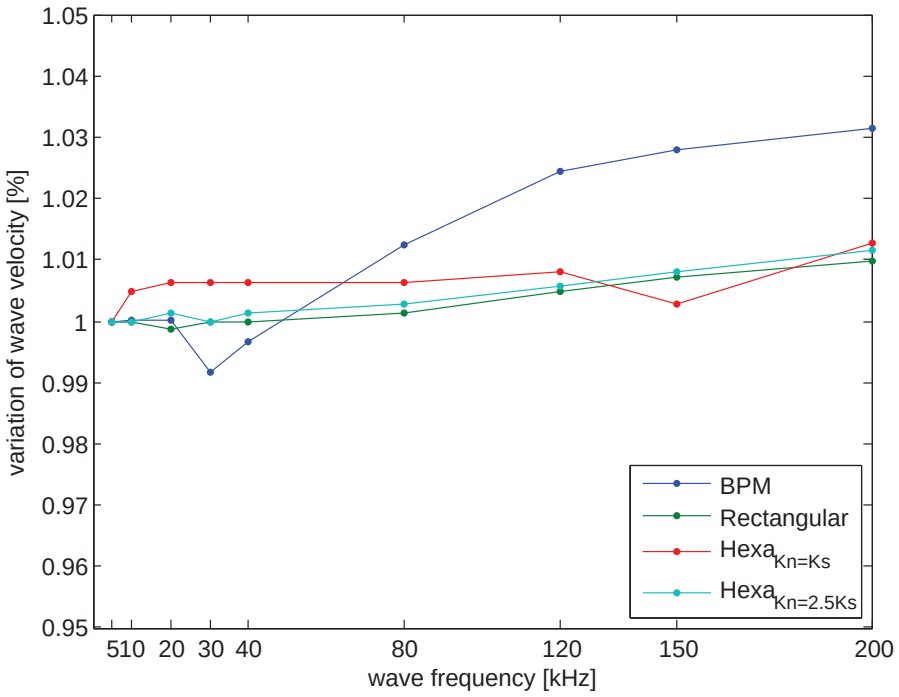


Figure 4.33: Relative variation of compressive wave velocity with peak frequency.

Table 4.3: Wavelength, defined as the distance between the negative peaks (see section 4.5.4) of the Ricker waves in the four packings. c_p is 4191, 4819, 6279 and 5750 m/s, for BPM, Rectangular, Hexa$_{kn=ks}$ and Hexa$_{kn=2.5ks}$, respectively.

Peak freq. [kHz]	BPM [m]	Rectangular [m]	Hexa$_{kn=ks}$ [m]	Hexa$_{kn=2.5ks}$ [m]
5	0.654	0.752	0.979	0.897
10	0.327	0.376	0.490	0.448
20	0.163	0.188	0.245	0.224
30	0.109	0.125	0.163	0.149
40	0.82	0.94	0.122	0.112
80	0.41	0.47	0.61	0.56
120	0.27	0.31	0.41	0.37
150	0.22	0.25	0.33	0.30
200	0.16	0.19	0.24	0.22

Wave attenuation

The other key parameter of wave propagation in numerical models is how quality of the wave degrades as it crosses the model. To assess this, waves of increasing frequencies are injected at the base and peak amplitudes are recorded along the model. Figure 4.34 shows how peak particle velocity amplitudes decrease when travelling through each of the four models. Decay of peak amplitude is chosen as the quantitative indicator of wave quality because it was observed that waveform degradation is proportional to decrease in the maximum amplitude.

The relative amplitude decay is plotted against distance divided by the average ball diameter. The reference value is not the amplitude of the input wave but that measured at section 1 which is 60 mm above the model's base. In all organized geometries the rate of amplitude loss is constant, meaning that wave degradation accumulates while the wave travels. In the BPM model degradation is higher at the bottom of the model, where the wave adapts to the particulate medium. After that initial adjustment, the rate of loss is also approximately constant.

Figure 4.35 illustrates how the velocity waveforms of three waves with increasing frequency change after travelling across the BPM assembly. These time histories, measured at probing sections 1 and 5, provide a qualitative assessment of the wave degradation, not possible with wave amplitudes. In the top graph, wave reproduction is perfect, while in the middle one the peak and the first lobe amplitudes decrease slightly and a ripple, characteristic of particulate mediums is observed after the wave passage. In the bottom graph, the wave at the top of the model is almost unrecognisable, and the ripple effect is almost as large as the wave peak. Figure

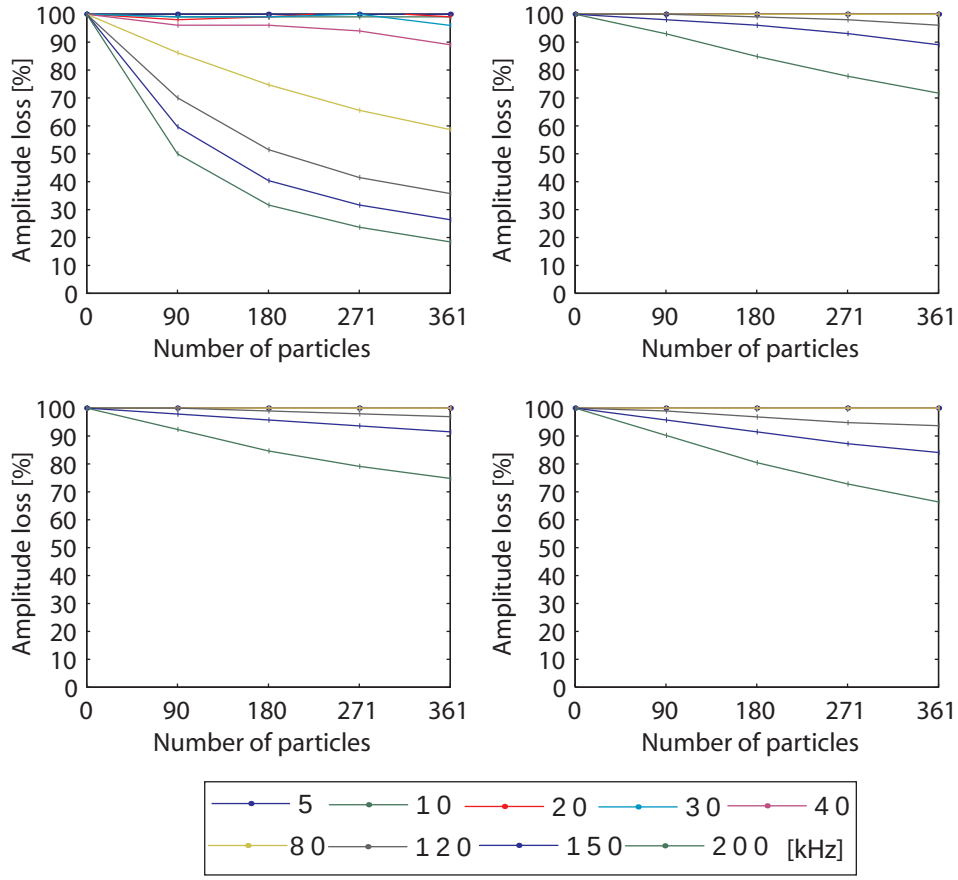


Figure 4.34: Relative variation of peak wave amplitude along the model for all tested frequencies. Clockwise from top left: BPM, Rectangular, Hexa$_k n = 2.5ks$ and Hexa$_k n = ks$. Legend shows peak frequency of the waves in kHz.

4.35 displays also the Fourier transform of the waves. It can be seen that the degradation is bigger in the frequencies higher than 20 kHz, while the lower frequencies are better reproduced. It must be noted that in these models there is no damping and no contact failure, the degradation of the waveform is not caused by loss of energy, but by conversion to other wave types and directions. A monitoring of the total energy in the model, possible by measuring all kinetic energy in the balls and potential energy in the springs shows that the energy in the model remains constant from the time the wave injection ends until the moment where the wave hits an absorbing boundary.

Finally, figure 4.36 provides a compact, convenient way to compare the performance of all models, representing the relative loss of velocity amplitude between the top and the bottom of the model, for all studied wavelength-ball diameter relations. It should be noted that only in the rectangular packing particles are perfectly aligned with the particle movement, thus only in this case the wavelength/ball diameter ratio is absolutely meaningful.

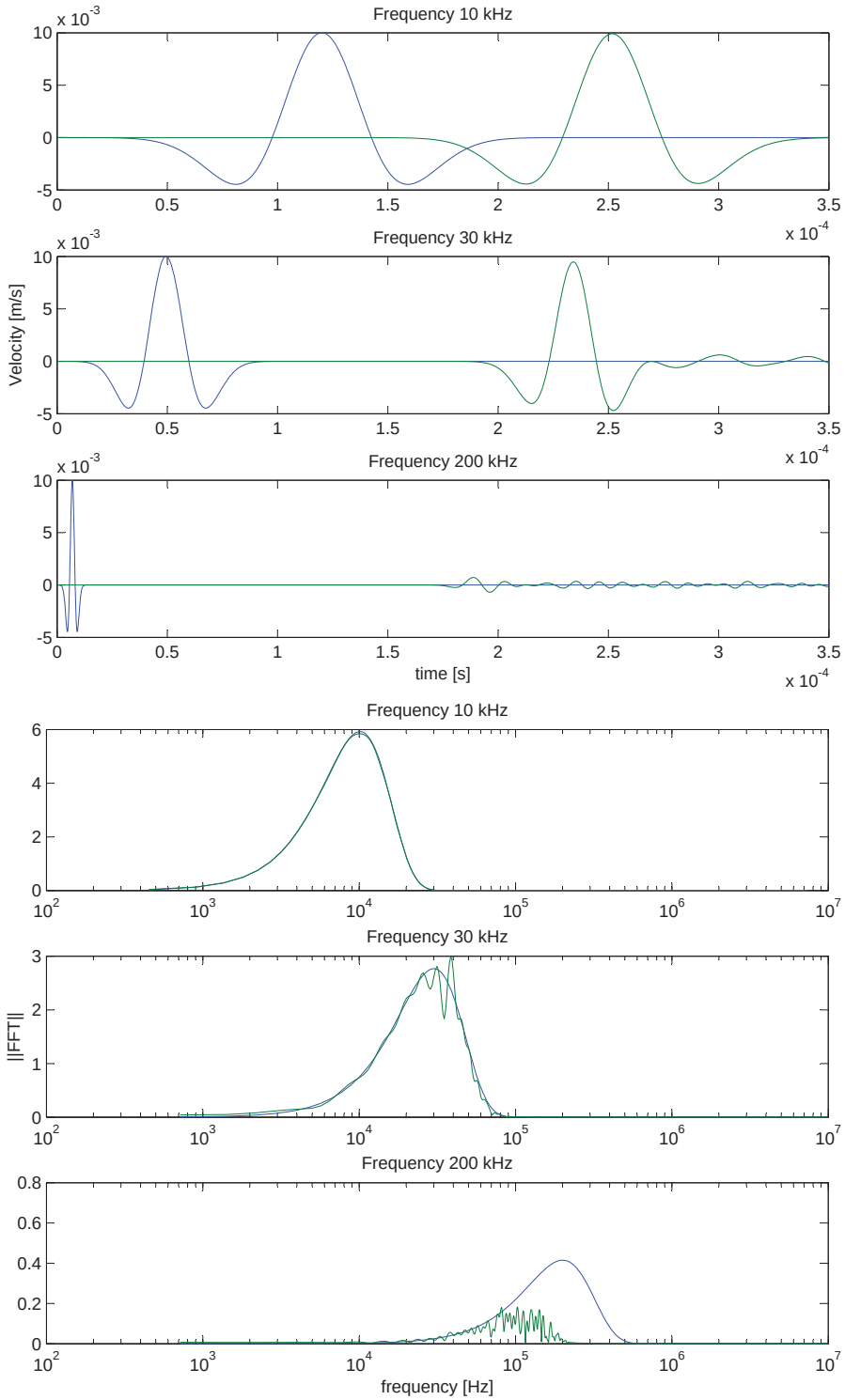


Figure 4.35: Velocity waveforms (top) and frequency content (bottom) of waves of growing frequency at the bottom (blue) and top (green) of the BPM assembly.

The wave frequency and associated wavelength/particle diameter relation that results in an amplitude loss below 5% is in bold in tables 4.4, 4.5, 4.6 and 4.7. BPM model is much more demanding than all organized packings. Of these, the Rectangular packing preserves better wave quality followed by the Hexa$_{kn=ks}$ and Hexa$_{kn=2.5ks}$.

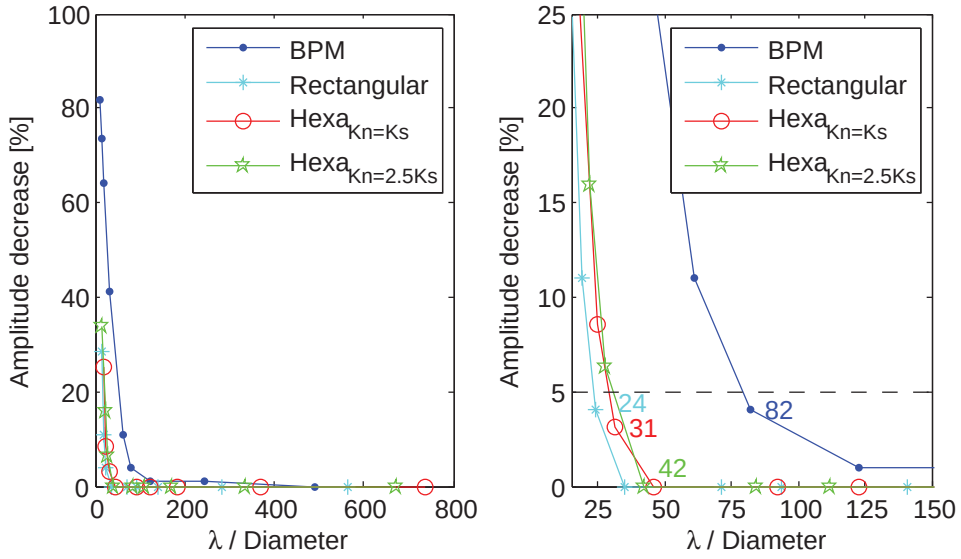


Figure 4.36: Relative variation of peak wave velocity measured at the bottom (section 1) and at the top (section 5) of the model. Right plot zooms in the axes origin, horizontal line marks 5% loss.

Table 4.4: Wave amplitude loss between sections S1 and S5 in the BPM model. Wavelength is the distance between negative peaks, average ball diameter is 1.33 mm.

Peak freq. [kHz]	λ [m]	λ/Diam. [m/m]	Amplitude loss [%]
5	0.654	491	0%
10	0.327	246	1%
20	0.163	123	1%
30	**0.109**	**82**	**4%**
40	0.082	61	11%
80	0.041	31	41%
120	0.027	20	64%
150	0.022	16	74%
200	0.016	12	82%

Table 4.5: Wave amplitude loss between sections S1 and S5 in the Rectangular model.

Peak freq. [kHz]	λ [m]	λ/Diam. [m/m]	Amplitude loss [%]
5	0.752	565	0%
10	0.376	283	0%
20	0.188	141	0%
30	0.125	94	0%
40	0.094	71	0%
80	0.047	35	0%
120	**0.031**	**24**	**4%**
150	0.025	19	11%
200	0.019	14	28%

Table 4.6: Wave amplitude loss between sections S1 and S5 in the Hexa$_{kn=ks}$ model.

Peak freq. [kHz]	λ [m]	λ/Diam. [m/m]	Amplitude loss [%]
5	0.979	736	0%
10	0.490	368	0%
20	0.245	184	0%
30	0.163	123	0%
40	0.122	92	0%
80	0.061	46	0%
120	**0.041**	**31**	**3%**
150	0.033	25	9%
200	0.024	18	25%

Table 4.7: Wave amplitude loss between sections S1 and S5 in the Hexa$_{kn=2.5ks}$ model.

Peak freq. [kHz]	λ [m]	λ/Diam. [m/m]	Amplitude loss [%]
5	0.897	674	0.0%
10	0.448	337	0.0%
20	0.224	169	0.0%
30	0.149	112	0.0%
40	0.112	84	0.0%
80	**0.056**	**42**	**0.0%**
120	0.037	28	6%
150	0.030	22	16%
200	0.022	17	34%

4.5.6 Discussion on wave propagation in BPM

Until now, to the author's knowledge, no work had focused on the dynamic performance of rock bonded particle models, particularly on the conditions for the propagation of stress waves. It has been found that, although the quality requirements for accurate representation of waves are demanding and special care must be taken with boundary conditions, the actual computational capacities are enough for small scale studies. It was demonstrated that the Bonded Particle Model is able to simulate the static and dynamic properties of hard rock. The major achievements are:

- Attenuation of stress waves is assessed and the conditions that ensure good propagation quality are presented.
- Boundary conditions for static loadings and for the injection of dynamic time-history loadings are developed.
- Silent, or absorbing boundaries for normally incident waves are implemented.
- A procedure to control spurious particle velocities when transferring a model from density scaling to dynamic calculation mode is devised.

Some points should be addressed in the continuation of this study:

- The study should be repeated with shear waves allowing for a complete representation of the dynamic properties and comparison with static values.
- The attenuation and propagation velocity study should be repeated with monochromatic waves of varying frequencies, as this would allow more general conclusions to be drawn and a comparison with other numerical methods.
- A test of propagation of circular waves from a model's central point, *i.e.*, a true unbounded test should be performed.

4.6 Propagation of compressive stress waves across fractures

Wave-fracture interaction numerical tests come in the sequence of the static joint closure tests described in section 4.4.4 and are also a result of the knowledge on wave propagation gained while developing the studies presented in the previous section. After each load increment of the joint static compression calculation, corresponding to a certain position in the normal stress *vs* joint closure curve (figure 4.21, repeated in figure 4.37 below), the model is saved together with all associated information: ball positions and movement, contact forces, exterior forces, and boundary conditions.

Without allowing the state of the joint (relative wall position, contact forces and displacements) to change, the procedure to pass the model from static to dynamic calculation mode,

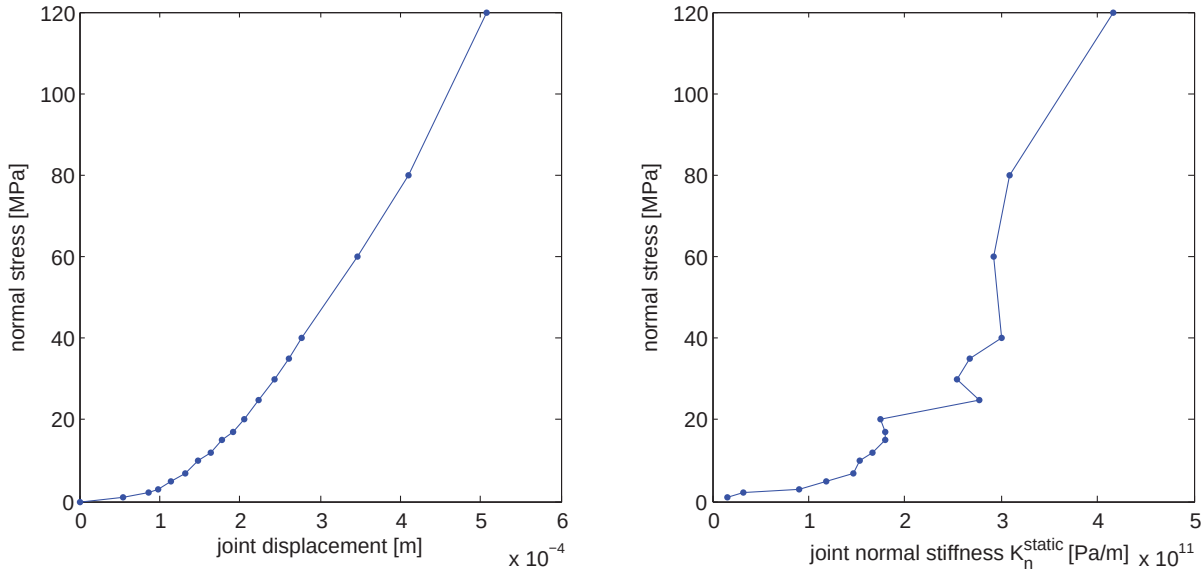


Figure 4.37: Vertical stress *vs* joint closure curve. Displacement is measured between joint walls.

described in section 4.5.4, is applied. This step is particularly important when high normal loads are applied because unbalanced forces are at their highest.

A wave is generated at the bottom boundary. The Input wave, the wave that crosses the fracture (Transmitted) and the wave that is bounced back at the fracture (Reflected) are processed and the dynamic characteristics of the fractures are calculated according to the Displacement Discontinuity Theory (Pyrak-Nolte *et al.*, 1990).

4.6.1 Test description

Wave passage tests are performed for each of the following normal stresses: 1, 5, 17.5, 25, 80 and 120 MPa. Boundary conditions of the model: at the bottom boundary, particles' velocity is restrained, and the wave is injected by imposition of a velocity history. Horizontal movement at the lateral boundaries is constrained to prevent formation of surface waves. During the joint closure tests, a vertical downwards force correspondent to the normal stress is installed in the top boundary. This force is maintained and an absorbing boundary is installed at this location, as described in section 4.5.4. No damping is used and timestep is set to 5×10^{-8} s, below the minimum stable timestep.

The wave sent against the discontinuity is a Ricker wavelet with a central frequency of 15 kHz. Such a wave has a wavelength of 210 mm. In the BPM model, average ball diameter is 1.33 mm, so the wavelength-ball diameter ratio is approximately 160, assuring that the wave crosses the model with very little loss of quality, as shown in figure 4.36.

Particle velocities are recorded at three sections located at the bottom and top of the model

and 135 mm (one and a half times the width) below the fracture located at mid-height. At each section five balls are probed. The input wave is extracted from the section nearer to the bottom and the transmitted wave from the section at the top border. The reflected wave is captured at the section below the fracture. As the upwards-going input and downwards-travelling reflected waves superimpose in time it is necessary to isolate the reflected wave by subtracting the input wave to the total recorded waveform. The section where the transmitted wave is recorded is chosen at a distance from the fracture that allows the reconstruction of the wave after the passage through the fracture since during the passage through the fracture the wave "squeezes" through the active contacts, as illustrated in figure 4.38. One of the rewards of micromechanical models is exactly the visualization of this kind of fast microscopic phenomenon.

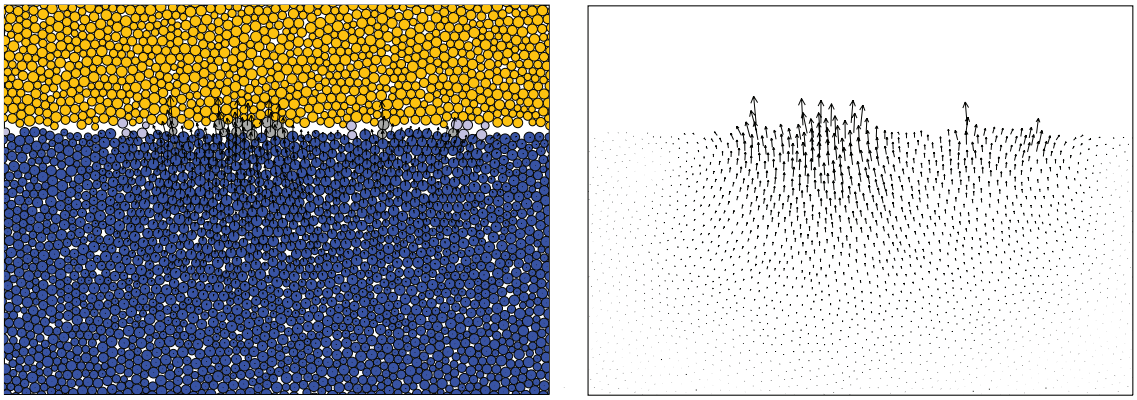


Figure 4.38: Ball velocity vectors of wave passing across fracture (left shows vectors and balls, right only the vectors; only vectors of the bottom half are shown).

4.6.2 Results discussion

According to the Displacement Discontinuity Theory (chapter 2), the analysis of the waves that originate from a rock fracture when it is excited by an incident wave allows, the identification of the dynamic, or seismic, stiffness of the fracture. It is expected that the more the fracture is compressed and closed the better it will transmit the wave to the other side and thus it will reflect less back.

The parameter that controls the amount of transmissivity and reflection of the compressive wave is the relation between the wave angular frequency and the joint dynamic, or seismic, specific stiffness, which was defined in chapter 2 as the quotient of the joint normal dynamic stiffness K_n^{dyn} and the intact rock material impedance $Z_p = c_p \rho$:

$$\frac{K_n^{dyn}}{Z_p\,\omega}. \tag{4.53}$$

The parameter $\omega Z_p/K_n^{dyn}$ is present in equations 2.30 and 2.31. These equations relate, in the frequency domain, the amplitudes of reflected $R(\omega)$ and transmitted $T(\omega)$ waves with the input $I(\omega)$ wave. These equations and the associated deduction were presented in chapter 2 and are rewritten here for the compressive wave case:

$$|R(\omega)|_{theoretical} = I(\omega)_{model} \left[\frac{4\left(\frac{Z_p\omega}{K_n^{dyn}}\right)^2}{4\left(\frac{Z_p\omega}{K_n^{dyn}}\right)^2 + 1} \right]^{1/2} \tag{4.54}$$

$$|T(\omega)|_{theoretical} = I(\omega)_{model} \left[\frac{1}{4\left(\frac{Z_p\omega}{K_n^{dyn}}\right)^2 + 1} \right]^{1/2} . \tag{4.55}$$

In the current study, the input wave frequency content is pre-determined and the intact material's impedance is measured from the model. It is possible, then, to find a dynamic stiffness that generates $R(\omega)_{theoretical}$ and $T(\omega)_{theoretical}$ functions that adjust the ones produced by the BPM model. In laboratory tests of rock fractures (*e.g.* Cai (2001) and Pyrak-Nolte *et al.* (1990)), a good adjustment between measured and theoretical wave amplitudes has been registered. Can the numerical model of a fracture that simulates the microscopic deformation mechanics do the same?

Figure 4.39 shows how the waveforms of the reflected and transmitted wave evolve while the compression in the joint increases. A minimum treatment of the time series was necessary to isolate the reflected and transmitted wave from other waves that pass the measurement spot simultaneously. A tapered cosine time-window with a tapper of 5% (Achenbach (1973)) is applied to the time series of the reflected and transmitted waves. Other time-windows were tested, namely the half-cosine, Hamming and Blackwell. Of these the tapered-cosine window resulted in the cleaner Fourier transform with the minimum intervention.

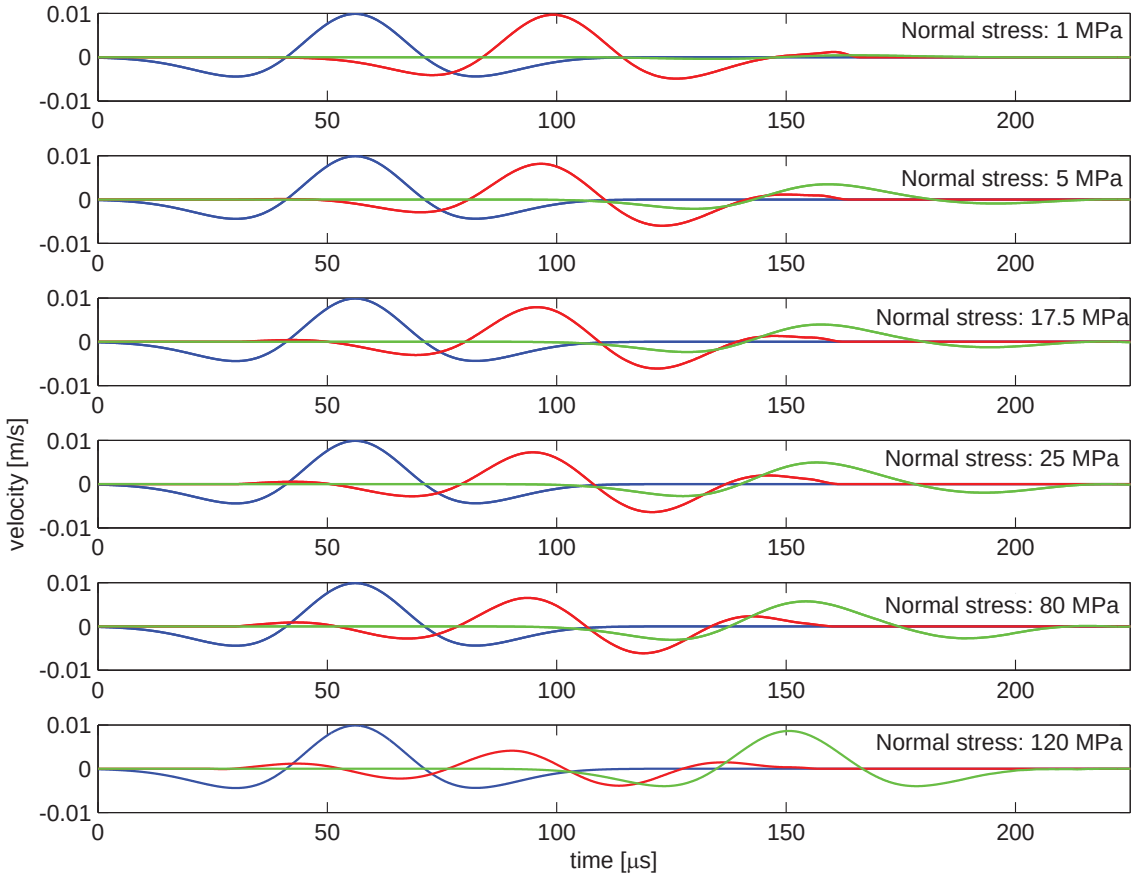


Figure 4.39: Reflected (red) and Transmitted (green) waves from fracture submitted to increasing normal stress. Input wave, in blue, is shown for reference.

When the joint is slightly compressed the transmitted wave is nearly imperceptible and the reflected wave almost equals the input wave. With increasing compression the transmitted wave grows and the reflected wave shrinks. This can be observed in the absolute value of the Fourier transform of the waves in figure 4.40.

Since each wave passage produces a reflected and a transmitted wave, two seismic stiffness values ($K_{n,R}^{dyn}$ and $K_{n,T}^{dyn}$) can be determined. This is an advantage in relation to the laboratory tests found in the literature where only the transmitted waves are captured.

To find the two dynamic stiffness values theoretical transmitted and reflected waves are calculated (equations 4.54 and 4.55) and compared with the waves extracted from the model. A curve fitting routine developed in MATLAB (MathWorks, 2009) finds the seismic stiffnesses $K_{n,R}^{dyn}$ and $K_{n,T}^{dyn}$ that lead to an optimum fit of the theoretical and model curves. The MATLAB routine optimizes the dynamic normal stiffness of the joint through unconstrained non-linear optimization method that performs a direct search without calculating function gradients.

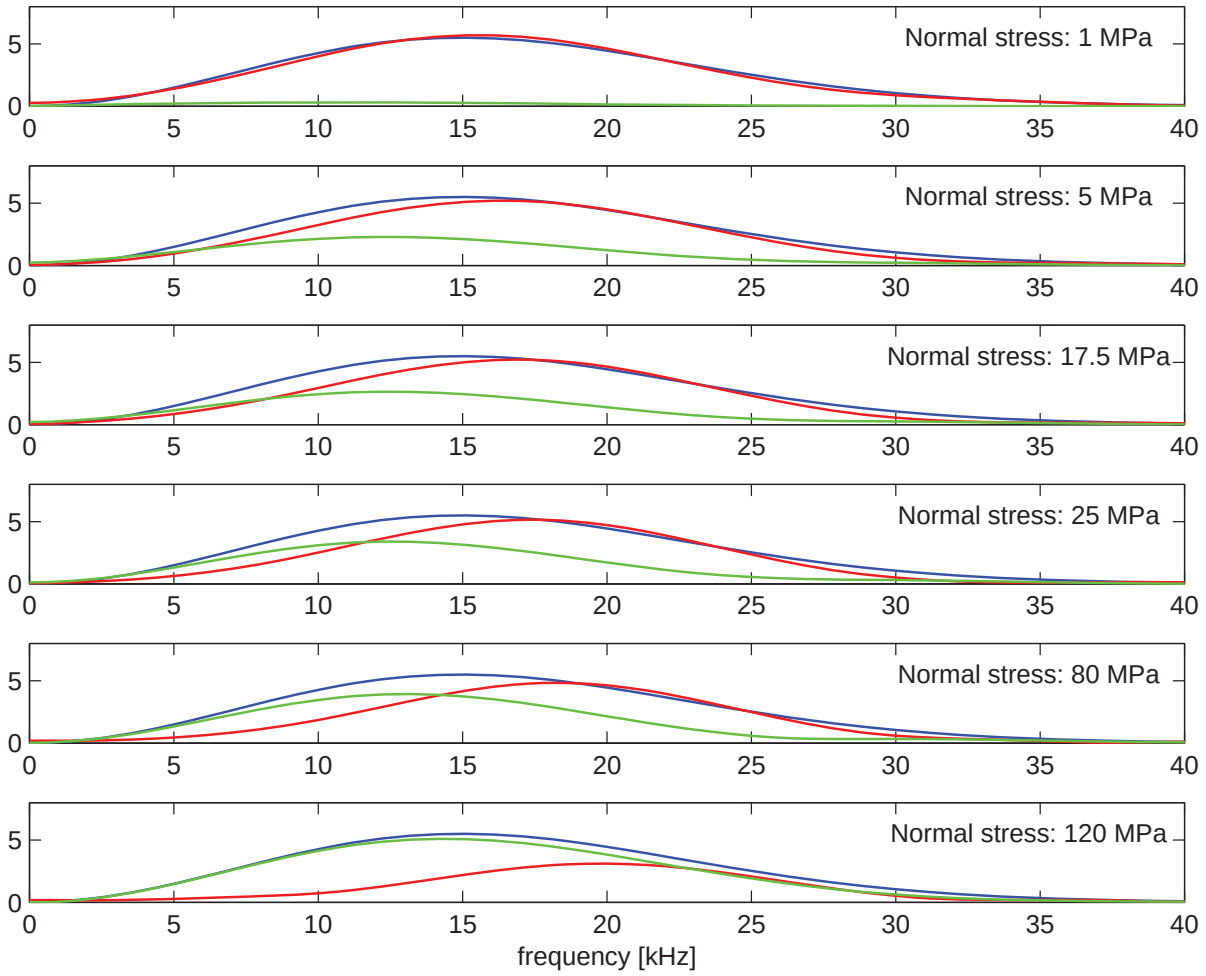


Figure 4.40: Absolute value of the Fourier transform of the Reflected (red) and Transmitted (green) waves from fracture submitted to increasing normal stress. Input wave frequency amplitude, in blue, is shown for reference.

Figures 4.41 and 4.42 show how the model waves frequency amplitude measure up to the theoretical prediction. The fit is better in transmitted waves, which can possibly be explained by the fact that these are not contaminated by the incident wave. Both model and predicted reflected waves' central frequency increase with compression stress but this effect is slightly stronger in the model causing the adjustment to degrade in higher stresses. Model and predicted transmitted waves match up well, the match being almost perfect in lower frequencies. In higher frequencies, the model's amplitude is slightly higher.

This divergence can be attributed to the hypothesis that, contrary to what is admitted in the Displacement Discontinuity Theory, dynamic stiffness is not constant, being a function of frequency. Pyrak-Nolte and Nolte (1992) investigated this hypothesis and attribute the variation of the stiffness with the frequency to the relation of the wavelength to the different

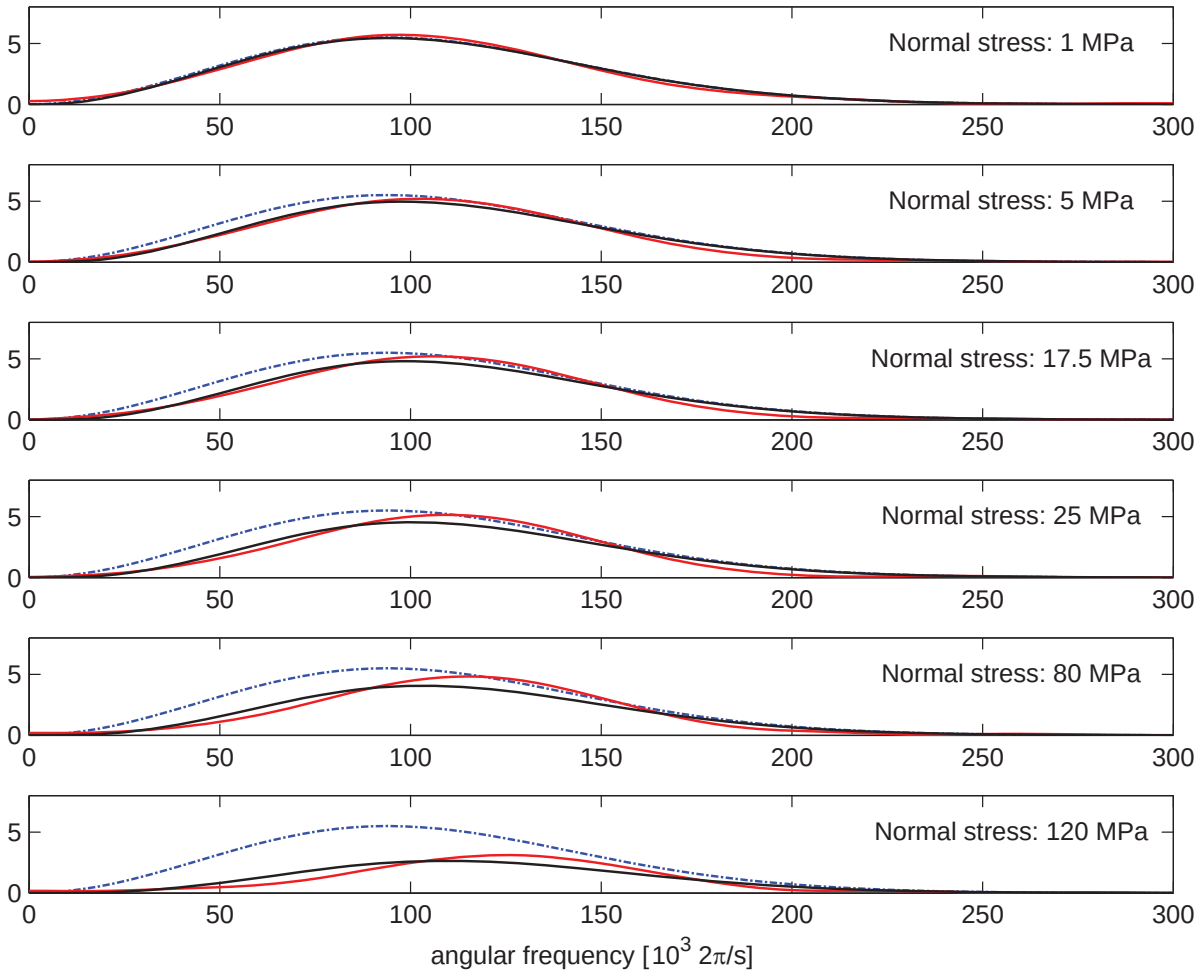


Figure 4.41: Reflected frequency amplitudes for the different normal stress tests. Predicted theoretical values in black, model's results in red. Input wave, in dashed blue, is shown for reference.

spacing between contact points. To test this hypothesis, more simulations where the effect of the average spacing between contact points on stiffness is studied are necessary.

As predicted by the Displacement Discontinuity Theory and observed in laboratory tests, the fracture acts as a low-pass filter, transmitting preferentially the lower frequencies and this effect is stronger in the lower normal stresses when the seismic stiffness is lower and the ratio $\omega Z_p/K_n^{dyn}$ is higher. But even at the maximum stress of 120 MPa the wave is not completely transmitted, and the reflected wave is still visible, which means that the fracture is not totally closed. The stress-displacement curve of the static joint compression test (figure 4.37) is also not completely at the maximum stress level.

The fracture behaves elastically: the wave does not lose energy when crossing it, so the square root of the sum of the square of the transmission and reflection coefficients is equal to one ($\sqrt{R^2+T^2}=1$, equation 2.32). Figure 4.43 confirms it in all but on the test with

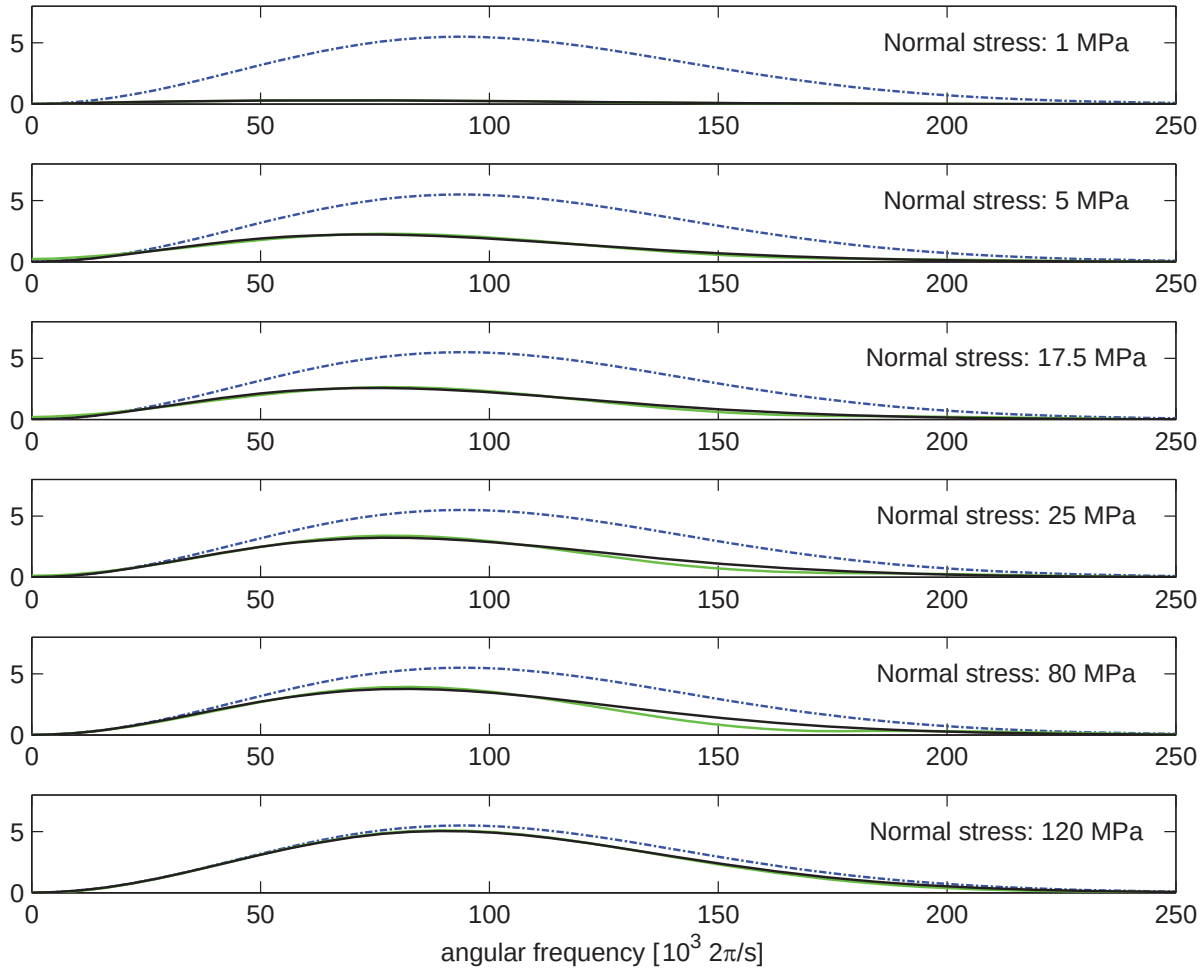


Figure 4.42: Transmitted frequency amplitudes for the different normal stress tests. Predicted theoretical values in black, model's results in green. Input wave, in dashed blue, is shown for reference.

lower stress (1 MPa). In this first test, the transmitted wave is nearly flat and the reflected wave almost equal to the input wave (figure 4.40). In this scenario, the error margin of the fitting routine that finds stiffness values that adjust theoretical and measured frequency curves is considerable.

The Displacement Discontinuity Theory, and common sense, indicate that the dynamic stiffness should grow with the joint normal stress. The evolution of the transmitted and reflected dynamic stiffnesses with static normal stress is similar (figure 4.44) and the small gap between them is thought to be due to the better quality of the transmitted wave. The energy balance and the match between both stiffness values demonstrate that the BPM joint correctly simulates the dynamic behaviour of rock joints.

Figure 4.44 also displays the evolution of static stiffness in the same joint. The trend followed by the static and seismic stiffness, both being tangent values, is similar with the

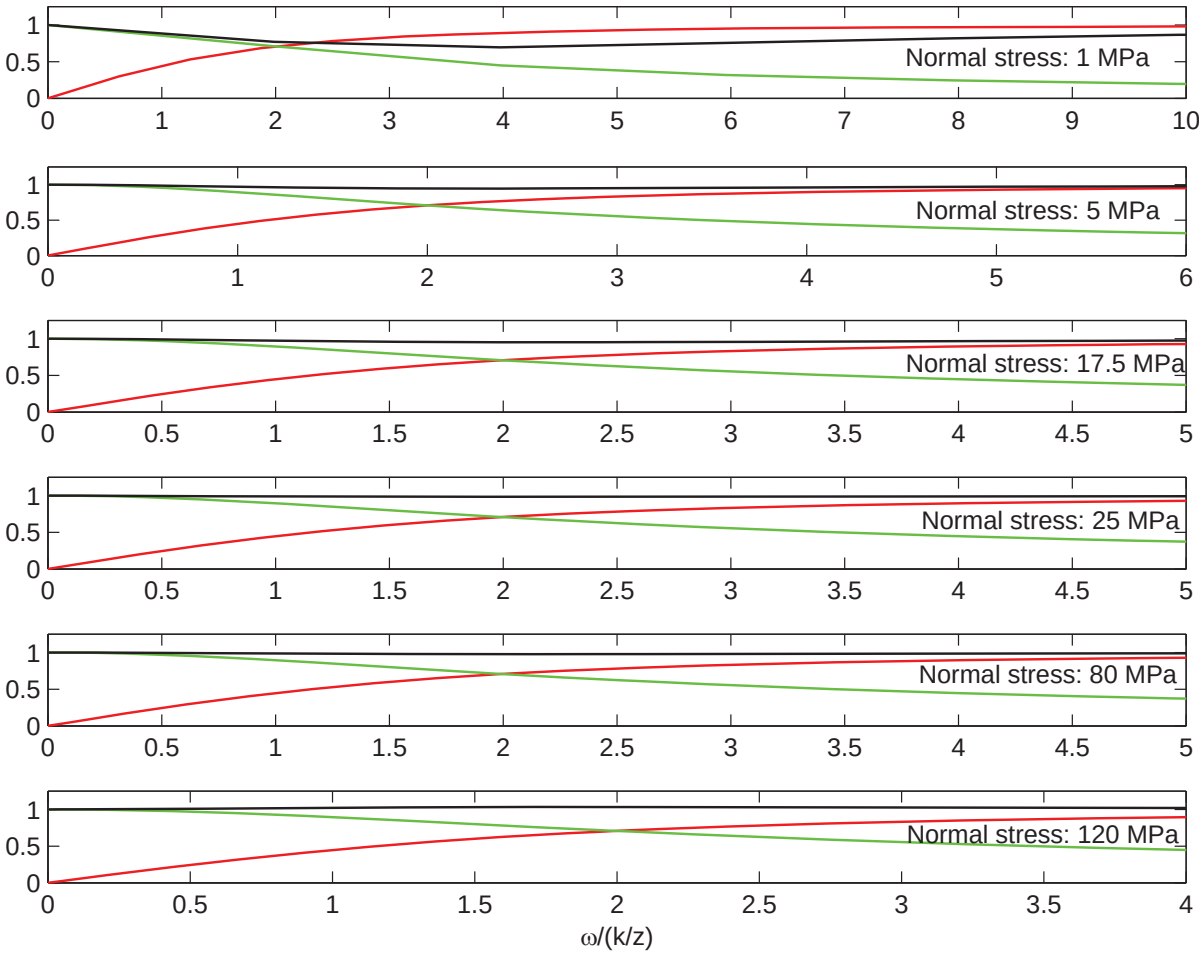


Figure 4.43: Reflection (red) and transmission (green) coefficients, and energy balance (black) in each test.

latter being always smaller. In all tests of static and dynamic properties of rock and rock joints, dynamic values (Young's modulus, shear modulus or joint stiffness) are invariably higher than static ones. Cai (2001) tested artificial cement mortar joints with compression stress from 2 to 20 MPa and a central wave frequency of 20 kHz under three growing deformation velocities: quasi-static, dynamic deformation on a dynamic press and ultrasonic waves. He found that dynamic stiffness on wave passage tests is typically 2 to 3 times the value of dynamic deformation tests, which is itself 1.2 to 2 times the static stiffness. Cai's values of seismic stiffness depend on the compression and on the density of contacts in the joint and are in the 20 to 1200 GPa/m range . The values found in the current study are in the same order of magnitude, increasing from 100 to 1,200 GPa/m for compression stresses of 1 to 120 MPa. However, values determined by Pyrak-Nolte *et al.* (1990) for transmission of waves across natural fractures on quartz monzonite compressed up to 85 MPa yielded much larger seismic stiffness

values, from 2000 to 150,000 GPa/m. In this case, the wave central frequency is higher, from 500 to 1000 kHz. The static stiffness for the same samples is in the same order of magnitude but always lower ranging from 2000 to 30,000 GPa/m.

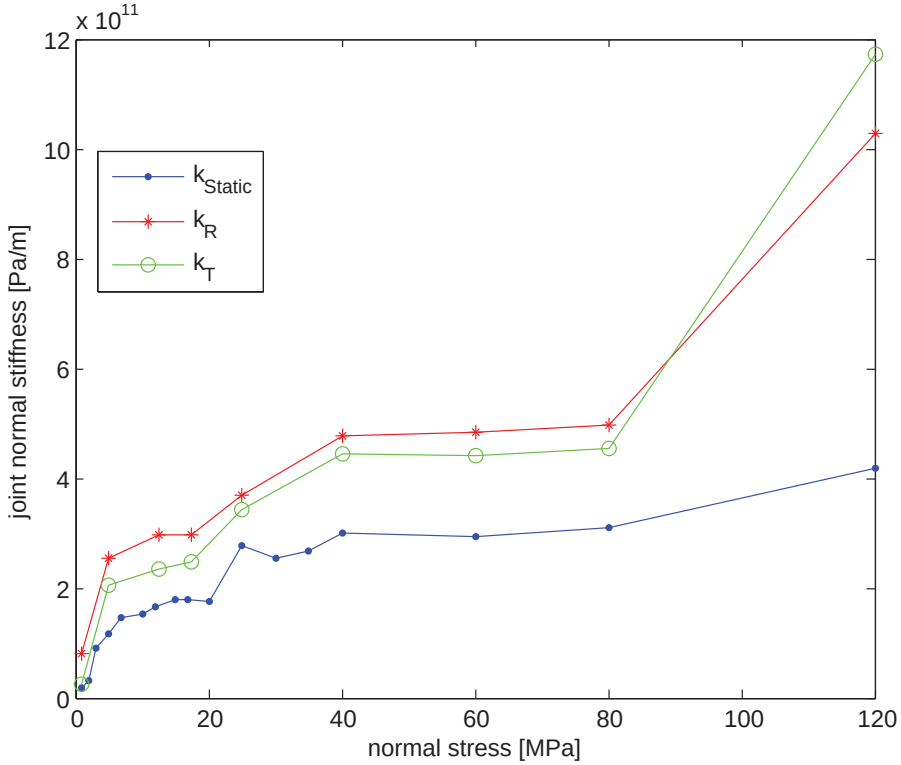


Figure 4.44: Evolution of the dynamic and static tangent stiffness with normal stress. Dynamic stiffness ($K_{n,R}^{dyn}$ and $K_{n,T}^{dyn}$) are from analysis of reflected and transmitted waves, static normal stiffness K_n^{static} is extracted from the stress-displacement graph.

Even though no viscous parcel is present in the discrete element model as it was employed and no strain-rate effects are included in the contact models of the joint and rock material, dynamic elastic parameters are higher than static parameters. The reasons for this difference, also found in laboratory and field tests, are identical for fractures and for intact rock. Firstly, due to inertia effects when rates of deformation are high, the fractures and asperities do not have enough time to deform. Secondly, the stress level induced by the dynamic wave is much smaller than the static stress. In the present study stress waves amplitude is approximately 0.1 MPa, which is one to three orders of magnitude smaller than the static stress installed in the joint. The wave with very small amplitude excites the fracture around the current location in the stress-displacement curve without perturbing the fracture state.

4.7 Discussion and future developments

Along the pages of this chapter, partial conclusions were drawn. They are summarized here, along with some general considerations about the results and the highlights and shortcomings of the work.

This chapter describes an innovative method for modelling rock fracture dynamic behaviour using BPM, focusing on the propagation of compressive waves across fractures.

A simple method to generate a fracture in the BPM model is proposed and a contact constitutive with stiffness hardening, compiled in C^{++} and linked to the source code of PFC^{2D}, is employed in wall-to-wall interaction. To the author's knowledge, this is the first time the normal behaviour of rock joints is modelled at microscopic level with BPM. The goal of this first part of the study is to reproduce the basic characteristics of a rock joint under normal loads including the increase in number of contact points and stiffness with stress. The limitations of this part of the study are also the ground for future developments. Firstly, in addition to joint non-linearity, rock non-linear behaviour and failure can be also integrated. Secondly, real joint profiles are extremely varied with peaks and valleys of different wavelengths and heights. The method used for the joint geometry generation does not reflect that, and the new contact model still has to be tested in other joint geometries. Thirdly, though having a physical meaning, the contact model parameters do not correspond to rock joint walls measurable characteristics like hardness or resistance of the wall material. Finally, 3D modelling will allow for a better representation of the joints rich spatial variation. This can be achieved with parallelized codes that run on multi-core or multi-processor machines.

On the second part of the work, the conditions for propagation of stress waves on rock bonded particle models are tested. The performance of dense non-uniform assemblies of particles is put alongside with known analytical results of organized packings and they are found to be demanding in terms of particles per wavelength but not enough to hinder the continuation of the work. A number of modelling details such as the transition from static to dynamic calculation modes, static and dynamic load conditions and absorbing boundary conditions are implemented. This shows that particle methods are no more a promising tool in rock mechanics but already a certainty, and a very adequate one for dynamic analyses.

The final part of the study, which is supported by the two previous steps, is the simulation of stress wave interaction with rock fractures. Compressive waves with wide frequency content are sent into compressed fractures and the resultant reflected and transmitted waves are captured and compared with the theoretical solutions. The first success to mention is that the physical phenomenon is consistently reproduced. Both transmitted and reflected waves are captured with good quality, energy conservation is verified, and dynamic fracture stiffness values calculated

from the Displacement Discontinuity Theory for both waves are in agreement. Moreover, when dynamic and static joint stiffness are compared, the former shows to be higher, as in laboratory studies.

The joint geometric representation is still limited by model size constraints. The major immediate task ahead is the implementation of more realistic joint geometries and contact models that simulate with more accuracy the mechanics of asperity deformation. Also, joint filling or weathering are sometimes encountered in nature and they alter the joint behaviour. Strategies to simulate their effect can be devised.

All tests should be also carried out with shear waves in order to try to calculate the dynamic shear joint stiffness as well as the rock dynamic shear and bulk moduli. Other waveforms can also be used and the consistency of the results checked. The study of waves oblique to the fracture will demand larger models and more sophisticated methods for wave extraction and separation but will also allow for the complete verification of the Displacement Discontinuity Theory.

Mixed static compression and shear loading are the general condition of joints in nature, and higher degrees of joint degradation may result, which affects their static and dynamic properties. The BPM should be able to simulate this.

Finally, the expansion to three dimensions will also allow for greater realism not only on the joint surface representation but also of the waves, which can then be polarized in relation to the joint.

Chapter 5

Stress Wave Propagation Test at the Bemposta Hydroelectric Complex

5.1 Introduction

Good quality hard rock masses can be good conductors of vibrations in particular at greater depths where fractures are tightly closed. When vibrations are generated in rock and other structures are also built or excavated in the same rock mass great care must be taken as vibration levels can be considerably high.

A situation that involved blasting near delicate equipment housed in a cavern in rock presented itself during the development of this thesis. It consisted on the excavation of a hydraulic circuit by drill and blast near a powerhouse that hosts three hydraulic turbines. These turbines are in continuous operation and therefore are subject to rather strict vibration limits. The maximum allowed charge per delay had to be determined for each phase of the excavation, as this influenced the whole planing schedule of the circuit excavation works. For this, a detailed knowledge of the way vibrations propagate in this underground complex had to be gained.

The tools available to address this kind of situation were discussed in general terms in chapter 3. The owner of the dam requested that low intensity test blasts be performed in order to define a Peak Particle Velocity (PPV) attenuation law for the site. This "traditional" approach does have some shortcomings as it cannot take in account: (i) geological accidents in the path of the waves, namely contact zones, faults and dykes, schistosity and fracturing; (ii) geometrical effects such as the "shadow" effect of excavations; (iii) the reflection at the ground surface and (iv) the effect of transition of vibrations from the rock to the structure that

supports the turbines.

Realistic numerical models supported by good site characterization or calibrated against *in situ* blast tests can deliver useful insights, or even approximated quantitative results. With this in mind, the goal of this chapter is to develop a greater understanding of the wave propagation throughout a field test and then to improve and develop the available means of modelling, thus contributing to bring dynamic modelling of rock blast vibration into everyday practice.

This chapter's structure is the following. Firstly, the site, existing structures and planned constructions are presented. Then the vibration blasts, measurement equipment, recorded data and signal treatment are described. The results are interpreted, opening the way to the next section, where numerical models are employed to reproduce some aspects of the test. In this last section of the chapter the emphasis is on the development of methodologies that improve on the more traditional methods while remaining relatively accessible to use.

5.2 Bemposta dam and underground hydroelectric scheme

The international stretch of the River Douro runs North-South and defines the border between Portugal (West–right bank) and Spain (East–left bank) in the Portuguese north-eastern region of Trás-os-Montes. This stretch of the river is, under the 1927 Luso-Spanish Agreement, jointly managed. The agreement attributed to Portugal the construction, management and exploration of three dams: Miranda, Picote and Bemposta (from North, upstream to South, downstream). They constitute the Douro International Hydroelectric Complex which is owned by the utility company Energias de Portugal.

Bemposta dam, located in the Bragança district (figure 5.1) was designed in 1957. It was finished in 1964. It is a 87 m high concrete arch-gravity dam, with an underground circuit and a powerhouse cavern on the right bank (the Portuguese side of the river) housing three 70 MW turbines. Auxiliary adits excavated in the rock to gain access to the powerhouse cavern and to the hydraulic circuit have not been used since. The powerhouse cavern is today reached through an elevator and stairs shaft from the command building.

An upgrade programme of all three dams in the Douro International Complex is under way, Bemposta dam being the last to suffer intervention. The upgrade involves the excavation of a new 420 m long hydraulic circuit with 12 m of diameter and a new powerhouse that will host a 190 MW turbine on the right bank. The hydraulic circuit will start just upstream of the existing intake and will go deeper in the foundation than the existing circuit, which will be in operation during the construction. The single turbine powerhouse will be placed in an 80 m deep shaft with a diameter of 22 m. It will be located near the outlet, which will return the water to the river approximately 150 m downstream from the end of the old circuit (figure 5.2).



Figure 5.1: Satellite image of Portugal with the Douro River and the Bemposta dam location (left) and close up image of the area (right). Adapted from http://www.earth.google.com.

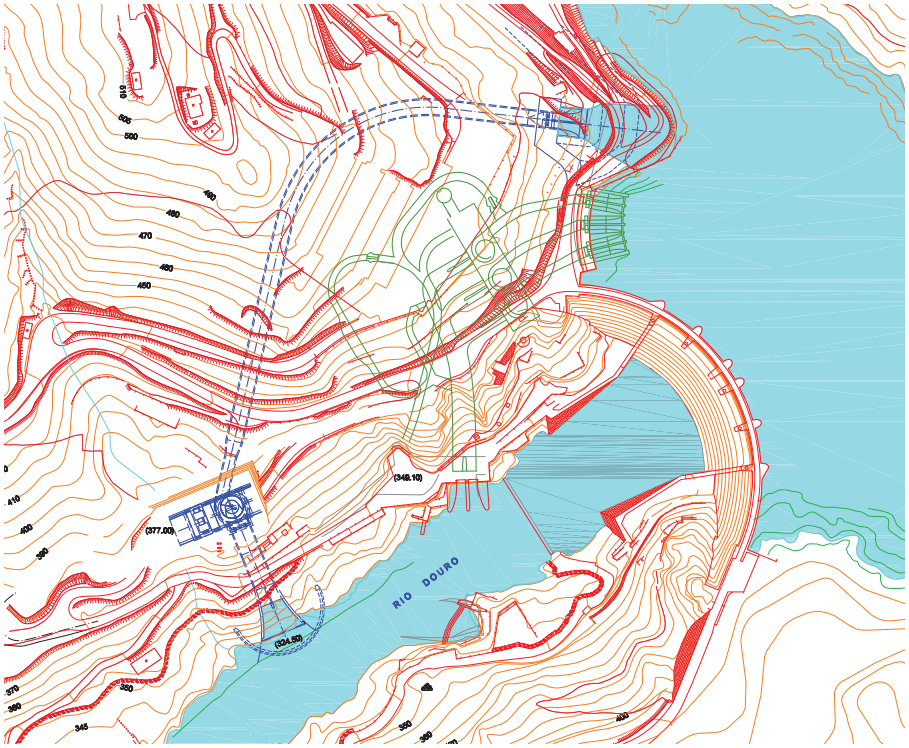


Figure 5.2: Map of the dam site, existing (in green) and planned (in blue) underground excavations at the time of the test (2006). Adapted from EDP (2007).

Presently, the excavation of the new powerhouse and circuit is under way, and it is due to start operation in 2011. Figure 5.3 shows views of the site.

5.2.1 Site characterization

When the dam and original underground cavern and circuit were designed, 50 years ago, a regional geological characterization followed by a thorough geological survey was done. It included geophysical prospection, excavation of adits, trenches and boreholes and mechanical testing on samples from the rock cores.

In 1966-1967 the upgrade which is now under way was first devised and some more studies were carried out. With the definitive decision to advance with the upgrade, in 2005, more investigation took place. Geological recognition at the surface and in the existing tunnels was done. Joint mapping was conducted at the surface and in the adits' walls.

Boreholes were drilled from surface where the powerhouse shaft will be excavated and from the existing adits to investigate the location where the hydraulic circuit will be set. Rock cores samples from both locations were tested for uniaxial and triaxial strength, deformability, tensile strength and sound-velocity.

In the place of the new powerhouse, borehole dilatometer tests to estimate the deformability of the rock mass were performed and strength envelopes of the joints from those boreholes' rock cores were determined through direct shear laboratory tests.

In the adits of the old complex, the *in situ* stress state of the rock mass was investigated using two different techniques: overcoring tests with LNEC's stress tensor tube and small flat jack tests.

From a geomorphological point of view, the dam site is set on a plateau with an elevation of 700 to 800 m. The Douro river has cut itself a valley in this plateau, leaving the bed at an elevation of around 330 m. At the dam location, the valley runs from NE to SW and is asymmetric, with a more abrupt right bank. The river bed is flat with visible rocky formations, as can be seen in figure 5.3.

The regional geological map indicates that the rock mass consists of gneissic granites and migmatites with pegmatitic intrusions. Figure 5.4 presents the surface geological characterization of the right bank. In the central part of the map the rock mass consists of migmatites/micaschists. The top and bottom are occupied by gneissic granites with migmatite and pegmatite intercalations. The dam, the old powerhouse and hydraulic circuit are set on the migmatite area, as well as the intake and most part of the new hydraulic circuit. The new powerhouse and the final part of the new hydraulic circuit, including the outlet will be excavated in the granitic zone.



Figure 5.3: Views of the dam and the valley. Taken from EDP (2007).

Figure 5.5 shows photographs of the gneissic granite and of the heterogeneous migmatite taken at the surface. In some small zones, located mainly along creek beds, there are loose deposit soils some metres thick with occasional boulders.

There are two active regional faults: the Variça fault and the Moncorvo fault, none of which intercepts the dam site. The former runs some tens of kilometres West of the dam, while the latter, less important, runs about 4 km NE.

The river runs from NE to SW at the dam site. Due to the slope steepness, most deposits are shallow. At surface, the rock mass is generally severely weathered and meteorized and fractures are open, but closer to the river, weathering gets less severe. With depth, rock quality improves and fracture spacing increases, the exceptions being in the vicinity of faults and dykes where, even at greater depths, water penetrates deeper and rock degradation is pronounced.

Schistosity in the migmatites is well defined, presenting a WNW-ESE strike and SW dip. Surveys at the surface and in the auxiliary adits of the old powerhouse showed the jointing pattern to be uniform across the volume of interest. Two major discontinuity sets, J1 and J2, were identified. The first one is approximately parallel to the schistosity and to the alignment of the minerals in the granites. Detailed results of the joint survey conducted in the adits where the blast test was performed are presented in figure 5.6 and in table 5.1.

Table 5.1: Statistical parameters and characterization of the discontinuity sets surveyed in the test site. Adapted from EDP (2007).

Set	Attitude	Importance [m]	Spacing [m]	Opening [mm]	Water	Filling
J1	N64°W, 89°NE	38%	0.06-0.2	< 0.1	Dry to humid, some dripping	Argilaceous film; silty/sandy material; iron oxides
J2	N22°E, 89°ESE	43%	0.2-0.6 and 0.06-0.2	1-5		
Other	-	19%	-	-	-	-

Attitudes of the faults identified on the right bank are presented in figure 5.7 and summarized in table 5.2. Although faulting has higher statistical dispersion, there is a correspondence between the fault orientation and the two most important joint sets. Faults are filled with crushed and fractured rock and clay in variable proportions, generally their thickness diminishes with depth and varies from 0.5 to 0.05 m. Fault set 4, though proportionally less important in the whole site, has been observed mainly in the adits. It is approximately 0.1 m thick, clay-filled

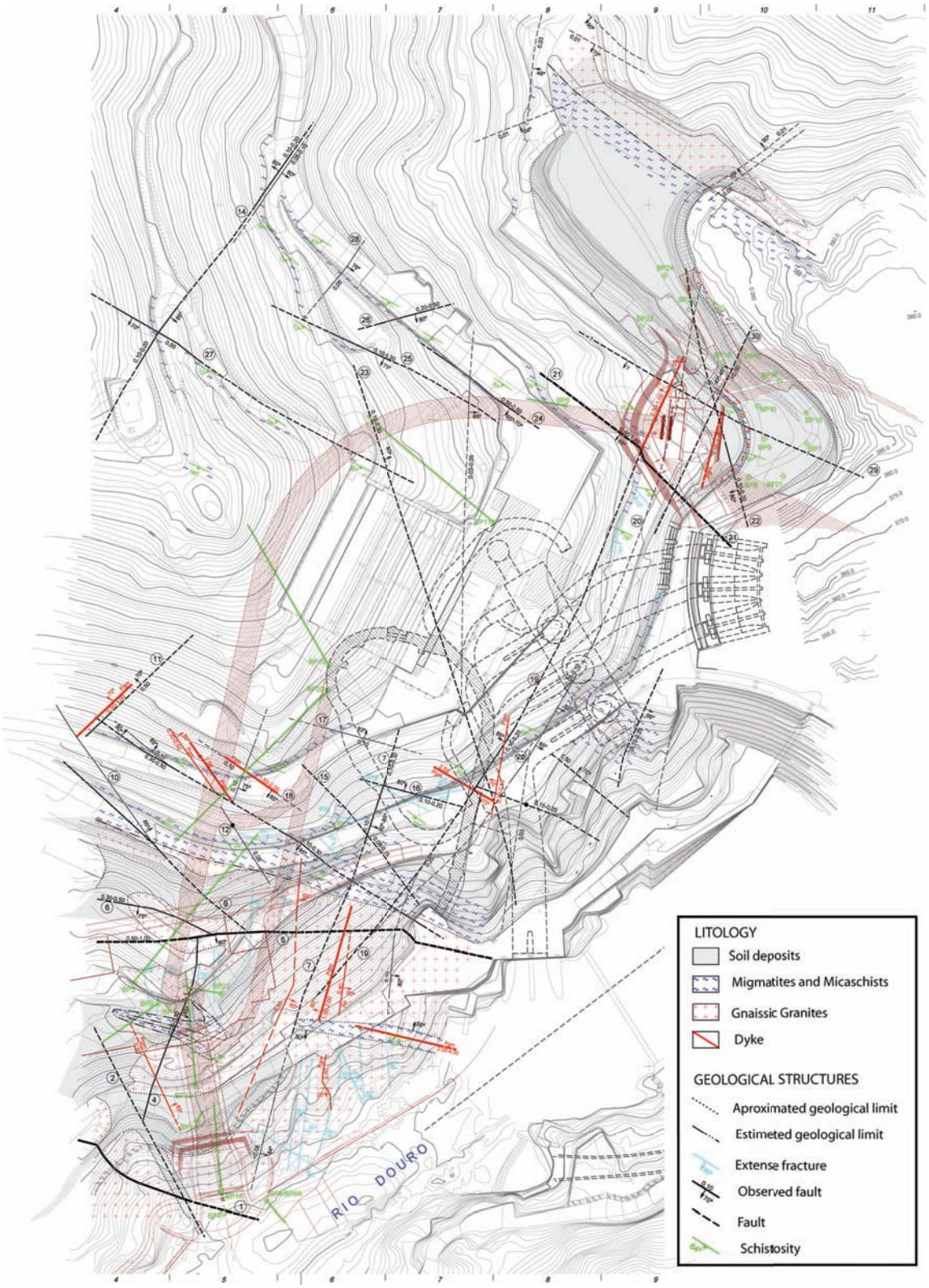


Figure 5.4: Surface geotechnical characterization map. Taken from EDP (2007)).



Figure 5.5: Gneissic granite (left) and heterogeneous migmatite (right) photographed at the surface. Taken from EDP (2007).

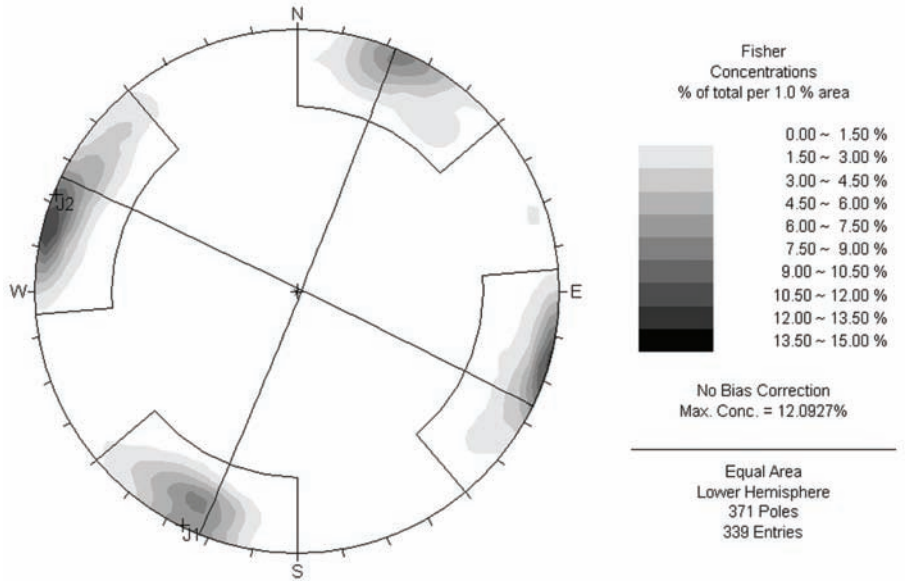


Figure 5.6: Test site discontinuity survey presented in a lower hemispherical projection. Taken from EDP (2007).

and displays low-undulating walls. Most dykes are several metres thick pegmatite intrusions. Quartz dykes and pegmatite masses were also found.

5.2.2 Geotechnical characterization of the test adits

The vibration tests were performed in the adits excavated for the construction of the first powerhouse. These excavations have been abandoned since. Due to their proximity to the new circuit and to the fact that part of them will be reused to gain access to the new circuit, they were thoroughly studied. Figure 5.8 shows their geotechnical characterization.

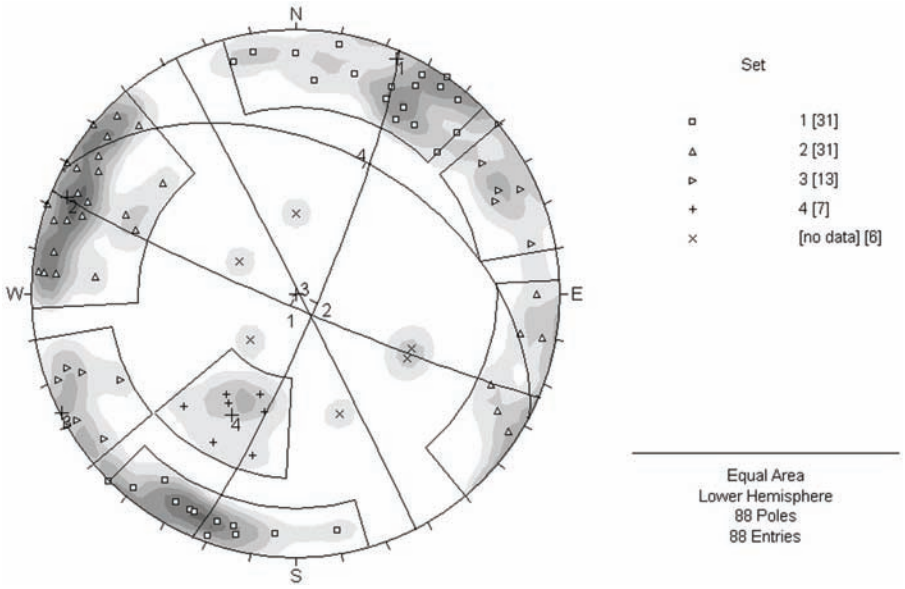


Figure 5.7: Right bank fault survey presented in a lower hemispherical projection. Adapted from EDP (2007).

Table 5.2: Statistical parameters and characterization of the faulting in the right bank. Adapted from EDP (2007).

Set	Average attitude	Importance
1	N67°W, 86°SW	35%
2	N23°E, 83°ESE	35%
3	N27°W, 89°NE	15%
4	N62°W, 43°NE	8.0%
Others	-	7%

The two main discontinuity sets are sub-vertical and perpendicular to each other. Fracturing ranges from F1 to F3, with some small F4 zones, possibly due to careless blasting (the excavation was performed around 1960). Migmatites and pegmatites coexist in the whole area and weathering was classified predominantly as W2 and W3 (fracturing and weathering classifications follow the ISRM Suggested Method ISRM (1978)).

From the logs of boreholes drilled from the adits to prepare the project of the new intake tunnel a geomechanical zoning of the blast test area was done. Except for the surroundings of expressive faults, the surrounding rock is of good quality, with a RMR greater than 60 and a RQD above 90.

The *in situ* stress state was investigated by the Stress Tensor Tube and the Small Flat Jacks techniques (LNEC, 2008). The stress state in the right bank is represented in figure 5.9. This representation shows that the horizontal stress state in the direction perpendicular to the river is very strong. Numerical studies performed to confirm the site measurements showed that this

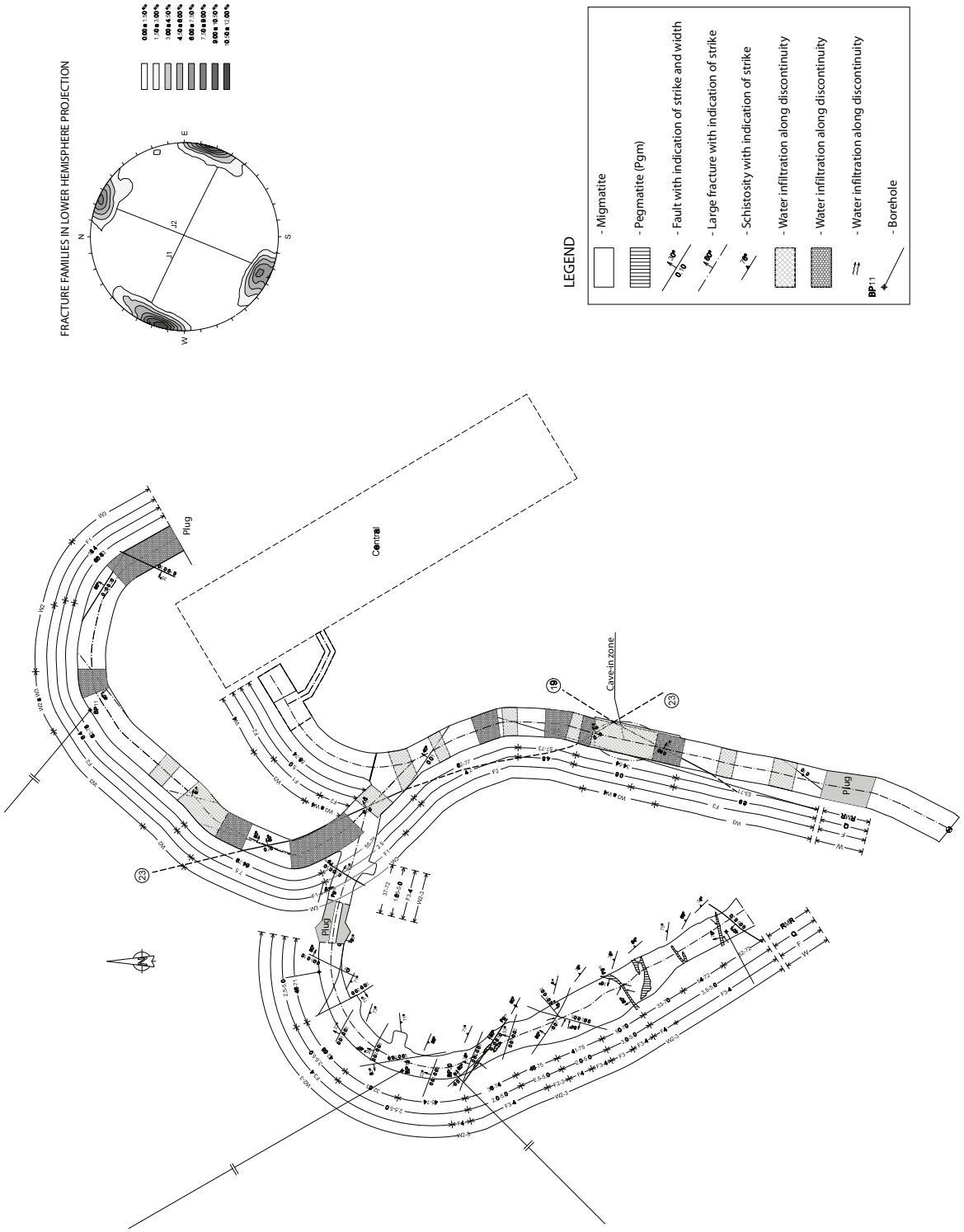


Figure 5.8: Geotechnical and geomechanical survey of the test adits. Adapted from EDP (2007).

stress state results from the orogenic process of excavation of the valley in a rock mass that had prior strong regional horizontal stresses. Later in this chapter the influence of this particular stress state in the rock mass properties and conductivity will be discussed.

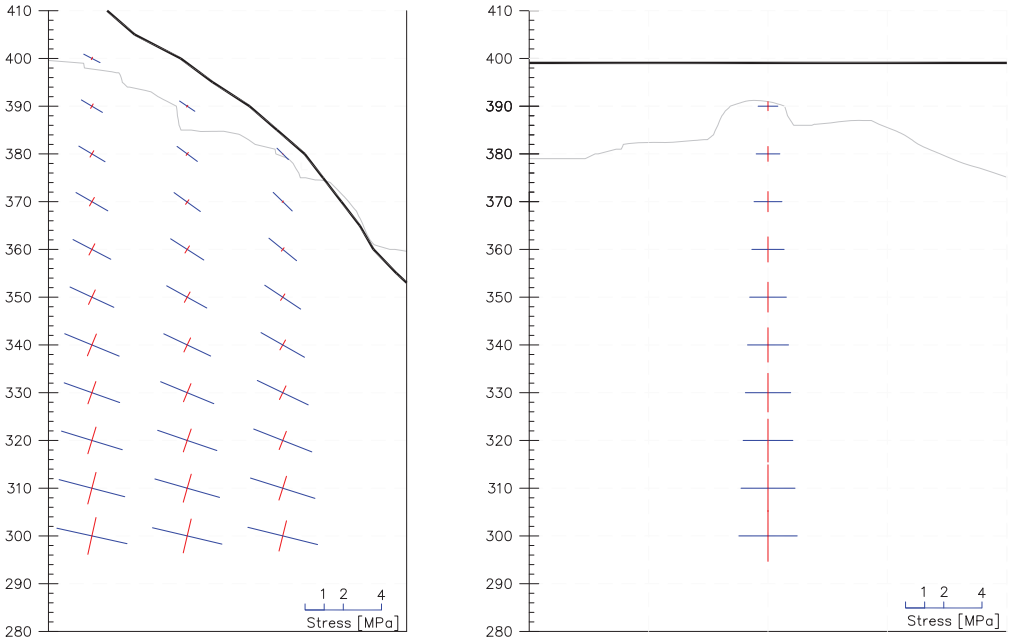


Figure 5.9: Stress state in the area of the underground complex. On the left, a section normal to the river; on the right, a section parallel to the river in the plane of the central stress alignment of the left side. Adapted from LNEC (2008).

Static and dynamic Young's modulus and Poisson's ratio, as well as static uniaxial and triaxial compression and Brazilian tensile strength parameters were determined in samples taken from the borehole cores. Average results for the granite, pegmatite and migmatite samples are presented in table 5.3. In the later case cores were tested in the directions parallel and perpendicularly to the schistotity so results for both situations are presented. Granite samples were taken from outside the test area at the zone of powerhouse, so their utility is limited.

5.3 Vibration propagation test

As stated in the beginning of this chapter, the purpose of the test was to assess the effect of the construction blasting on the existing underground structures and in the turbines and associated control equipment housed in the powerhouse cavern.

The test was performed in 18, 19 and 20 December 2006 and consisted on the measurement of the vibration caused by 21 low-intensity blasts in holes drilled on the walls of the auxiliary

Table 5.3: Mechanical properties of the tested rock cores. Taken from LNEC (2008).

	E	ν	σ_c	σ_t	c_p	c_s
	GPa	[-]	[MPa]	[MPa]	[m/s]	[m/s]
Pegmatite	46	0.2	89	7.8	4900	3000
Migmatite*	19/55	0.2	20/90	5.1/6.8	4500	2750
Granite	41	0.19	67	5.9	4900	3100

* Normal/parallel to schistosity.

adits. Each charge was installed in a borehole with a diameter of 25 m, with variable depth, and was detonated by electric caps with zero delay. In one of the blasts, charges in three neighbour holes were detonated simultaneously. Three different types of vibration measurement equipment were used, as the blast results were studied with different degrees of detail. In the simplest analysis, performed right after the blasts, peak particle velocities were used to calibrate a peak velocity attenuation law (LNEC, 2007). These peak values were obtained directly from a measurement system comprised of two triaxial geophones. But the blasts were also recorded by two additional systems: three independent seismometers that were installed on key points that needed be protected and an array of 18 accelerometers linked to a data acquisition system. The records from this last system were thoroughly analysed and used in the subsequent analyses.

5.3.1 Description of the test site

The valley, dam, original underground complex and the projected upgrade were depicted in figure 5.2. Figure 5.10 displays in greater detail the original complex, omitting the upgrade circuit and power plant that did not exist at the time of the test.

Figure 5.11 shows the outcome of a geometrical and topographic survey of the test zone. Sections' width ranges from 5 to 6 m, with the exception of the places where it is enlarged and where a cave in occurred, as described ahead. The height ranges from 4 to 5 m. They were excavated by drill and blast, in the beginning of last century's sixth decade. There is no wall, roof or floor lining but, where blocks detachment was possible, rock bolts were installed in the roof and walls. Most rock bolts are heavily deteriorated by rust.

At the time of the test, access to the underground complex (powerhouse cavern and accessory adits) was possible by the elevator shaft. One of the adits ends at the surface, not far from the outlet, but passage has been blocked by a concrete plug. To facilitate visualisation of the complex, perspectives of a three-dimensional drawing of the complex are represented in figure 5.12. In this drawing, the intake and outlet hydraulic tunnels that enter and leave the main cavern (shown in figure 5.10) at its lower level are not represented, as they are not in the path

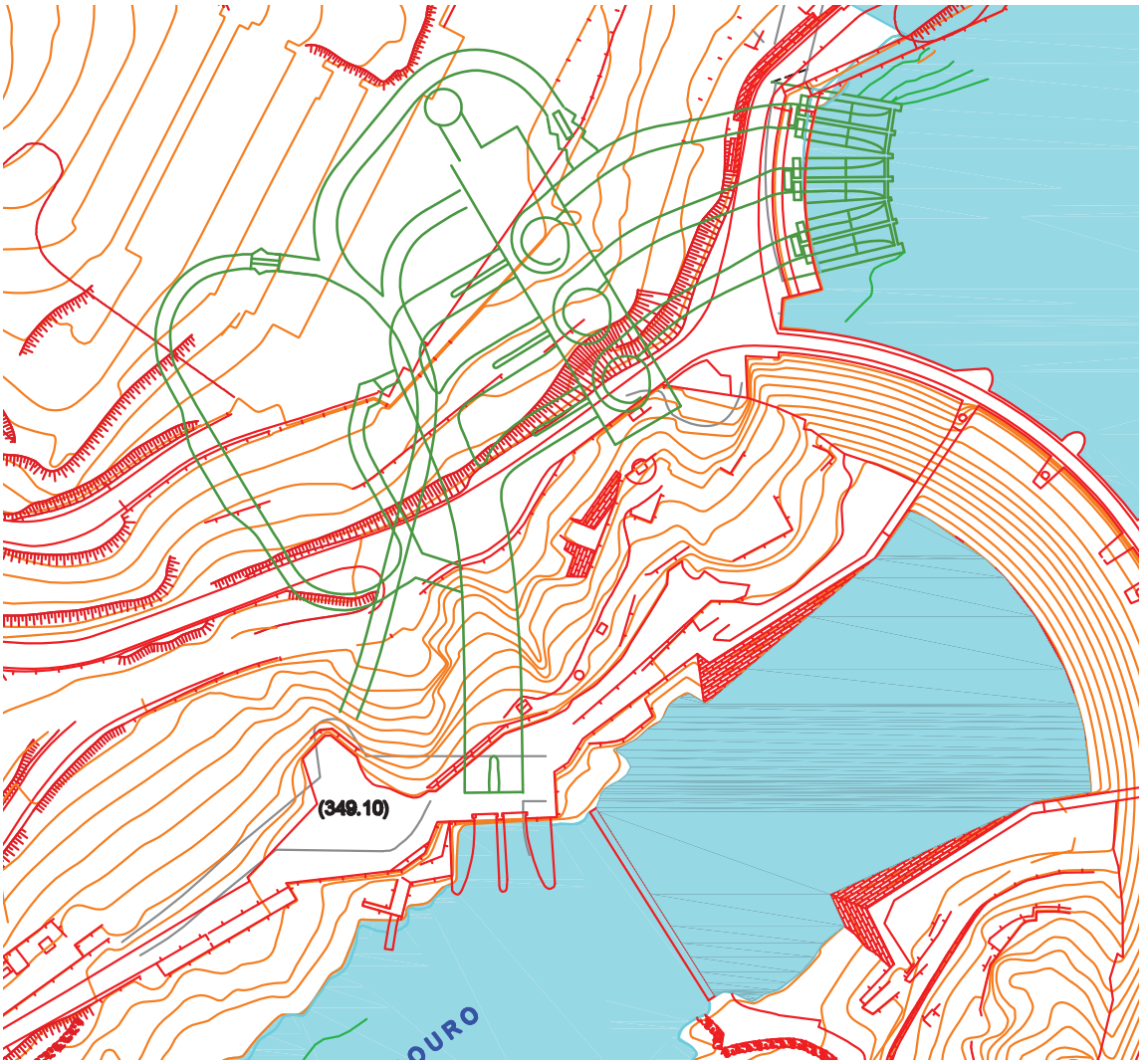


Figure 5.10: Map of the surface, hydraulic circuit, powerhouse and auxiliary adits. Underground complex is represented in dark green. Adapted from EDP (2007).

of propagation of the stress waves of the test and their geometry is rather complex. In the next paragraphs, each of the auxiliary adits is described and a name is attributed for ease of analysis.

The Access adit is short, starting at the powerhouse cavern at section PF4 (level 342 m and overburden of approximately 100 m) and ending at section PF10, at the union of the three main adits. It runs practically horizontal for about 33 m with a width slightly smaller than the rest of the adits. Access to the cavern is done through a short passage with a smaller cross-section (PF1-PF3) which is not represented in the 3D models because it has been sealed in section PF4. The small passage and the initial part of the Access adit floor's have a thin concrete covering, represented in blue in figure 5.11.

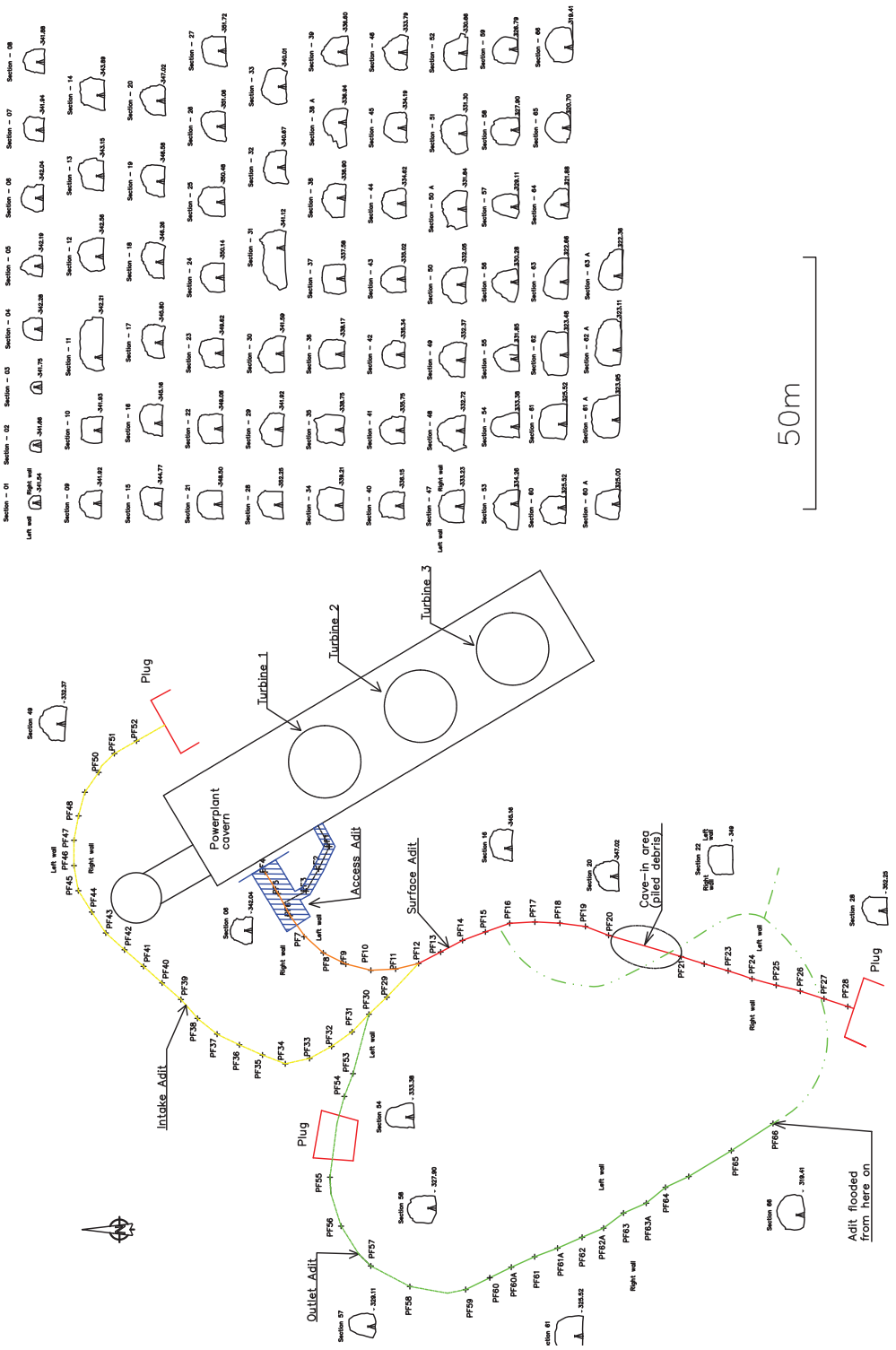


Figure 5.11: Test adits topographic survey and adits names. Adapted from EDP (2007)).

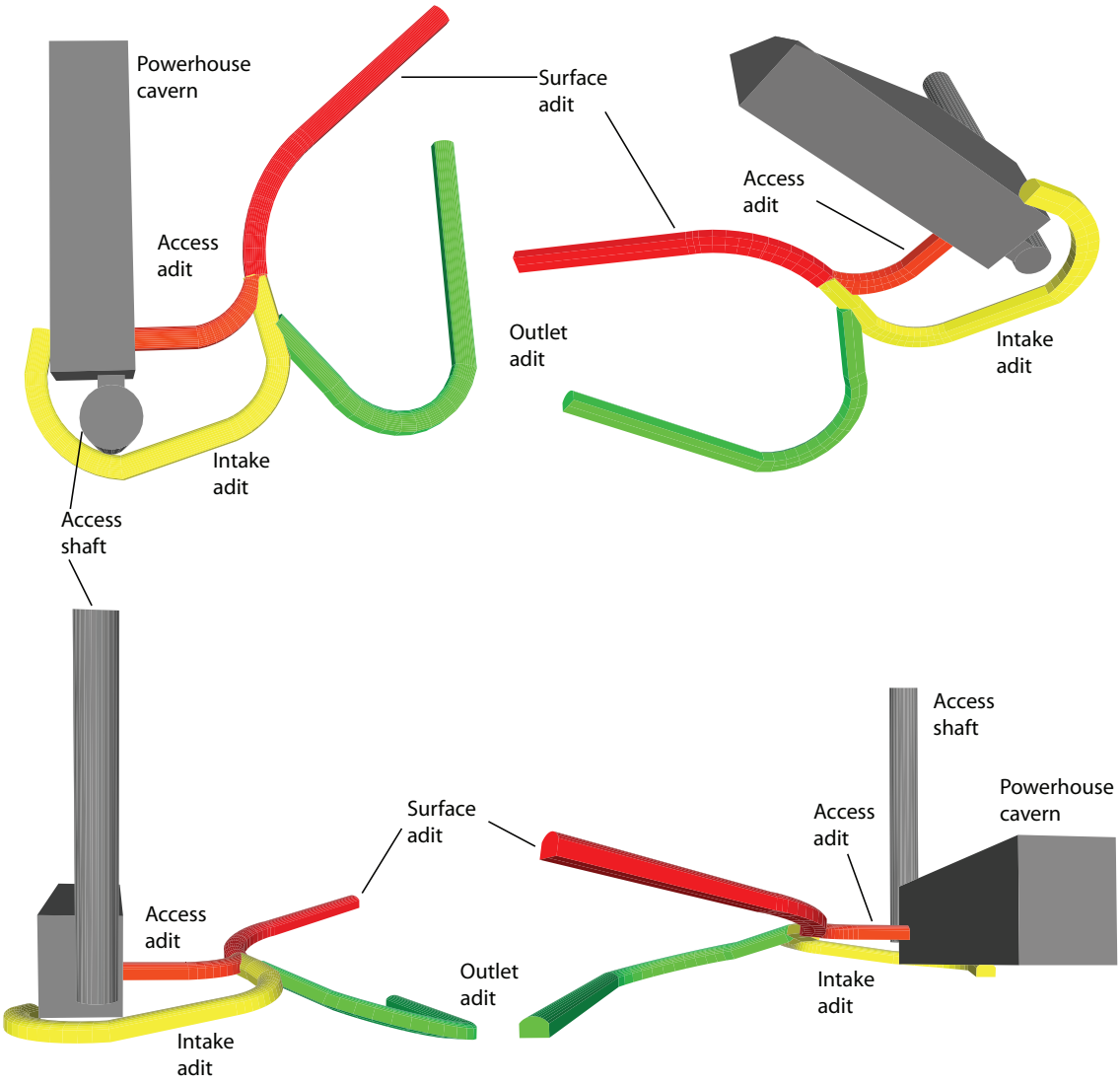


Figure 5.12: Three-dimensional representation of the underground complex (hydraulic intake and outlet tunnels are not represented).

The Surface adit starts at the union of the three main adits at section PF12 (level 342 m and overburden of approximately 105 m) and runs for 90 m, ending at a sealed concrete plug near the surface (section PF28 at level 352 m and overburden of around 25 m). With a width of about 6 m, it has an upward constant slope of 10.5%. This adit was used as access to the complex for its construction. A part of the roof and the left wall between sections PF20 and PF21 caved in due to insuficient support in this area, where the schistosity and the jointing of the rock favoured the formation of small blocks.

The Intake adit starts at the junction with the Surface adit on section PF12 and goes down for 129 m with a 9.5% slope, until it ends on a sealed concrete plug that intercepts the intake

circuit at section PF52 (level 331 m and 110 m overburden).

The Outlet adit starts at the junction with the previous adits (section PF30 at level 342 m and 105 m overburden), crosses an open concrete plug and then goes down with a constant slope of 11.25%. It curves to the left and reaches the outlet circuit, where it ends on a sealed concrete plug in. In this adit there is an enlarged section (sections PF60 to PF64) that allowed the transit of two trucks, during the construction of the complex. Up to the time of the test, the Outlet adit was filled with water up to the level of the open concrete plug (level 332 m and 80 m overburden). This indicates the undisturbed water level during the winter. The water was pumped about 2 weeks before the test and the level was kept at the level of the floor of section PF66 (level 319 m and 90 m overburden) during the test. It is not known the extent of the rock volume affected by this lowering of the water level, so it cannot be assumed that the rock mass is dry or wet away from the adits. The geological mapping of the adits, presented in figure 5.8 indicates that they are set in a migmatite zone with some pegmatite intercalations.

The powerhouse is brick-shaped, with approximately 19 by 76 m and a total height of 25 m divided in three levels. The elevator and stair shaft has an exterior diameter of 9 m. Both the cavern and shaft are lined with cast reinforced concrete which is 0.5 m thick in the shaft and 1 m thick in the cavern. The shaft is connected to the powerhouse through two adits: one at the main level, and the cable adit. This adit carries cables from the powerhouse to the shaft and is located one level below the main level of the powerhouse.

5.3.2 Blast description

The blasts took place in the Outlet (12 blasts) and Intake adits (9 blasts). The employed explosive was Gelamonite. Explosive charges were low, always smaller than 0.5 kg, with minimal rock fragmentation and associated blast energy consumption. The boreholes were all drilled perpendicular to the wall, at a height of approximately 1.5 m. Boreholes, with 25 mm diameter and length between 0.8 and 3 m were drilled in places where the rock was sound, avoiding faults, dykes and loose zones. The explosives were cased in plastic tube to facilitate the loading of the holes. Holes were carefully stemmed with wet sand to minimise ejection (figure 5.13).

Figure 5.14 shows the location of the blasts and of the vibration measurement points, while table 5.4 provides detailed characterization of each blast.

5.3.3 Vibration measurement system

The vibrations were measured by three independent systems but only one is used for this analysis. The other two were employed for quick on the spot measurements necessary to guarantee vibration levels were safe for the powerhouse equipment.



Figure 5.13: Explosive ready to be loaded (left), stemming of loaded borehole (right) (LNEC, 2007).

Table 5.4: Blast characteristics.

Blast	**Adit**	**Section***	**Wall***	**Hole depth [m]**	**Explosive [kg]**
1	Outlet	59-60	Left	1.0	0.0368
2	Outlet	59-60	Left	1.0	0.036
3	Intake	37-38	Right	0.8	0.0566
4	Intake	36-37	Right	0.8	0.0645
5	Intake	35-36	Right	0.8	0.057
6	Intake	34-35	Right	0.8	0.0723
7	Outlet	60A-61	Left	1.5	0.1126
8	Outlet	60-60A	Left	1.5	0.0951
9	Outlet	60-61	Left	1.5	0.1006
10	Outlet	59-60	Left	1.5	0.0764
11	Outlet	65-66	Left	2.0	0.1835
12	Outlet	65-66	Left	6.0	0.496
13	Outlet	64-65	Left	3.0	0.2468
14	Outlet	64-65	Right	3.0	0.2796
15	Outlet	63A-64	Left	1.5	0.1936
16	Outlet	59-60	Left	1.0	0.1261
17	Intake	44-45	Left	2.0	0.1133
18	Intake	40-41	Left	1.0	0.1059
19	Intake	36-37	Right	1.5	0.0704
20	Intake	34-35	Right	1.5	0.1194
21	Intake	34-35	Left	2.0	0.1656

* See figures 5.11 and 5.14.

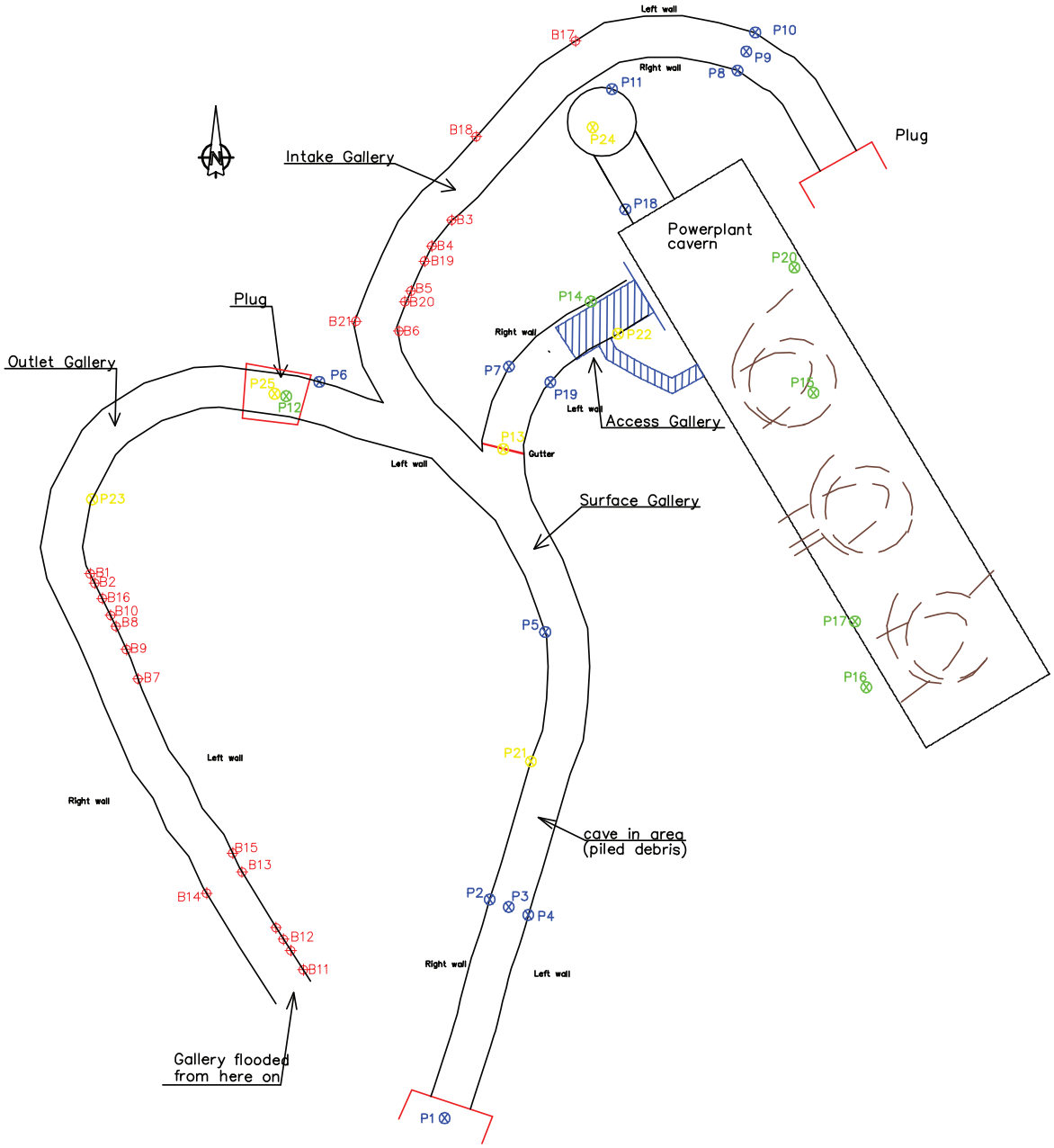


Figure 5.14: Blasts (red) and monitoring devices location (cyan represents the triaxial accelerometer, green the GSR seismometer and yellow the geophone bases).

The main measurement system is composed of an array of 18 accelerometers assembled on six triaxial bases that were installed in the walls and floor of the adits, the powerhouse cavern and elevator shaft. The accelerometers are from PCB Piezotronics, model 393A03. They have a range of ±5 g (g being the acceleration of gravity), a dynamic frequency range of 0.5 to 2000 Hz and a sensitivity of 1000 mV/g.

The second system consisted of three seismometers, models GSR-16 from Geosig that record accelerations in three directions. They have an acceleration range of ±2 g, a dynamic frequency range of 0-1000 Hz and sampling ratio that can be set between 50 and 500 Hz. As the GSR-16 can be self-powered and has an internal memory that records vibration time-histories, they are able to work as stand-alone units and were installed in locations that could not be reached by the accelerometers, like the support of one of the turbines, the top of the powerhouse cavern and the drainage adit of the powerhouse. Figure 5.15 shows one seismometer connected to a laptop that retrieves the recorded data and configures the GSR trigger parameters, record's length, etc.

The third system was employed to quickly give an estimate of the peak particle velocities in some key locations during the test, and was constituted by two geophones connected to an acquisition and signal treatment central that immediately gives the peak particle velocity in three directions in each of the geophones. The system is a 6-channel "S-6 Peak Vibration Monitor" made by Slope Indicator Co. It has two triaxial geophones that work on the 4-200 Hz frequency range and displays, right after the blast, the frequency of the frequency peak.

The accelerometers were considered as the main source for reliable acceleration time-series for several reasons. Accelerometer records are synchronized between each other, have coherent installation methods and were all recorded with the same sampling frequency. The GSR seismometers recorded the vibrations with much lower sampling frequency and in most situations



Figure 5.15: GSR-16 seismometer connected to a laptop (left) and S-6 Peak Vibration Monitor seismometer and geophone (right).

the noise to signal ratio was considerable. They were also installed in rather different situations: rock floors covered by thin concrete layer (P14 and P20), on the reinforced concrete support of the girder crane (P17) near the ceiling of the powerhouse cavern, in the support of the first turbine, etc. Geophones, on the other hand, only provided peak velocity values and used much lower (up to 150 Hz) sampling ratios.

In each accelerometer base, the three accelerometers were tightly screwed to a solid copper cube that was glued and bolted with epoxy resin to the adits' rock wall or to the concrete lining. When the copper bases were applied directly to the rock mass a sound spot was chosen and the surface was evened with a hydraulic hammer to remove loose bits. The accelerometers' orientation was such that they formed a normal right-hand side oriented system (L→V→T): the longitudinal (L) accelerometer was always placed horizontally in the direction of the adit pointing to the confluence of the adits where the Data Acquisition Centre was installed (section PF10); the transversal (T) accelerometer was oriented horizontally pointing to the centre of the adit; the vertical (V) accelerometer oriented vertically upwards. In bases P1, P11 and P3 this rule cannot be unequivocally applied, so figure 5.16 shows the accelerometer orientation.

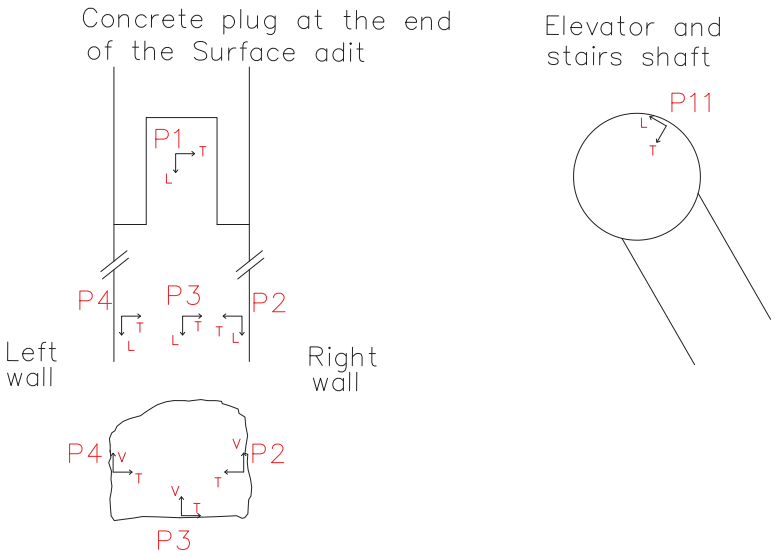


Figure 5.16: Detailed representation of accelerometer bases installation.

Figure 5.17 shows the data acquisition system installation and one accelerometer base. Images of the installation spots of the accelerometers and seismometers are in Appendix I. In each blast six triaxial bases recorded the vibrations. Accelerometers were connected through coaxial cables to a PCB Piezotronics signal conditioner model 481A01 and from there to a National Instruments SCXI-1531 data acquisition central. The software used to digitize and

record the data was LNEC's SPA v 1.0, a stand-alone application built over the National Instruments *Labview* environment (Mendes and Campos Costa, 2007).

It was not possible, due to time and budget limitations, to install accelerometers inside the rock mass, where the free-field response could be measured, away from adits or cavern's cavities' influence. When vibrations are measured at a free surface several undesirable effects can take place. First, the rock around the adits has weaker mechanical properties due to damage during construction. The extent of the excavation damaged zone (EDZ) was not measured but, due to the excavation method (blasting), it can be up to several tens of centimetres or more than one metre. In some locations the base was not directly applied in the rock but on a concrete cover or a concrete bench that was built onto the rock floor of the adit. The quality of the bond between the rock and concrete is not known and therefore some reflection and attenuation probably takes place at this interface. Finally, when a wave hits a free surface, it is reflected back at an angle equal to the incidence's and its amplitude doubles. This effect's relevance grows as the waves' dominant wavelengths become similar to the opening's size.

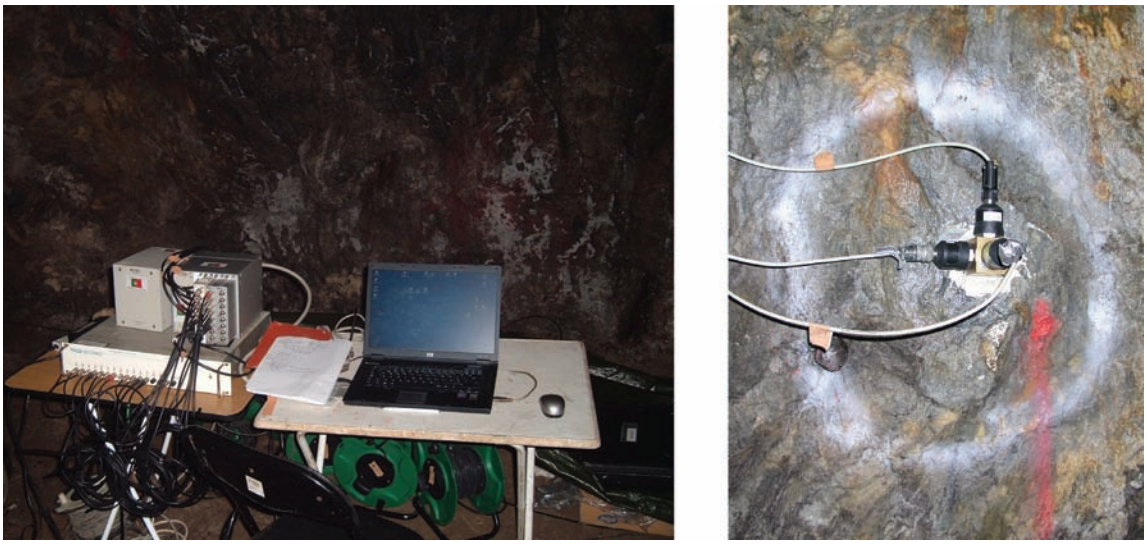


Figure 5.17: Data acquisition system (left), triaxial base installed in the wall of a adit (right).

Table 5.5: Location of vibration sensors.

Nome	Location	Sensor type	Support
P1	Concrete plug - Floor	Triaxial accel. base	Dry
P2	Section 22-23 - Right wall	Triaxial accel. base	Wet
P3	Section 22-23 - Floor	Triaxial accel. base	Wet
P4	Section 22-23 - Left wall	Triaxial accel. base	Wet
P5	Section 15-16 - Right wall	Triaxial accel. base	Dry
P6	Section 54-55 - Right wall	Triaxial accel. base	Wet
P7	Section 8-9 - Right wall	Triaxial accel. base	Dry
P8	Section 48-49 - Right wall	Triaxial accel. base	Dry
P9	Section 48-49 - Floor	Triaxial accel. base	Dry
P10	Section 48-49 - Left wall	Triaxial accel. base	Dry
P11	Elevator shaft - 5 m above cavern	Triaxial accel. base	Dry
P12	Section 54-55 - Concrete plug floor	GSR station	Dry
P13	Section 10-11 - Floor	Geophone	Dry
P14	Section 5-6 - Floor	GSR station	Dry
P15	Turbine 1 - 3 m below cavern floor	GSR station	Dry
P16	Not used	GSR station	Dry
P17	Cavern roof - Floor	GSR station	Dry
P18	Cable adit - Left wall	Triaxial accel. base	Dry
P19	Section 7-8 - Left wall	Triaxial accel. base	Dry
P20	Drainage adit - Floor	GSR station	Wet
P21	Section 20 - Floor	Geophone	Dry
P22	Section 5 - Floor	Geophone	Dry
P23	Section 58 - Left wall	Geophone	Dry
P24	Elevator shaft - 1.5 m above cavern	Geophone	Dry
P25	Section 54-55 - Concrete plug floor	Geophone	Dry

5.3.4 Digital signal processing

To obtain velocity records and peak particle velocities from the acceleration time-histories these had to be processed. The digital signal treatment consisted on the following steps (Bendat and Piersol, 1986):

1. The acceleration time series was converted from binary to ASCII format with 8 significant digits.
2. The absolute peak in each time series was identified and the series cropped leaving around 0.25 s before and after the blast vibration.
3. A band-pass filter was applied in the frequency domain of the acceleration erasing all frequencies below 100 Hz and above 1000 Hz.
4. A Tukey window with a tapper ratio of 0.25 was applied, cleaning the series before and after the waveform. This prevents signal leakage in the subsequent integration.
5. A Fast Fourier Transform (FFT) was applied to the acceleration series and the norm and phase of the FFT were calculated.
6. The acceleration series was integrated in the time domain using the trapezium rule.
7. A high-pass filter was again applied in the frequency domain of the velocities erasing all frequencies below 100 Hz.
8. A Fast Fourier Transform (FFT) was applied to the velocity series and the norm and the phase of the FFT was calculated.

The philosophy behind the digital treatment of the signal was to modify it the least possible, in order not to loose its characteristics. A comment on the frequencies chosen in the high-pass and low-pass filters is necessary. The high-pass filter at 100 Hz cuts all signal oscillations with a period below 0.01 s, which is approximately the duration of the shortest wavetrains in the shortest-distance direct blasts. This corresponds to a baseline correction in the blasts.

The low-pass filter is applied to clean erratic high frequency spikes that do not correspond to the blast vibration and stand in the way of the analysis. A sensibility analysis shows that the maximum velocities are not heavily altered by this digital signal treatment.

Once the "clean" acceleration and velocity series were obtained, further analysis of the results was possible, namely the calculation of the peak particle velocity (PPV) in the series. The PPV is the maximum of the absolute value of the norm of the velocity vector series and is obtained by the formula:

$$PPV = max\sqrt{v_x^2 + v_y^2 + v_t^2}, \tag{5.1}$$

where v_x, v_y and v_z are the components of the velocity vector in the longitudinal, transverse and vertical directions, respectively.

As a double integration of the signal amplifies the background noise to a degree that the signal quality is very low, the displacement is not calculated.

5.3.5 Baseline situation

Noise measurements were performed before each blast. Acceleration noise records are integrated (after high-pass filtering) and noise PPVs were determined. These values fall between 0.002 and 0.008 mm/s, a level that is below most, but not all, the blast record vibration levels.

In some blast records the signal-to-noise relation was too weak, due to large distances between the blast and the sensor. These records were not used in the subsequent analysis.

During the tests the only evident sources of vibration at the underground complex were the powerhouse's turbines. The test was performed at the end of December, which is in Portuguese's rainy season. Having a low capacity relative to the river flow, the dam's reservoir was nearly full and it was not possible to completely stop any of the three turbines. As an alternative, in blasts 7 to 10, the turbine nearer to the measurement system was taken off the grid. When this happens water flows through the turbine and it continues to spin but no electricity is produced and thus it produces less vibrations. However, when this happened, no significant decrease of vibration level was observed. Also, no visible trend is apparent when noise vibration levels are plotted against the distance to the powerhouse. This may mean that the baseline noise may have other sources than the turbines' mechanical vibration, possibly their strong electromagnetic field directly influencing the accelerometers.

5.4 Results of the vibration propagation test

Firstly, a global analysis of the results is presented and then, to better grasp the results of the test which produced a large amount of data, the blasts were separated in four sets. In each set, the blasts are located in a common area and the sensors' location is constant.

As referred before, the following analysis relies on the main measuring system. Only acceleration-time series recorded by the interlinked accelerometers system can be directly compared with one another, due to variations in the type of sensor, placement and type of fixation (accelerometers were bolted and glued to the walls), and, above all, sampling frequency.

Some time-series do not yield information on the blast. This happens for different reasons: very low signal-noise ratio, saturation of the sensor and, in a few cases, cutting of the cables during recording. Only valid time series could be used in subsequent analysis and therefore some of the blasts only have two or three valid PPV values. As this was expected, a large number of blasts was done.

A PPV *vs* scaled distance ($R/W^{1/3}$) of all the blasts, divided in sets, is presented in figure 5.18. The sets are presented in detail in the next sections.

The two first sets have more limited scaled distance ranges with higher $R/W^{1/3}$ values. This is due, not to particularly low charges, but to larger distances between blasts and sensors.

The PPV data cloud, represented in a log-log scale, has typical shape vibration plots: dispersion is high and proportional to the velocity values. Figure 5.19, showing the same data classified according to the blast-to-sensors path, explains some of the dispersion. In the records where there is a direct path between the blast and the sensor, the vibration is higher and shows less dispersion. In the cases where stress waves go around an obstacle to reach the sensor the vibration is generally smaller and the dispersion higher.

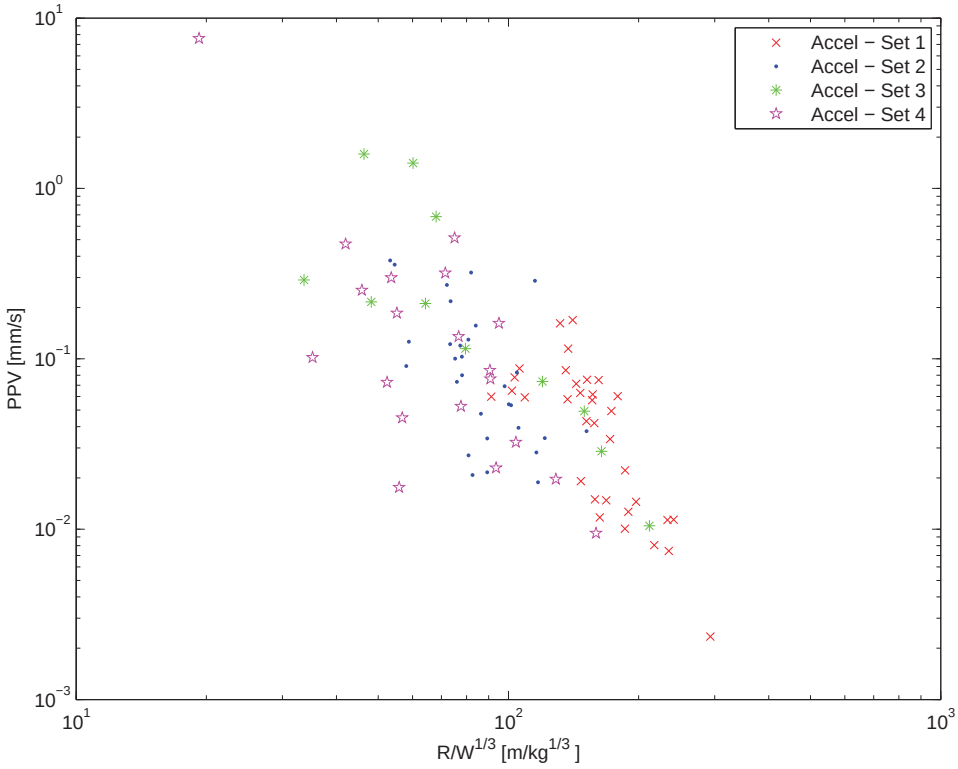


Figure 5.18: Plot of the four sets' peak particle velocity *vs* scaled distance.

5.4.1 Blast set 1

In this set, blasts were all in the upper part of the Outlet adit (blasts B1, B2, B7, B8, B9, B10 and B16). The charge weight varied from 0.036 to 0.126 kg.

The accelerometers were placed along the Surface adit (P1 to P5) and in the area where the

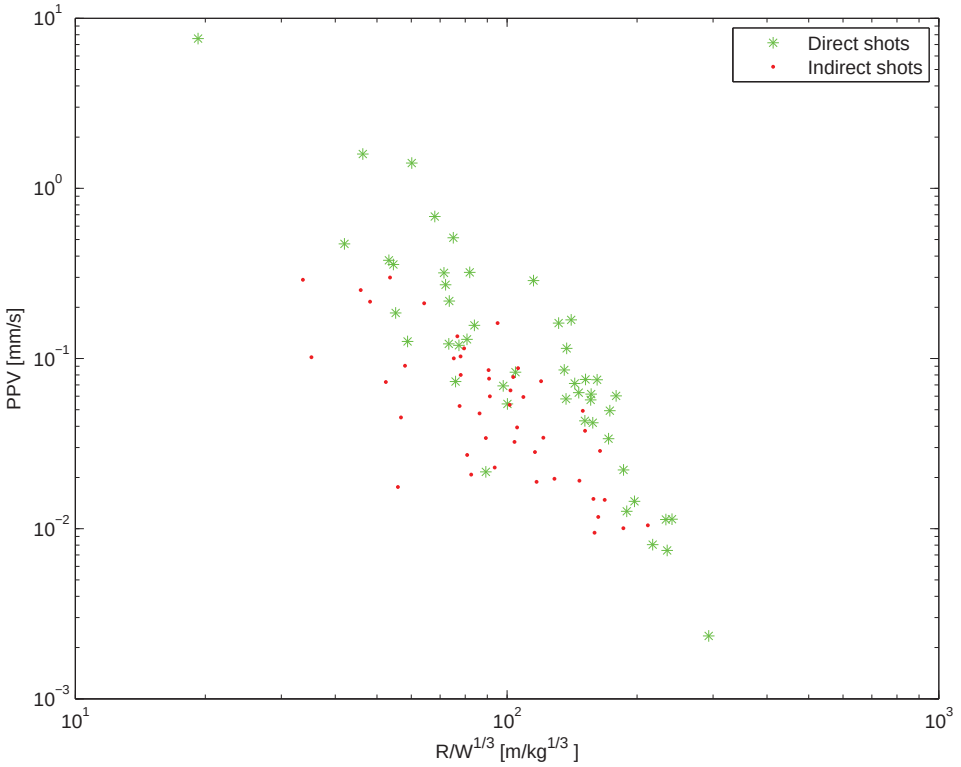


Figure 5.19: Plot of direct and indirect peak particle velocity *vs* scaled distance.

Intake and the Outlet adits meet (P6). Figure 5.20 illustrates the blasts and sensors location.

The first and second sets are the only ones where a adit section is instrumented on both walls and on the floor (accelerometer bases P2, P3 and P4). Also, on both sets, part of the accelerometer bases (P1 to P4) are located nearer to the surface where, in principle, fractures are less tightly stressed and the rock is more weathered. But, due to particular conditions of the stress state installed in the river bank's rock this effect is not significant and not perceptible in the results.

In this set peak velocity values are all under 0.2 mm/s. A PPV - scaled distance plot (figure 5.21) shows two different trends. Indirect shots, recorded in bases P4 (points with higher scaled distance) and P6 have lower PPVs than direct shots.

A PPV *vs* distance plot of blast 16, in figure 5.22 (other blasts' plots are in Appendix II), allows a more detailed discussion. Three measurement bases are located in the same cross-section: P2 on the wall closer to the blast, then P3 on the floor and P4 on the opposite wall. Peak velocity evolution here is not commanded by distance but by the wave path (see figure 5.20). P3, at the floor of the adit, yields a PPV higher than P2, while base P4 in the wall opposite to the blast, records a much lower value than both P2 and P3. Blasts B7, B8, B9 and B10 show this pattern too (in B1 and B2) only two bases recorded valid signals).

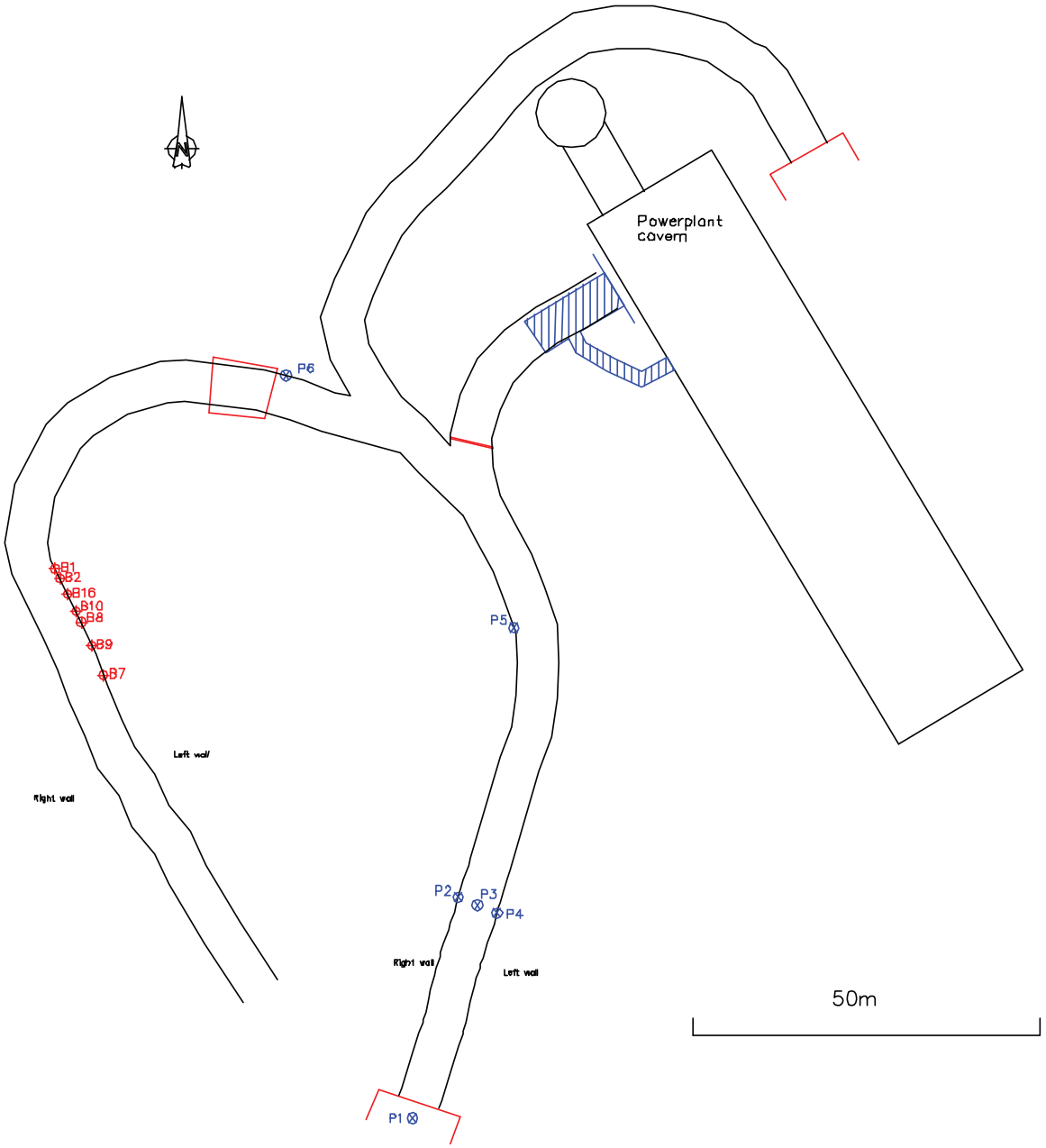


Figure 5.20: Location of blasts and measurement points of the first blast set.

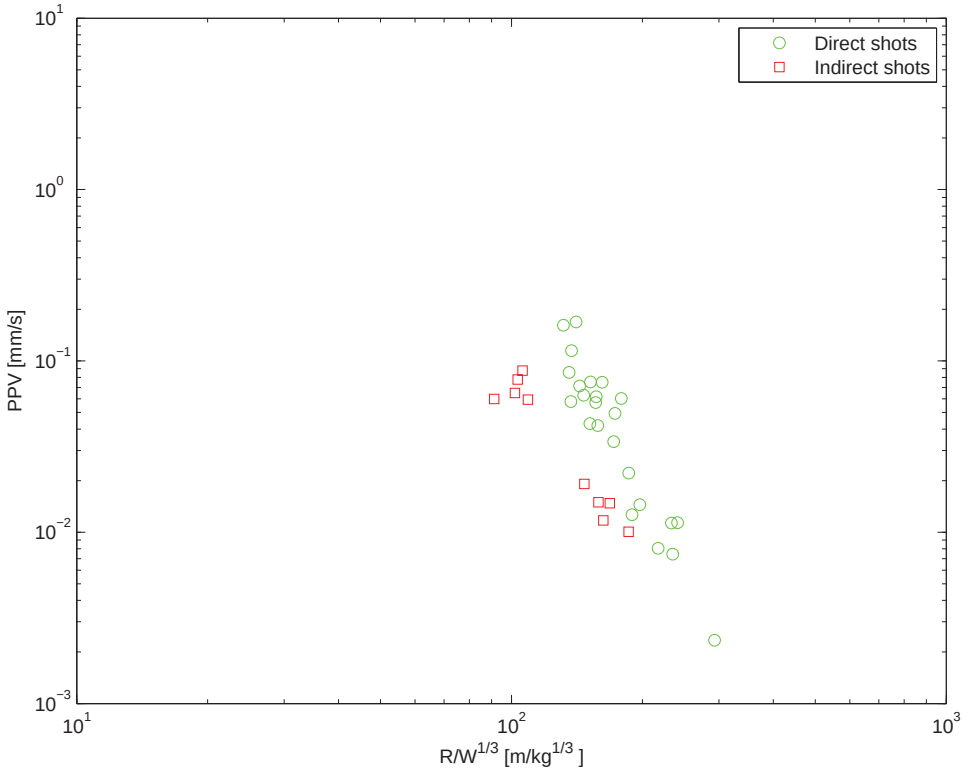


Figure 5.21: Plot of peak particle velocity *vs* scaled distance of the first blast set.

Also due to the indirect propagation path, vibration at P6 is one order of magnitude lower than the value that could be expected from the attenuation tendency observed between P5, P2-3 and P1. This trend is visible in most blasts in this test: path of wave propagation is more relevant than the distance to the blast.

5.4.2 Blast set 2

In this second set, blasts B11, B12, B13, B14 and B15 were also in the Outlet adit, but now in its lower part. All blasts except B14 were in the left wall of the adit. The charge weight in this set varied from 0.180 to 0.496 kg, the highest charge in the whole test. In the largest blast (B12) three boreholes were detonated simultaneously. The cooperative charge was 0.496 kg.

As in set 1, accelerometer base P1 is located near the surface, and a adit section is instrumented in the floor and in both walls (accelerometer bases P2, P3 and P4). The main differences are that the scaled distance range is smaller in this set and the blasts occur in an inferior position to bases P1 to P4. Figure 5.23 illustrates the location of the blasts and all sensors.

Analysis of the blasts, in figure 5.24, shows that the scaled distance range is quite small and it is not as easy to interpret and to infer attenuation lines as in the previous set. Nevertheless,

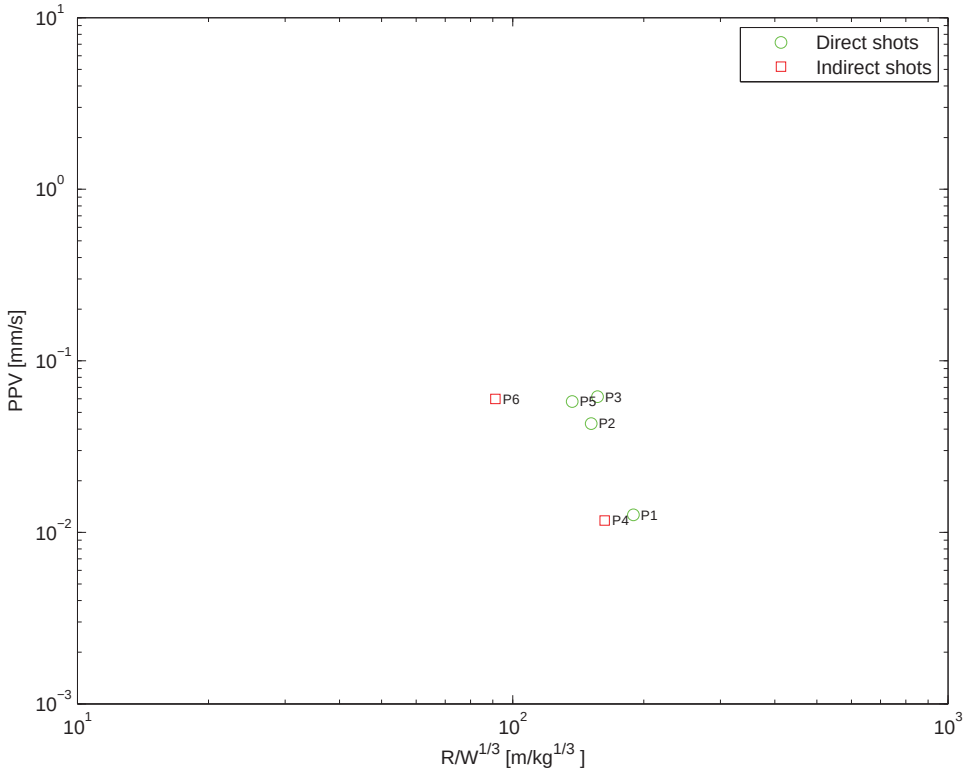


Figure 5.22: Plot of peak particle velocity *vs* scaled distance for blast 16 (Set 1).

there is a strong difference in amplitudes between direct and indirect shots.

Through observation of the plot of blast B15 in figure 5.25 (other blast plots are in Appendix II) it is possible to find the cause for the tall data cloud. P2, P3 and P4 are nearly at the same distance to the shots but P4's amplitude is much lower than P2 and P3. This is difficult to distinguish in the plot with all blasts. It is interesting too, to notice that the relative positions of P2 and P3 are not constant across the blasts in this wall. In B15, P3 is slightly higher than P2 (as in blast set 1) while in B11, B12 and B13 it is P2 that is higher.

Finally, the PPV recorded in base P6, which lies in an indirect path from the blasts shows lower vibration levels than the ones that could be expected by simply extrapolating the tendency observed on the other sensors.

Blast B14, which was performed in the right wall of the Outlet adit, was also analysed. As expected, vibration levels (figure 5.26) are smaller than in the other blasts, as the path of propagation from the blast to all the accelerometers is indirect. Still, the effect of the position of bases P4 and P6 is still visible.

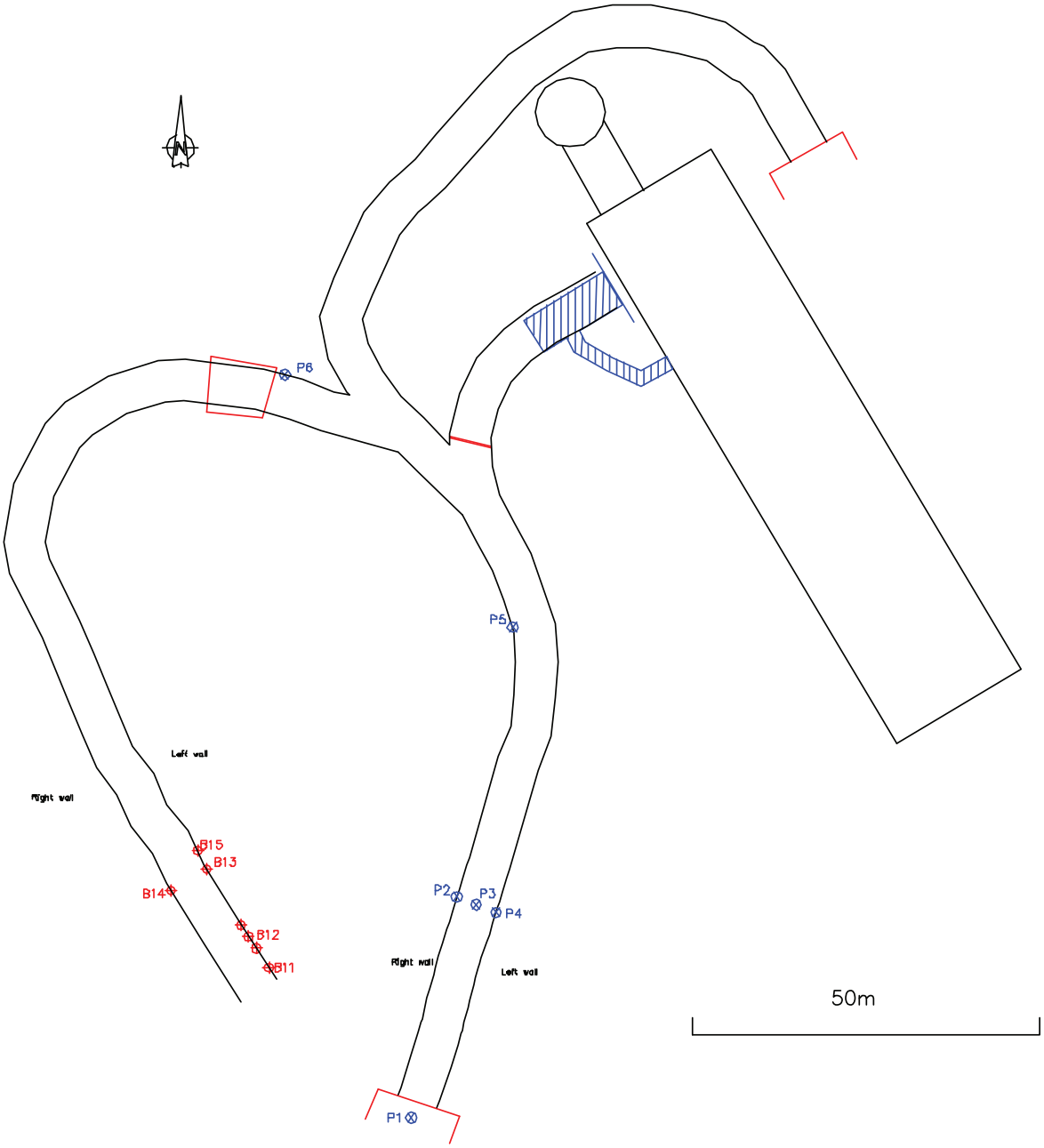


Figure 5.23: Location of blasts and measurement points of the second blast set.

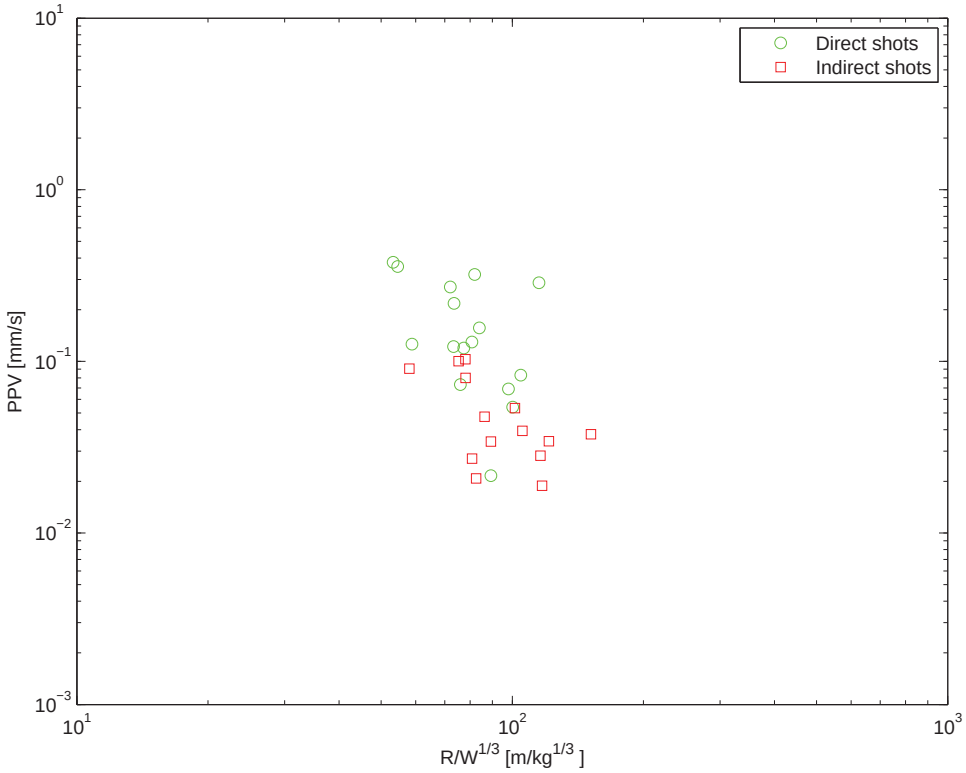


Figure 5.24: Plot of peak particle velocity *vs* scaled distance of the second blast set.

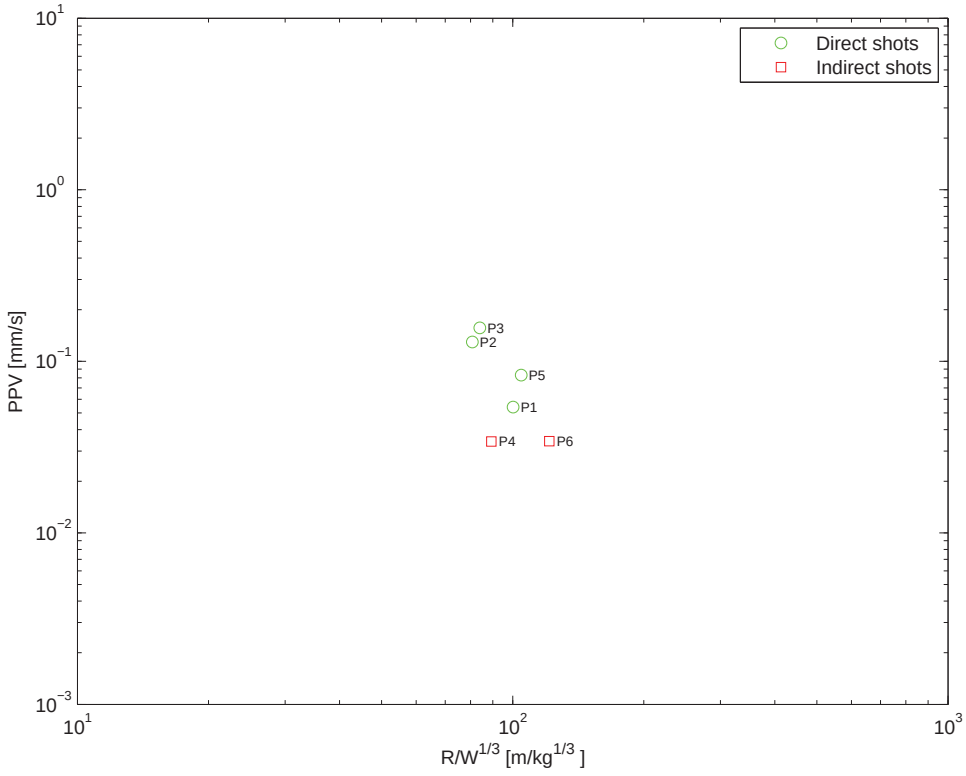


Figure 5.25: Plot of peak particle velocity *vs* scaled distance for blast 15 (Set 2).

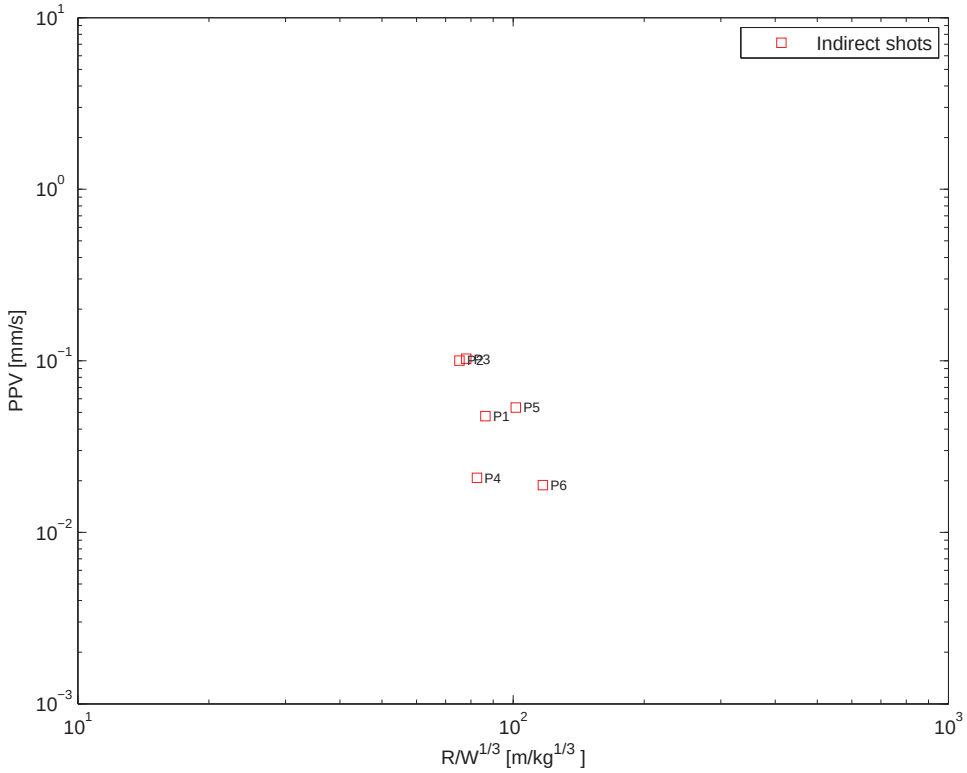


Figure 5.26: Plot of peak particle velocity *vs* scaled distance for blast 14 (Set 2).

5.4.3 Blast set 3

In the third set, blasts were all in the beginning of the Intake adit (boreholes B3, B4, B5 and B6). The charge weight in this set was very low and almost constant, ranging from 0.057 to 0.072 kg. All blasts were in the right wall of the adit.

Figure 5.27 illustrates the location of blasts and sensors. The accelerometers were placed along the Surface adit (P1, P4, P5), at the place where Intake and Outlet adits meet (P6) and in the Access adit (P7). An accelerometer base was also set in the Intake adit (base P8) but the cables were damaged by projected rock from blast B3 (the first blast in this adit) and this could not be fixed in the field.

Due to the large distances involved it was not possible to distinguish the blast vibration from the baseline noise in base P1 (figure 5.28). Even base P4 is only perceptible in blast B6, the most intense of the four blasts.

Once again it is possible to distinguish different tendencies for direct and indirect shots. In the latter the attenuation tendency can be observed over a large range of scaled distances and is not linear over a log-log plot. This non-linearity can possibly be attributed to the superposition of geometric and material attenuation (due to fracturing) but it should be noted that the three points were not measured in the same adit.

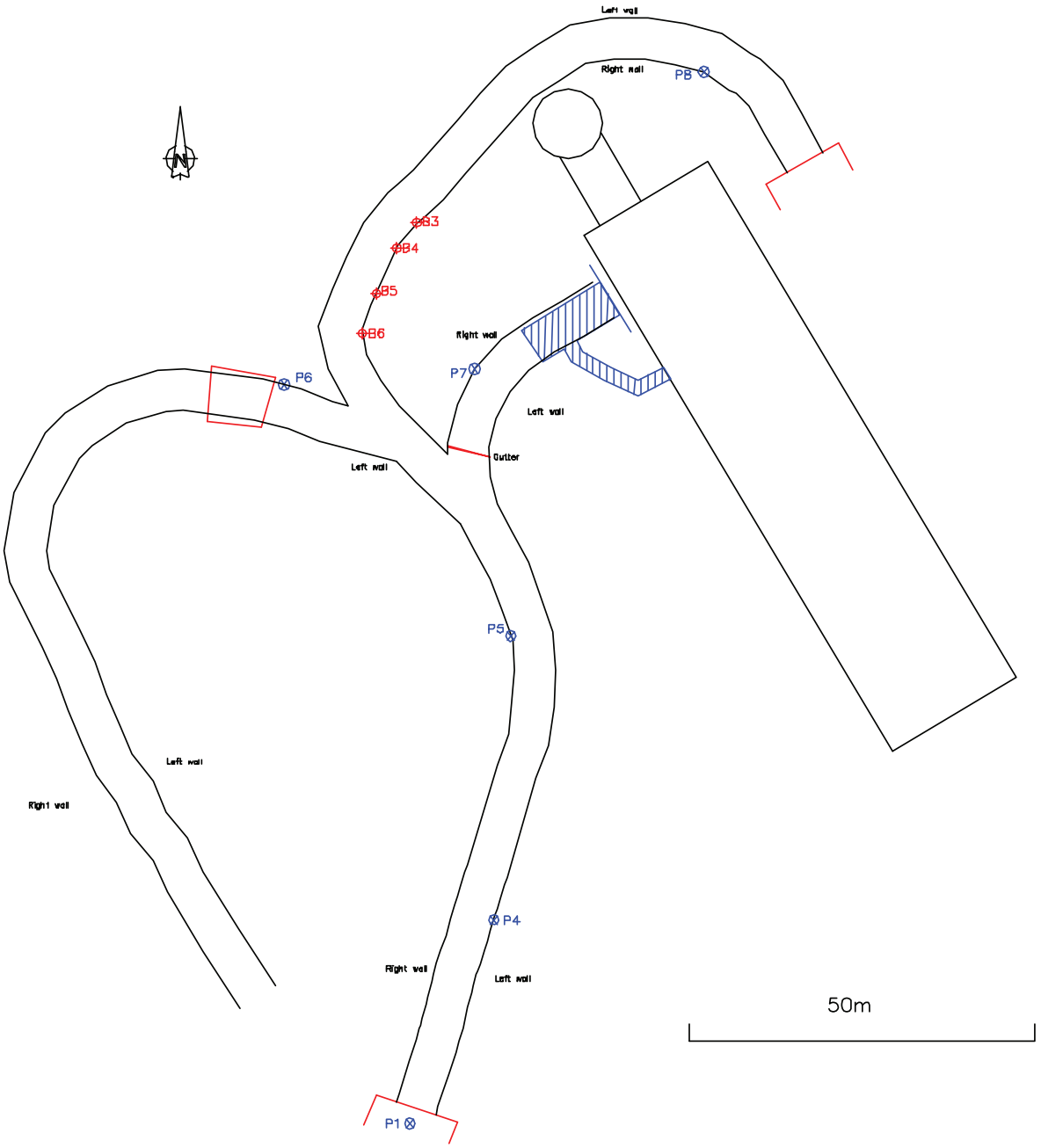


Figure 5.27: Location of blasts and measurement points of the third blast set.

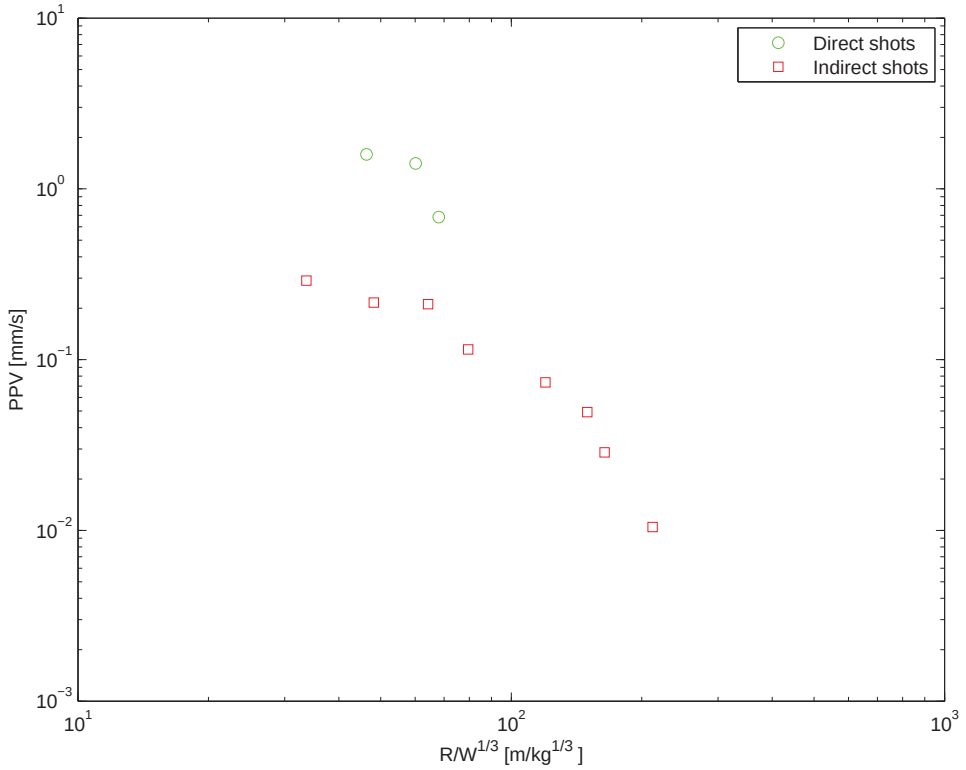


Figure 5.28: Plot of peak particle velocity *vs* scaled distance of the third blast set.

Figure 5.29 shows the data points in blast B6 (other blasts' plots are in Appendix II), the blast with more points, and allows an easier interpretation of the set. Vibration at base P7 is more intense than at P6, even when P6 is closer to the blast, due to P7 being in a direct path to the blast.

5.4.4 Blast set 4

This is the most heterogeneous set of blasts. All blasts were in the Intake adit: at its end (B17 and B18) and close to where this adit meets the Surface adit (B19, B20 and B21). Charge weight ranged from 0.070 to 0.165 kg.

Figure 5.30 illustrates the location of blasts and sensors. Accelerometers were placed in the Surface adit (P2), at the junction of the Intake and the Outlet adit (P6), at the Access adit (P7 and P19), at the Elevator shaft (P11) and at the Shaft Cable adit (P18).

The heterogeneous distribution of the blasts (figure 5.31) makes it hard to interpret the set results as a whole, and the set itself could be divided in two or three sub-sets.

Figure 5.32 shows the PPV-scaled distance plot of blast B20 (other blasts' plots are in Appendix II). As in previous shots, indirect shots have less intense vibrations than direct shots. Even among indirect shots it is interesting to see that P11, that is less "hidden" than

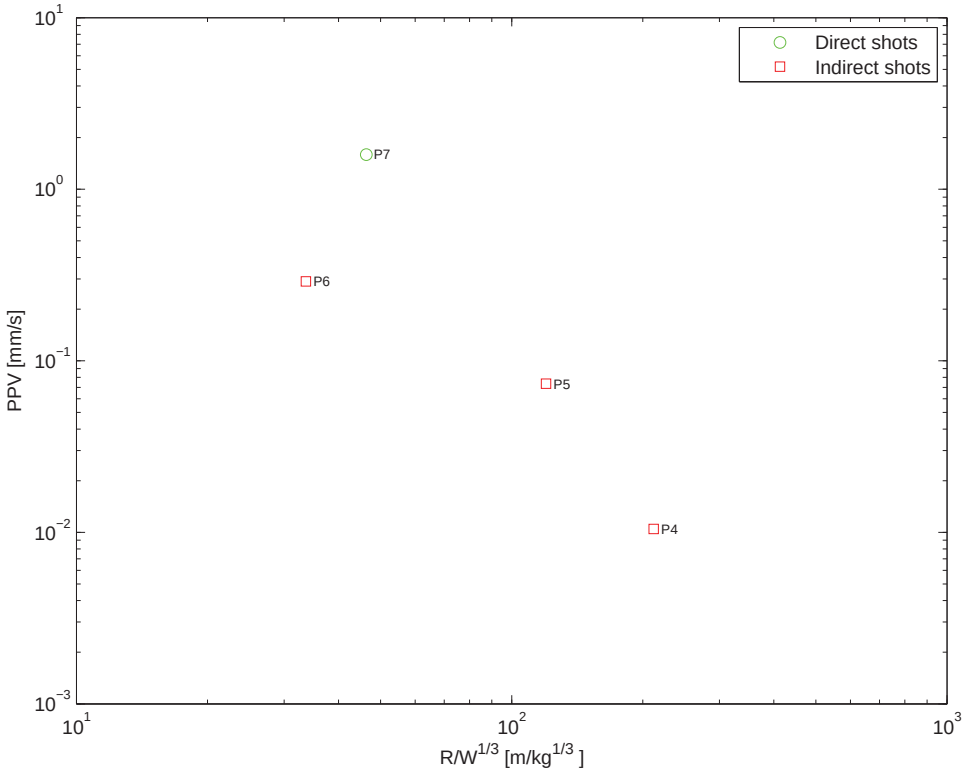


Figure 5.29: Plot of peak particle velocity *vs* scaled distance for blast 6 (Set 3).

P6 and P19, has a higher PPV than what could be expected from extrapolation of the other indirect shots.

Figure 5.33 shows the plot of blast B21. All shots are indirect but the waves have to go around two adits to arrive at P19, that displays a less intense vibration than the other blasts.

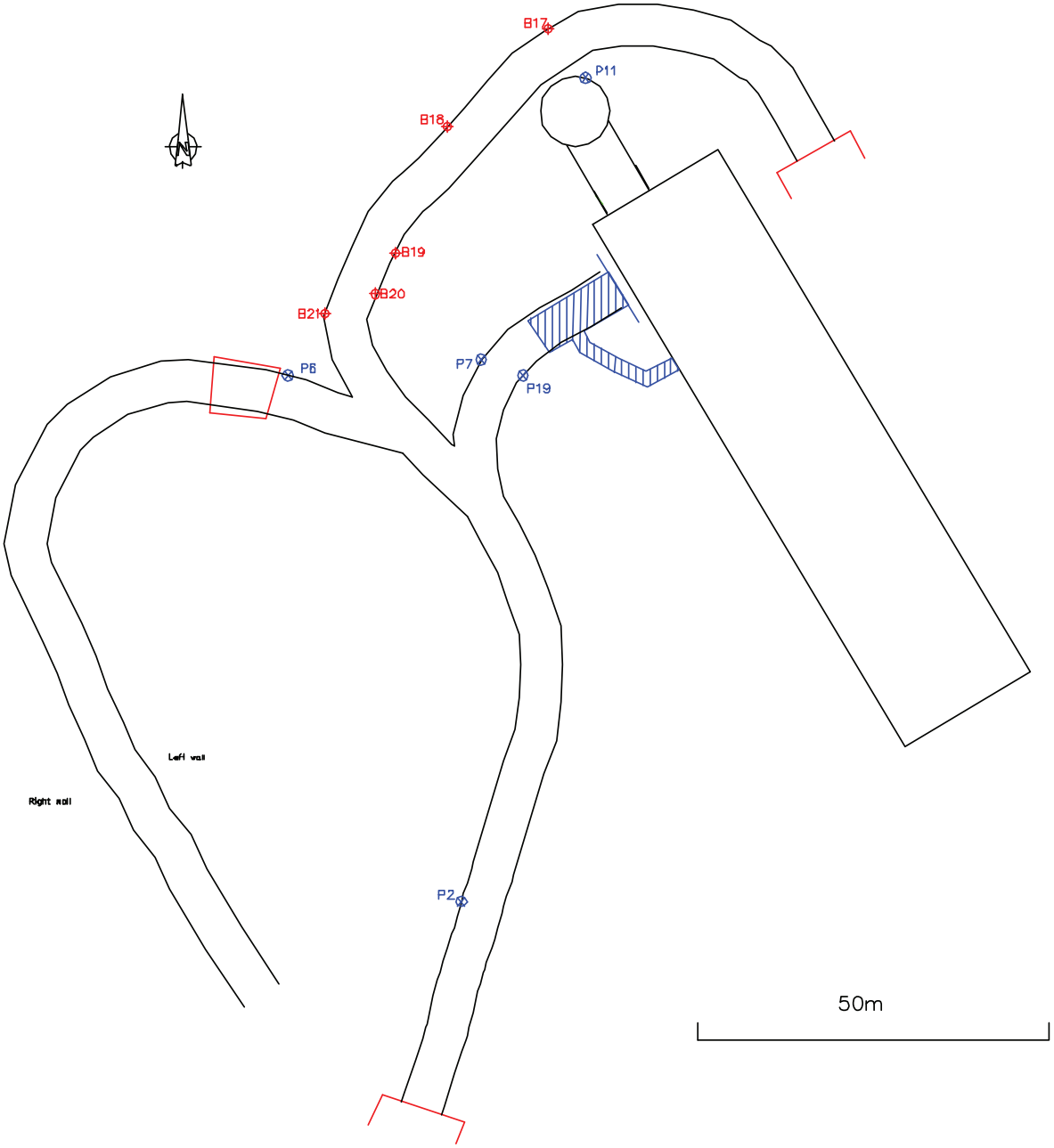


Figure 5.30: Location of blasts and measurement points of the fourth blast set.

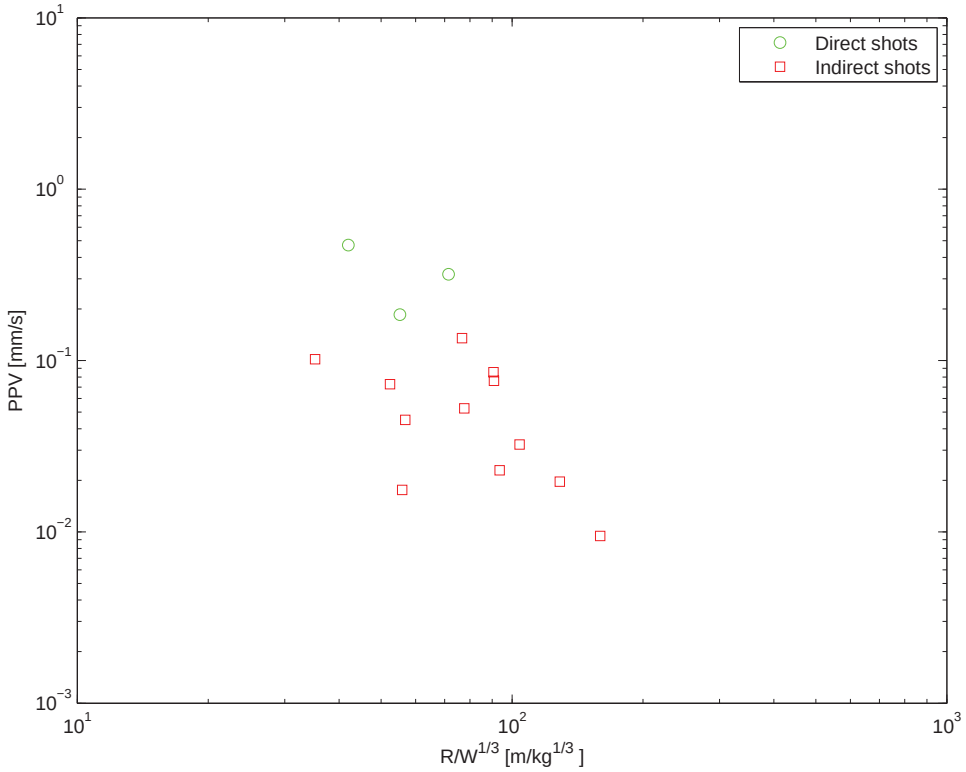


Figure 5.31: Plot of peak particle velocity *vs* scaled distance of the fourth blast set.

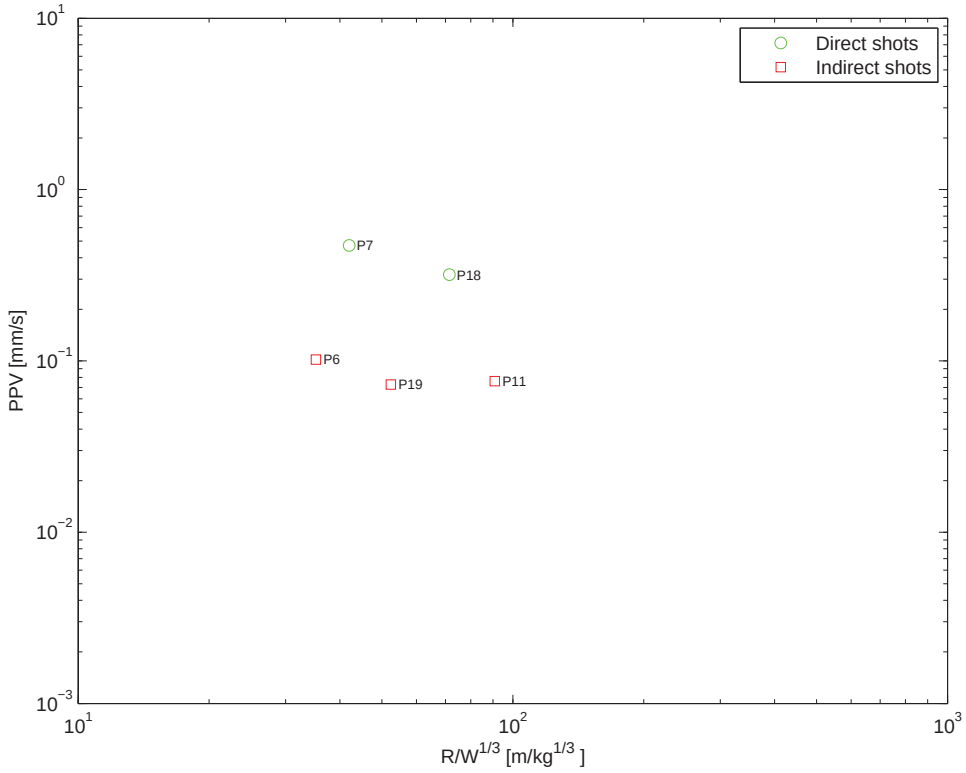


Figure 5.32: Plot of peak particle velocity *vs* scaled distance for blast 20 (Set 4).

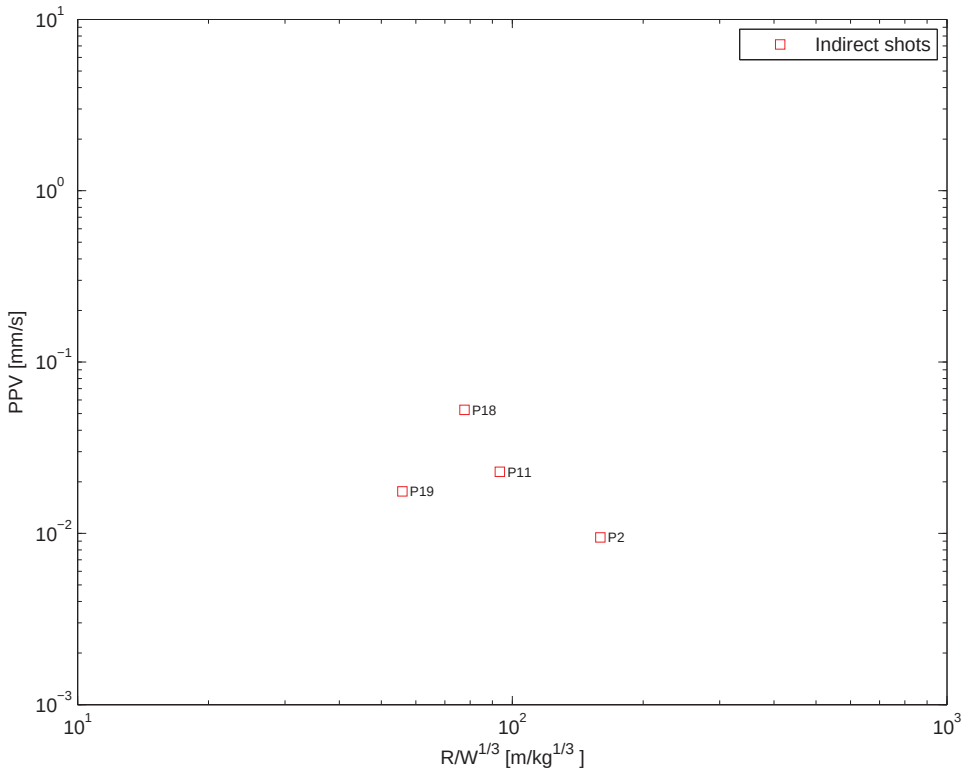


Figure 5.33: Plot of peak particle velocity *vs* scaled distance for blast 21 (Set 4).

5.5 Numerical modelling

Numerical modelling of blast generated stress waves remains relatively rare. Practising engineers depend almost exclusively on empirical attenuation laws to predict vibration levels. The reasons for this are valid and strong. Waves generated by blasting are three-dimensional and their attenuation is governed by distance and by ground singularities such as fractures, faults or voids. The location and characteristics of these singularities are frequently scarcely known and, influence vibration in a way that is scarcely known and hard to model.

There are, however, good reasons to give numerical modelling a try in some situations. A numerical model can take into account factors that are not included in attenuation laws like the site geometry and geological heterogeneities or inter-hole time delay.

The definition of an attenuation law with an acceptable degree of confidence demands a high number of blasts and measurements, and still little understanding of the local's characteristics is gained.

Numerical models, on the other hand, can be developed and run before the first test blasts. The hypotheses on the foundation of their development can be confirmed or changed rapidly compared with the first on site results. This is possible because, contrary to the attenuation laws, there is a correspondence between the model's assumptions and the phenomenon's mechanisms.

Once the principal characteristics of the problem have been correctly captured the model can be used and enhanced, given that the changes do not take it outside its valid working area. The boundaries of this working area must be well delimited and understood. A correctly defined numerical model can study aspects of the vibration propagation problem such as the evolution of excavation geometries, fire sequences, the effect of known or hypothetical geological features or the influence of mitigation measures. It can also estimate wave propagation in a rock mass from its geometrical and geotechnical characteristics and from laboratory tests of the rock material. A numerical model can be used to gain a better understanding of why a given vibration level is higher or lower than an expected value by testing different hypotheses.

The best an attenuation law delivers is an estimate of the order of magnitude of the PPV. Simple numerical models can confirm, explain and narrow this estimate, while studying scenarios that are completely out of the reach of an empirical equation. As with attenuation laws, as more information is available the model will be richer and more reliable, provided that the available information is correctly incorporated and the model's complexity does not become counter-productive, as discussed in chapter 3. Most numerical problems related to wave propagation in FEM, FDM or block discrete elements, such as mesh quality or silent boundaries have been addressed satisfactorily (this is not the case of micromechanical models, which were

studied in chapter 4).

With these points in mind, the specific goal of this section is to work on some of the bottlenecks of an economical and productive numerical analysis of blast wave propagation in rock masses:

- When can 2D and 3D models be used and what are their minimum requirements.
- How should blast loads be applied.
- When and how must fracturing of the rock mass be modelled.
- How should vibration measurements be conducted underground.
- What is the influence of excavations, and how realistically must they be represented.
- How does the rock stress influence wave propagation.
- How surface or large excavations influence wave propagation.
- How does the excavation damaged zone (EDZ) influence vibration?
- What is the sensitivity of the model's output to variations in its geometry and parameters.

5.5.1 Dynamic modelling using finite difference models

When modelling a rock mass the first and most important choices are between a continuous or a discontinuous representation and whether to model in two or three dimensions. These choices influence and are influenced by the chosen numerical method and implementation. As discussed in chapter 3, the discrete element method, for example, is particularly suited for the explicit representation of the discontinuities. Even though other methods, such as the finite element method, can represent discontinuities they do it in a limited way. Particle and lattice methods, on the other hand, are well suited to model the micromechanical structure of materials but are still too computationally demanding.

Most rock masses are fractured, and the volume where the blast tests were performed was not an exception. Major joint sets and faults were surveyed and the results presented in section 5.2.1. Fractures can play an important role in wave propagation but in this case it was decided not to represent them explicitly since, in this situation, the influence of the fracturing is thought to be considerably smaller than other features such as the adits' relative position and geometry. Several reasons support this decision. The low blast charges generated stress waves with amplitudes that are insufficient to mobilize the fractures. That is, they work in the elastic regime. Nevertheless, as the analysis in the precedent chapter showed, attenuation due to reflections and refraction in the fractures still occurs but, as reported earlier in the text, the geological history of the rock mass lead to the build-up of high vertical and horizontal stresses that tightly close the fractures. This is confirmed by the low apertures and scarce water presence in the fractures visible in the adits walls and ceiling. Finally, the computational cost

of a jointed model, when joint spacing is in the order of 0.06 to 0.2 metres is still out of the reach of 2009's hardware. It was therefore decided to use a continuum representation whose dynamic properties are equivalent to those of the rock mass.

Among the several numerical methods that can be used to model the propagation of vibrations with a continuous model, finite difference models are among the most popular. FLAC and FLAC3D (Itasca, 2008b, 2010) are two and three dimensional finite difference codes, widely used in soil and rock mechanics. The robust, conditionally stable, time-stepping explicit integration algorithm makes these codes especially suited for dynamic calculations in the time domain. The finite-difference formulation does not imply the assemblage of a mathematical representation of the model such as a stiffness matrix, as in the case of the finite-element method. This means that the alterations to the model's properties during calculation are applied directly to the grid-points and considered in the following calculation cycles without increasing the computational cost.

Both FLAC and FLAC3D employ linear deformation elements, triangular in FLAC and tetrahedral in FLAC3D. The element size to shortest wavelength relation that ensures a good quality wave representation is similar in both codes. The software's manuals (Itasca, 2008b, 2010) indicate minimal wavelength to element size ratios of 6 to 10.

5.5.2 Blast representation in numerical models

The process of explosives' detonation in a borehole has been described in chapter 2. It involves a complex chain-reaction of processes. The temperature and strain rate are extremely high and stress values are many times higher the rock strength. As the pulverisation and fracturing of the rock takes place, gases produced by the explosion penetrate fractures and cracks driving their growth.

In addition to the more traditional observational and theoretical methods, numerical models have been used to study this process with encouraging results. One of the most complete approaches resorts to hydrodynamic codes that include the termo-chemo-physical transformations of the explosive and its interaction with the rock around it, and material models that incorporate the behaviour of rock under extreme heat and pressure. Block and particle discrete element methods have also been used, as they represent efficiently the generation and growth of fractures and the movement of the rock pieces afterwards (*e.g.* Chen *et al.* (2000), Mortazavi and Katsabanis (2001b), Mortazavi and Katsabanis (2001a), Wang *et al.* (2009)).

However, the object of this study is not the small volume of rock around the borehole where the highly non-linear explosion-rock interaction takes place but the surrounding rock mass where the energy of the explosion that was not consumed in rock pulverization and breakage

escapes in the form of stress waves. As such, the modelling of the explosion process is not an objective in itself: it is sufficient to model the blast in such a way that it generates correct stress waves in the surrounding rock mass.

Representation of a blast load in a numerical model involves two parts: what load waveform should be used and how it should be applied in the model. A dynamic input is generated in the model but not necessarily exactly in the same volume and shape of the real borehole. If a velocity or acceleration time history of the vibration wave recorded near the blast is available, that record can be used as an input. In the test performed at the Bemposta complex such a record was not available and a generic load history was used.

The most common way of measuring blast waves in soil or rock is through velocity or acceleration transducers in contact with the ground. As strain is directly related to velocity, acceleration records are usually converted to velocity and all subsequent work is performed over these records.

A complete triaxial time-history contains a large amount of information, and it is necessary to extract meaningful parameters that allow comparison of records and model results. In the author's opinion, the most important features of a blast induced vibration time-history are, in first place, the peak particle velocity, then frequency content and finally wave duration. When comparing a numerical result with a real blast record, these parameters can be compared with the field measurements and the model input variables, namely the blast waveform parameters can be adjusted accordingly until an acceptable agreement between the model and the monitoring results is achieved. This adjustment can be done by trial and error or by using an automated back analysis routine, but a perfect fit cannot be expected, as the model and the input load are crude simplifications of the reality.

Blast wave input function

Input blast loads are synthetic time-histories or mathematical functions composed by a rapidly ascending branch that peaks at an amplitude p_0 at a time t_{peak} and then descends sluggishly to zero. These functions aim to represent the complex process of the explosive detonation, rock pulverization and gas expansion that takes place inside and around the borehole in the few milliseconds of a conventional detonation.

In this work, the criteria considered for the choice of the most adequate load function were: it should be as simple to parametrize as possible, easy to implement on the model, and generate waveforms as similar as possible to those measured in the test blast.

Duvall (1953) proposed a function composed by the product of the peak pressure p_0 and

the sum of two exponential functions. The analytical expression is:

$$p(t) = p_0 \left(e^{-\alpha t} - e^{-\beta t} \right), \tag{5.2}$$

where α and β are adjustable parameters. By deriving and finding the zero of the function, the peak-time t_{peak} can be found:

$$t_{peak} = \frac{ln\left(\frac{\beta}{\alpha}\right)}{\beta - \alpha}. \tag{5.3}$$

The main advantage of this expression, which is the most complex of all that are presented here, is the possibility of customization. The user can choose the rise time of the pressure, it's peak and the falloff time. Several authors proposed relations between parameters α and β and the characteristics of the rock mass, the borehole radius and velocity measurements at a small distance from the source. Figure 5.34 presents graphical representations of equation 5.2.

A simplification of the previous equation consists on a single negative exponential function that does not allow the choice of the falloff time but only of the peak time and amplitude. Figure 5.35 presents a graphical representation of equation 5.4.

$$p(t) = p_0 \frac{t}{t_{peak}} e^{1 - t/t_{peak}}. \tag{5.4}$$

A triangular function is even simpler but it has serious drawbacks in relation to the previous functions: it has sharp corners that generate high frequency content and must be defined by a branched expression which is less practical to implement. Figure 5.36 presents a graphical representation of equation 5.5.

$$\begin{cases} p(t) = p_0 \frac{t}{t_{peak}} & , \quad 0 \leq t < t_{peak} \\ p(t) = p_0 - p_0 \frac{t - t_{peak}}{t_{falloff} - t_{peak}} & , \quad t_{peak} \leq t \leq t_{falloff} \\ p(t) = 0 & , \quad t > t_{falloff} \end{cases} \tag{5.5}$$

Some authors employed variations of the triangular function, such as a negative exponential function on the descending branch of the pressure load (e.g. Kiehl and Werfling, 2003), as presented in figure 5.36.

Finally, other authors such as Chen *et al.* (2000) used hydrodynamic codes to model the explosive detonation process inside a chamber. From that calculation they extract a pressure time-history that is then used as input in a model of the rock mass. The time history function is similar to a complete cycle of a sine wave with a positive peak followed by a less intense negative peak and then a number of small amplitude waves (figure 5.37).

The single negative exponential function was chosen as the blast input load to be used in the present work. It is a compromise between the larger number of parameters of the double exponential function and the more crude triangular functions. The model has two parameters,

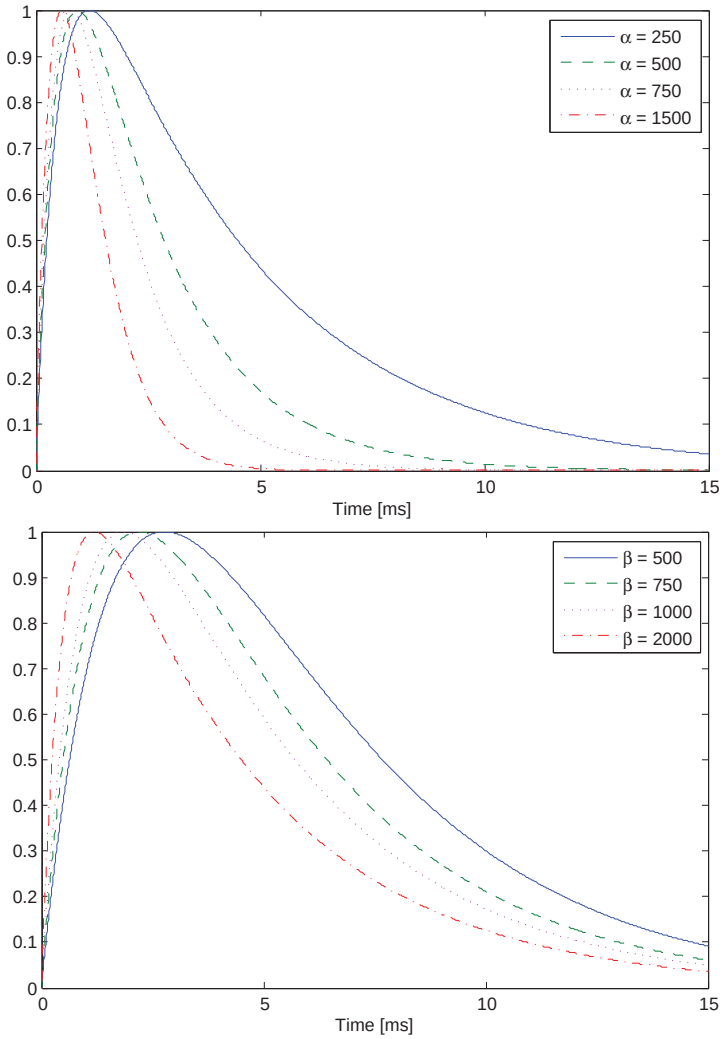


Figure 5.34: Duvall double exponential blast pressure function. Variation of α with $\beta = 2000$ (top) and variation of β with $\alpha = 250$ (bottom).

peak-time and peak amplitude. Peak amplitude is arbitrarily chosen, since the results can later be scaled to fit the experimental values. As for the peak-time, analysis of the literature show that it's value is around 0.5 to 1.5 milliseconds for explosives with high velocity of detonation in rock. A parametric study in a 2D model showed that the PPV values are not very sensitive to variations in the peak-time. A value of 0.7 ms is used. The fall-off time of the negative exponential function is about seven times the peak-time.

Application of blast wave input function

Explosives employed in construction or mining blasting are loaded in boreholes with diameters that typically range from a few centimetres (careful blasting in hard rock) to more than a metre

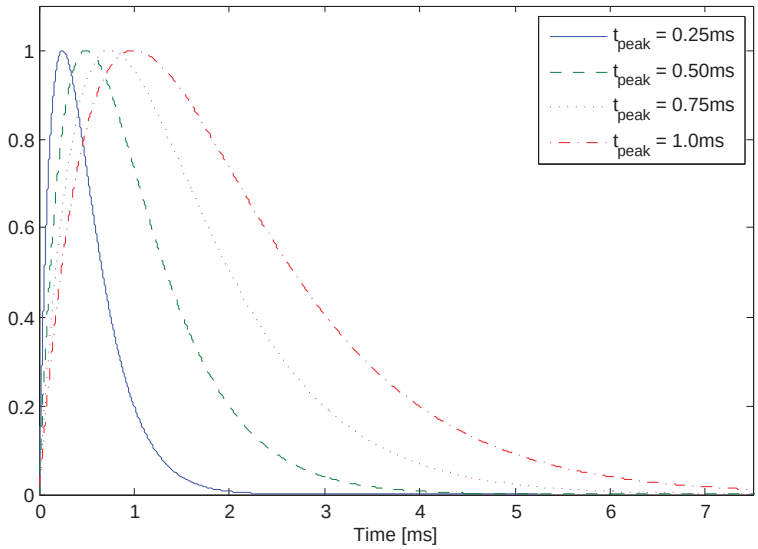


Figure 5.35: Exponential blast pressure function.

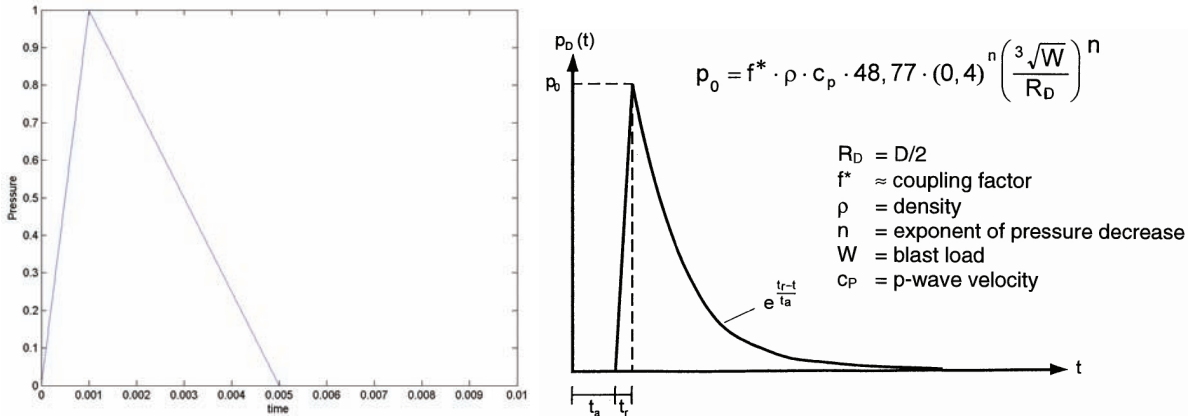


Figure 5.36: Triangular (left) and linear-exponential (Kiehl and Werfling, 2003) (right) blast pressure functions.

(in surface mining where boreholes are loaded with bulk explosives). In the Bemposta complex blast test boreholes were drilled with a diameter of 25 mm and loaded with the explosive cartridges, the smallest commercially available size.

In a model grid that spans tens of metres with cubic elements with approximately one metre long edges, it is not feasible to truly represent boreholes with dimensions one hundred times smaller. It is therefore necessary to devise efficient and representative ways to simulate the explosive loads.

The simplest method is to model the explosion as a time-history applied in a gridpoint/node of the finite-difference/finite element grid, without representing the tunnel or excavation from where the borehole is drilled and loaded. However, when waves are generated in, or near, an excavation, there is a rebound effect that adds to the initial impulse. In blasts generated in a

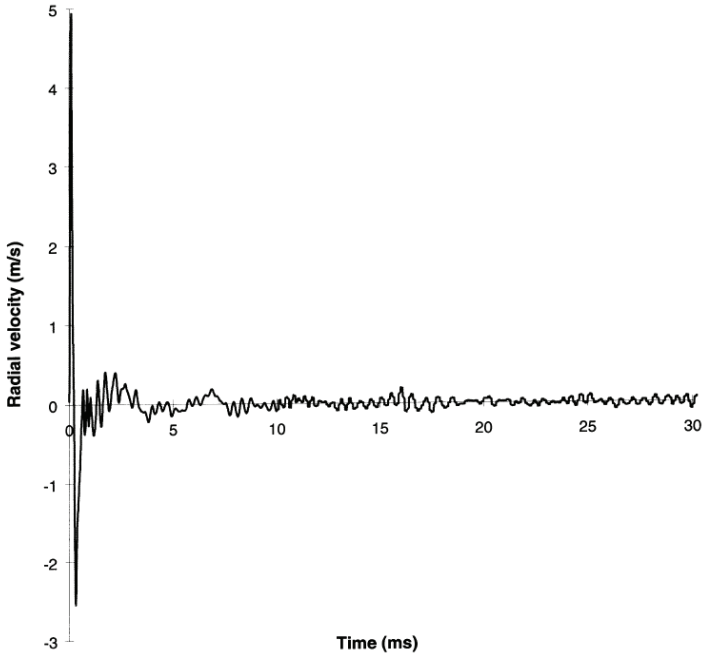


Figure 5.37: Blast wave generated by AUTODYN-2D hydrodynamical code. Taken from Chen *et al.* (2000).

continuum this rebound does not occur or is much smaller and the wave sent into the model will lack the after-peak vibration.

Another loading option, more complete than the above-mentioned method, consists of applying the pressure function in the walls of the excavation section (represented in two or three dimensions) in the region where the real borehole is located. If the wave is applied uniformly as a pressure load in the whole section of the tunnel, a predominantly compressive wave is generated, but if it is applied in just a part of the section, a more complete and realistic waveform containing compressive and shear waves is created.

A subsequent step in the direction of greater complexity is the application of the blast load in the interior of an element, either by removing it and applying the load in the walls of its ex-neighbours or by forcing the element to expand according to the blast time-history. These options are graphically represented in figure 5.38.

One difficulty that arises when comparing results of the methods is that, for the same blast time-history, the energy that is released into the model is proportional to the area of the surface where it is applied. To avoid this problem either the time history is scaled up or down according to the loading surface or a common reference point in the model is chosen and all time histories are adimensionalized relatively to that place's PPV.

The application of a time-history load to a particle model was discussed in chapter 4. Although here we are working with a continuous finite-difference model, the mathematical and

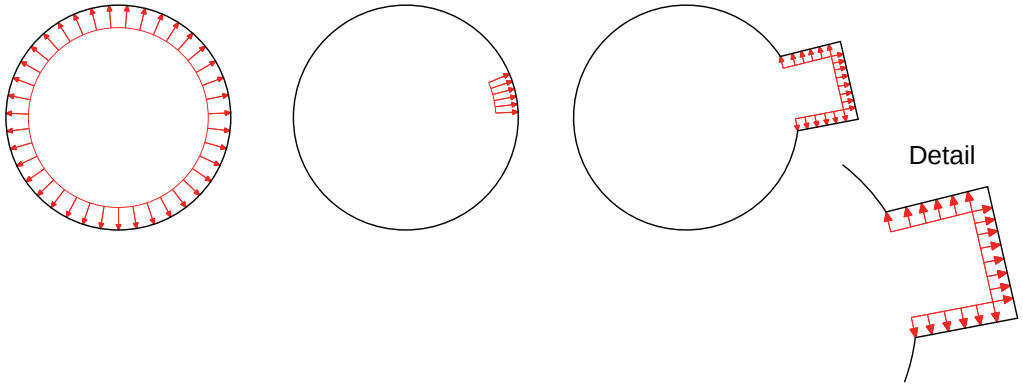


Figure 5.38: Three methods of application of the blast load in a finite-difference mesh: load in the whole tunnel section (left), load in an element face (centre) and load in the place of a removed element (left).

numerical issues are similar. Both models reproduce the application of a dynamic load to a continuum body's surface. Time-histories can be applied either by constraining the movement (displacement, velocity or acceleration) of gridpoints, or by mechanically loading stress/force loads.

In the case of prescribed movement, the gridpoints are removed from the calculation cycle and their motion is exactly that of the loading function. As these gridpoints are clamped, waves that hit them are reflected back into the model with a symmetric value.

When the waveform is applied as a force loading the gridpoints are included in the calculation cycle like any other unconstrained gridpoints. They do not offer resistance to wave passage and, if at a boundary, that surface will behave like a free boundary, reflecting the waves back into the model with the same signal. Absorbing boundary conditions can be applied at these gridpoints.

When a force loading is applied in unconstrained gridpoints an elastic rebound may occur generating lower intensity waves. Depending on the damping of the material and on the shape of the loaded surface this reverberation may last for a long time. If the loading constrains the movement, this rebound cannot happen.

It can be concluded that the application of blast load time-histories is more realistic if done through a force loading that does not interfere with the motion calculation of the gridpoints. Equation 4.47, presented in chapter 4 and repeated here, relates stress σ and velocity $\dot{u}$, performing the conversion of time-histories from stress to velocity and vice-versa:

$$\sigma = \rho c \dot{u} \Leftrightarrow \dot{u} = \frac{\sigma}{\rho c}, \tag{5.6}$$

where ρ is the medium's density and c the velocity of propagation of whichever body wave (shear or compressive) is being considered.

In the following sections different methods of loading are tested in the numerical models of

the Bemposta blast tests and conclusions are drawn regarding their effectiveness.

5.5.3 Two and three dimensional modelling of stress wave propagation

Unlike earthquake-generated stress waves whose source is usually located deep in the earth and usually far away, blast stress waves propagate spherically from the source, which tends to be much smaller than the volume of interest. As a consequence, blast wave propagation demands a three-dimensional representation (see figure 2.9 in chapter 2) which is expensive in terms of processing time and memory.

Two and three-dimensional modelling have been discussed in general terms in the introductory chapters. In dynamic modelling of geotechnical problems the computational cost factors are frequently overwhelming and there are several advantages in modelling in two dimensions: faster and easier grid generation, much faster run-times and less data to store. No less important, results are more easily visualized and interpreted.

But, the use of two dimensional calculations is limited, as spherical propagation can only be simulated in 2D by using axisymmetric models. These are able to represent very simple geometries only. Planar features such as fractures, underground openings and other of the sort cannot be correctly represented in an axisymmetric formulation. A way around this limitation is to employ plane strain models in which the input function is calibrated to fit the peak vibration at a certain distance from the source. Two dimensional strategies, even though being correct only in a part of the domain can be useful in the early modelling steps, as is done here.

On the other hand, in three-dimensional models the geometry of the ground, geological features such as faults and fractures can be correctly represented. As less simplifying assumptions are needed better quality results are attained. Three dimensional modelling of dynamic phenomena is still behind the general state of practice of other geomechanics disciplines. This is due to the high level of mesh refinement that good quality wave propagation demands all across the domain, which leads to excessively large models that may exceed the capacity of available hardware. It is, therefore, necessary to explore and take advantage of the contributions of both two and three dimensional models.

Two and three dimensional modelling options were tested. All models use the same elastic material model with a bulk modulus of 21.6 GPa, a shear modulus of 16.2 GPa (equivalent to a Young's modulus of 40 GPa and a Poisson's ratio of 0.2) and a density of 2700 kg/m^3. These properties result in propagation velocities of 4000 and 2449 m/s for P and S waves. No material damping is used. The elements are squares with a side of 0.25 m.

The dynamic load is a continuous sinusoidal wave with unit amplitude and a frequency of 1000 Hz. The P-wave propagation speed is 4000 m/s so the wavelength is 4000/1000 = 4 m. As

the elements' length is 0.25 m, the ratio of wavelength to element size is 16, which guarantees excellent wave propagation conditions and virtually no quality loss in the transmission across the grid. All attenuation is then due to geometric effects. The movement of eleven gridpoints is recorded along the bottom boundary and the maxima and minima of these velocity time-series are extracted.

The models are described in the following sections. The 2D models were run in finite-difference software FLAC version 5.0, and 3D models in FLAC3D version 3.1, both from Itasca.

Plane wave propagation using one dimensional plane strain model

Plane wave propagation can be modelled in a 1D model consisting of a single row of elements in plane strain (null strain in the plane normal to the model) as shown in figure 5.39.

An absorbing boundary condition is applied at the right end of the model and the load is applied at the left boundary. The vertical displacement is constrained at the top and bottom boundaries, simulating an infinite medium in the vertical direction.

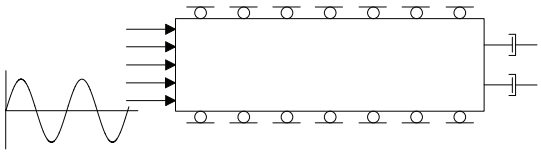


Figure 5.39: One dimensional plane strain model for plane wave propagation.

Cylindrical wave propagation using two-dimensional plane strain model

A 2D model in plane strain (figure 5.40) can be used to represent a wave propagating cylindrically from an infinite tunnel that has its length in the plane perpendicular to the model's.

Figure 5.41 shows the finite difference model of a tunnel with a 10 m radius. The model's side is 110 m long and elements are square-shaped with the exception of some elements on the tunnel's border that are triangular. The boundary conditions are: movement in the normal direction at the bottom and left sides is constrained through null velocity conditions to create a double symmetry condition. Absorbing boundaries are employed in the top and right sides. The pressure time history is loaded as a pressure wave normal to the tunnel wall, generating a circular compression stress wave that advances through the model until it reaches the top and left walls where it is absorbed.

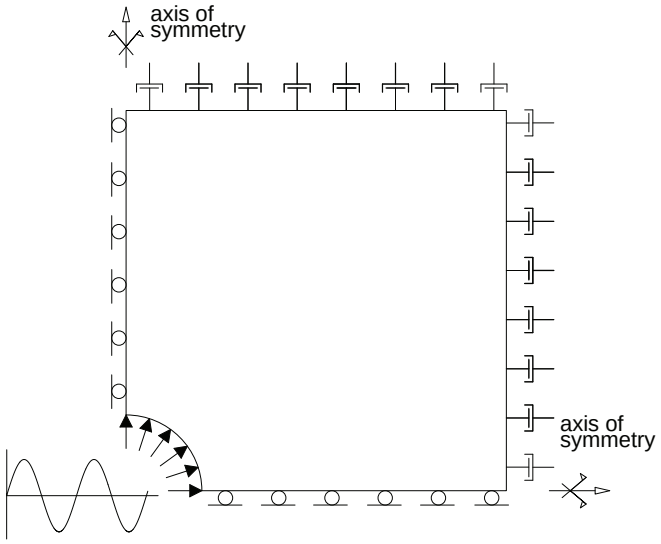


Figure 5.40: Two dimensional plane strain model for cylindrical wave propagation.

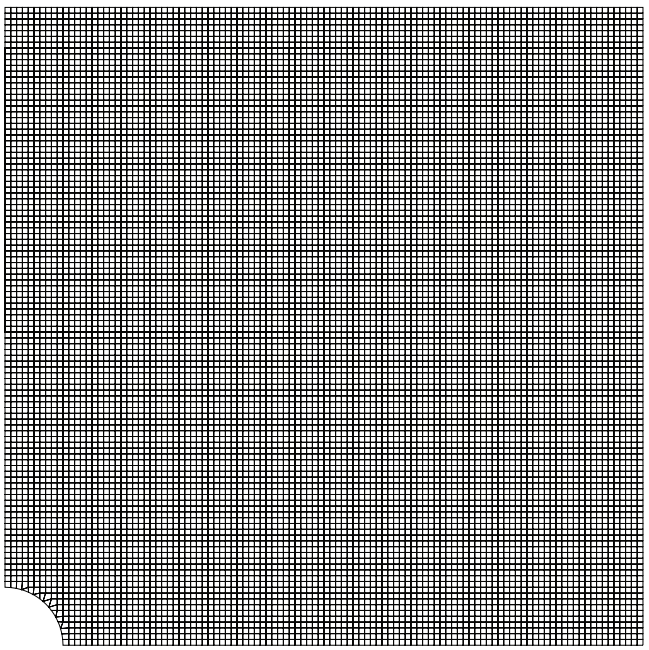


Figure 5.41: Finite difference model assessment of 2D and 3D wave propagation.

Cylindrical wave propagation using one-dimensional axisymmetric model

As represented in figure 5.42, cylindrical wave propagation can also be achieved through a 1D plane model if an axisymmetric geometry condition is used. The axis of axysimmetry is located at the axes origin, and the model starts at x = 10 m. The loading and boundary conditions are similar to the unidimensional model (section 5.5.3) but the position of the axisymmetric axis makes the wave amplitude attenuate as in the previous 2D plane model.

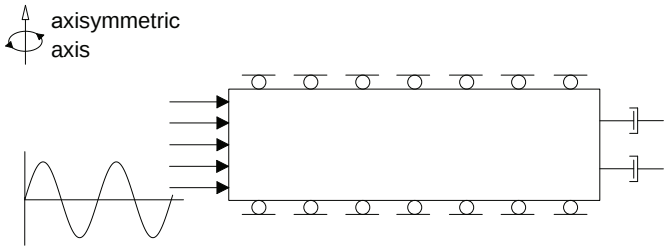


Figure 5.42: Cylindrical wave propagation in axisymmetric 1D finite difference model.

Cylindrical wave propagation using three-dimensional plane strain model

The three-dimensional code FLAC3D was used to simulate a plane model. The mesh, loading and boundary conditions are the same as in the 2D plane model with the addition of out-of-plane thickness and the restriction of movement in that direction to emulate plane strain behaviour. Figure 5.43 shows a detail of the model and a plot of the velocity amplitude.

Spherical wave propagation using two-dimensional axisymmetric model

Finally, the two dimensional model of figure 5.41 is run maintaining the loading and boundary conditions but with symmetry conditions in the bottom horizontal boundary and an axisymmetric axis in the left boundary (figure 5.44). This simulates not a cylinder-like tunnel but a three-dimensional spherical cavity. Waves produced at the cavity boundary propagate spherically attenuating faster than the waves in the 2D plane strain model.

Models performance

Figure 5.45 displays the analytical solutions for cylindrical and spherical attenuation, as deducted in chapter 2. The peak amplitude of the numerical models' results are shown in the same figure.

No material damping was used and dispersion due to the numerical wave representation is very small due to excellent numerical wave propagation conditions. As a consequence, the peak

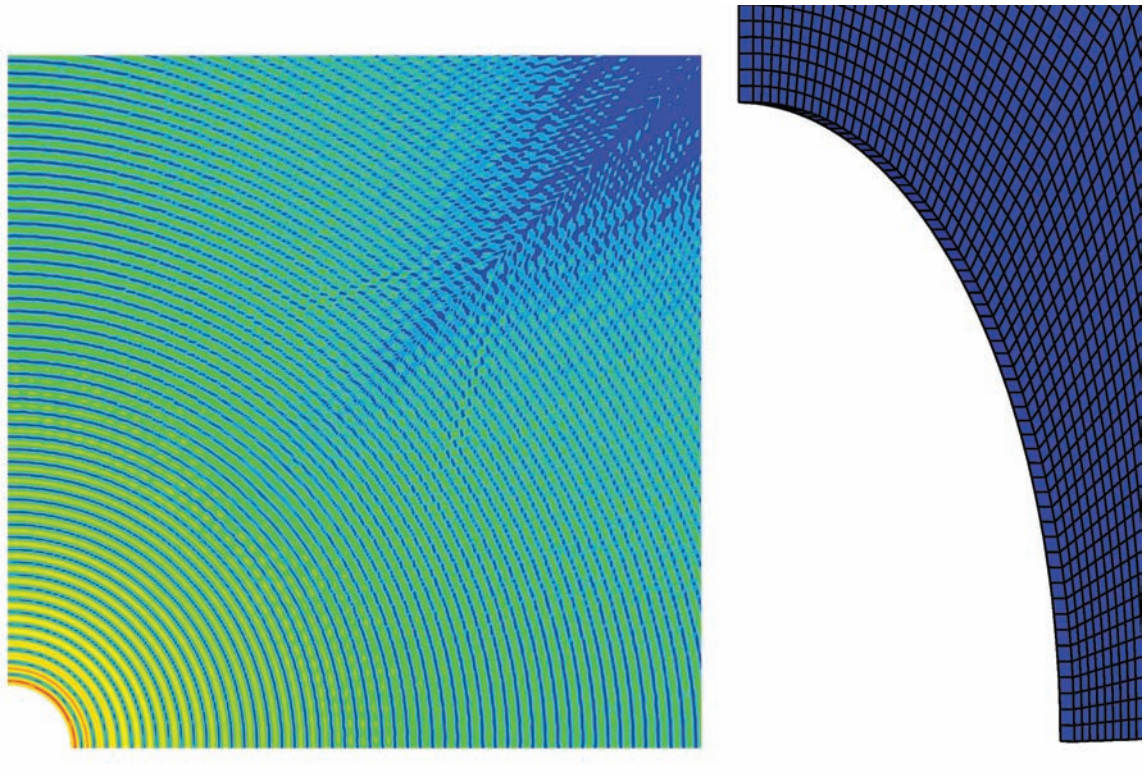


Figure 5.43: Absolute velocity amplitude plot of cylindrical wave propagation on a 3D plane strain model. Amplitude decreases with distance to the source, top right corner shows imperfect absorption due to smaller angles of incidence at the boundaries (left). Detail of the model's grid (right).

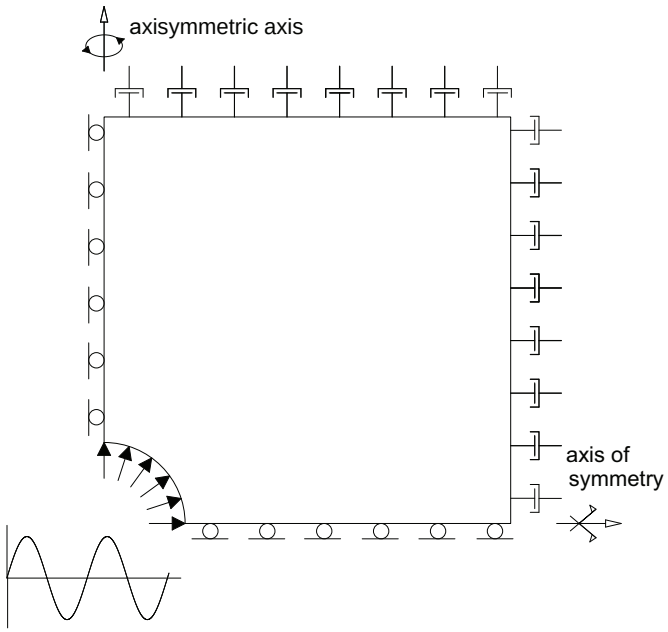


Figure 5.44: Two dimensional axisymmetric model.

amplitudes follow the theoretical solutions closely. The exception is the area further away from the cavity in the 2D and 3D models where the model is slightly off the theoretical result due to imperfect absorption at the boundary.

In the 1D plane model the amplitude is constant all through the model: there is no geometrical attenuation in a plane wave. Plane wave propagation is typical of earthquake-generated waves that travel vertically from the bedrock to the surface. One dimensional models are frequently used, for example, to determine the effect of soil layering on the earthquake action emanating from the bedrock. A cylindrical or spherical wave can be perceived as a plane wave if the "target" of the wave is much smaller than its perimeter, as illustrated in figure 2.10.

The peak amplitudes of the 2D model with plane strain formulation, the 1D model with axisymmetric formulation and the 3D plane model with plane strain condition match the cylindrical attenuation, with amplitude decreasing with the square root of the distance. Cylindrical wave propagation occurs, for example, in the close vicinity of the boreholes where the blast takes place. As the distance to the borehole increases and gets larger than its length, wave geometry becomes spherical.

The 2D axisymmetric model, on the other hand, follows the spherical attenuation law typical of loads generated in a small region.

Wave arrival times at the monitoring plots are similar in all models since the propagation conditions influence attenuation but do not influence wave propagation velocity.

The presented finite-difference models correctly simulate the geometrical attenuation from the simple 1D plane wave problem to the 3D spherical propagation. It has been observed that the 16 elements per wavelength ratio performs excellently on 1D, 2D and 3D models, not interfering with the quality of wave propagation (as expected). Unfortunately, on real problems it is often not possible to ensure such high levels of mesh refinement. In addition, the absorbing boundaries do not perform as well when the angle of incidence of waves becomes smaller than 60^{o}. For this reason, it is advisable no to place boundaries under these conditions near places where the stress waves will be measured. Finally, it can be concluded that, given that the assumptions are justified, considerable economy can be attained through the use of 1D or 2D models to simulate more complex propagation modes.

As described earlier in chapter 2, waves propagating in a real medium with no obstacles attenuate due to geometrical and material damping. The former is simulated in numerical models as a consequence of the model geometry and wave generation mode. The latter, however, must be introduced either in the material's constitutive model and/or as a part that opposes movement in the equation of motion. Either way, it must be calibrated against experimental results.

In good quality rock masses, such as the one in the Bemposta underground complex, the

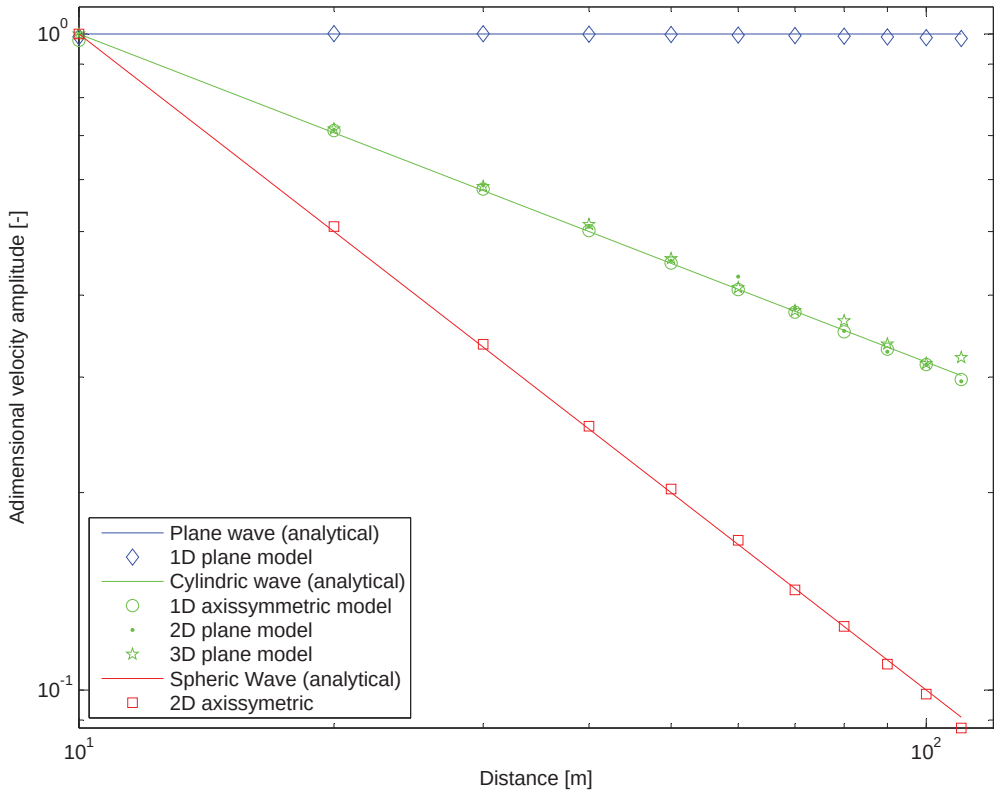


Figure 5.45: Non-dimensional peak amplitude plot of numerical models' and analytical's cylindrical and spherical wave attenuation.

geometrical attenuation is predominant in the vicinity of the blast and becomes less important as the wave front curvature gets less pronounced.

5.5.4 Modelling of the Bemposta test

The dimension and complexity of the Bemposta site make it too large to be represented in one single model, so two and three dimensional partial models were developed. From them, conclusions about the importance of the method of generation of the blast waves, tunnel geometry representation, input function and rock material modelling can be drawn.

Modelling of blast wave propagation is in itself still relatively uncommon. Many papers on the subject use attenuation laws or, more recently, artificial intelligence techniques such as neural networks, but publication of descriptions of the steps of modelling process is not frequent rendering the whole process still obscure. The intention of this section is to shed some light on this modelling process, with an emphasis on some of the available paths and how the final result is influenced by these choices.

Numerical modelling of rock

Constitutive models which can be used to model rock and soil material are briefly laid out in section 3.2.4 of chapter 3. The sophistication of the existing models allows the faithful reproduction of stress-strain relations in rock materials. These may include non-explicit forms of fracture representation in the rock mass, non-linearity or plasticity. For dynamic problems, the frequency-selective degradation of wave amplitude with distance or cycle number can also be modelled via the material's constitutive model or through the introduction of damping in the time-stepping algorithm. From elastic, reversible, continuous, undamped behaviour to hysteretic non-linear plasticity, there is a large array of possibilities and a sensible choice may refine the final results, but also lay a heavy burden on the parametrization of the simulation.

The most important rock mass qualities to be considered when evaluating wave propagation in a rock mass are the spatial zoning of rock properties and fracturing and the stress state distribution. It is the author's opinion that answering the following questions may help define the kind of modelling, in particular in what regards the ground material's model.

- What is the level of characterization of the rock mass geometry?
- Is there sufficient information about the materials response (field and/or laboratory tests or previous work on the same zone) to parametrize the model? If not, will the net return of a parametric study or back-analysis be positive?
- Will increasing the model's sophistication result in meaningful gains in the results?

The geotechnical characteristics of the rock mass in the test zone, described in section 5.3.1, showed that there are no marked macroscopic differences in the rock characteristics among the different zones of the test site: it is, in a several metres scale, uniform. The greater part of the rock mass is composed of migmatites with some intercalations of pegmatites occurring in the lower part of the Outlet adit. The geomechanical classification, using the Q-system, the Rock Quality Description (RQD), the Rock Mass Rating (RMR) and degree of fracturing (F) performed along the adits (figure 5.8) does not show dramatic changes from place to place and does not provide information as how to classify the volume between the adits. The migmatites do show relevant schistosity, but its attitude changes dramatically from place to place.

High *in situ* stress increases the dynamic conductivity of the fractures thus leading to higher propagation speed and lower peak attenuation due to reflections. Rock properties are also changed in a similar mannerdue to closure of microscopic voids and cracks. Chapter 2 discussed the fracture dynamic behaviour while chapter 4 showed how this mechanism can be reproduced using simple micromechanical models.

The influence of fractures in the dynamic rock mass response can be simulated in several ways. The most correct is to include fractures explicitly in the model with their real stress-

dependent stiffness. This requires their characterization through fracture dynamic compression testing, which is still in its infancy and available in very few laboratories around the world. Follows the utilization of an equivalent continuous material model with dynamic properties that increase with applied stress. A simpler alternative is to assign elastic stiffness in the model according to the available *in situ* stress, through a stress-stiffness law. Region-wise distribution of damping can be used to simulate the same effect, if damping parameters are assigned according to the stress state. Both methods require a trial-and-error fitting procedure, given that no information is available on how to relate the damping formulation or the rock properties to stress state.

A more direct and larger scale approach is the use of geophysical tests that provide a spatial distribution of compressive and shear wave speeds. Such tests are regularly used in rock mass characterization, but, unfortunately, not in this case. The P and S velocities obtained from direct testing in the rock cores are, of course, a valuable indicator, but they do not include the important scale effect caused by fracturing and weathering.

An elastic linear model is, therefore, used. The model's parameters, bulk (K) and shear (G) modulus are set uniformly in the whole model, including the concrete plug near the end of the Surface adit, which should not differ much from the rock. The bulk and shear modulus values were determined by a mixed analysis of the field and the laboratory tests, justified and explained in the following paragraphs.

When building any model, one of the most decisive decisions is the choice of materials' properties. In this case, a number of sources, both from laboratory and site tests, directly provide the parameters necessary for a linear elastic model: Young's modulus and Poisson's ratio.

In the geothecnical investigation for the construction of the new hydraulic circuit, good laboratorial characterization was performed: Young's modulus and Poisson's ratio and compressive and shear wave velocities of rock cores of the kinds of rock found in the underground complex (migmatites and pegmatites) were determined (table 5.3). As stated before, these values do not reflect the exact rock mass response because, in all near-surface fractured rock masses, properties taken from small samples are higher than field values. The large number of rock core tests and their distribution across the rock mass is, however, useful to establish an average value for the properties. The stress tensor tube and small flat jack, on the other hand, provide not only information on the stress state but also on the rock's elastic properties, and do so on a larger sized sample. Unfortunately, these tests were confined to two locations, both on the Outlet gallery, and the measured elastic parameters are very dependent on that location.

The parameters for the numerical models were extracted from other important and available source: the analysis of wave arrival times from the test blasts. When a sufficient number of

unequivocal wave arrival times could be extracted these were used to find a value for the compressive wave velocity (it was not possible to distinguish P and S wave arrival in most blasts).

The main reason for this choice is that it is directly related to the phenomenon to be modelled and at the correct scale. Remarkably, given that there are zones of the complex with quite different overburdens, there were no appreciable differences in the dynamic properties and the same value was used for the whole test site. The variation between sets, in different zones of the test volume, was of the same order as the difference among blasts in the same set. Results of the study of the *in situ* stress state, synthesised in figure 5.9, show that as a result of the high horizontal stresses the discontinuities are not much more alleviated near the bank than in the places where the overburden is larger.

In these test blasts, there is no direct way of knowing the time of the blast. This is unfortunate because it would have permitted the determination of wave velocity in all the blast-sensor paths. An indirect method was employed. As the acceleration records of the six accelerometer bases are synchronized and their distances to the blast point are known, it is possible to determine the detonation instant in the blasts that give three or more valid records and where there are no obstacles in the blast-accelerometer path. Since it is not possible to determine shear wave arrivals, only the P-wave arrival times can be determined. The P-wave velocity values were consistent in all the sets, with an average value of about 4000 m/s.

To determine a value for the shear wave velocity, it was postulated that the c_p/c_s ratio is constant in the rock cores and in the rock mass, *i.e.*, that the scale effect influences equally the shear and the wave velocity. This ratio, related to the Poisson ratio, is relatively immune to scale effects in all but very loosely fractured/disturbed rock masses (Barton, 2007). In the dynamic laboratory tests, this ratio's value was of about 1.63 in the rocks (migmatites and pegmatites, table 5.3) that occur in the test volume. If the same ratio is applied to the rock mass' P-wave velocity, a shear wave velocity of 2450 m/s is arrived at. As the input parameters for the FLAC3D model are the bulk and shear modulus, conversion yields 21.6 and 16.2 GPa, respectively. This is equivalent to assuming that the static and dynamic Poisson ratio is constant in laboratory and field, with a value between 0.19 and 0.20.

Wave velocity for the rock mass, determined through the test blasts, is between 11% and 20% smaller than the values for the migmatite and pegmatite rock cores. This indicates that, despite the relatively modest depth of the complex, the degradation of the properties due to fracturing and weathering is modest, confirming that fractures are closed. As for the density of the rock mass, a value of 2700 kg/m^3, as measured in the rock cores was assumed, since the scale effect from the rock core to the rock mass is usualy negligible (Barton, 2007).

In all excavations but, in particular, in those excavated by drill and blast, a volume of rock

around the excavation is damaged by the construction: the rock in this excavation damaged zone (EDZ) is softer and weaker due to fracturing which is microscopic and sometimes visible. This fracturing is a consequence of the high stresses and temperatures that occur during explosions, but are also due to the permanent radial and tangential stress distribution in the rock after the excavation. When blasting is carefully conducted (through the use of small charges and/or pre-splitting techniques) the EDZ will reach some tens of centimetres outside the tunnels, but in this case, the irregular surface of the excavation (see photographs in Appendix I) points to a larger volume of damage, maybe in the order of 1 to 3 metres (Persson *et al.*, 2001). The rock cores tested in laboratory were taken from boreholes drilled from the adits, but, unfortunately, as the site investigation was focused on the properties of the rock mass where new excavations will be done, and not on the existing adits' state, the tested cores were chosen at distances outside the EDZ. The reduction in the properties is variable with rock and blasting operation type, *in situ* stress or water level. Reductions between 1000 to 2500 m/s in the longitudinal waves velocity are frequent.

As stated before, the in-situ stress state was not considered in this calculation, so that there were no exterior forces applied to the model. An absorbing boundary condition was applied at all exterior free surfaces to simulate the situation in which the model is surrounded by an unbounded medium into which stress waves can travel indefinitely without reflections.

Two-dimensional model

The tests are inherently three-dimensional: the adits have curves, they do not run parallel to each other and blast wave propagation, originated in a small volume, propagates three-dimensionally. Nevertheless, two dimensional models, in addition to being more economical, can be effective in exploring some of the aspects of the modelling process. In this case, a plane model (figures 5.46 and 5.47) is used to simulate a cross section that intercepts the two adits involved in sets 1 and 2: the Outlet adit and the Surface adit. Although the two tunnels are not parallel, they are represented as such, as it is the only way they can be included in a 2D model.

Models' width and height are 61 and 48 m, leaving 10 m between the centre of each adit and the nearest boundary. Absorbing boundary conditions are installed at the base, top and sides of the model to simulate an infinite medium. Finite-difference zones are square shaped, except for some zones in the top of the adits, where some triangles are used. Zones' sides are 0.25 m long, which guarantees good transmission of waves with frequencies up to 1500 Hz.

Across the complex adits' cross sections dimensions are approximately constant, except for the irregularities typical of blasted excavations, and two limited areas: an enlarged area in the

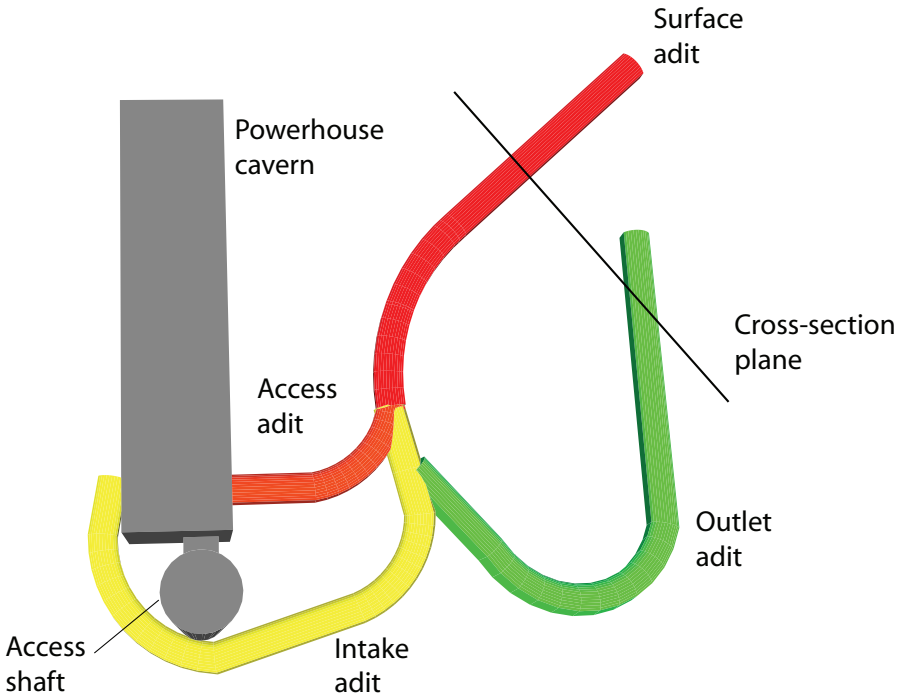


Figure 5.46: Underground complex showing section of the 2D model. The plane goes through the sections where P2-P3-P4 are installed in the Surface adit and sections where blast B15 was performed in the Outlet adit.

Outlet adit (sections PF61 to PF63), and a zone in the Surface adit (sections PF20 to PF21) where a cave-in occurred (as described in section 5.3.1 and shown in photographs in Appendix I). Figure 5.48 shows the superposition of a typical cross section and the model's, as surveyed topographically.

The blast is numerically simulated via a normal compressive exponential time-history (as explained in section 5.5.2) applied at the face of a zone on the wall of the Outlet tunnel, 1.5 m from the floor, in the location of blasts B13 and B15. Two different kinds of load were applied: a pressure/stress loading and a velocity loading. Figure 5.49 shows the velocity time-histories recorded at the wall of the Surface adit that faces the blast.

When the stress loading is applied at a free surface there is a rebound at the end of the loading which originates an inverted peak of smaller amplitude. The rebound intensity, frequency and duration depend on the way the source cavity vibrates, and this depends on its material and shape.

As the stress loading replicates reality better than the displacement, velocity or acceleration loadings, stress loadings were applied in all subsequent simulations.

Figure 5.50 shows the PPV along the three bases on the walls and floor of the Surface adit, P2, P3 and P4. On the same figure the test results of blasts B11, B12, B13 and B15 (which

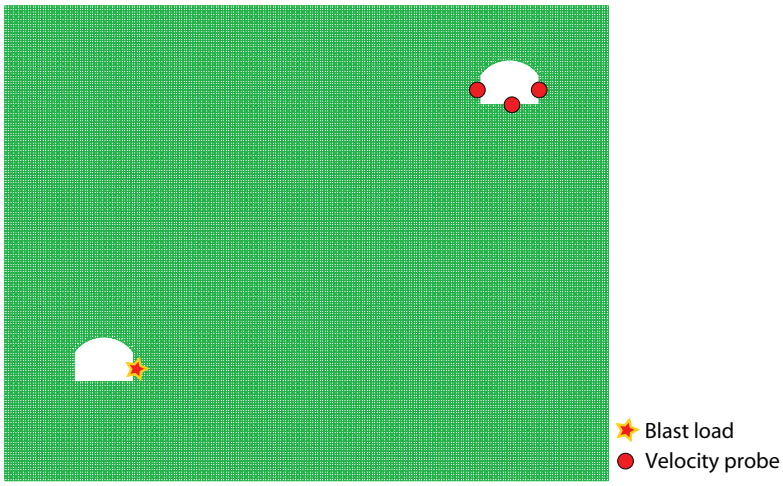


Figure 5.47: Finite-difference two-dimensional model of blast B15. The Outlet adit is in the lower left and the Surface adit is in the top right.

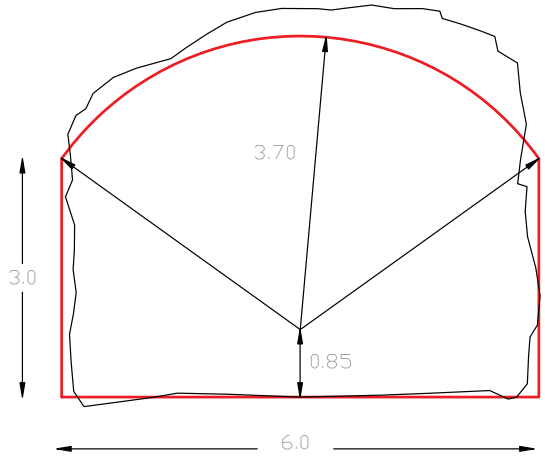


Figure 5.48: Adit's real cross section and finite-difference model representation.

were performed in the same area, see figure 5.14) are also shown. All results are normalized in base P2. The test blasts were performed near each other (distance between B11 and B15 is approximately 20 m) but the evolution from the wall nearer to the blast to the floor and from there to the opposite wall is not constant. Base P4, which lies in an indirect path from the blast source, always yields lower PPV, but from P2 to P3 PPV grows or diminishes without apparent justification. The two-dimensional calculation, however, shows itself able to reproduce, in average, the influence of the location of the bases in relation to the vibration source.

The limits of this model in simulating the test blasts are clearly related to it being two-dimensional. It can represent the wave transmission between the two tunnel sections but it has to disregard the fact that they are not parallel to each other. It cannot simulate the wave arrival at several spots along the Surface adit, for this, a 3D model is necessary.

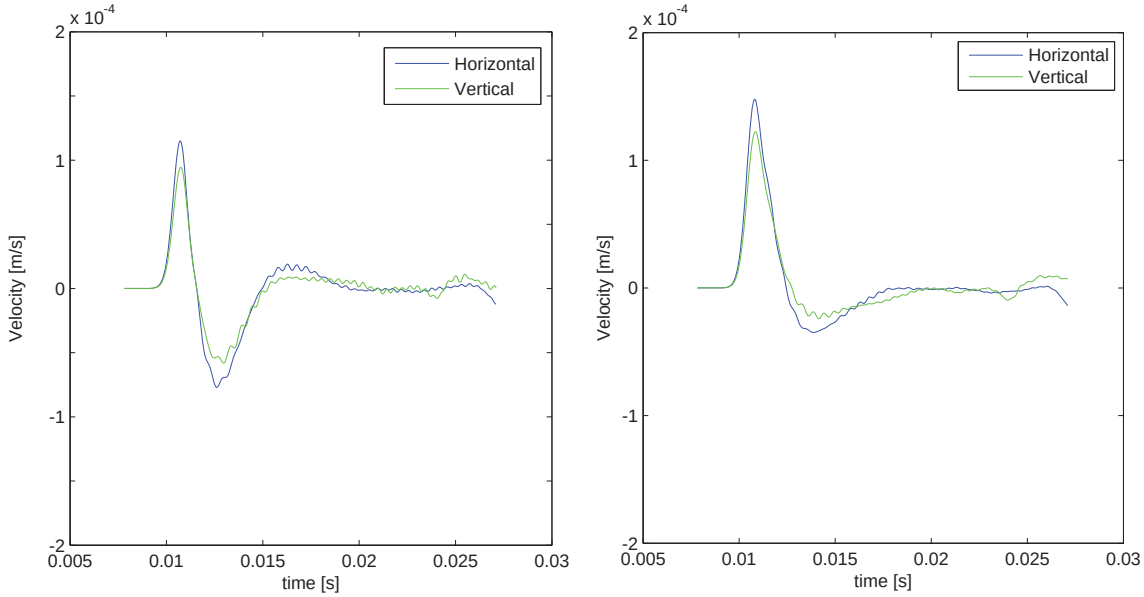


Figure 5.49: Velocity time-histories recorded at the Surface tunnel caused by stress (left) and velocity (right) blast loading in the Outlet adit.

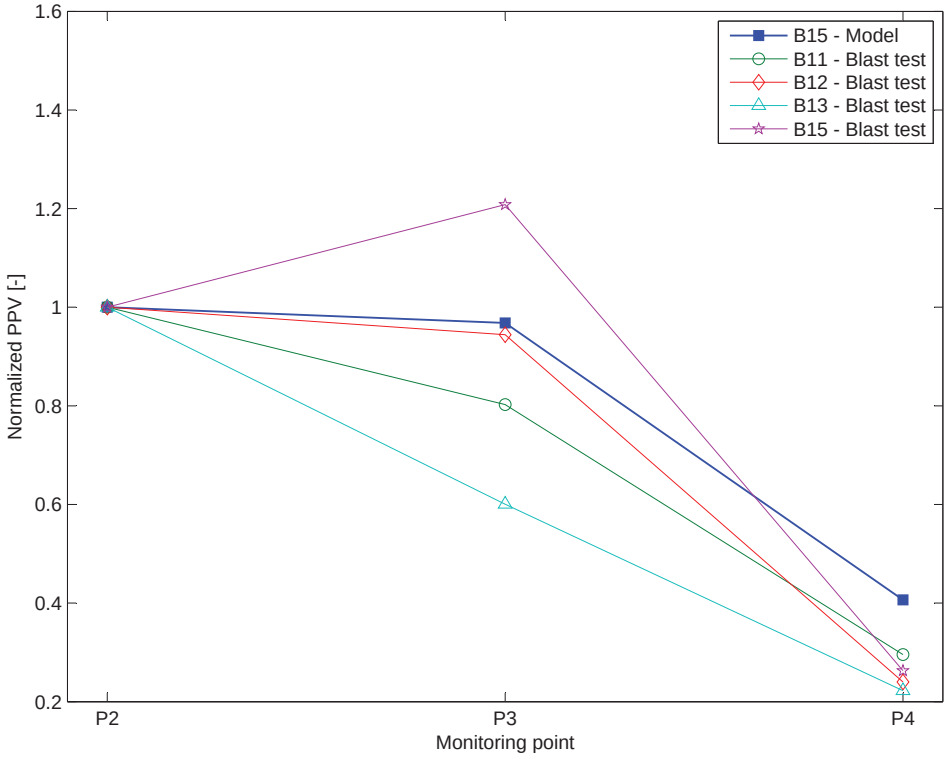


Figure 5.50: PPV in bases P2, P3 and P4, normalized in P2, from blast test and two dimensional numerical model.

Three dimensional model of the second blast set

The finite-difference grid, developed using FLAC3D's model generation functions, represents the straight part of the Outlet adit (where blasts of the first and second set were done) and the Surface adit (where accelerometer bases P1 to P5 were installed). The grid is 110 m long, 60 m high and its width varies from 40 m at the front to 110 m at the back. The adits are modelled by removing selected zones inside the model. The Outlet adit is excavated in the zone where it runs straight (between sections 59 and 66, see figure 5.11). The Surface adit is excavated from section 16 to the end of the model, being interrupted for approximately 5 m to represent the concrete plug near the end of the adit. Figure 5.51 shows the whole complex and the model bounding box while figures 5.52 and 5.53 show the finite-difference grid from several perspectives. As the adits are excavated in the grid, they are not visible from outside so their "negative" (the elements that are removed to represent them) are superimposed on the grid.

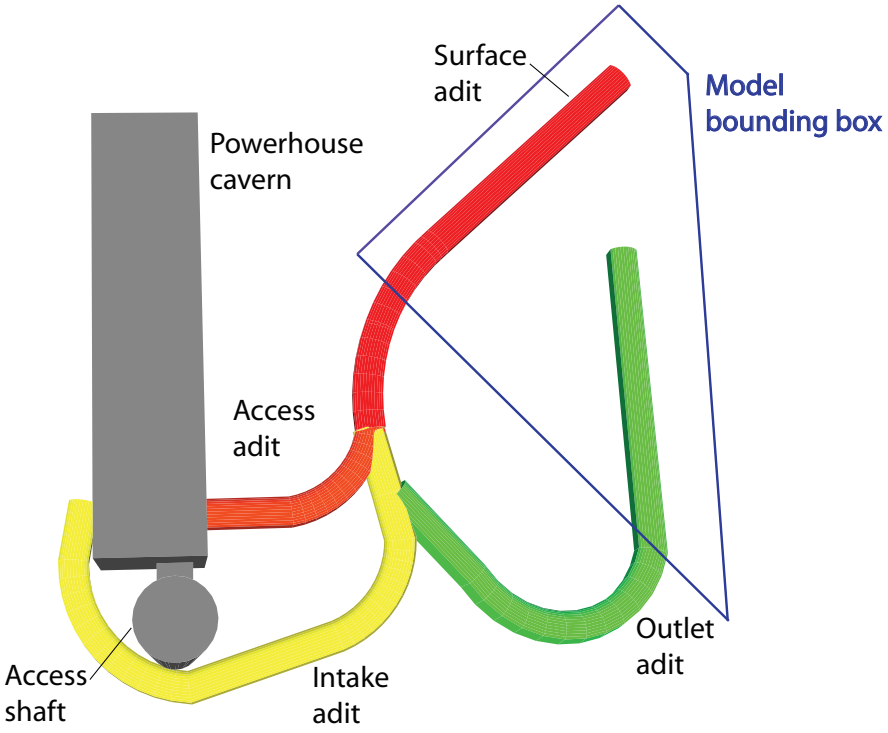


Figure 5.51: Representation of the underground complex showing the 3D model bounding box.

The adits' cross sections are shown in figure 5.54. The Surface adit, where the velocity measurements are made, is modelled in detail. The Outlet tunnel representation, on the other hand, is much less faithful since it is generated by deleting the zones that fall inside a 3 m distance from the adit's axis. If it were discretized with more minutia the model's grid size

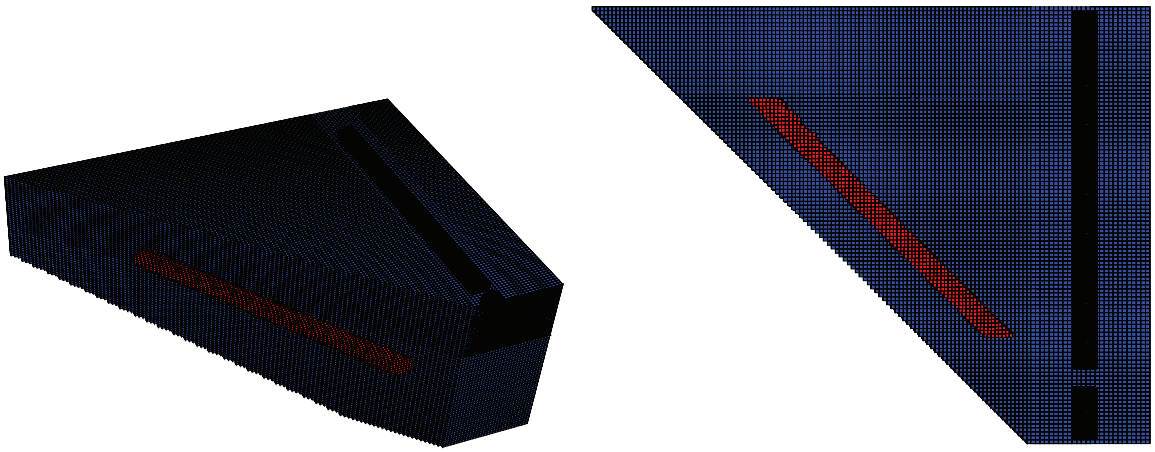


Figure 5.52: 3D model of the Surface and Outlet adits with the excavated adits' "negative" superimposed on the grid.

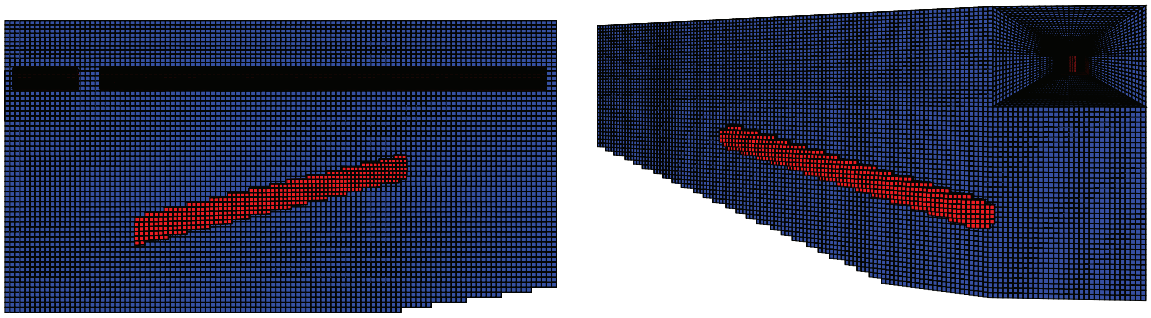


Figure 5.53: 3D grid of the Surface and Outlet adits with the excavated "negative" superimposed on the grid.

would be too big to run in the available hardware. This grid has 640,000 zones and 670,000 gridpoints, taking about 2 Gbytes of RAM.

Figure 5.55 shows the "negatives" (the zones that are removed from the model) of the Outlet and Surface tunnel in detail. As can be seen in the photographs of the adits, they are unlined. From the point of view of modelling economy, this is very advantageous, as the lining numerical representation penalizes the run-time. Shell or thin brick-shaped elements usually employed to represent concrete lining have stiff nodes that frequently become the most rigid nodes in the model, resulting in larger timesteps.

The Surface and the Outlet tunnels have slopes of approximately 10.5% upwards and 11% downwards. However, the Surface adit was assumed to be horizontal and the Outlet adit compensates with a downwards slope that is the sum of the two slopes: 21.5%. As the *in situ* stress state effect is not included in the model, only the relative positions of the tunnels mater, and this rotation does not have an influence in the results.

Figure 5.56 is a plan view of the model showing the locations where blast loads can be

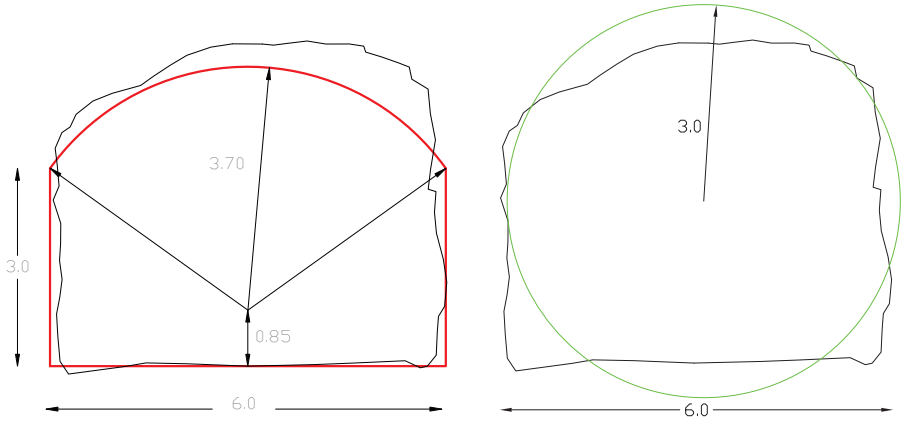


Figure 5.54: Surface (left) and Outlet (right) adit's real and 3D model's cross sections.

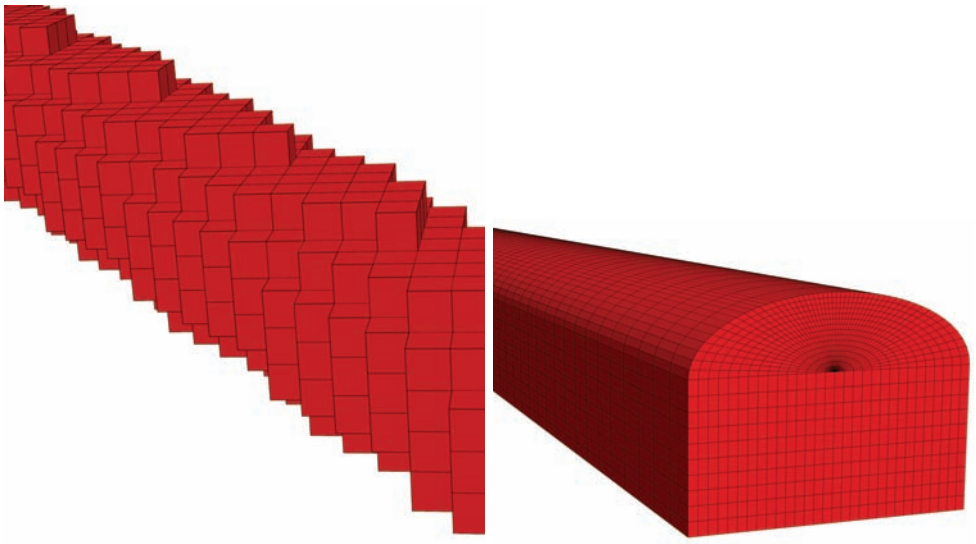


Figure 5.55: Detail of the "negative" of the Outlet (top) and Surface (bottom) adits.

applied and where gridpoints' movement is recorded. All loads and movement probes are at mid-height of the adits' walls, except for P1 and P4 which are on the floor. Figure 5.57 shows in detail the place where velocities are taken, while figure 5.58 displays the position of the blast load in detail.

The choice of the zone dimension is a compromise between model size and quality of wave transmission. Contrary to what is commonly done in static stress analysis, in wave propagation simulations it is not advisable to refine the mesh in the vicinity of the regions where a detailed result is desired and then smoothly increasethe zones' size in the direction of the borders.

According to the FLAC3D manual (Itasca, 2010), to faithfully represent one complete cycle of a monochromatic sinusoidal wave in FLAC3D, between 6 and 10 zones should be used (see

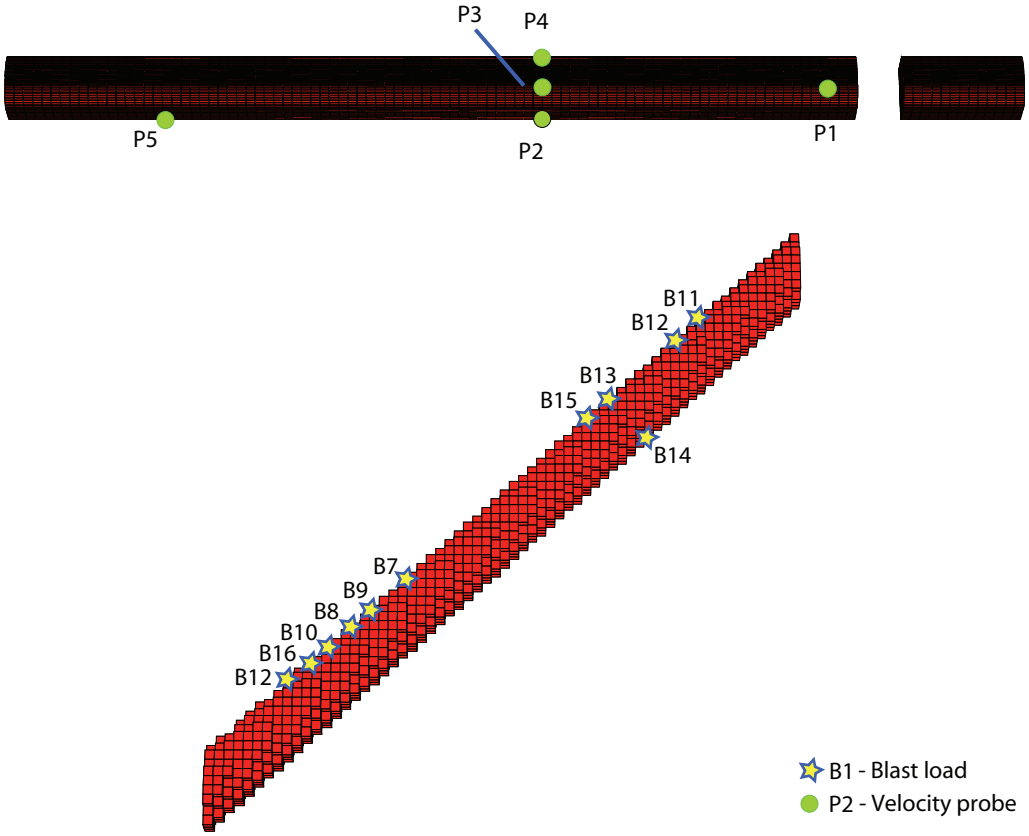


Figure 5.56: Plan view of the adits "negative" with location of blasts (blue and yellow stars) and accelerometer bases (green circles). All blasts are in the adit wall as well as measurement bases P2, P4 and P5. Remaining bases P1 and P3 are on the floor.

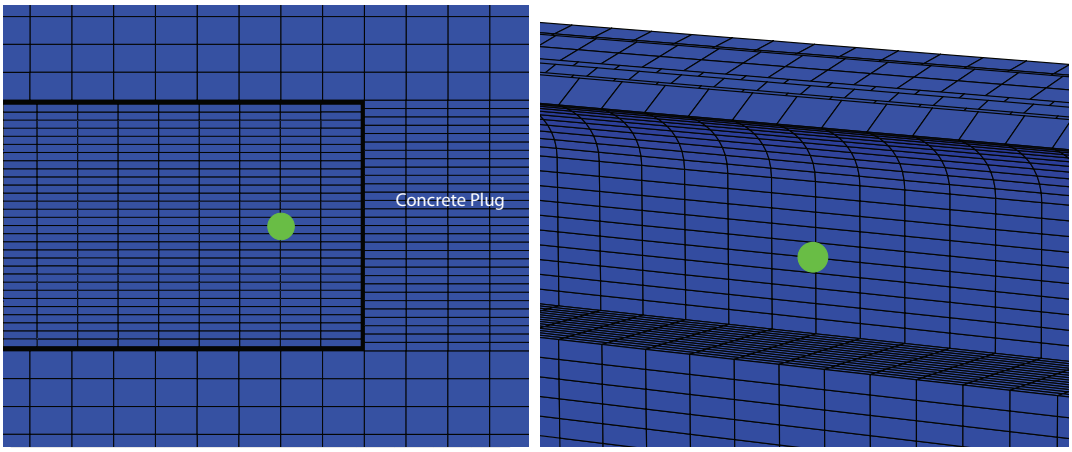


Figure 5.57: Plan view of the Surface adit near the end concrete plug showing the velocity measurement point P1 (left). Perspective of the velocity measurement points in the Surface adit's walls (P2, P4 and P5) (right).

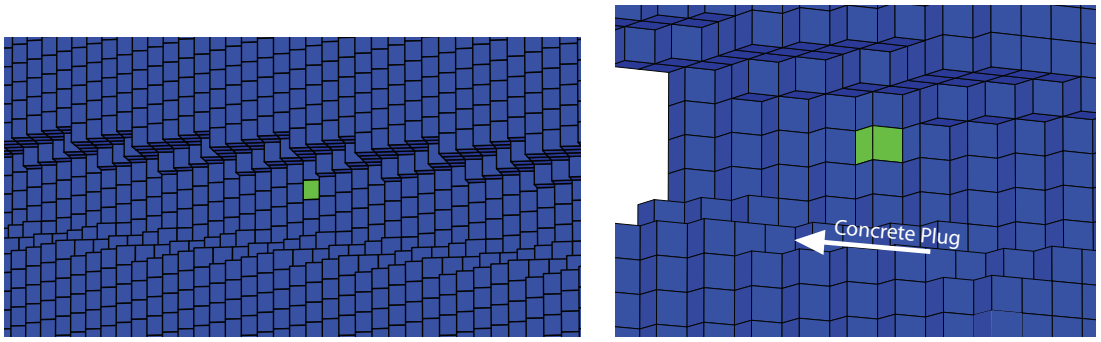


Figure 5.58: Perspective of half section of the Outlet adit with the zone where the blast is applied (left). Detailed view (right).

figure 4.29). If the zone's length is l_z, the smallest wavelength is:

$$\lambda_{min} = (6 \text{ to } 10) \cdot l_z \tag{5.7}$$

Because the wavelength of a wave is the quotient of the wave's propagation velocity and its frequency ($\lambda_{min} = c_p/f_{max}$, for a compressive wave), and since the wave propagation velocity of a compressive wave (the fastest of the body waves) is a function of the material's elastic properties ($c_p = [(K + 4/3G)/\rho]^{0.5}$), the top frequency that can be correctly reproduced is determined by the zone length. c_p is 4000 m/s and the smallest zone size that results in a runnable model is 1.0 m:

$$l_z = \frac{c_p}{(6 \text{ to } 10) \cdot f_{max}} \Leftrightarrow 1.0 = \frac{4000}{(6 \text{ to } 10) \cdot f_{max}} \Leftrightarrow f_{max} = 400 \text{ to } 666 Hz \tag{5.8}$$

These frequencies are low when compared with the maximum frequencies of the signals recorded in the field tests, which go up to 1400 Hz in some of the short distance direct shots of sets 3 and 4. It was found, however, that the majority of the energy of the signal in the first and second sets lies in the 800 to 900 Hz range. The peak time of the blast load function was chosen to reflect this (figure 5.59):

When travelling across a finite-difference mesh waves loose quality, accumulating damage at each cycle. When their wavelength is larger than the 6 to 10 ratio, the degradation is taken as acceptable, but it will nevertheless take its toll if the wave travels long distances. This quality criterium is, however, subjective and made to suit general situations. In the author's experience, a case-to-case definition of what is an acceptable quality loss can be set. It should take into account the purpose of the study and the distances (or wavelength number) travelled by the waves.

In the current case, given that only the peak of the waves is necessary (in contrast to what was shown in the previous chapter where the complete waveform was captured and used), and

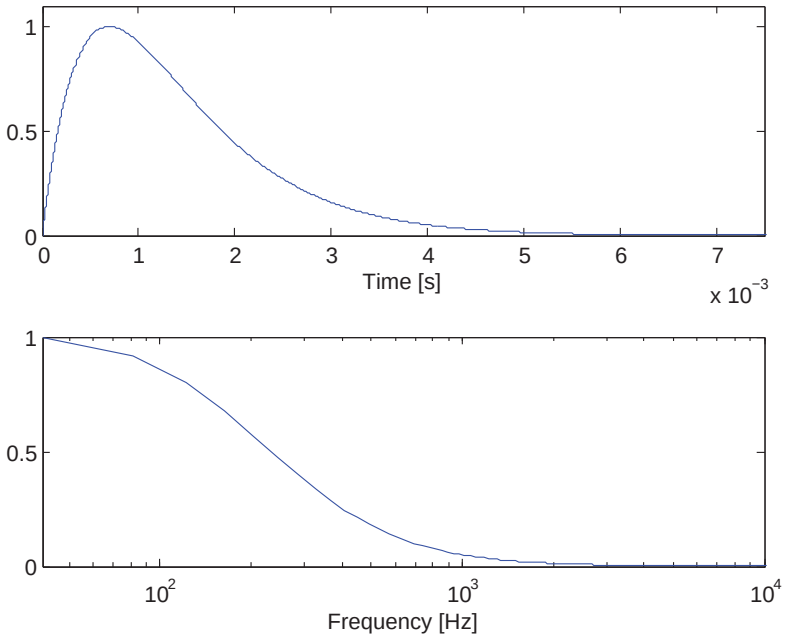


Figure 5.59: Plot of the blast load function (top) and its frequency content (bottom).

taking into acount the general dispersion of results, the wavelengths and the distance between the tunnels, it was found that a grid with 1 m sided elements could performed acceptably.

To confirm this, two simpler models without the Surface tunnel were created. The models's grid size was 0.75 and 1 m. Blasts were generated in the Outlet tunnel and the waveforms were captured along lines originating from the blast. Waveforms and velocity peaks recorded along these lines showed no dramatic differences between both models.

The zones in a grid that uses the explicit technique to solve the motion equations should have similar sizes, so that all the gridpoints critical timestep is in the same order of magnitude. Unfortunately, the triangular zones in the top of the Surface tunnel are much smaller than the zones in the rock mass, which have sides of approximately 1 m. This causes the critical timestep to be controlled by those few triangular zones, becoming around 20 times smaller than the timestep of the hundreds of thousand zones in the rock mass. FLAC3D presents a strategy to alleviate the problem through a multi-stepping option that cycles less often through the gridpoints that have larger timesteps (Itasca, 2010).

The next sections describe a series of calculations that investigate the performance of the 3D numerical model and how options in the way the vibrations are measured, the blast is generated, the model geometry and properties input influence the response.

In all calculations presented in the next sections, the blast location was near that of borehole B15 (see figure 5.14). As described in section 5.4.2, blast B15 was performed in the final part of the Outlet adit. This blast of approximately 0.2 kg was recorded by accelerometers in the

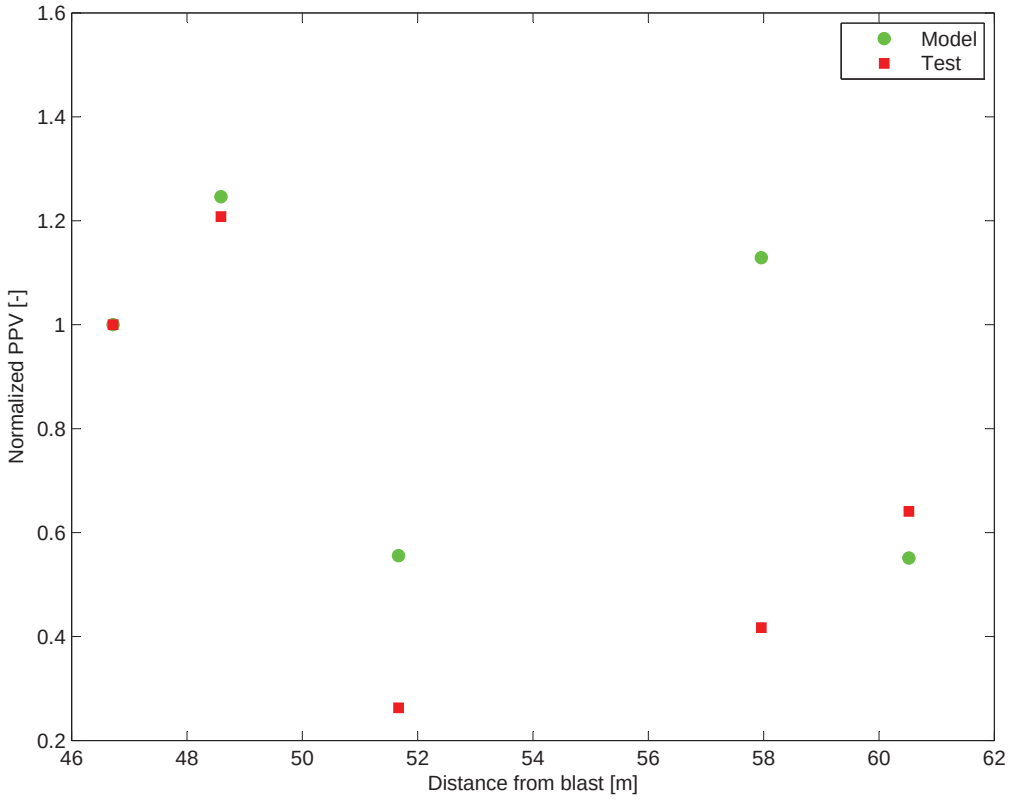


Figure 5.60: Comparison of the PPV from the test blast and the 3D numerical model. PPV in bases P1 to P5, normalized in base P2 from blast test B15 and two dimensional numerical model.

Surface adit (P1 to P5) and in P6, which is not represented in the model.

As the model runs, the velocity time-histories of gridpoints in locations equivalent to the accelerometer bases are recorded. The time-histories are then analysed and compared with the physical tests'.

Comparison with test blast

The result of the numerical simulation of blast B15 is shown alongside the same blast's test result in figure 5.60. Given the variability of the blasts results, shown in the previous sections (namely in the comparison of the two dimensional blast and the test) the match is reasonable to good in points P3, P4 and P5 (PPVs are normalized in P2). In P1, installed inside the concrete plug, the model visibly overshoots the test result. A refinement of the model in this zone of the model, presented later, will address this problem.

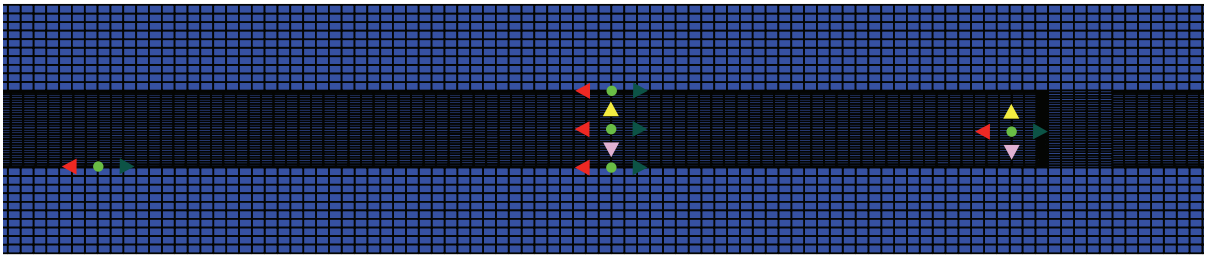


Figure 5.61: Plan view of the Surface adit interior showing the exact (green circles) and alternative (coloured triangles) measurement points.

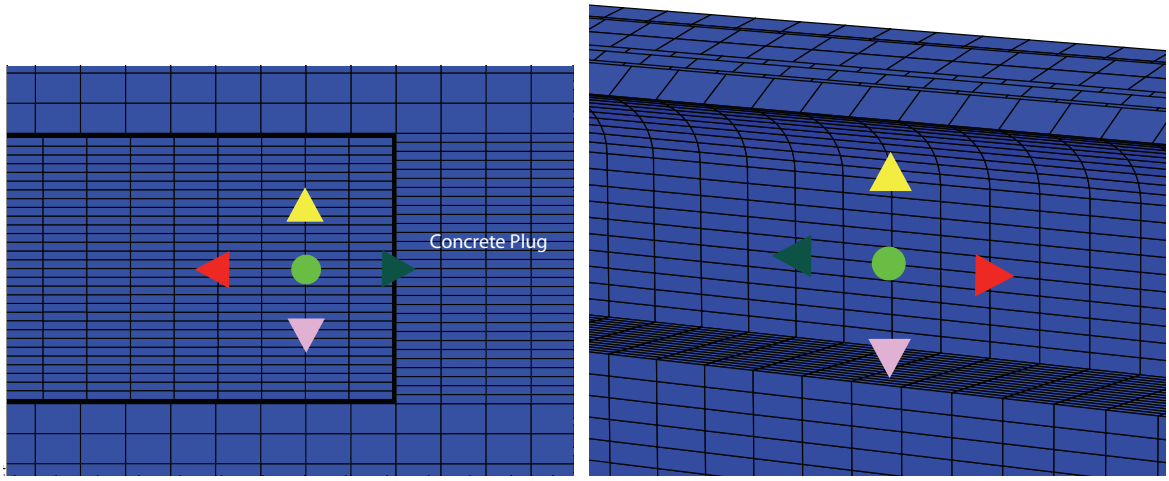


Figure 5.62: Plan view of the Surface adit near the end concrete plug showing the exact (green circle) and alternative (coloured triangles) point P1 (left). Perspective of the exact (green circle) and alternative (coloured triangles) measurement points located on the Surface adit's walls (P2, P4 and P5) (right).

Influence of the location of velocity measurement

This section evaluates the sensitivity of peak particle velocity to small changes in the measurement locations, both on the surface of the tunnel that receives the vibrations and inside the rock mass.

In the first part, the velocity time-histories are recorded in the location of the accelerometer bases P1 to P5 but also in gridpoints 1.5 m around, as represented in figures 5.61, and 5.62.

Figure 5.63 shows how the PPV evolves when the place where histories are recorded is changed. It may seem a surprise that such large variations in PPV are caused by small changes in the place where vibration is measured. Moving the probe in the direction of the adit's length ("Before", in dark green and "After", in red) has no expressive influence, except in P1, where the location "Before" is very close to the concrete plug that interrupts the adit, destroying the amplification that occurs in the floor's free surface. The fact that moving the probe away from the plug does not amplify the vibration significantly means that the original distance is already

sufficient to amplify the vibration.

When the probe is moved up ("Above", in yellow) and down ("Below", in pink) in the walls that face the blast (probes P2, P5), the effect is also considerable. Moving the probe away from the centre of the wall attenuates the vibration. This happens more intensely in P2, in the floor corner, that is more abrupt. In P4, located in the wall opposite to the blast, the lower probe receives more energy than the middle and top ones, which is explained by the fact that the blast comes from an inferior location.

When probes P2 and P1, on the floor of the adit, are moved closer to the wall that faces the blast, the vibration decreases and the opposite happens when it is moved away from the blast. In P1 the effect is smaller, perhaps due to the angle at which waves hit the adit and the presence of the plug.

There are two interesting conclusions from this analysis. Firstly, there is a large vibration amplification or attenuation due to small changes in the way they are picked up. Secondly, these tendencies should be even more pronounced when the size of the openings is scaled up (as in a large cavern).

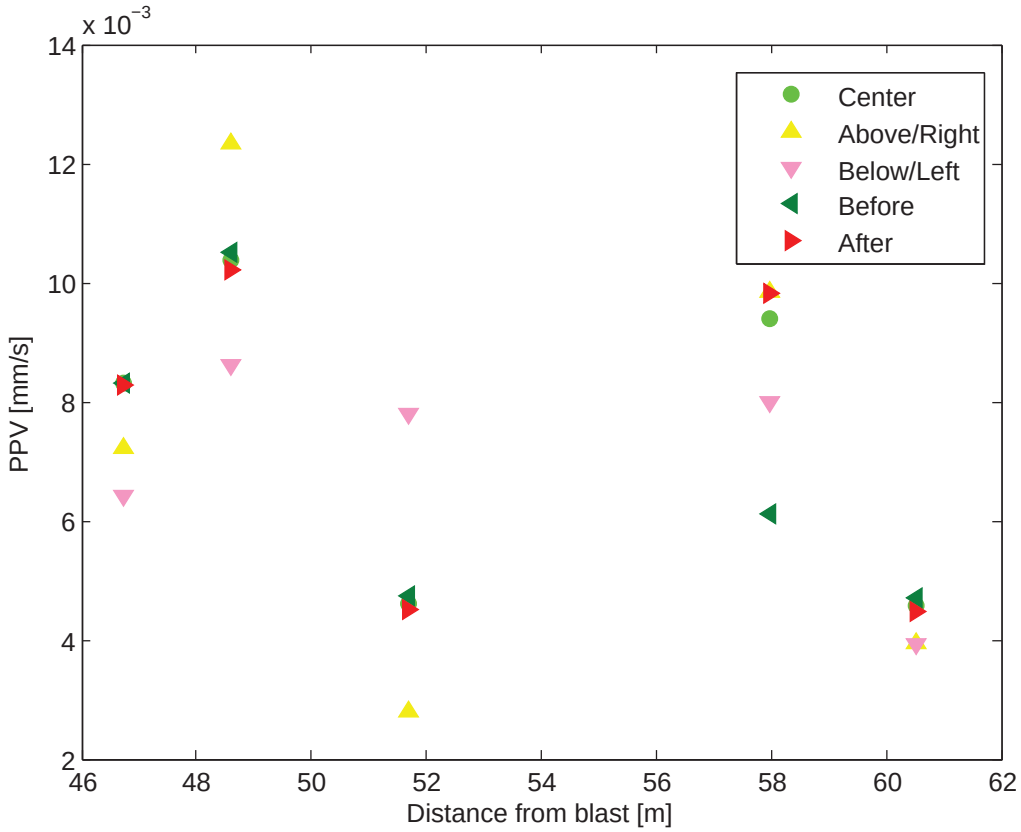


Figure 5.63: PPV evolution when place of velocity probing is changed in the Surface adit's wall and floor (from left to right: P2–P3–P4–P1–P5).

In the previous test, the location of the vibration measurements was changed in the tunnels' walls and floor. A second calculation was performed in which vibrations were measured inside the rock. In this way it is possible to estimate how the waves amplitude change when approaching the free surface. The alternative locations are along a line that starts on the correct location on the tunnel surface and enters the rock perpendicularly to the tunnel surface. Velocities are measured 1, 2, 3 and 4 metres inside the rock mass.

Figure 5.64 shows the PPV evolution with distance from the surface. The decrease in amplitude is explained by the free-surface amplification effect that occurs in the first three metres around the adit. The more oblique the path between the blast and the base, the smaller the amplification is. In base P4, given that the waves do not arrive directly to the wall, but more from above and below, there is no amplification at all.

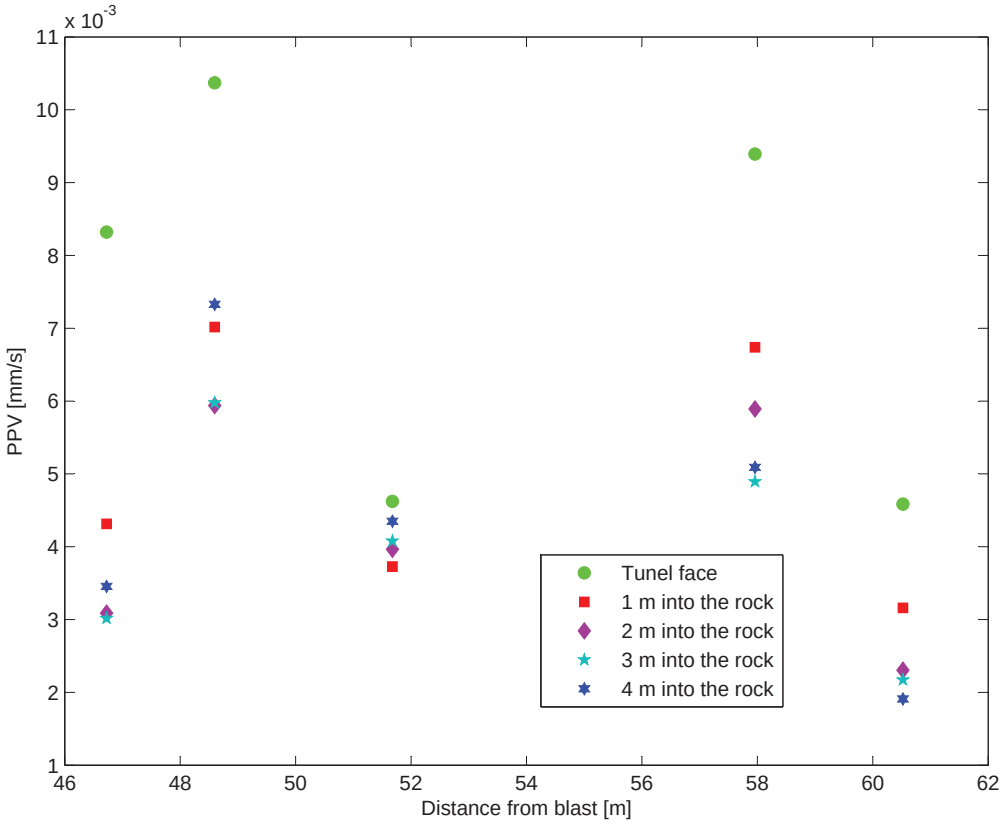


Figure 5.64: PPV evolution when velocity is recorded in the rock mass interior (from left to right: P2–P3–P4–P1–P5).

Method of load application

This section studies the effect of variations of the way the blast is applied. Five different models are run. In the first the load is applied in the visible face of one zone in the Outlet adit's wall, equivalent to the correct blast loading. In the other four runs, the load is applied in faces above, below, ahead and before the correct place. The purpose of this test is to find out how coherent the model is when small changes in the conditions occur. Figure 5.65 shows two perspectives of a longitudinal section of the Outlet tunnel with the central and alternative faces.

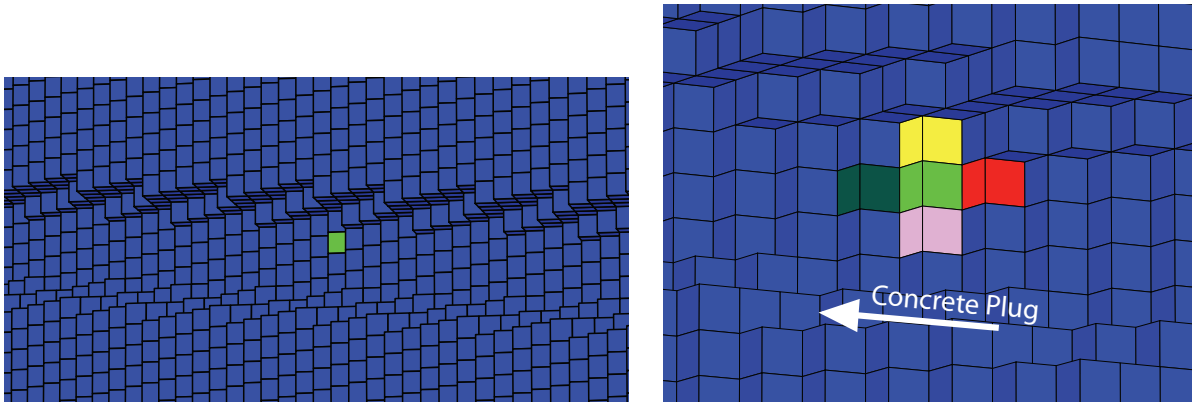


Figure 5.65: Perspective of half section of the Outlet adit with the zone where the blast is applied (left). Detailed view of the exact and alternative blast loading locations (right).

Figure 5.66 displays the PPV recorded at each probing station. It is not easy to find consequent explanations for the variations. The blasts "Below" and "Before" the correct position result in higher PPVs, while "Above" gives less intense vibration. The most solid explanation is that the opening where the blast takes place is excited by the blast and vibrates with greater amplitude when the load is applied in a flatter surface. A more detailed representation of the tunnel is necessary to confirm this hypothesis. Vibration intensity in P5, the point farther from the blasts, seems to be insensitive to this effect.

Influence of the adits length

In the model's grid, the Surface and Outlet adits are simulated by removing zones where they run straight and are omitted in the curved zones. In the Surface gallery, zones are also not removed in the location that corresponds to the concrete plug.

To investigate if this simplification of the adits' path influences the results, two models were run. In the first model, the Surface adit is excavated from the back to the front face of the model (it does not stop at the curve and the concrete plug is not represented). In the second

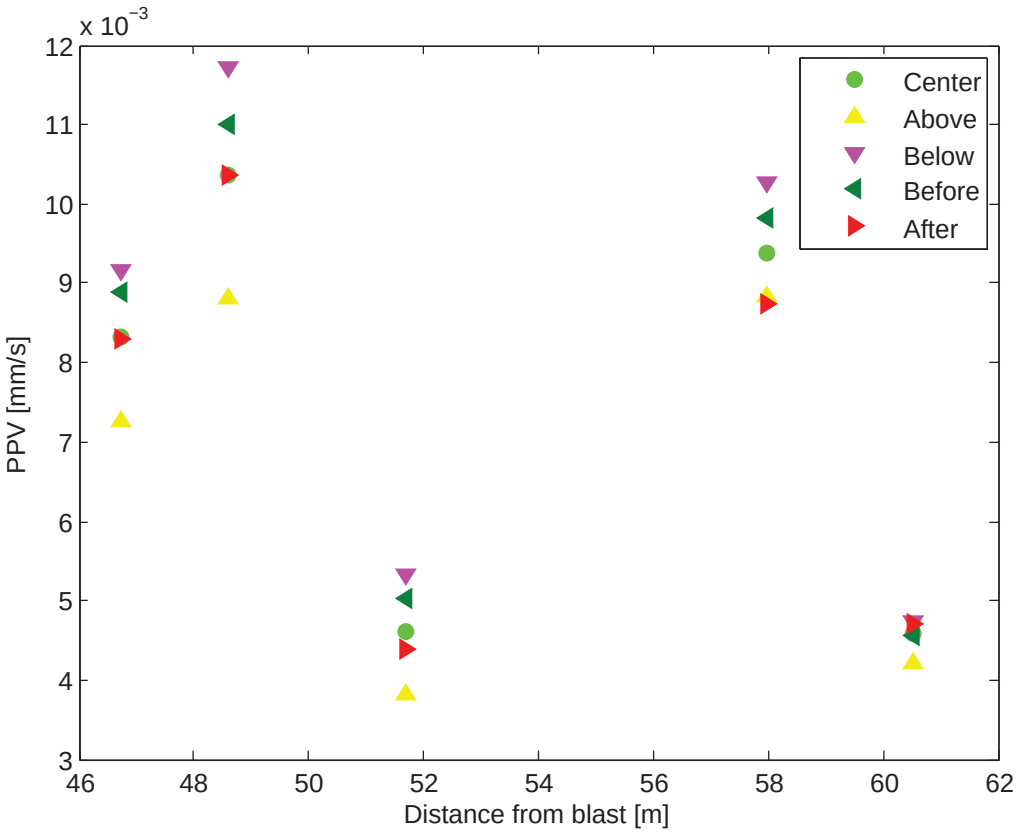


Figure 5.66: PPV evolution when place of blast is changed (from left to right: P2–P3–P4–P1–P5).

run, the same thing is done in the Outlet adit.

This calculation tries to find out how important a more refined representation of the adits and the plug really is. The conclusion, as shown in figure 5.67, is clear: it is not important at all. This confirms the option of not modelling the adits' curvature which would make the model much more difficult to develop. It should be noted that another useful calculation would be to simulate the Surface adit curvature in the local of P5.

Influence of Excavation Damaged Zone

It is well known that the material around an excavation, in particular excavations performed by blasting, presents weaker mechanical properties and higher permeability (this was discussed in section 5.5.4). This zone is called the Excavation Damage Zone, or EDZ.

In a numerical model it is possible to qualitatively assess if this change in properties significantly changes the way vibrations are transmitted. The EDZ was simulated by decreasing the elastic properties bulk and shear modulus in an annulus two metres wide around the Surface adit, as represented in figure 5.69. In excavations in rock, the degradation of properties is not

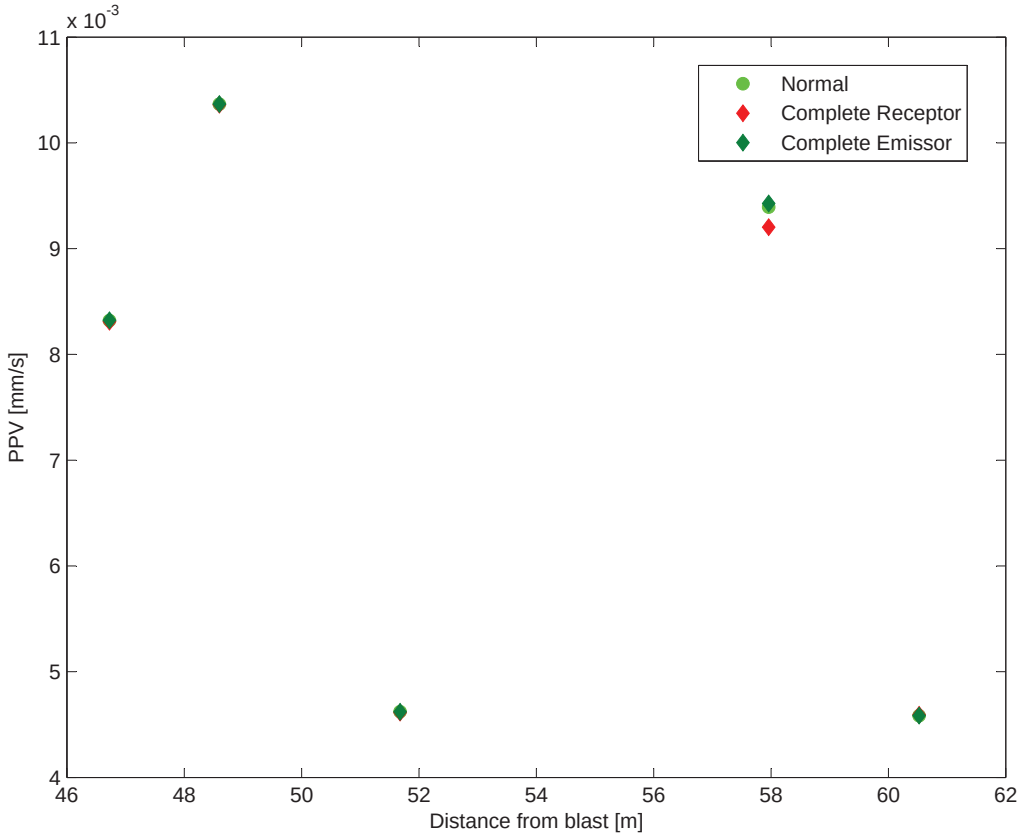


Figure 5.67: PPV evolution due to changes in the adits length (from left to right: P2–P3–P4–P1–P5).

abrupt, as shown here. The variation of properties is gradual and it may even not be monotonic, as the excavation-induced peak in tangent stresses around the opening can cause the properties to rise above the virgin rock's (figure 5.68). The length of the zones around the tunnel is of the same order as the EDZ's depth so the gradient cannot be reproduced adequately.

When a stress wave crosses the interface between two materials of different elastic properties, the amplitude of the wave (in terms of velocity) changes proportionally to the ratio of impedances. As the EDZ stiffness is 30% of that of the remaining rock, the ratio of impedances will be $\sqrt{1/0.3} \approx 1.8$, and the increase in amplitude should be around this number. However, when a wave crosses an interface, a new wave is created: a reflected wave that travels back into the original medium with an angle given by Snell's law, taking with it some of the energy of the original wave. In reality, more waves, such as interface waves, can be created, but they are not relevant at this level of the discussion. Figure 5.70 shows that when EDZ is simulated, the PPV increases by a factor that is between 1.7 and 2.2. In the probes on the wall that receive the wave directly, P2 and P5, the amplification is 1.8 and 1.7. In the probes on the floor, that also receive the wave directly, the amplification is 2.1 and 1.9, while P4, on the wall that indirectly receives the waves, sees the greatest amplification: 2.2.

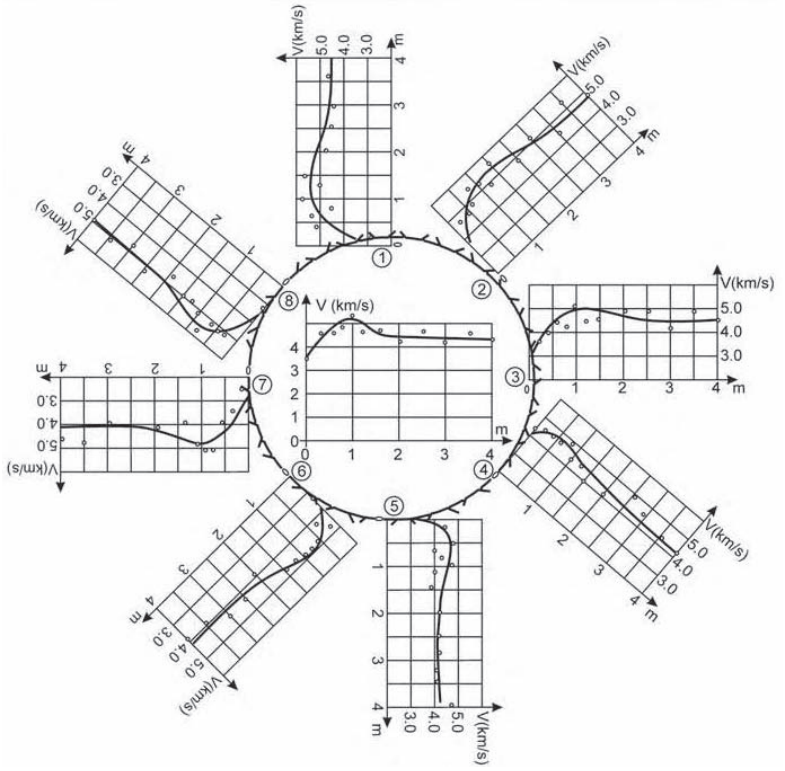


Figure 5.68: Seismic velocity variation as a function of radius in a blast-excavated pressure tunnel. Taken from Kujundzic *et al.* (1970).

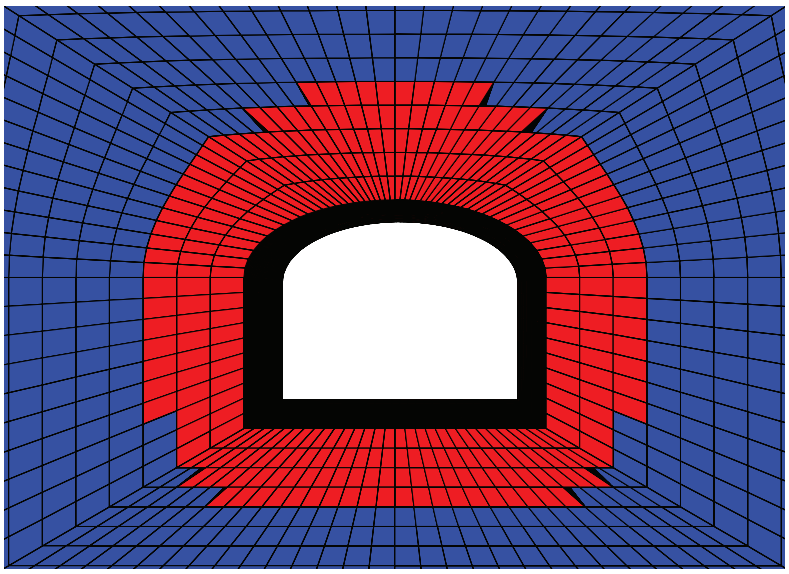


Figure 5.69: EDZ simulation on Outlet adit. Red zones have a 70% reduction in elastic properties.

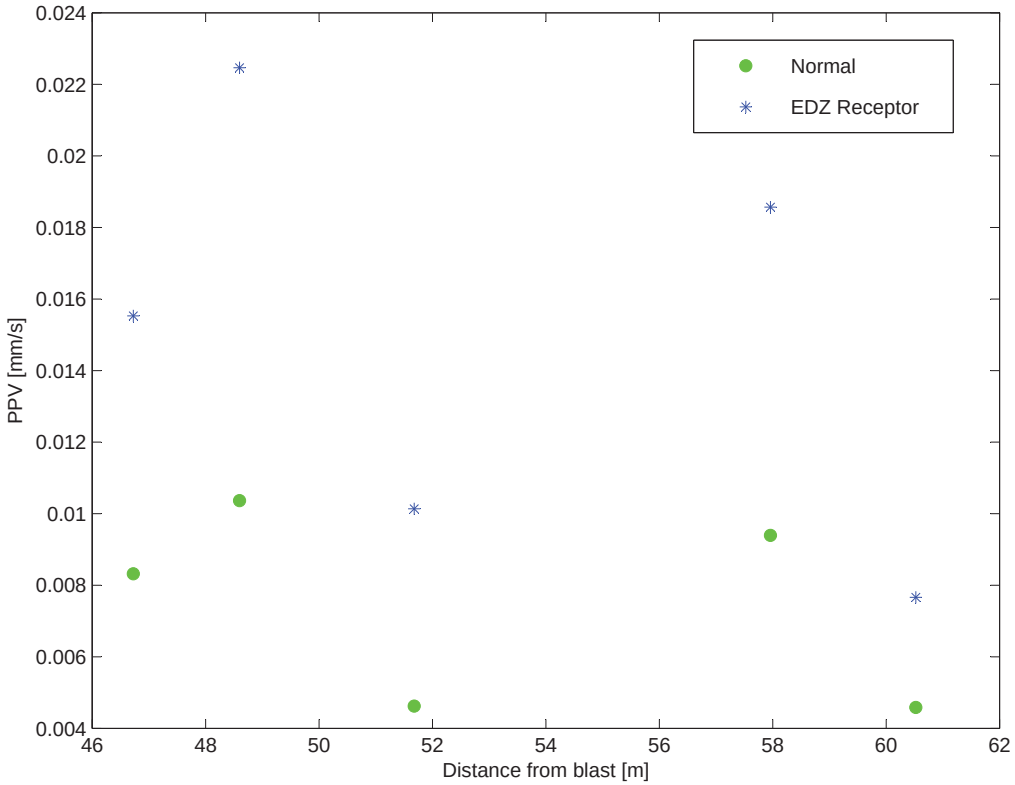


Figure 5.70: PPV evolution EDZ (from left to right: P2–P3–P4–P1–P5).

One other effect can also influence vibration in a degree that is not investigated here: the EDZ's depth (2 metres) is smaller than the dominant wavelengths of the blast wave (more than 4 metres). The wave, after crossing the rock mass/EDZ's interface, hits the wall. It is then reflected back into the rock mass and hits the interface again, where part of the wave is reflected back to the adit and part is released into the rock mass. A part of the energy can be "trapped" inside the EDZ, especially given that the model is run without attenuation. In real excavations, the gradual boundary of the EDZ prevents, or at least diminishes, this trapping effect, as there is no abrupt discontinuity in the material properties.

Detail of concrete plug discretization

The Surface adit ends at the surface. After the construction of the original complex it was sealed with a concrete plug. The plug (shown in photographs in Appendix II has a 5 m long hollow initial part (starting from the interior) where the base P1 was installed. In the models presented this far, this hollow part was not represented, as it was considered that the plug starts when it occupies the whole section, and base velocities corresponding to base P1 were picked from the floor of the adit.

This test investigates how a more realistic representation of the plug influences the vibration.

Figure 5.62 illustrates how base P1 was represented in the models so far while figure 5.71 shows the more detailed and correct situation. PPVs in figure 5.72 show that other bases' results were not affected by this change (both points are in the same position). The PPV in P1 is lower when the vibrations are measured inside the plug. The reference model, which did not represented accurately the plug geometry, grossly overestimates the vibration in this point (figure 5.60). This last calculation shows that this was due to a smaller free-surface amplification effect and illustrates once again that the model is very sensitive to changes in the way vibrations are measured.

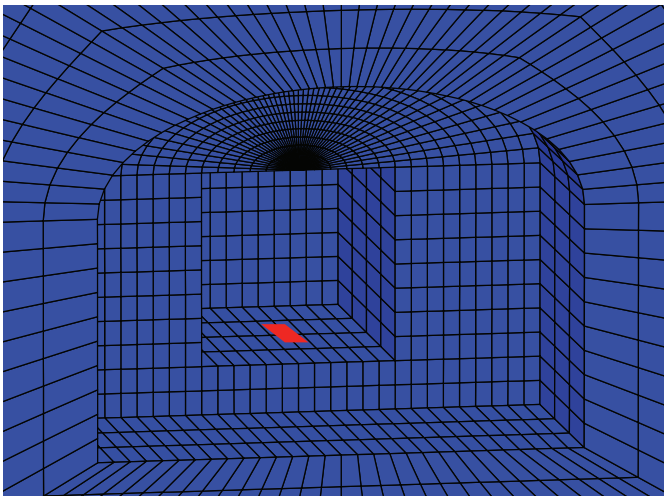


Figure 5.71: Realistic geometrical representation of the Surface adit's concrete plug and base P1.

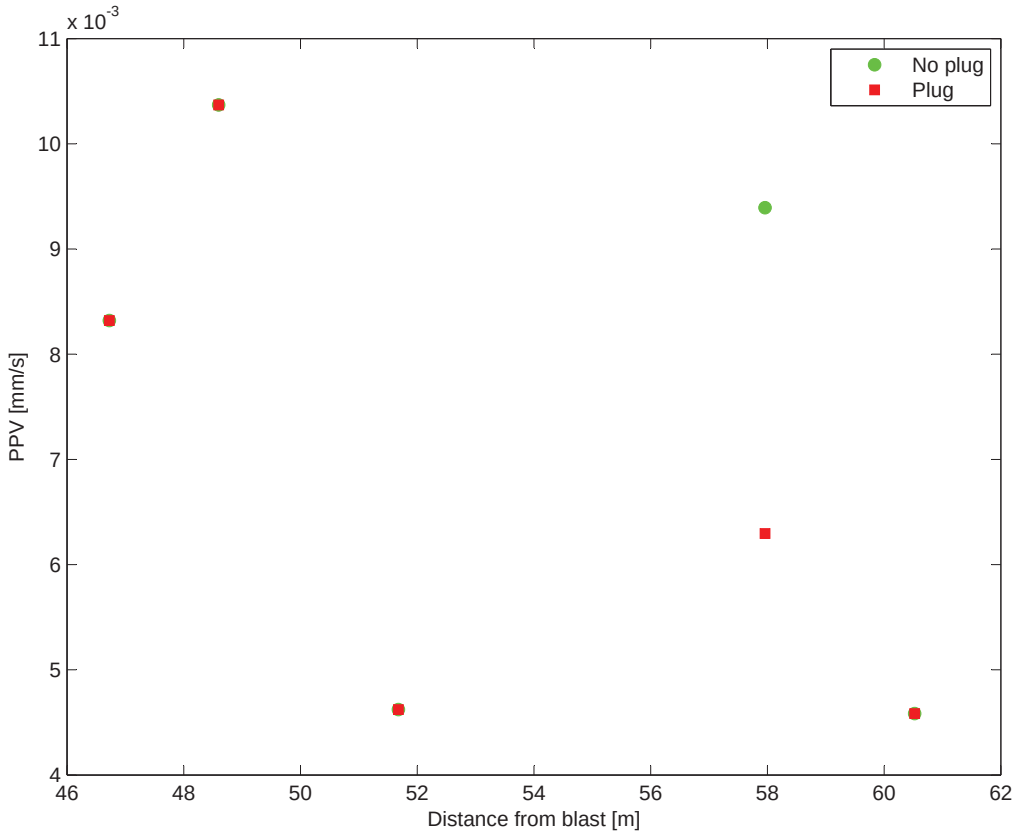


Figure 5.72: PPV evolution with realistic geometrical representation of the Surface adit's concrete plug and base P1 (from left to right: P2–P3–P4–P1–P5).

5.6 Discussion and future developments

This chapter's work is an incursion into the still very much uncharted territory of the numerical simulation of stress wave propagation in rock masses. The purpose of the study was to provide simple and relatively inexpensive tools for this purpose.

In the previous chapter the emphasis was on the detailed comprehension and simulation of wave propagation at a very small scale. From one chapter to the other there is a hundred to thousand-fold jump in scale. Obviously, the level information on the rock mass and detail in the model falls with the same pace.

The goal here is to grasp the factors that command wave propagation in a rock mass with several excavations and to develop models that capture the key aspects of the problem. Numerical models constitute an invaluable tool to support the resurge in the construction of large dams and upgrades that this decade is witnessing.

The chapter started with a description of the Bemposta dam site, the excavations existing in the river's right bank and of the upgrade works. The auxiliary adits where the blast test was performed were described in detail, as well as the relevant available information on the rock mass around them.

The test results were described and the results were analysed in two steps. An ensemble look showed that, even in such a controlled environment, the dispersion of the PPV is high. The main cause for this dispersion could be identified with the travel path of the waves. Followed a more detailed look in which the test was divided in sets according to the blasts and sensors locations. Through analysis of the sets and of some of the individual blasts it was possible to understand how waves propagate from each blasting adit to the others.

Numerical modelling of stress waves was then discussed: what are the requirements of a model that captures the main traits of the tests? The discussion that followed looked upon the possible geometrical representations of tunnels in rock, the simulation of rock under dynamic loading and blast representation and input.

Finally, blasting was simulated with two and three dimensional models. The first showed the possibilities of plane stress wave simulation, but also its limitations. With the three dimensional model it was possible to run a series of different models that studied the impact of the way vibration is picked up from the model, of the detail of geometrical representation, of the properties of the rock around the excavation and the input of the blast.

5.6.1 Contributions

This chapter's contributions are grouped in three parts.

First part comes from analysis of the blast tests. It show that a considerable part of

the vibration dispersion can be attributed to the path that stress waves go between their origin and the recording point. This is the most important factor affecting vibration levels in this underground complex, where the rock mass is of good quality and therefore no strong attenuation mechanisms are present. Even if this conclusion does not hold so strongly in other scenarios, such as when fracturing is more pronounced, it should always be reminded as very important, and it is out of the reach of attenuation laws.

The second set of contributions is on modelling wave propagation in rock masses with excavations.

The possibilities and limits of the conditions in which wave propagation can be simulated in one, two and three dimensional finite difference models were presented. The two-dimensional run and the parametric study of the test blast in three-dimensions helps in establishing the conditions for good numerical simulation practice in stress wave propagation and monitoring, while also hinting how deep a numerical analysis can go in exploration of this class of problems.

Partial conclusions throughout this chapter are assembled here in form of recommendations on how to conduct numerical simulation of blast stress wave generation, propagation and arrival in structures in rock masses.

The two most significant limitations of dynamic calculations are the characterization of the rock and consequent need of parameters for the material models, and the size of the models. Material models should be chosen carefully in accordance with the level of knowledge and the importance of the constitutive models sophistication weighted relatively to the other factors. Large models may exceed the available RAM memory or be too slow to run. It is established that stress wave representation demands minimum element size to wavelength ratios all across the domain. In situations that demand it, parametric studies of the element size can be worth considerable time savings with no perceptible decrease in the quality of the results.

In models with explicit integration algorithms, the maximum stable timestep is a function of the most rigid gridpoint. Radial discretization of small areas or volumes with triangular or tetrahedral zones results in very small timesteps. Multi-steeping techniques can only partially alleviate the problem.

The placement of models' limits must be carefully considered: is the representation of free-surfaces necessary or is the representation of an interior volume surrounded by absorbing boundaries that simulate an infinite medium enough? Viscous absorbing boundaries' efficiency decreases when the wave fronts hit them at shallow angles. If objects of interest are placed near this kind of model limits, parametric studies must judge if they are reflecting waves back into the model and if this is interfering with results.

The most important characteristics of load representation and stress wave capture were found. When motion is extracted in underground openings' surfaces it is amplified, so the

underground opening geometry should be faithfully represented and motion recorded in the gridpoint or node nearer to the more correct place. Adits and caverns' dimensions, corners, lining properties or the excavation damage zone should also be simulated as perfectly as possible since their influence can be important.

The geometry of the place where the blast is simulated does not seem to be so important, but it should emulate the basic shape of its real correspondent in order to retain its dynamic characteristics. Blast loads should be generated as stress/force instead of displacement/velocity/acceleration loadings. In the latter case motion in prescribed and the after-blast rebound effect cannot take place. The third and final set of contributions focuses on the control of vibrations in underground structures.

The regulations that limit blasting vibrations are focused on above-ground structures, mainly buildings. When protecting targets housed in caverns or tunnels, guidance on how to perform vibration measurement is, to say the least, scarce. Though this work is still insufficient to support the definition of definite rules, some general indications can already be extracted. Vibrations are significantly altered by excavations, so they should be measured both inside the rock mass outside the excavations' influence zone and in their openings. Since the shape of the excavations influences the way they are amplified appreciably, the placement of the sensors should take this into account. Contrary to what happens in buildings, where the energy enters the structure through its foundation and most of it is dissipated in the structure, excavations are surrounded by the medium that carries and transmits the energy, so there is no pre-defined pathway for it to enter and leave the structure.

5.6.2 Future developments

The room for improvement in observation, understanding and simulation of blast wave propagation in rock masses is great.

As for the blast tests, the synchronization of the blast and the acceleration records and the measurement of vibration directly in the rock mass outside the influence of excavations would have been interesting. This would have allowed a more detailed characterization of wave velocities in the rock mass and the separation of the effect of cavities in the stress waves.

Monitoring of the dynamic stress or strain in the rock, concrete and rock bolts in the support in the powerhouse cavern, more difficult to perform, would also allow for a new level of analysis of the excavations and interaction with their support.

A relationship between the instantaneous blast charge and the load function needs to be established for the most common blast charge type. It is not clear if there is a direct linear connection between the maximum instantaneous amount of explosive in each blast and the

amplitude of the load function or if the connection is more complex. This is one of the most important questions in modelling blast vibration, but must be addressed by a study with a larger range of blast loads under more controlled conditions.

It would have been interesting to simulate blasts from sets 1 and 2, using the same model, and from other sets, in new models. It is also planned, in future developments of the work, to perform simulations of the excavation of the new hydraulic circuit and the vibrations effect on the powerhouse cavern and on the reinforced concrete slabs that support the equipment.

Although three-dimensional calculations are becoming standard in geomechanics and multi-core processors and cheap memory make them more accessible every day, it will always be easier to perform two-dimensional calculations when the results are equivalent, if not only for the simplicity in the model generation. In blast wave propagation, however, the use of these latter models is limited due to the nature of wave expansion from the source. To achieve practical three-dimensional simulations, there are still difficulties such as the generation of the grid. Three-dimensional detailed representation of excavations is extremely challenging, adding to the fact that dynamic calculations demand constant elements' sizes all across the model. Recent developments in computers processors (multi-core technology with large built-in cache memory) make them particularly suited to run large models, and simulation software has been adapting to this reality. Another emerging trend is the distribution of calculations across a large number of processors which are accessible via the internet–cloud computing.

The area in greater need of improvement is probably the rock mass (rock material and joint) characterization. There are many sophisticated numerical and material constitutive models but little knowledge on what parameters to employ. This is true also in static calculations but even more evident in dynamic problems such as this one.

Properly calibrated micromechanical numerical models can be a great help investigating static and dynamic properties links or scale and fracturing effects, but they are still in their early days.

Next chapter will also look upon a real blasting problem on a ten times larger scale but this time at the surface. The level of information on the rock mass is also much smaller so different techniques for the investigation of the way stress waves behave are used.

Chapter 6

Vibration Monitoring, Control and Analysis in Large Scale – Deepening of the Leixões Harbour

6.1 Introduction

6.1.1 Background

This chapter describes a statistical and numerical investigation of vibration attenuation in a large area, based on the vibration monitoring of the project of deepening of the Leixões Harbour. This is an important harbour in the North of Portugal that is set in a densely populated urban area. A large volume of submerged rock had to be blasted and the Douro and Leixões Harbours Administration (APDL) requested that an institution independent from the construction company monitor vibrations. The Portuguese National Laboratory for Civil Engineering (LNEC) was contracted for that purpose and the author, by then starting work on this area, was actively involved.

Upon completion of the blasting, LNEC was again contracted to provide the Harbour Administration elements to assess on the fairness of the complaints from the population, mainly related to cosmetic cracking in the interiors of buildings. The Portuguese blast vibration norm only takes into account damage in constructions, making no direct provisions regarding disturbance of the population. Vibrations measured at the monitoring points were extrapolated using the classical method of fitting an attenuation equation with the general formulation $PPV = f(W, R)$ and equations associated to 50% and 95% percentiles were estimated for the whole affected area. This allowed the Harbour Administration and the blasting companies ad-

dress complains according to the limits set by the Portuguese vibration standard DGQ (1983).

A second estimation method, also introduced in chapter 3, was used. It employed Multilayer Perceptron Neural Networks on the same data set used to fit the attenuation law. The neural network and the attenuation laws were applied to the real blasts charges and locations and peak particle velocity distributions were estimated for the region around the harbour, allowing iso-velocities maps to be drawn. These were compared with measurements made by the blasting company and another independent official body (Faculty of Engineering of the Oporto University) in several buildings and a good match was registered.

Finally, numerical modelling was employed to investigate possible causes of the high dispersion of vibration maxima. Contrary to the statistical methods used during the construction, numerical models can test scenarios that can cause variation of vibration evolution with blast type and location, ground properties and singularities. To test these different hypothetical scenarios a simple finite-difference model of a part of the harbour is built and peak particle vibration maxima caused by blasting in the harbour is recorded and analysed along.

6.1.2 Vibration monitoring in urban areas

Rock blasting in urban environment was mentioned in the introductory chapters. This area of vibration control fits this chapter perfectly, so some aspects are again discussed before the description of the blasting works.

Rock blasting in urban environment has negative impacts which must be carefully handled. Ground vibrations are usually the most aggravating. They damage buildings and sensitive equipment and, even when consequences are not visible and lasting, populations are disturbed.

Vibrations impact is a function of intensity and frequency content. These depend mainly on the blast load per time delay, on the distance from the blast location and on the geology of the soil crossed by the waves between the blasting point and the target. Other relevant factors are the type of rock where the blast occurs and the geometric configuration of the blast, such as the existence of free surfaces, borehole depth and angle. When blasting is underwater, as in this particular case, another factor to be taken into account is that boreholes are submerged and water is not only a variable overload on the rock mass (due to the different blast depths and tides) but also an extra path for the propagation of vibrations (compressive waves). The presence of water in boreholes also changes the transmission of the detonation shock wave to the rock mass.

In urban blasting it is impossible to monitor all structures that may be affected. This can be due to several reasons such as large blasting areas, high number of buildings or several simultaneous excavation fronts. As a consequence, the spots where vibrations are measured must

be picked carefully, having in mind two goals: the immediate protection of existing structures and future analysis that will try to extrapolate the results to places where measurements could not be made. Unfortunately, it is sometimes difficult to determine places where it is possible to safely install the monitoring devices and satisfy both requirements. In densely built urban areas the ground is covered by roads, buildings, parking lots, etc. making it difficult to find the kind of geological material in buildings foundations. To add to the complexity of the problem, the large number and variety of buildings difficult the definition of vibration limits, frequently leading to over-conservative decisions.

6.2 Description of the deepening works of the Leixões Harbour

6.2.1 The harbour and surrounding urban area

The Leixões Harbour is located in the metropolitan area of Oporto, the second largest Portuguese city with a population of 1.6 million. Set on the mouth of river Leça, the harbour is crossed on the Eastside by a 6-lane motorway (figure 6.1).



Figure 6.1: Leixões harbour aerial view. Taken from http://www.apdl.pt.

The ground's geotechnical characteristics are not thoroughly available. The underlying rock mass consists of fractured alkaline granite, with a medium to coarse grain size. Outcropping schist formations are visible at the transition from land to sea. The soil overlying the rock substratum inside the harbour area was deposited there during construction. With the exception of the beach, North and South of the Harbour, the terrain is almost completely built on. From contacts with the population it was learned that a number of buildings have shallow foundations on sand deposits of unknown extension and depth.

6.2.2 Blasting description

Rock blasting took place between December 2005 and August 2007. This work only considers blasts up to December 2006. The purpose of the blasting was to lower the bottom of the harbour to twelve metres below average sea level. This was the necessary height for Panamax-class ships navigation in harbours. The depth of rock to be blasted, after dredging of sediments, varied from less than one metre to little more than three. The blasting area included the interior channel and docks and the turning basin, which is the large area outside the coast line defended by the breakwaters, used for ship maneuvering and loading/unloading oil-related products.

Three different companies operating the same number of drilling and loading barges were involved, meaning that at a given time drilling and blasting could be performed in three different areas of the harbour.

The *modus operandi*, except for a few minor differences, was similar. Each blast consisted of successive detonations in boreholes arranged in a regular mesh with 2.0 to 2.5 m spacing. The number of boreholes per blast went from one (very rarely) to more than twenty, arranged in several rows. Electronic delay caps were used to reduce the instantaneous charge but in the occasions when the number of boreholes was higher than the number of available caps two or more columns were detonated simultaneously. Figures 6.2 and 6.3 show photographs of the drilling, blasting and blasted rock loading.

6.2.3 Monitoring

LNEC was contracted to monitor vibrations independently from the construction companies, which also measured all blasts to adjust plans on a day-to-day basis. Having been contacted just prior to the start of the construction, LNEC had no intervention on the preparation of the blasting plan or in the pre-blast survey.

Monitoring points were chosen between the blasts and the built areas, and also in some of the most representative structural typologies. Due to the characteristics of the work, the monitoring plan was continuously adjusted over the time. Figure 6.4 presents the location of



Figure 6.2: Drilling barge in the rotation bay during drilling operation (left). Two of the three drilling barges in the rotation bay wait while blasted rock is picked from the bottom (right).



Figure 6.3: Close up view of the pick-up and loading of blasted rock into the barge (left). Detail of a barge's drilling boom in repair (right).

all the monitoring points, while figures 6.5 and 6.6 show the diversity of structures present in the area around the harbour.

Three 16-bit Geosig macro-seismometers, model GSR-16, were used. As mentioned, their location had to be changed frequently to follow the location of the blasts, to address complaints from the population and to adapt to the peak velocities in each location. Figure 6.7 shows a seismometer installed in monitoring station 1 (see figure 6.4).

The GSR-16 seismometer is a multi-purpose vibration recording device. Due to its versatility and configuration possibilities, it can be used in blasting or seismic monitoring. It houses three triaxially assembled force-balance accelerometers with a range of 4.905 m/s^2. The analogical voltage from the accelerometers is digitized using 16 bits meaning that a precision of $4.905/2^{15}$=1.49^{-4} m/s^2 is attained.

When the seismometer is active it continuously reads, amplifies, filters and digitizes the



Figure 6.4: Monitoring points location. Total length of the harbour from the end of the channel to the exterior breakwater is 2.8 km.



Figure 6.5: Reinforced concrete building with one basement and with foundation in unknown ground in Leça (monitoring point 4 was located in the basement of this building) (left). House founded on rock located North of the harbour (Northeast of monitoring point 18) (right).



Figure 6.6: Small rise buildings in different conservation states and in unknown foundation ground in Matosinhos, South of the harbour (monitoring point 11 was located in the second building from the left) (left). Cereal silos founded partially in rock and partially in soft soil Northeast of the harbour (monitoring point 7 was located at the top of the silos) (right).

signal and stores it in buffer memory, only recording in permanent memory the records of acceleration values which exceed a prescribed limit value. Since they depend on the level of existing noise, those values are defined site-wise. Therefore, when establishing new observation points, trigger levels were adjusted slightly above the ambient vibration. Setting triggers is, in some cases, difficult. If the trigger is set too high blasts of lower intensity are not recorded, whereas if the trigger is excessively conservative there is the risk that many false events are recorded, depleting the internal memory.

Each recorded event was set to last five seconds, of which one second corresponded to the vibration arriving before the peak that triggered the recording (which is not necessarily the



Figure 6.7: Geosig's GSR-16 macro seismometer (left, taken from http://www.geosig.com). Seismometer connected to laptop being installed at monitoring station 1 (right).

.

highest, but the first to exceed the trigger level). The effective duration of each waveform varied with the measurement point, the blast charge and the sequence of shots. It was, usually, about several tenths of second long, but lasted in some cases almost 2 seconds. The acquisition rate was 250 Hz, which corresponds to a time interval between points of $dt = 1/250 = 0.004$ s. With this acquisition rate, it is theoretically possible to identify frequencies up to 125 Hz, which is above the maximum recorded frequency.

Along with the three transducers, analogical and digital pre-processing systems and memory card, the seismometer houses a battery that can keep it working for up to three days with no external power. The seismometer has terminals to link it to external 220 Volt electric power and to a computer. The employed seismometers' storage capacity was of 1024 Kbytes, which stores around 28 minutes at the chosen sampling rate.

6.2.4 Recorded data, digital time-series processing and PPV scattering

997 blasts were done resulting in 2006 records. In average each blast was recorded in two different positions. However, not all records were used in the subsequent analysis. In specific monitoring spots seismometers had to be installed on building floors or on quay walls which amplified the ground vibration. These values were used to control vibrations arriving at those locations but are not useful to determine vibration propagation laws. They reflect, not the vibration propagation in the ground, but the behaviour of a specific structure. Of the 2006 blast records pairs, 1157 were used in the law fitting analysis.

Figure 6.8 characterizes both distance between monitoring spots and blasts and instantaneous explosive mass in each blast. Instantaneous charges ranged from 5 to 95 kg and distances

from about 95 to 1200 m.

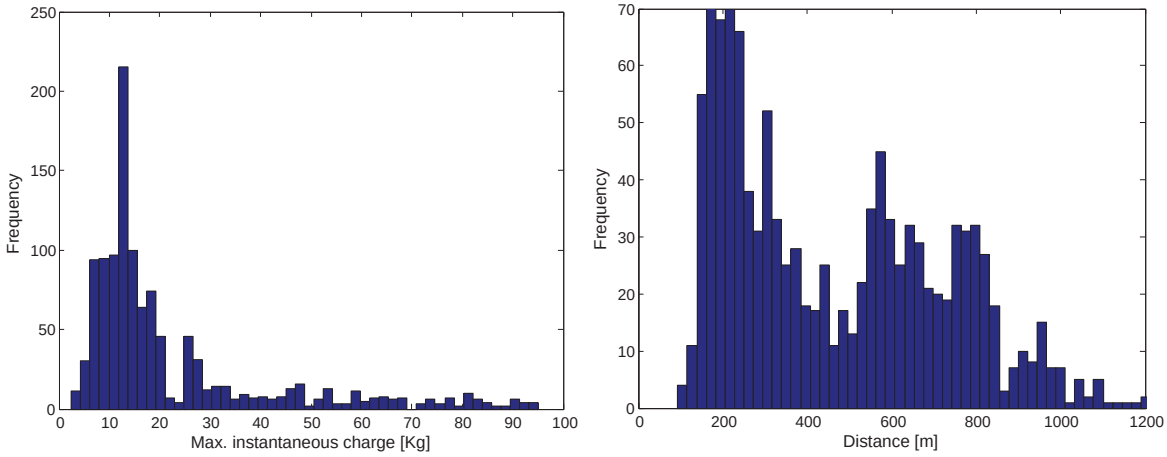


Figure 6.8: Instantaneous blast charge (left) and distance (right) histogram.

Since the seismometers record accelerations time series in three orthogonal directions these must be converted into velocities to be compared with the limits established by the Portuguese legislation DGQ (1983). Figure 6.9 shows the acceleration time series and corresponding frequency content of a typical blast record before the filtering and integration.

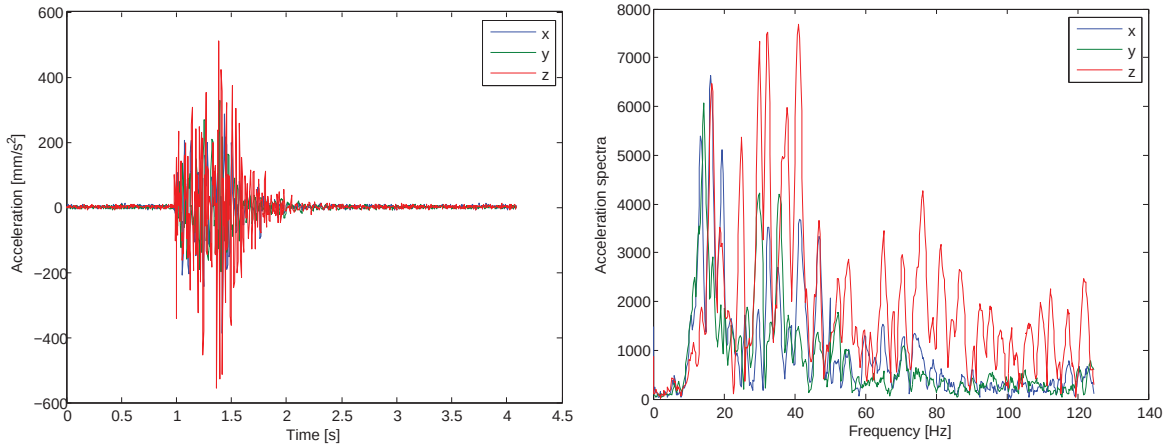


Figure 6.9: Acceleration record (left) and corresponding frequency component (right) orthogonal components of a typical vibration record.

The procedure to extract peak particle velocities from the acceleration record tries to intervene the least possible in order to preserve the series characteristics. It should be noted that in lower intensity records the blasting vibration is slightly higher than the level of ambient noise.

This makes unambiguous identification difficult. In these cases blast records were identified by comparing blast's and the vibration record's time stamps.

After collecting the records from seismometers to a personal computer the following signal treatment was applied following a methodology proposed by Bendat and Piersol (1986):

1. Application of a Cosine Taper Window in the time domain with a 10% taper . This window eliminates the signal in the ends of the record, avoiding frequency leakage in the subsequent integration.
2. Application of a bandpass filter in the frequency domain that eliminates frequencies below 1.5 Hz and above 100 Hz.
3. Integration in the time domain using the trapeze rule, thus obtaining the vibration velocity.
4. Application of a Cosine Taper Window identical to the previous to eliminate noise introduced by the numerical integration.
5. Application of a high-pass filter in the frequency domain eliminating frequencies below 1.5 Hz.
6. Determination of the maximum norm of the velocity vector, PPV, and the moment it occurs through the equation.

In some monitoring points additional narrow band filtering was necessary to eliminate ambient vibrations emanating from installed equipment.

Figure 6.10 shows the velocity record and corresponding frequency content that results from the application of the described signal processing to the acceleration time series shown in figure 6.9. The norm of the same velocity time-series is plotted in figure 6.11 where the value of the PPV of the record is also shown. Peak particle velocity histogram is displayed in the same figure. Maximum PPV values reach 20 mm/s but more than 95% of the peak velocities were less than 6 mm/s.

6.3 Determination of PPV attenuation laws

Attenuation laws, introduced in chapter 3, were one of the tools used to predict peak particle velocities in the area impacted by the blasts. It is possible (Dowding, 1996) to establish such a law with the form:

$$PPV(R, W) = kR^m W^n, \tag{6.1}$$

where W is the charge weight, R is the distance, k, m and n are parameters that depend on the characteristics of the blast and of the propagation path, and are determined by curve fitting.

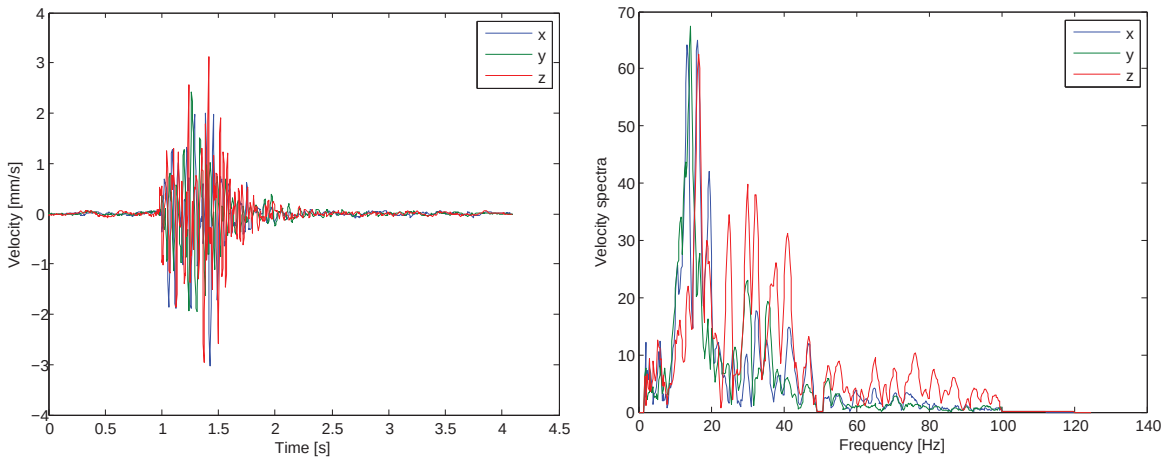


Figure 6.10: Velocity (left) and frequency (right) orthogonal components of a typical vibration record.

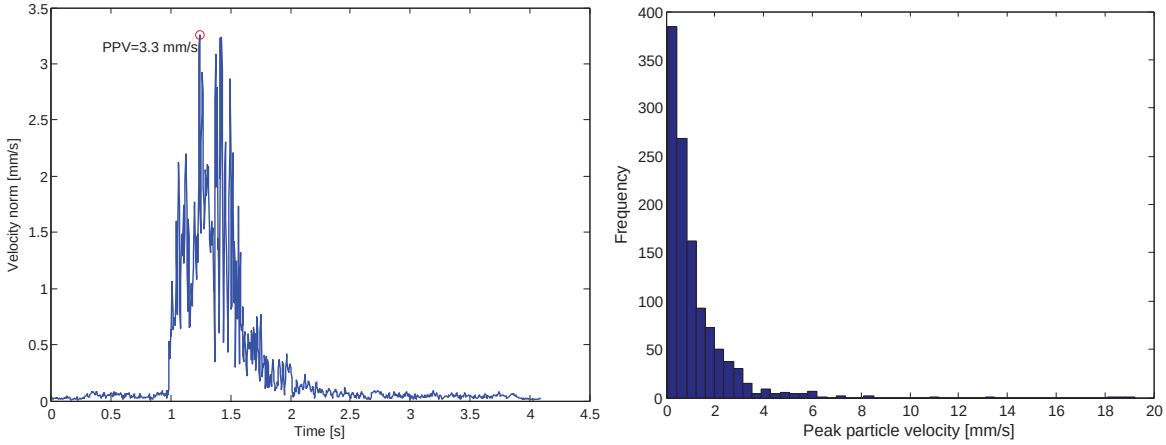


Figure 6.11: Norm of the velocity time series plotted in figure 6.10, red circle indicates the PPV of the record (left). Histogram of the peak particle velocities (right).

If the exponent of the charge weight is pre-set to 1/2 or 1/3, a new variable is defined: the quotient of the distance and the cubic or square root of the blasting mass. The result is a simplified form of previous equation 6.1. The use of this "scaled distance", also presented in chapter 3, makes it easier to graphically represent results rapidly.

In the current analysis of the data the simplified cube root version was used in plots prior to the determination of the complete attenuation law with three parameters k, m and n.

The three parameters were determined through Newton-Raphson minimization of the squares of the deviations of the logarithms of PPV, charge and distance. The values of the law parameters were 1904, -1.46 and 0.31 for k, m and n respectively. The resulting equation is $PPV_{50\%}(W,R) = 1904\,R^{-1.46}W^{0.31}$, the 50% subscript meaning that this equation averages the behaviour of the data cloud.

Since it is not the average but the extreme PPV values that are dangerous, it is more

interesting to obtain an attenuation law that adjusts to these extreme values. To obtain it, the methodology presented in section 3.2.2 of chapter 3 is used. The threshold value of 95% was choosen, meaning that only 5% of the points are above this curve. The m and n parameters are considered to be constant and it is k that goes from 1904 to 5481. The attenuation law is therefore $PPV_{95\%}(W,R) = 5481\ R^{-1.46}W^{0.31}$.

Both attenuation curves and observed points are represented on a log-log plot in figure 6.12. The linear correlation coefficient for the law that averages PPV (50% percentile) is 0.63 and is within the normal values reported for this kind of analysis.

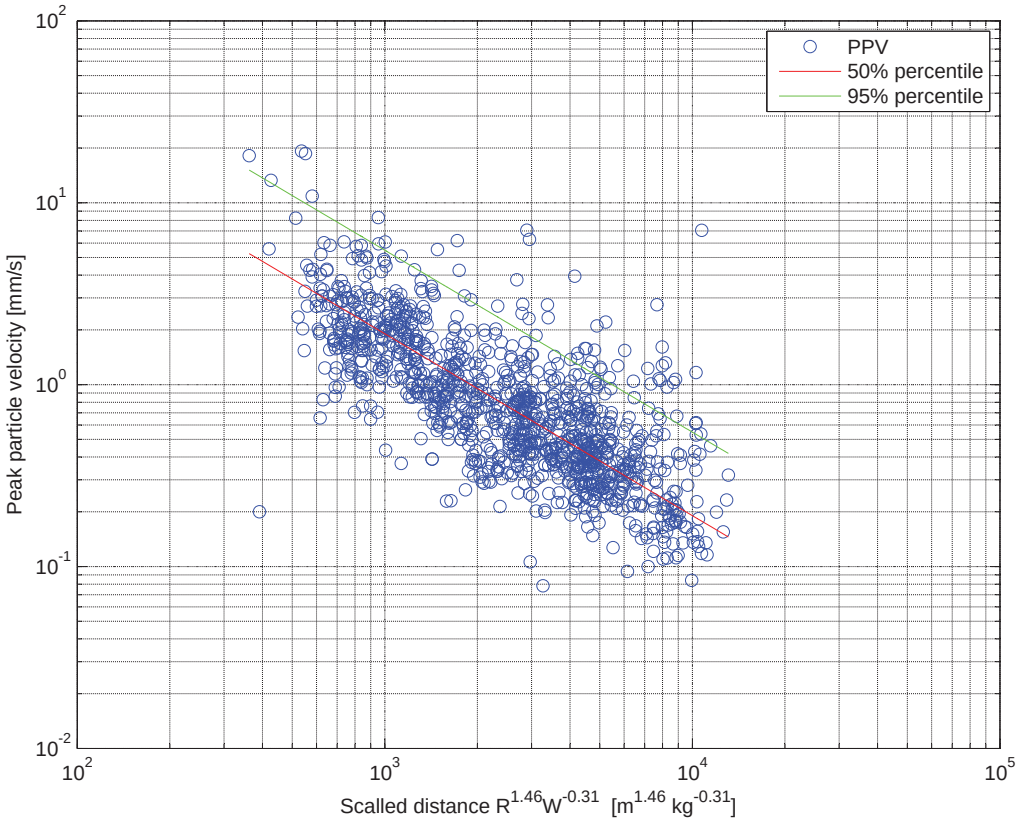


Figure 6.12: PPV scattering and 50% and 95% percentile attenuation laws.

6.4 Multilayer Perceptron Neural Networks applied to PPV attenuation

6.4.1 Network architecture

Multilayer Perceptron Neural Networks (MLP), presented in chapter 3, are computational methods based on the efficiency of the brain process. The interest for this method derives from their learning ability, which relate the variables without imposing prior relationships between them (Mata *et al.*, 2007).

Multilayer Perceptron networks base block is the unit cell, which is equivalent to the brain neuron. A unit cell is an operator with a set of inputs and an output. A weight is associated to each input, and the final sum of the weighted inputs is filtered by a transfer function (figure 6.13). Cells are arranged in layers: the first layer receives the inputs and the last layer produces the outputs. The middle layers, of variable number, are called hidden layers since they have no connection with the external world. Each cell in a layer is connected to all cells in the next layer by means of synaptic connections.

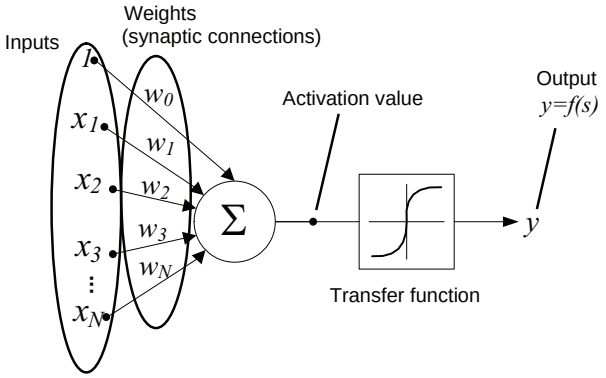


Figure 6.13: Neural network unit cell.

The information is constantly "feed forward" from one layer to the next via the synaptic connections. Multilayer Perceptron Neural Networks learn by an iterative process, adjusting themselves to correctly learn the training data in order to, after the testing phase, predict unknown data.

A neural network is trained by being fed a set of patterns. Each pattern corresponds to an observation of the response of the system that is being simulated. In the case in analysis, a pattern is a set of two inputs, the inverse of distance $1/R$ and charge weight W, and one output: peak particle velocity PPV. Figure 6.14 illustrates a generic MLP with an input layer with two input parameters, one hidden layer and an output layer with one output. The set of

patterns, or observations, available to train the neural network was the same that was used for the attenuation law: 1157 sets of distance, charge and resulting PPV.

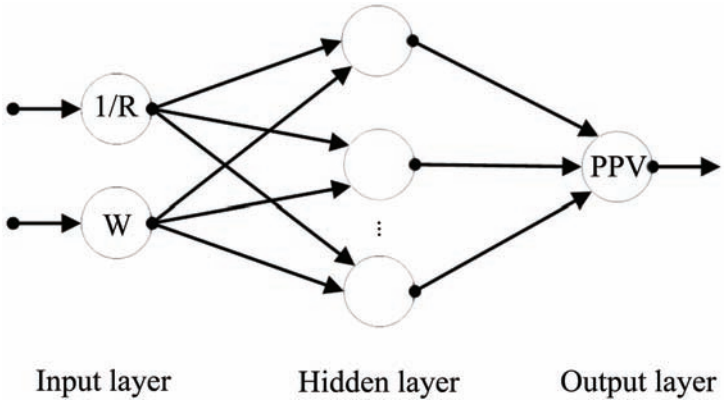


Figure 6.14: Multilayer Perceptron network structure. Adapted from Mata *et al.* (2007).

A cross validation criterion was used to optimize the duration of the learning process. From a randomized set of input and output data pairs two sub-sets were extracted: the training set, with 65% of the points and the cross-validation set with 35%. This is usually done when training neural networks because the performance for the training set can improve continuously but, after a certain number of iterations, the error for the cross validation set starts to increase. This indicates that the neural network is loosing its generalization capacity: it is adjusting excessively to the training set. At this point the model has the best generalization capacity: it has the optimum set of weights (figure 6.15).

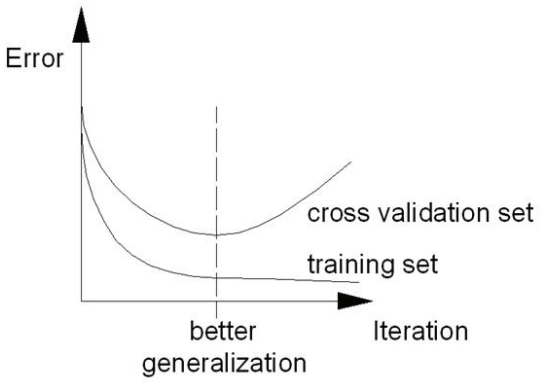


Figure 6.15: Cross-validation criteria and optimum training point. Taken from Resende *et al.* (2008).

As each initialization of the weights can lead to a different local minimum, five random initializations were established for each neural network. The inverse of the distance between

the monitoring vibration point and explosion area $1/R$ and the weight of the blasted charge W were the inputs. Several network architectures with different numbers of cells per layer and number of hidden layers were trained. The adopted architecture presents two hidden layers with three units in the first and eight units in the second hidden layer.

The output of the neural network is an estimation of the expected output value for the corresponding input pattern. The inputs were simultaneously considered and, thus the results are presented by two plots, in figure 6.16. In the first plot the instantaneous blast charge is kept constant and the peak particle velocity is plotted with distance, while in the second plot it is the distance that is constant. In both plots it is evident that the attenuation equation is more rigid than the neural network, since it assumes a linear shape in the log-log plot. In the first plot, the attenuation equation touches the neural network in the distance range of 200 to 300 m, where more data points are available (see figure 6.8) and vibration values are high due to the relatively low distance. On the second plot the two methods coincide in the range when blast charges are greater: 60 to 90 kg. This zone of the charge weight range is less representative but generates greater vibrations and therefore weights more on the attenuation equation fitting procedure (based on square root of the square of the deviations). The neural network seem indifferent to the charge weight when its value is lower than 20 kg.

6.4.2 Results and discussion

The overall performances of the attenuation laws obtained by regression methods and by artificial neural networks are presented in table 6.1. The neural network presents slightly better results on the most commonly used model performance indicator, the linear correlation coefficient, and in the mean absolute error. The linear correlation coefficient is in the order of the values usually found in this kind of analysis.

Table 6.1: Empirical models' performance. Taken from Resende *et al.* (2008).

	Neural Network	Regression
Mean squared error	1.24	1.38
Mean absolute error	0.55	0.51
Maximum absolute error	14.44	15.76
Linear correlation coefficient	0.66	0.63

The best way to compare the predictions of the two empirical strategies, attenuation law and neural network, is to plot PPV isolines of both models on a map. Since the neural network captures the average attenuation, it is compared with the attenuation law that corresponds to

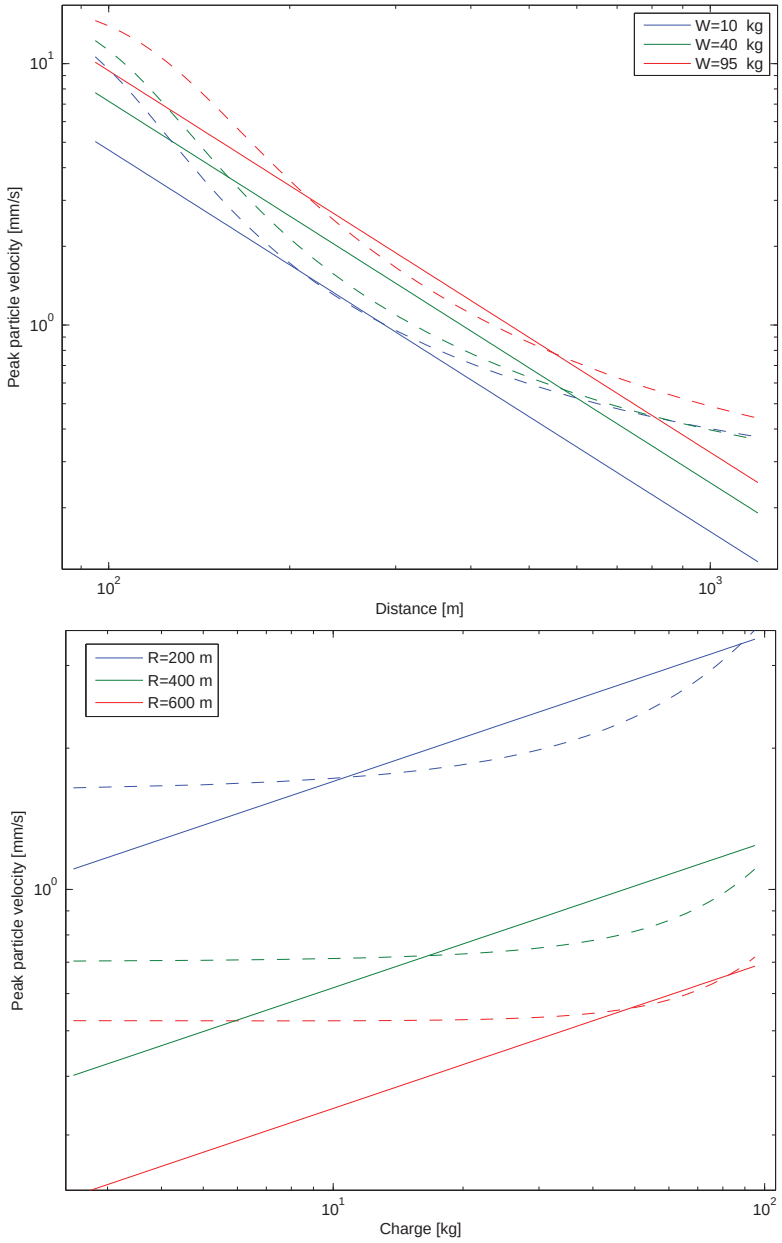


Figure 6.16: Variation of peak velocities as a function of input variables: distance (top) and charge weight (bottom). Dashed lines correspond to the Multilayer Perceptron Neural Network and solid lines to average attenuation equation $PPV_{50\%}(W,R) = 1904\, R^{-1.46} W^{0.31}$.

the 50% percentile. Figure 6.17 shows the PPV iso-velocity lines over the harbour area. To draw the map, the neural network and the attenuation law were applied at each blast location and PPV values on a 10-by-10 m grid were obtained. A complete grid corresponds to each blast. In the end, a final grid, containing the highest PPV value in each grid point is generated and iso-velocity lines are then traced.



Figure 6.17: Iso-velocity lines calculated using the regression equation $PPV = 1904\, R^{-1.46} W^{0.31}$ (continuous lines) and the Multilayer Perceptron Neural Network (dashed lines). Velocities increase from the inside to the outside (real values of the isolines can't be shown due to confidentiality of the results). Adapted from Resende *et al.* (2008).

Both models present reasonable results, given the large working area. The 95% percentile attenuation law was used by the Harbour Administration to address complains from the population. It matched quite well maximum PPV values recorded by other intervenients.

One of the advantages of neural networks comparatively to the statistical regression model is that the relations between variables are learnt by the network from the observations without

a priori definition of a relation between variables. This makes it possible to emphasize the performance of the analysed sample, the model being the more representative of the phenomenon studied the closer to reality the data sample is. The main disadvantage of such models is the need to provide abundant data in all the areas where the predictions are to be done. Also, its use is inappropriate for extrapolations out of the range of the data provided during the learning process.

In the case of the attenuation law, which is based on statistical regression, and since it has some relation with the physical reality of the attenuation phenomenon it may be possible to extrapolate beyond the range of calibration. The extrapolation should be done cautiously because factors such as variation of the geology may frustrate that correspondence.

From an economic point of view the neural networks are less expedite and more costly to use. They are harder to master and optimize. Also, neural network programs are not as readily available as curve-fitting ones and take longer to run. From this experience, the author found that they gave useful insights on the phenomena, but at considerable cost. One of the most promising possibilities of the neural networks is exploration of other input and output variables, leaving to the network the determination of their relative weight in the response. Both neural network and curve-fitting approaches allow the consideration of probability distributions for the measured data, permitting the calculation of conservative estimations of peak values, instead of average values (as was the case).

The application of numerical dynamic models, presented in the next section, may help understand how factors that are not considered in the empirical methods, such as geological variations, building foundation conditions and blasting methods and geometry influence the peak attenuation.

6.5 Finite difference numerical modelling

6.5.1 Introduction

The previous section highlighted the application but also the limitations of strategies that are unable to include the diversity of situations that can occur from vibration generation to impact. Numerical models that represent the geometry and geology of the medium and the blast generation in its multiple possible variations can replicate the mechanisms of wave reflection, refraction and attenuation in obstacles but also demand a detailed knowledge on the ground properties and blast characteristics.

The simulations in this section aim to offer some concrete explanations for the widely scattered vibration amplitudes, in this case and in general. A model representing one of the simplest

parts of the harbour is developed: a cross section of the channel. Vibrations are recorded along a straight line perpendicular to the channel, starting at the quay wall. Then, a series of situations regarding alternative blast type and position and singularities on the ground are simulated.

6.5.2 Model description

An elastic finite-difference model that represents a cross-section normal to the channel, which is 15 m deep and 100 m wide, is represented in figure 6.18. The model was developed and run in finite-difference software FLAC3D, version 4.0 and run on a 2.8 Gbyte QuadCore PC with 4 Gb of RAM. The model has a total length of 850 m: 250 m to the North side of the channel (Leça) and 500 m to the South side (Matosinhos). The model width in the y direction (which coincides with the channel's axis) is 90 m and its total height is 165 m, and thus the bottom boundary is 150 m below the bottom of the channel. The model has 475,695 zones and 502,016 gridpoints. The vibration time-histories are recorded on the Southern side (the longer one) every 25 m starting on the quay wall.

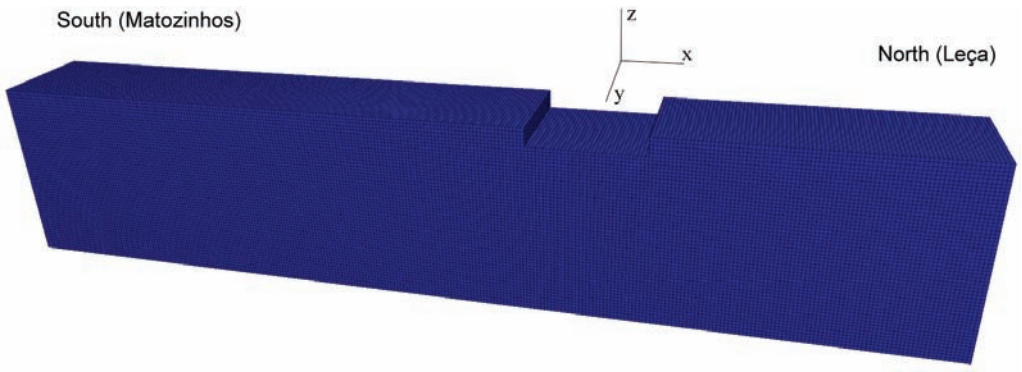


Figure 6.18: Reference finite difference model grid.

A parametric study to test the performance of the model was carried out. Absorbing boundary conditions were installed in the bottom and on all four lateral exterior surfaces to ensure that 3D spherical wave propagation occurs. The only problem that could not be easily overrun was the performance of the absorbing boundaries at the ends of the model, since some wave reflection is observed. This is due to the fact that viscous boundaries do not perform well against surface (Rayleigh) waves.

Compressive and shear wave propagation speed in the model was set to 3000 and 1500 m/s, respectively. Finite-difference are cubes with 3 m sides, so frequencies at least up to 125 Hz are correctly transmitted (Itasca, 2010).

The loading is simulated by a single-pulse negative exponential wave with a peak time of

1 ms (see section 5.5.2 of the previous chapter) applied in the faces of zones in the bottom of the channel. Real loadings consisted on multiple non-simultaneous blasts but it is considered that, since time-delays between boreholes were greater than 25 ms, wave cooperation was prevented. Detail of the loading location is shown in figure 6.19. Figure 6.20 shows the location of grid-points velocity probing.

In the next sections, results of the several simulated scenarios related to the vibration source and to the ground characteristics are presented, starting with the reference situation.

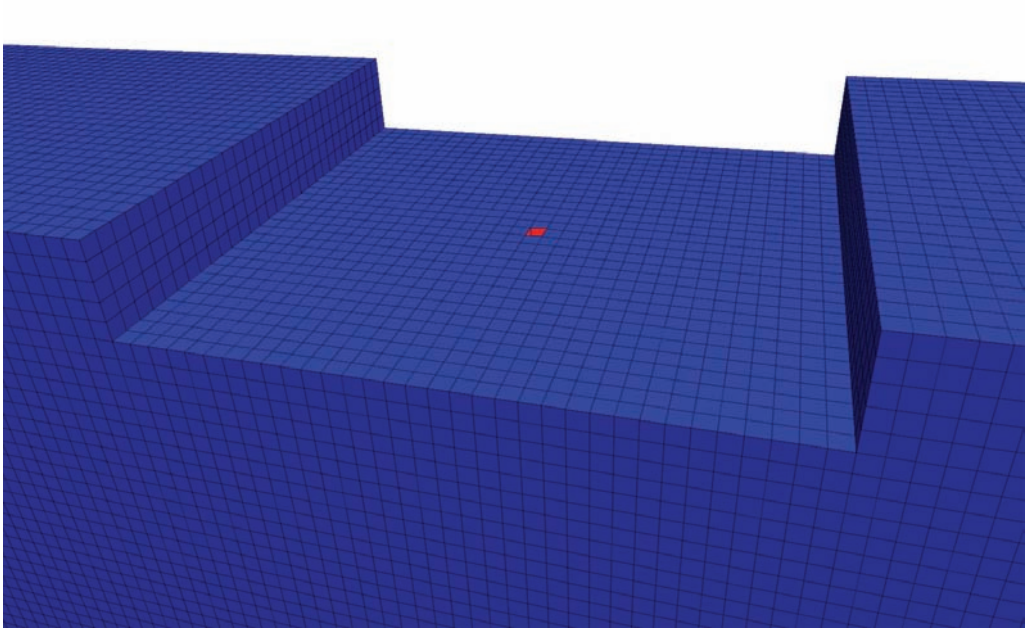


Figure 6.19: Detail of the harbour channel showing the removed element in which walls the blast load is applied.

6.5.3 Reference model and influence of distance

Figure 6.21 displays the vertical and horizontal (in the direction normal to the channel axis) displacements in some of the gridpoints where vibration is recorded. Displacements were directly obtained from integration of the velocity time-histories. The curve is not closed, since there is a residual displacement that corresponds to a rigid body motion (translation and rotation) of the whole model. The elliptical shape of the load path, starting at the axes origin, is typical of a surface Rayleigh wave. Initial horizontal motion is in the direction of wave progression and the vertical axis of the ellipse is greater than the horizontal one, if a correction for the rigid body rotation is accounted for. The first plot (upper left corner) corresponds to a gridpoint at the top of the quay wall. The wall vibrates with a frequency that is higher than that of the

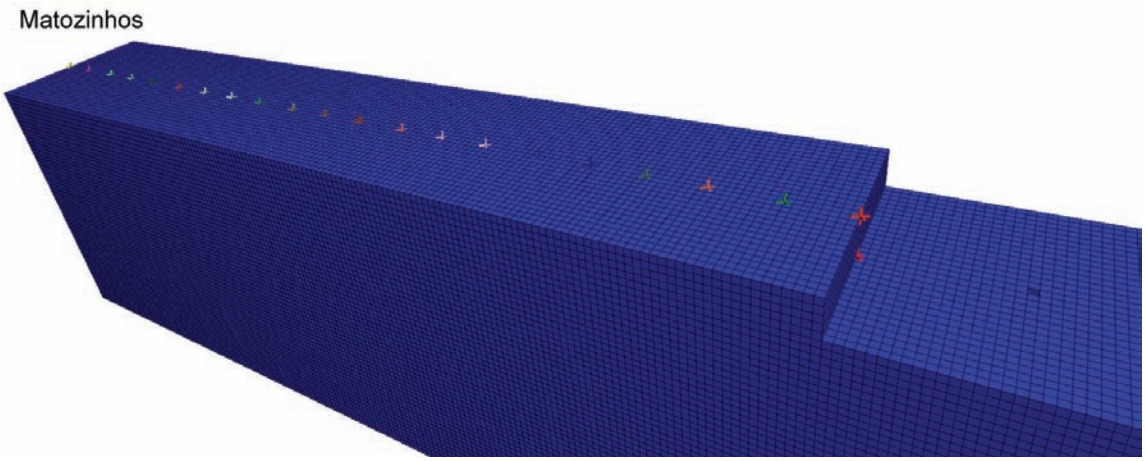


Figure 6.20: Location of vibration velocity recording points, 25 m apart, in the Southern side of the channel (Matoinhos side).

blast stress wave's. This causes the line in the plot seem thicker. The same thing happens in the other plots but is less marked, due to higher frequency and lower amplitude vibration.

Figure 6.22 shows the velocity peaks plotted along a line (shown in figure 6.20) that starts at the quay wall. The first point on the line corresponding to this reference numerical model is the PPV recorded in the channel bottom, at the base of the quay wall, which is, in this case, not very different from the value at the surface. The PPV obtained through the attenuation lawis also plotted. The analytical expressions are scaled to fit the numerical model at a distance of 125 m from the channel centre.

Contrary to the attenuation laws, the numerical model's curve is not linear (in the logarithmic space). It has an initial part where the attenuation is lower and a final part where it is similar to the empirical attenuation law. It is richer – especially closer to the source – than the attenuation equation.

6.5.4 Influence of blast load location and application

This section describes models that simulate different ways to apply the blast load and also the influence of its location. Blasting was performed all along the channel's width. Two models were created to test how blasting closer and farther from the quay wall influences vibration. In the first model, the blast was placed right next to the Southern (Matosinhos) quay wall, while in the second, the blast is on the opposite wall, further away from the start of the line where velocities are probed. Figure 6.23 shows the location of the blast near the South quay wall.

The second analysis in this section looks on the influence of the confinement of the blast load. In the reference calculation one zone is excavated and the load applied to the faces of the boundary of this excavated area. This is equivalent to a first blast, when the blast is

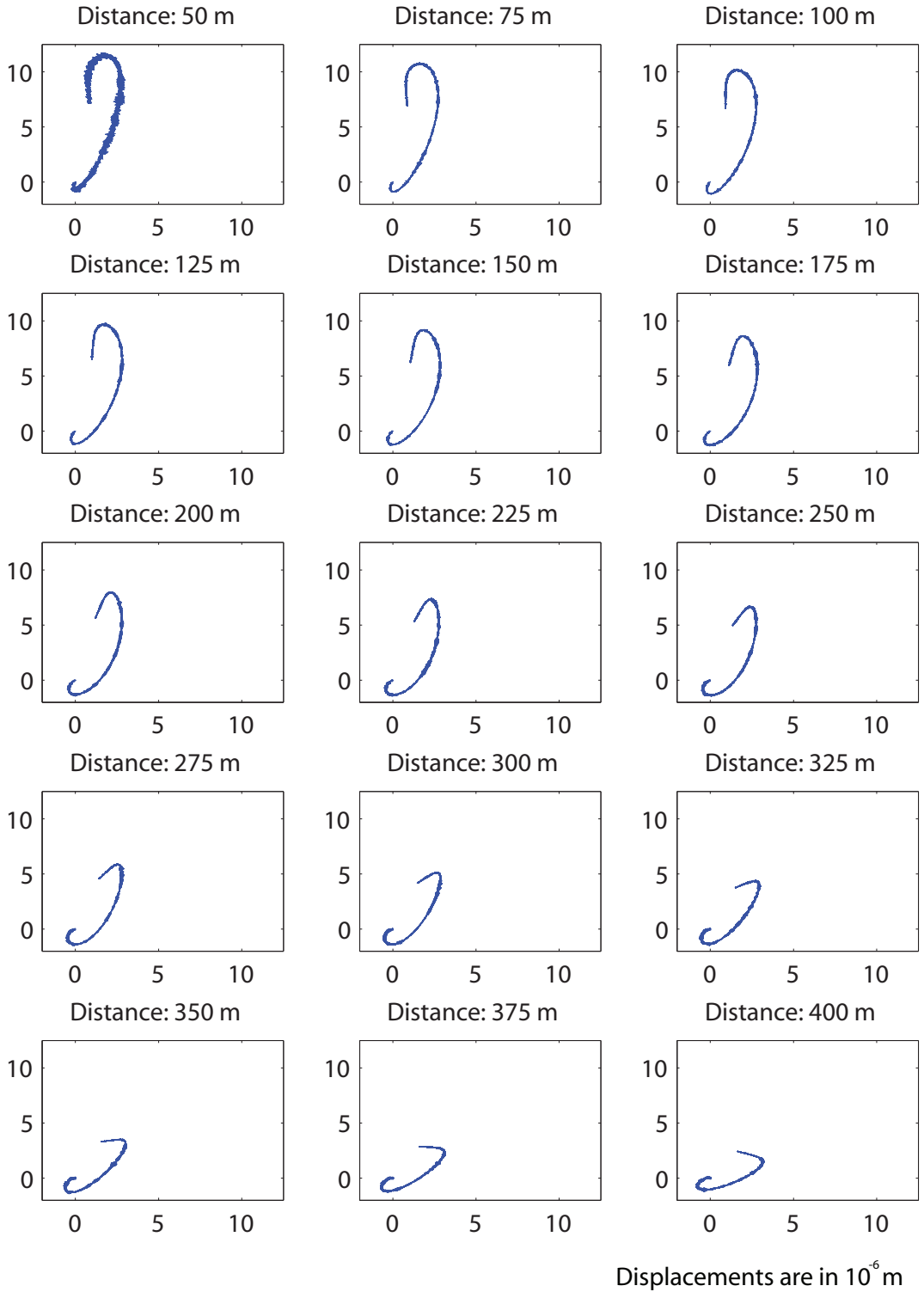


Figure 6.21: Plots of horizontal *vs* vertical displacement along the monitoring line. Wave progresses in the positive horizontal direction.

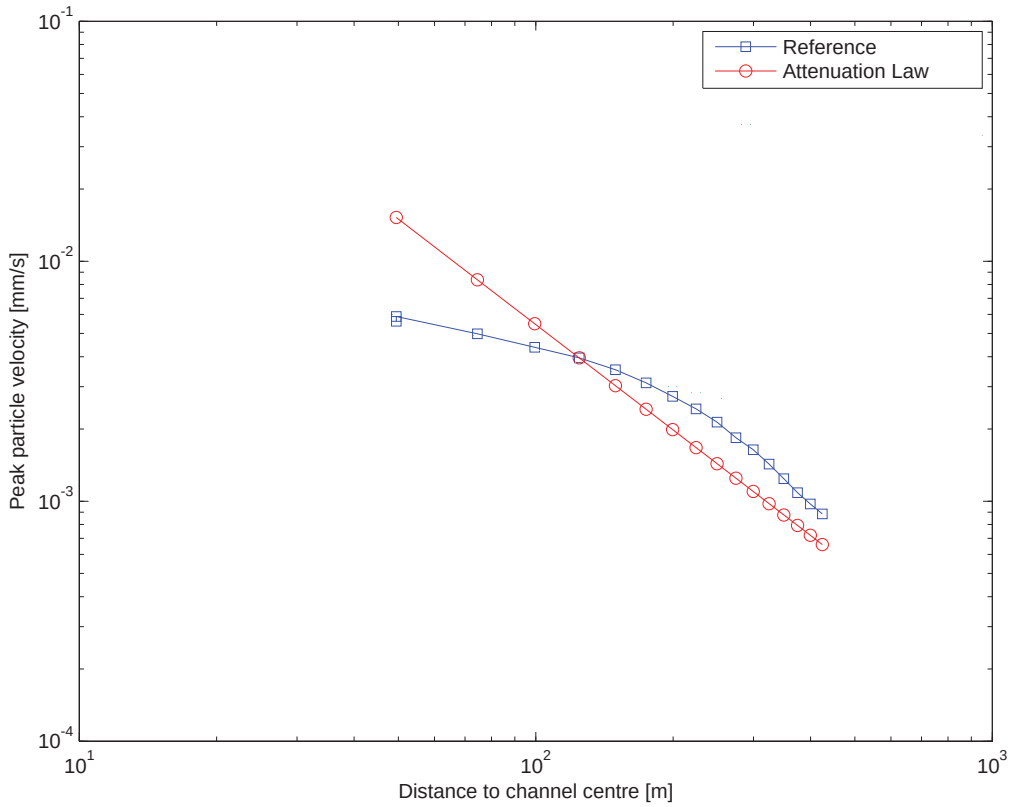


Figure 6.22: Plot of PPV *vs* distance to channel axis for the reference numerical model and the attenuation law (section 6.3).

surrounded by rock on all sides and there are no free surfaces. Figure 6.23 shows a situation where a pit has already been excavated and the blast loading is applied at one vertical and one horizontal surfaces. The major influence of confinement in a real situation is in the way energy is transmitted to rock and how rock is fractured and projected, which is not simulated in this elastic calculation.

Finally, a simulation is run in which the load is applied at the surface of the bottom of the channel, not in the faces of an excavated zone.

Figure 6.24 displays the resulting attenuation curves. Blasting in the end of the channel opposite to the where movement is measured (blast in the Northern wall, in cyan) has the effect of lowering slightly the vibration levels, compared to the reference situation, without altering the shape of the curve. When the blast is right next to the monitored channel wall, the consequences are more dramatic: vibration levels rise tenfold on the base of the quay wall and on the top of the wall, returning to "standard" levels shortly after. As to the way the blast is applied, the application of the stress wave at the surface produces no effect, as in the previous chapter had happened. When the load is applied in an already open pit (open blast), vibration levels rise very slightly, possibly because the impulse is directed to one side only.

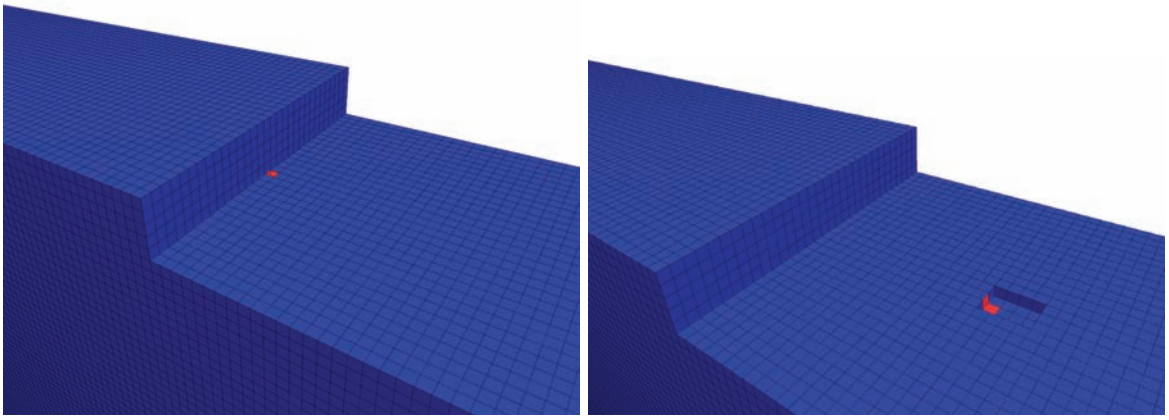


Figure 6.23: Detail of the harbour channel showing the location of the blast near the quay wall (left) and the removed elements and the zone face in which the blast load is applied (right).

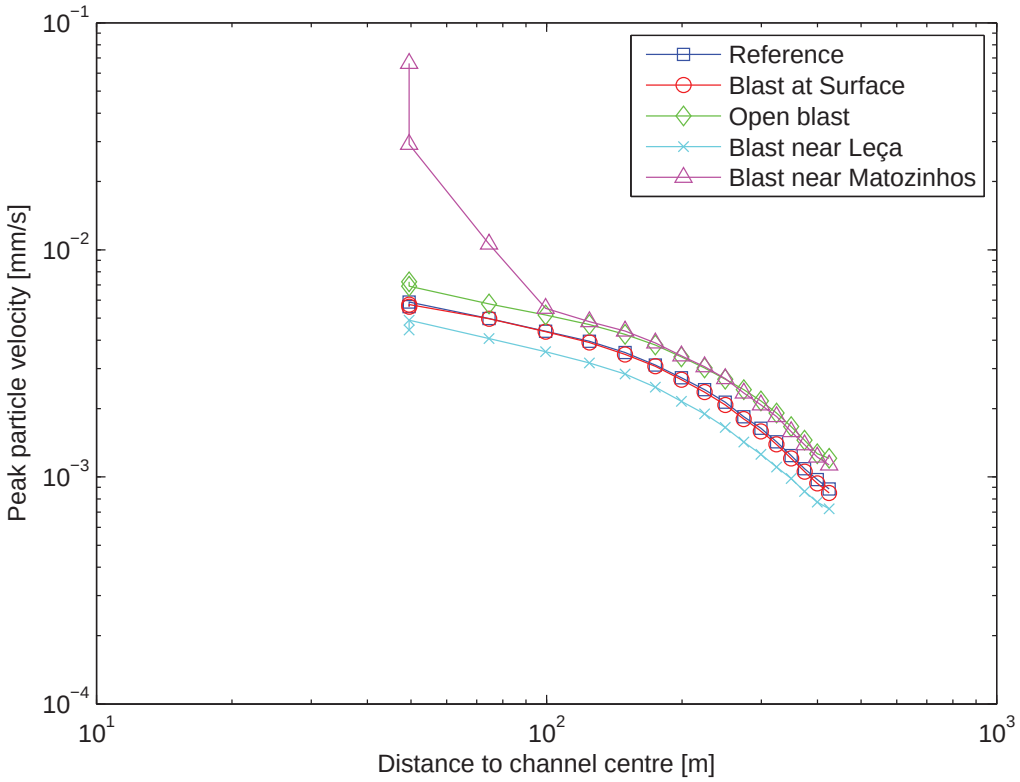


Figure 6.24: Plot of PPV *vs* distance to channel axis for the reference numerical model and for the variations in load application.

6.5.5 Influence of dyke filled with soft material

In this series of simulations the presence of a dyke, located 60 m away from the quay wall and filled with soft material is evaluated. Dyke width and filling variations were considered. On a 3 m wide dyke, the Young's modulus of the filling material was set to values one hundred, five hundred and one thousand times smaller than the Young's modulus of the rest of the domain. Then, setting the stiffness to 1/500 of the remaining domain, the width was varied to 3 and 9 m. Figure 6.25 shows perspectives of the dyke zone.

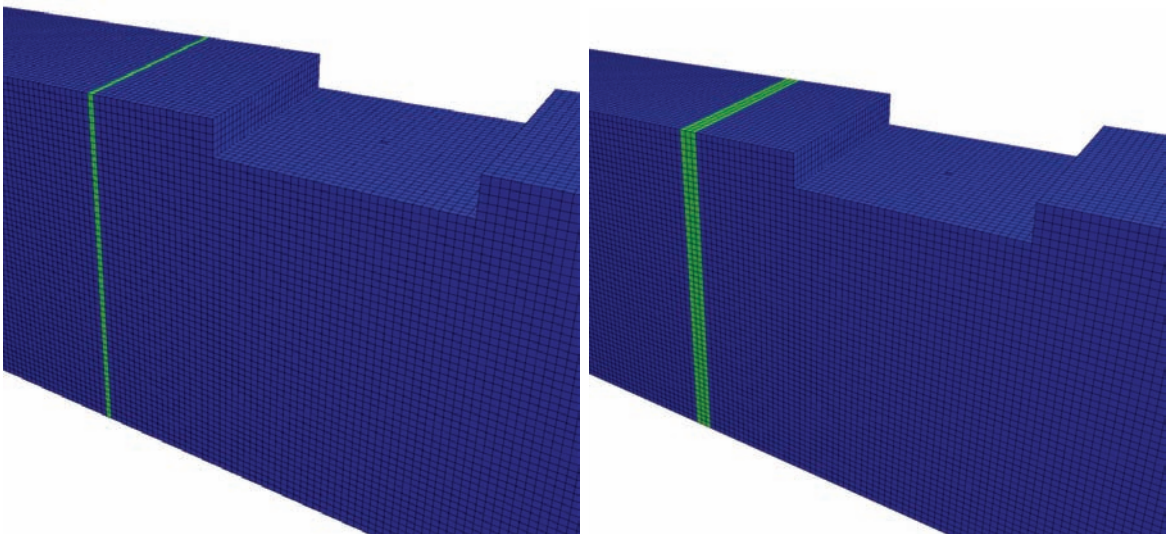


Figure 6.25: Models with 3 (left) and 9 m (right) wide dykes, located 60 m away from the quay wall.

Figures 6.26 and 6.27 show the velocity peaks of the reference model and both simulations: dyke filling stiffness and width. The intercalation of softer material causes the stress wave to be partially reflected, the reflection being greater when the impedance contrast is greater or the width higher. The reflection causes the vibration levels to increase before the dyke, because the reflected wave superimposes on the incident wave, and decrease after the dyke. The slope of the attenuation graph after the intercalation is approximately similar to the reference model's. Different locations for the dyke would lead to different effects, especially in the area before the dyke, since wave superposition would be different.

6.5.6 Influence of ditch in vibration path

In this section a 3 m wide and 3 m and 6 m deep ditch, 60 m away from the quay wall is modelled. Ditches are sometimes suggested as a means to mitigate vibration, so it was considered interesting to investigate their hypothetical influence. For economic reasons, excavation of a 6

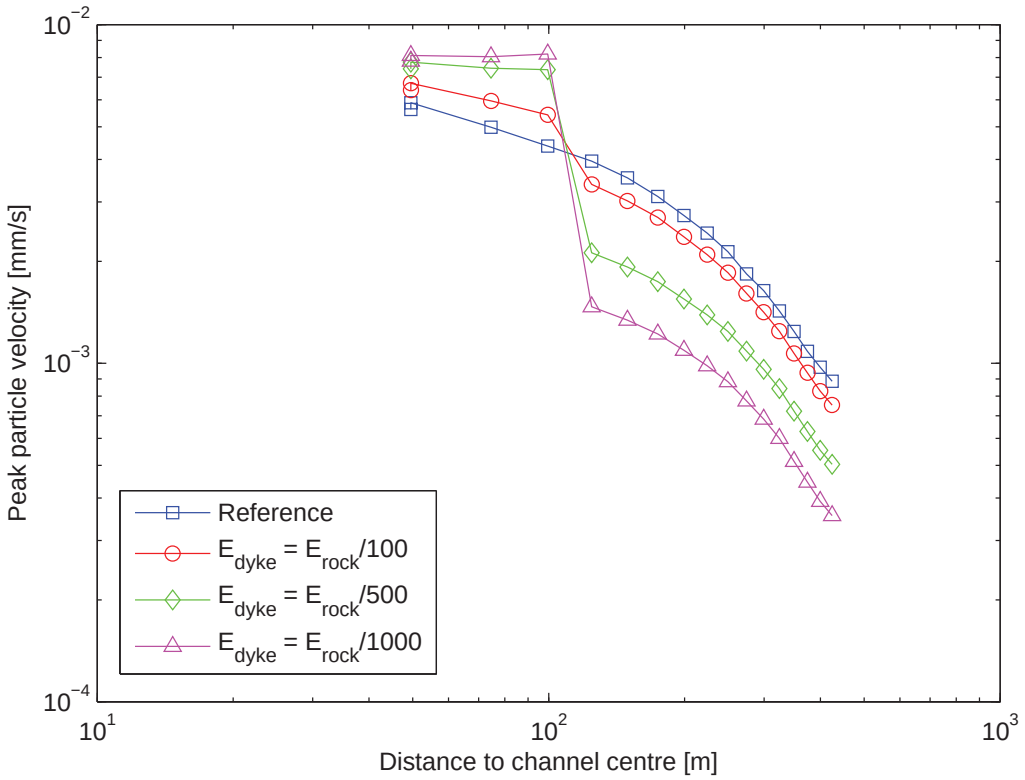


Figure 6.26: Plot of PPV *vs* distance to channel axis for the reference numerical model and the models with varying dyke materials.

or even a 3 m deep ditch is unreasonable in a temporary situation such as this one, except if there would be no other alternative to blasting and there were buildings of extreme sensitivity and value.

Figure 6.28 shows the model with the 3 m ditch, while figure 6.29 shows the resulting PPV maxima curve. The verdict on the effectiveness of the ditch is clear. The wavelength of the surface waves is greater than the ditches depth so its effect on the waves is negligible.

6.5.7 Influence of filling material in the quay walls

Before the construction of the harbour channel, the river Leça used to run where the harbour channel is today. To build the channel, walls were erected in both margins and rock and sand were deposited leaving the river to run between the walls. A model to investigate the influence of this loose material on the passage of the waves was developed. Two simulations were run, assuming that the filling material is 100 and 500 times softer than the ground. In the calculation shown, its slope is of 60º (see figure 6.30). Other calculations showed the geometry (slope angle) of the filling material not to be very relevant.

Figure 6.31 displays the velocity peaks of the reference model and of the two different

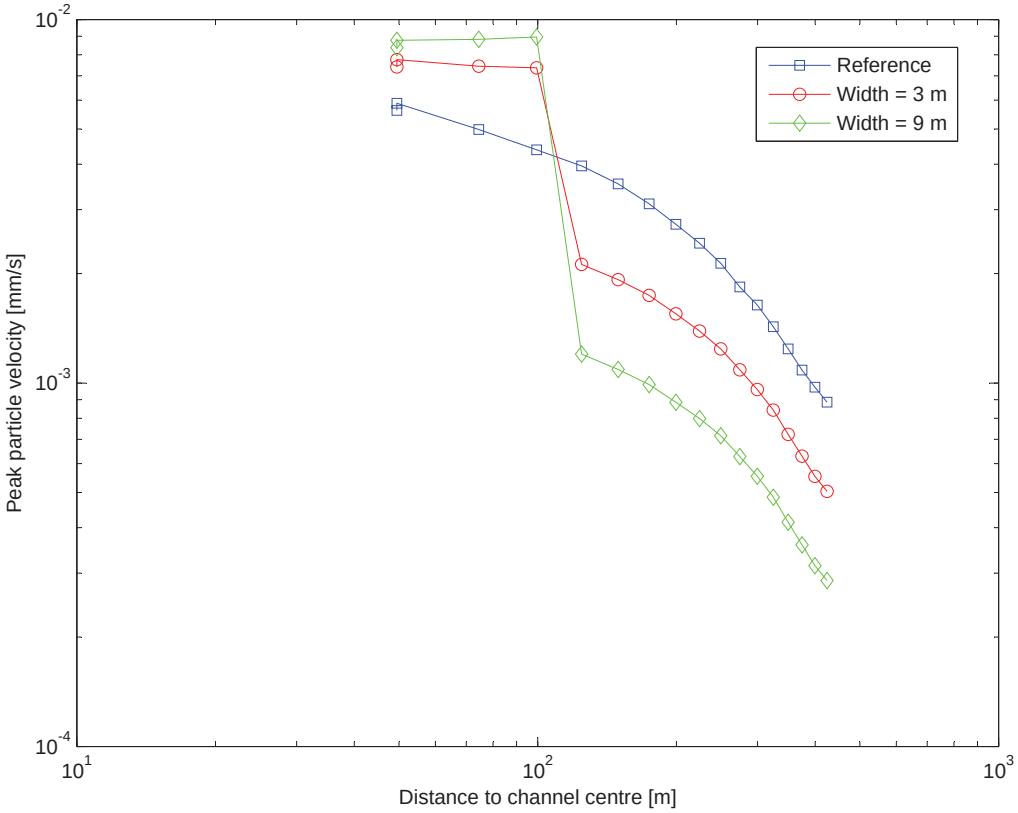


Figure 6.27: Plot of PPV *vs* distance to channel axis for the reference numerical model and the models with varying dyke widths.

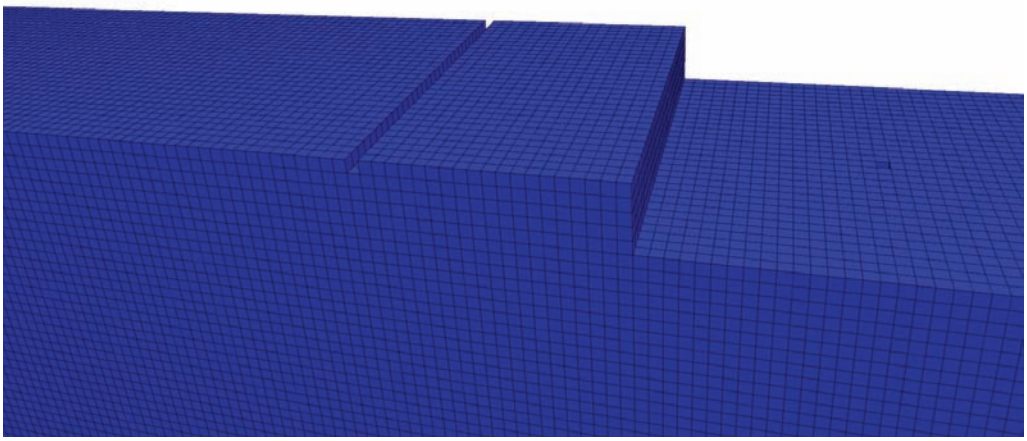


Figure 6.28: Model with 3 m wide, 3 m deep ditch excavated 60 m away from quay wall.

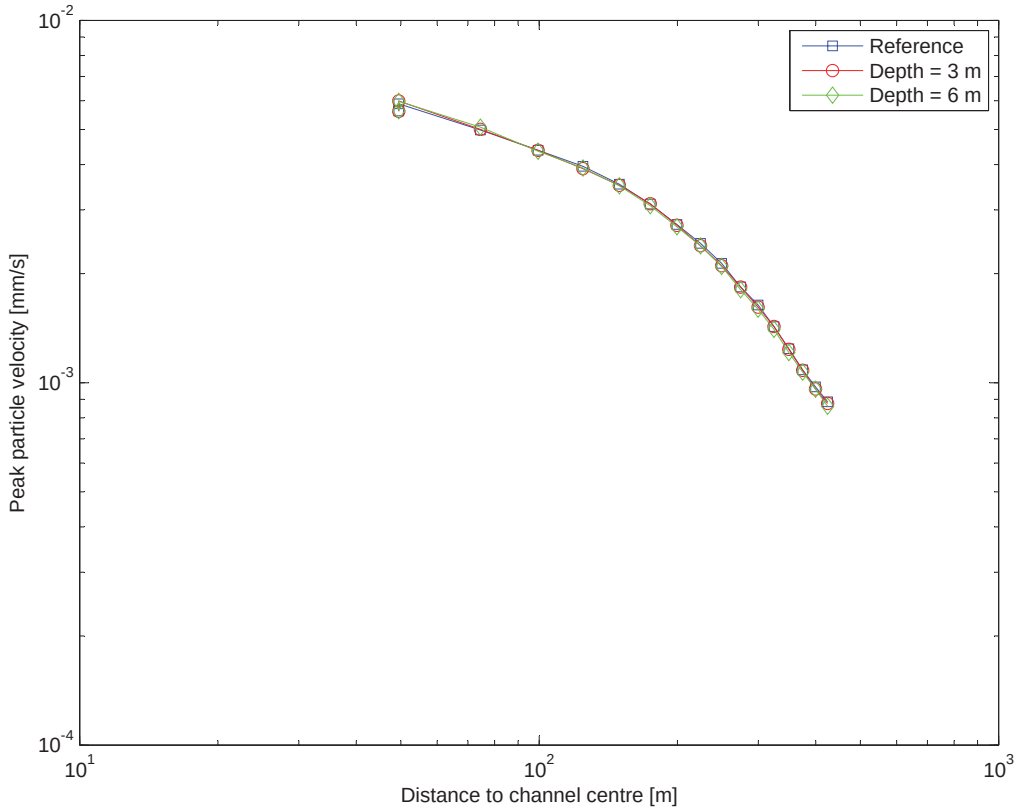


Figure 6.29: Plot of PPV *vs* distance to channel axis for the reference numerical model and the models with 3 and 6 m deep ditch.

materials. The influence of the change is, unsurprisingly, not felt at the bottom of the quay wall, but it is felt at the top, where the vibration is much stronger. The vibration increase is proportional to the contrast of the impedance between the quay-filling material and the rest of the ground.

6.6 Discussion and future developments

The work in this chapter is a sequence of the previous two, in the sense that there is another tenfold increase in the scale of the problem. The reverse of the coin is that the complexity of the blasts and information on the way they were performed and on the ground characteristics is much lower. The strategies employed to estimate and understand the blast wave propagation are adjusted to this reality.

The first sections of the chapter described the monitoring of a large and long construction work involving underwater blasting in a densely populated area. The size of the working area, the duration of works and the large number of buildings inside the blast vibrations' area of influence are the ingredients of a difficult case of vibration monitoring and prediction.

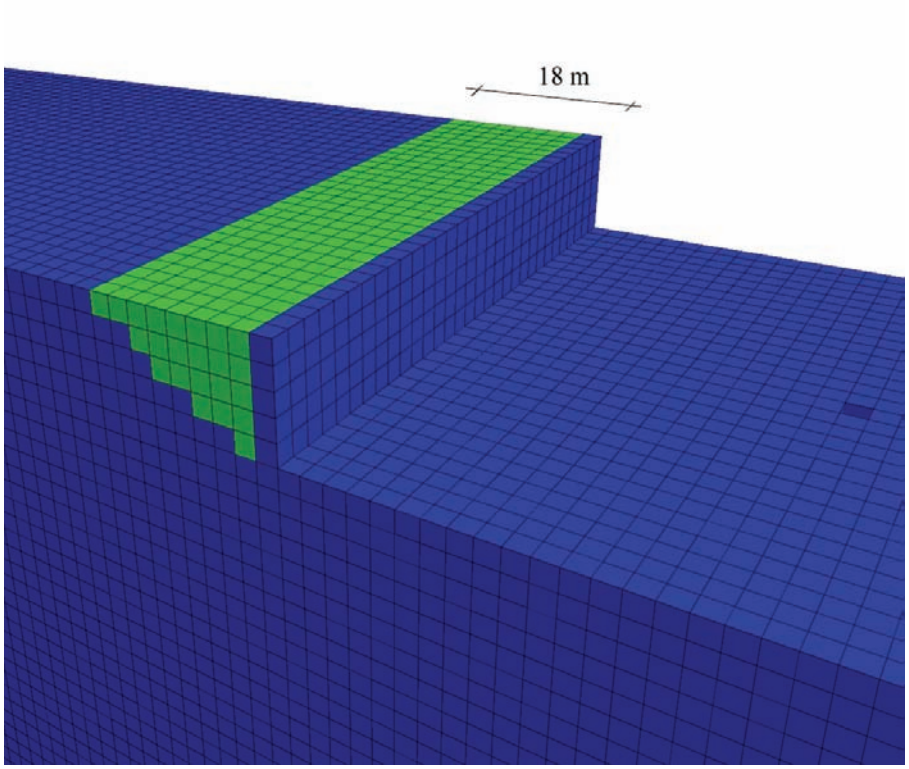


Figure 6.30: Detail of the filling material (in green) in the channel quay.

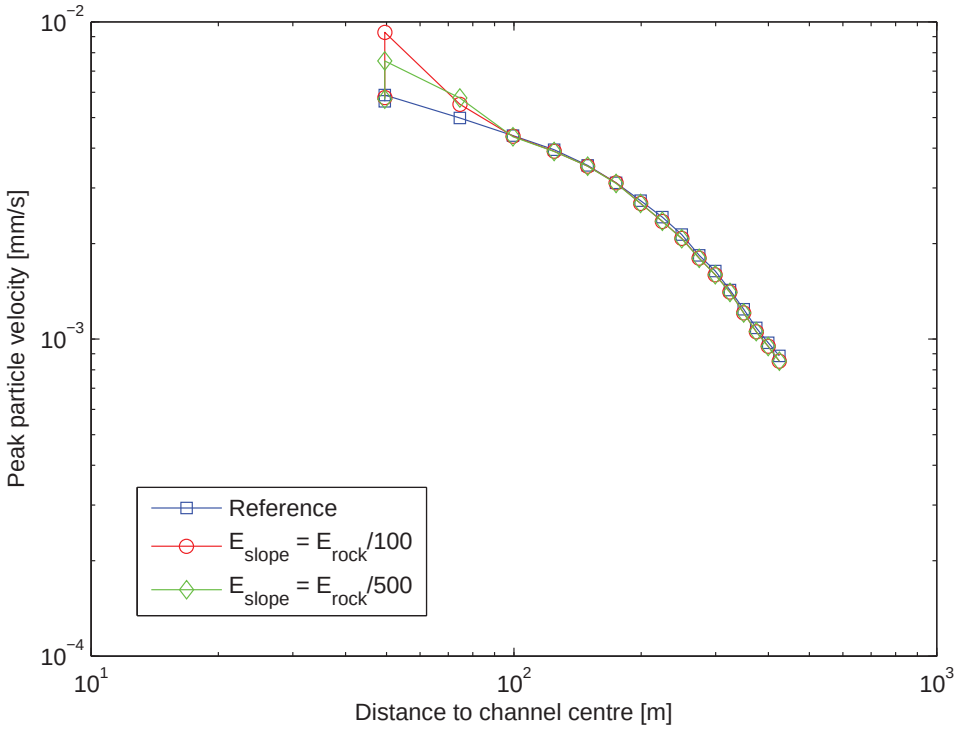


Figure 6.31: Plot of PPV *vs* distance to channel axis for the reference numerical model and the models with softer material in the quay interior.

The major difficulties in the application of the Portuguese regulation were described. Firstly, due to the short and vague descriptions, it is often difficult to define the vibration limits of the structures. A more detailed description of the building classes, possibly with examples of the typical and more common construction types would be a welcome upgrade in a long due revision of the 1983's NP 2074 standard.

As in most urban blasting situations, only a small fraction of the constructions can be monitored simultaneously. This forces the purpose of the monitoring to be two-fold: it has to provide daily feedback on the attained vibration levels and also gather data to support the estimation of a propagation model. In this case study, blasting was done simultaneously in separated locations and the number of monitoring devices was low (often only 3 devices), so the second purpose of the monitoring was very frequently left behind. Most measurements were done in the boundaryof the urbanized area and few in its interior, where they would have allowed a more complete characterization of the evolution of vibrations with distance.

One aspect of the Portuguese regulation that was felt as particularly penalizing when setting maximum peak particle velocity levels is the definition of ground type in the foundation of the buildings. The frequency of the vibration entering the buildings is linked to the stiffness of the ground, but the regulation does not contemplate the direct use of the frequency measured by seismometers. Instead, ground must be classified directly by observation or indirectly through its dynamic properties (propagation velocity of stress waves). Both were unavailable and conservative hypothesis were assumed, thus penalizing the blasting, perhaps unnecessarily.

What the author proposes, similarly to Bernardo (2004), to other regulations (*e.g.* DIN (1999)) and to current proposals of regulation revision, is that vibration frequency is directly accepted when defining the PPV's threshold levels. It is the frequency of the vibration, or, more precisely, the proximity of this frequency to the structure's, that is relevant. The ground characteristics are an indication of the kind of frequency that can be expected: stiffer soils or rocks are associated with higher frequencies, while soft soils filter them leaving the lower frequencies, more dangerous to structures. But if monitoring devices can, as they do for a number of years, directly indicate the frequency content of the recorded vibrations, there is no reason not to use this more accurate information.

The scatter in peak velocity values in relation to the average is significant, as expected in conditions such as those of the case study. Founded on detailed analysis of vibration data collected in the monitoring points two distinct strategies were applied to build empirical models that provide expected PPVs given a distance and an instantaneous blast charge. One was a equation with the form $PPV(R,W) = k\,R^m\,W^n$, while the other was a neural network whose entry variables were also blast charge and distance. Their statistical indicators of performance were found to be similar as well as the shape of their iso-velocity curves, plotted on a map of

the harbour. The neural network, though having some advantages such as a greater flexibility and possibility of experimentation with other variables, does not deliver significantly better results and is much less economical than attenuation laws. It may prove to be superior in other scenarios.

Since the attenuation law, being the most commonly used method of vibration propagation, does not indicate the extreme values of the vibration, an attenuation law that is greater than 95% of the measured velocities was defined. This simple process was essential for the Harbour Administration to manage complains. It is the author's belief that this should be standard method for PPV prediction, replacing the average PPV law that does not indicate the likeness of extreme, damaging values that can be several times larger than the average.

Finally, through a simple numerical model, it was possible to shed some light on how vibrations propagate from the channel into the surrounding area and on how different blasting options and singularities of the ground can lead to considerable variations on the vibration amplitude. More detailed models and simulation of scenarios related to the ground properties and topography and to the blast conditions demand can easily be studied.

This was a brief incursion on the application of numerical models in the analysis of blast vibration propagation. The models were used on qualitative investigations. The geometry was very simplified (though not very different from the real one, which is also simple), only a part of the harbour was represented and the modelled features such as the dyke, the quay material, the blast type and geometry were loosely adapted from reality. The employed models were not very far from the end of the employed hardware capacities so, the considerations about CPU power and RAM and software's evolutions apply here. It should be noted, however, that some of the simulations could have been run in two-dimensional axisimmetry.

Many of the conclusions of the previous chapter related to numerical modelling of stress wave generation and propagation are also valid here, so they will not be repeated. One interesting development here is the inclusion of simple models of buildings and study how they interact with different kinds of foundation materials and stress waves. This will allow, for example, the analytical testing of many hypotheses linked to the ground-structure interaction.

It is, for its great importance, worth to draw attention to one of the most important studies needed for the simulation of blast loading, which is the correspondence between real charge weight and the input function on the numerical model.

Chapter 7

Conclusions

7.1 General

This thesis aims to contribute to a better understanding of the propagation of blast generated stress waves in rock masses and to the progression of the methods employed in the simulation of the phenomenon, namely dynamic numerical models.

A deep understanding of the stress waves' interaction with the naturally occurring geological features such as fractures or dykes and with excavations such as tunnels, adits or caverns will contribute to improving design of blast plans and monitoring of potentially dangerous vibrations. With effective numerical models that simulate stress wave transmission it is possible to tackle the large uncertainty associated to propagation in environments with complex geometries and properties, the examination of hypothetical scenarios or the efficiency of mitigation measures.

The second chapter of the thesis presented a brief description of the generation and propagation of vibrations in rock masses. Particular attention was paid to the theoretical framework of the interaction with rock joints. The third chapter explained the methodologies for the monitoring and simulation and the standards proposed by international associations and national regulatory bodies for the control of blast-vibration impact. These chapters only went so deep as to provide a basis for the understanding of the work developed in the later chapters, but can also be taken as an introduction to the subject, directing to bibliographical references that provide a more profound analysis.

The fourth chapter described the development of a micromechanical model that is able to represent the main features of the rock joint–stress wave interaction. This original model employs discrete element bonded particle assemblies to reproduce the rock structure and the joint geometry.

The fifth chapter described low intensity blast tests between adits belonging to a hydro-

electric underground power scheme and their simulation with two and three-dimensional finite-difference codes.

The sixth chapter reported a large and long urban blasting work, depicting the monitoring and simulation of the vibration impact on the surrounding area with statistical and artificial intelligence techniques and numerical simulation.

These last three chapters do not, evidently, aim to address every angle of the blast vibration problem, but to contribute to it in key points at diverse physical scales, levels of detail and scope of intervention, from the more fundamental research to the usual engineering practice.

7.2 Conclusions and contributions

The main findings reached in this thesis have been presented in the course of the text and the most significant scientific contributions were also listed in each chapter's closing. They are here summarized and integrated.

In the second chapter of the thesis the phenomenology of stress wave propagation in rock masses was detailed. The Displacement Discontinuity Theory was described and identified as the most consistent theory to address stress wave interaction with rock joints. In the closing of the chapter, the issues still under discussion and in need of further work were identified.

Chapter three presented the Observation-Modelling–Regulation pyramid as an integrated toolbox to minimize and control vibration impact on populations and edifications. The Portuguese standard and other international standards were presented and a comparative analysis identified some shortcomings of the Portuguese standard. It should be revised in order to allow for the direct consideration of vibration frequency in the formula that calculates threshold values, which is justified in face of the present vibration measurement technology. Similarly to all other standards, the vibration limits also depend on the kind of target structure. A more detailed description of the structural classification criteria should be included in order to avoid conflicts. The classification should cover geotechnical structures in general and underground structures such as water, gas, electricity and communication infrastructures, tunnels and other excavations. Finally, the standard should describe in greater detail how the measurements should be performed, since apparently small differences in the devices installation can have a great influence on vibration readings.

Micromechanical modelling of rock masses

The fourth chapter's main original contributions are:

- A new bonded particle model for rock joints was developed that successfully recreates the

typical hyperbolic force-displacement curve through the replication of the main mechanisms of joint closure: contact creation and evolution with loading.
- Hybrid static/dynamic loadings boundary conditions were defined and implemented for particulate media.
- Compressive stress wave propagation in bonded particle models was characterized and the quality requirements were defined.
- Compressive stress wave interaction with the developed joint model was investigated and found to reproduce adequately the increase in joint stiffness with normal stress.

A more detailed account of the work in this chapter and of the mentioned contributions are given in the next paragraphs.

Simulation of rock joints under compression with particle models was done and this is innovative. Hydromechanical and seismic response of rock masses is connected to joint aperture, so simulation of joint normal behaviour should become more important and integrated with shear. A ball-ball contact constitutive model was developed and integrated in the particle discrete element code PFC^{2D}. This constitutive model replicates the deformation and crushing of the asperities that transmit forces across the joint under compression. Simulation of joint compression tests demonstrated that the developed joint model adequately reproduces the micro and macroscopic real behaviour of rock joints in compression, namely, contact deformation and crushing, increase in the number of contacts and increase in the global joint normal stiffness. The model stress-closure curve and the static stiffness resemble those of real rock joints under the same load conditions.

The propagation of compressive stress waves in unorganized assemblies of bonded particles with non-uniform radii representing a hard rock specimen was investigated. The velocity of propagation and attenuation of compressive waves were characterized. To conduct this study it was necessary to experiment and define new ways to generate controlled dynamic loadings and to implement absorbing boundary conditions that simulate an infinite medium. Stress and velocity loadings were discussed and it was demonstrated that stress/force loading provides superior control over the model and replicate better most real loading conditions. A hybrid boundary that allows static loadings, viscous absorbing boundary conditions and stress dynamic loading in the same location was defined and successfully tested. This allows simulation of *in situ* stress state, stress wave loading, as well as a dynamic unbounded space.

The developments described in the previous points allowed the simulation of compressive stress wave interaction with the developed joint model under several static compression loads. Since movement of one particle may not be representative of the "equivalent continuum" it was necessary to develop methods for extraction of incident, transmitted and reflected waves. The

following observations were possible from analysis of these waves. Transmitted waves amplitude grows with joint compression, while reflected waves' decreases. The largest number of contacts and increase in conductivity in each one causes the global conductivity of the joint to grow with applied stress, as observed in laboratory and field tests of rock joints described in the literature.

Analysis of the resultant waveforms under the assumptions of the Displacement Discontinuity Theory permitted the determination of dynamic normal stiffness values and determination of reflection and transmission coefficients for each static normal stress installed at the joint. It was shown that dynamic stiffness evolves with stress in a fashion similar to real joints and its value is greater than the static stiffness for the same installed stress. Analysis of reflection and transmission coefficients shows that the energy balance is consistent with the assumed hypotheses. The model correctly reproduces the basic static and dynamic normal behaviour of rock joints.

Stress wave propagation test at the Bemposta hydroelectric complex

The fifth chapter's main original contributions are listed and then summarized and detailed in the following paragraphs.

- Low intensity tests blasts in an underground complex set in hard rock demonstrated the important role played by excavations and the course of waves between source and target in the vibration intensity.
- Different geometrical simplifications were tested in one, two and three-dimensional simulations of blast stress wave propagation and their performance compared with analytical results.
- Simulation of a test blast in two and three-dimensional finite-difference models demonstrated the limits of the former in this kind of situation.
- Three-dimensional modelling showed how a simplified numerical model replicates adequately the main features of the stress wave generation, propagation and impact in this environment.

Analysis of the plots of peak particle velocity *versus* distance scaled with blast charge displayed a large dispersion of peaks, even in this controlled environment with a relatively homogeneous rock mass. Through division of the results in smaller sets with similar characteristics it was possible to conclude that the positions of blast and sensors relative to excavations and the path of the stress waves have a decisive influence on vibration amplitude readings.

One, two and three-dimensional finite difference modelling of blast wave propagation was discussed and several geometrical symmetry formulations for stress wave geometrical attenuation were tested and compared with analytical results. These calculations showed that excellent

waveform representation can be achieved when the ratio of element size to wavelength is small enough. The deficient performance of the viscous absorbing boundaries when wave direction and boundary angle becomes smaller was also demonstrated and recommendations on how to avoid this were made.

Different kinds of blast wave input functions were presented and their advantages discussed, as well as methods of vibration generation in continuous models. It was then demonstrated that it is more advantageous and realistic to generate vibrations through stress than velocity loadings because, since the loaded region is not constrained its response is closer to reality and the resulting waves are richer.

The quality of wave propagation in the model was weighed against the maximum size of the numerical model that could be run in the available hardware configuration. Specific testing showed that even though the ratio of the minimum wavelength to the maximum element size did not conform to the usually recommended values, it was still possible to obtain acceptable results, having in mind that only the peaks of the vibrations were necessary. This showed that when concrete situations demand it, testing of the quality of the mesh may validate situations that are outside the usual quality criterion.

Two-dimensional simulation of a blast showed that this type of model cannot realistically reproduce the whole test but does deliver useful insights on a limited region. A reference three-dimensional model simulated the same blast. The model successfully reproduced the test showing that simple numerical models can replicate stress wave generation, propagation and interaction with man-made excavations.

A number of different modelling options was tested on the three-dimensional reference model. Geometric representation of the excavation where blast is generated is much less relevant than that of the receiving excavation. Correct amplification of the stress waves in the surfaces (walls, floor and ceilings) of the target excavation requires its geometry to be correctly reproduced. Properties of the rock excavation damaged zone around the openings should be correctly represented because this zone reflects part of the vibration before it arrives at the excavation boundaries but also amplifies the parcel of the wave that enters the damaged zone.

Vibration monitoring, control and analysis in large scale

The sixth chapter main original contributions are listed. Over the next paragraphs they are developed and some other contributions described:

- Comparison of empirical attenuation equations and neural networks, both calibrated with peak particle velocity, distance and charge weight as independent variables showed that neural networks are more flexible and deliver better results in the less populated (in

terms of observations) distance and charge ranges, but the overall performance is not very different.

- Application of an attenuation law corresponding to the upper 5% of the peak particle velocity values demonstrated how this kind of laws can deliver more usefull results in the protection of structures.
- Three-dimensional models' performance was demonstrated and showed the importance of singularities on the ground properties and of variations in the way blast loads are applied.

A one-year long monitoring of an underwater blasting in an extensive area was the platform for discussing vibration control in urban areas with a rich variety of constructions. The difficulties of this task and of the application of the Portuguese vibration standard were analysed and the strategies to respond to this challenge presented and justified.

A traditional exponential vibration attenuation law with peak particle velocity, blast charge and distance as independent variables and three adjustable parameters was tuned to the average of the very disperse peak particle velocity *versus* scaled distance data cloud. Then, the same law was adjusted to fit under the upper 5% percentile. This "maximized" law, definitely not a novelty, is still not used regularly in real situations. Its application on a case where it was very important for the Harbour Administration to judge on fairness of complains in what regards the applicable standard may contribute to increase its use.

An artificial intelligence technique (Multilayer Perceptron Neural Network) was employed with the same end and entry data as the averaging (50% percentile) attenuation equation. The neural network and the attenuation law results were compared with one another and with the field data. It was shown that the neural network, not being constrained to a predetermined shape as the attenuation equation, is more flexible across the distance and the charge weight domains, but its results are, overall, not very significantly better in the areas of greater construction density.

On very large sites or with complex or unknown geology, statistical analysis, attenuation laws and artificial neural networks may be the best and the only sensible way to interpolate vibration values in places where they could not be measured. Numerical methods may then be employed with a different purpose. A three-dimensional finite-difference model of a region of the harbour with a simple geometry investigated the wave propagation from the harbour's channel into the surrounding land and how some generic loading and ground properties such as dykes and lower quality ground affect stress wave intensity. The modelling results indicate that singularities on the ground properties, such as intercalations of softer material, produce the most significant changes in the attenuation profile, penalizing the area before the singularity and diminishing the vibrations thereafter.

7.3 Future developments

Ground stress wave propagation, and blast vibration in particular, are areas still wide open to new work and innovation. The above-presented contributions do not shut the doors closed, but quite the opposite, especially in what regards micromechanical simulation. The future developments of the work are grouped in three parts: micromechanical modelling is the first, monitoring, observation and testing are the second and field scale numerical modelling the third.

Micromechanical modelling of rock and rock joints

Micromechanical numerical models of rock masses at the scale of real underground works, with the detail of the simulations run in this thesis, is still not possible, even in two dimensions. But, the expansion of the calculations of small rock samples to three dimensions may already be possible and allows for greater realism not only of the joint surface representation but also of the waves, which can then be polarized in relation to the joint.

Regarding joint representation, a major task ahead is the implementation of other joint geometries and contact models that simulate with more accuracy the mechanics of asperity deformation and also shear loadings. In addition, strategies to simulate the effect of joint filling and weathering can be devised.

The rock dynamic shear and bulk moduli can be calculated if the wave propagation tests are performed with shear waves. This will allow a comparison of static and dynamic properties of rock particle bonded models. In order to calculate the dynamic shear joint stiffness, shear waves can be sent into the fracture and the reflected and transmitted waves analysed. The study of waves oblique to the fracture will demand larger models and more sophisticated methods for wave extraction and separation but will also allow for the complete verification of the Displacement Discontinuity Theory in these models.

The bonded particle model can be employed to simulate joints loaded by mixed normal and shear forces. This results in more complex interactions at asperity level and higher degrees of joint degradation affecting their static and dynamic properties.

It is believed that micromechanical models may, when computational capacities allow it, simulate all kinds of mechanical loadings, be they external static loading, excavation of material or dynamic loadings, in three-dimensional jointed rock masses under static *in situ* stress states. While this is not possible, hybrid continuum-particle models are being developed and used. In these models the majority of the domain is represented with continuum elements (finite-difference zones or finite elements) which are replaced by particles in the regions where the non-linear behaviour is to take place. These models can be used to represent rock joints, but

their dynamic performance, especially the continuity of stress waves in the particle-continuum interface, has not been tested yet.

Monitoring and observation of stress wave propagation

To gain more understanding of stress wave propagation in rock masses, and also to calibrate numerical models, more blast tests in the interior of rock masses are necessary. Some improvements are suggested regarding this kind of blast tests. The first is the installation of sensors inside the rock mass, outside the volume of influence of excavations. The installation of sensors near to the source will allow the synchronization of the blast and of the acceleration records and through this a direct characterization of wave velocities in the test volume is possible. The characterization of the blast waveform before it is changed by the rock mass will also benefit. This is not, however, easy to perform because the vibration amplitudes near the source are very high and the environment very aggressive due to fly rock and gas production. Also complicated is the monitoring of the dynamic stress or strain in the rock and in linings, but it allows, among other studies, the determination of properties of the rock-lining interface and its influence on stress wave propagation.

In the Leixões harbour monitoring, a greater knowledge of the conditions of wave propagation was limited by the number of monitoring devices, by the fact that some of them had to be located in specific buildings to address complaints and also by the very low level of knowledge on the ground properties. It will be interesting to continue studying this or a similar situation with better site characterization and without the weight of enssuring the fulfilment of the standard in the existing buildings.

Monitoring equipment and electronics have evolved very fast over the last years. Devices are smaller, cheaper and more independent but evolution is expected. The sensors may in the future have digitizing, signal processing and storage capabilities embedded in them. Lower price, greater autonomy, high-precision internal clocks, GPS and wireless communication will also facilitate installation and management of large arrays of monitors and enrich the information that can be extracted and correlated.

Numerical modelling of stress wave propagation

Three-dimensional modelling of blast stress wave propagation and dynamic modelling in general is limited, among other motives, by hardware capacity. Blast vibration dominant frequencies are higher than earthquake's and mesh quality must be maintained throughout the domain, leading to large models. Thus, detailed reproduction of the real geometries can only be attained when more potent computational means become widely available. Parallelization of codes and their

adaptation to new processors and cloud-computing are two possible pathways.

The need for richer rock mass dynamic properties characterization and how these properties are introduced in the numerical models as constitutive model parameters is transversal to the whole thesis. There are sophisticated numerical and material constitutive models but it is difficult to choose what parameters to employ. A good example is the explicit representation of jointing. Several models can include joints and several joint constitutive models exist. But is the information necessary to calibrate these models usually available? This is true also in static calculations but even more evident in dynamic problems.

Regarding the tests in the underground complex (chapter 5) the information gathered from the blasts contains potential for continuation of the numerical modelling. A more complex model is necessary to simulate the two other blast sets, since the excavations' geometry is more complicated. Three-dimensional detailed representation of excavations is challenging and more advanced automated mesh generation techniques are necessary. Automated meshes' element size and proportions must be controlled to ensure economy and good representation of stress waves across the whole domain. Also worth pursuing is the simulation of the propagation of vibrations into the powerhouse cavern's reinforced concrete internal structure that supports the turbines and other equipment.

On a broader perspective of the numerical simulation of blasting, it is necessary to establish the relation between instantaneous blast charge and numerical blast loading. This is one of the most important questions in modelling blast vibration and must be asserted under more controlled conditions and with a wider range of loads.

Use of numerical models in the design and study of mitigation measures such as vibration barriers and vibration isolation surely will increase and become more important. This must be accompanied by comparisons with field testing, which are expensive, but unavoidable until more confidence on the models is gained.

In propagation of stress waves at longer distances the importance of amplitude decay due to ground damping increases over geometrical attenuation. This is a problem not yet settled in numerical models. Frequency dependent Rayleigh damping, commonly used in earthquake analysis does not address this in a satisfactory manner. Methods such as hysteretic damping inclusion in contact or continuous constitutive models is one of the stronger alternatives, since it replicates the phenomenon more realistically.

Finally, more situations can be explored with numerical methods regarding, for example, topography of the ground where waves propagate and of the channel and other geological variations such as superficial patches of softer ground or the influence of multiple blasts at distance. But, all these modelling activities are founded on soft ground themselves until more complete comparisons with monitoring are done.

List of References

Abe, S., Place, D. and Mora, P. "A parallel implementation of the lattice solid model for the simulation of rock mechanics and earthquake dynamics." *Pure and Applied Geophysics*, 161(11): 2265–2277 (2004).

Achenbach, J. *Wave Propagation in Solids.* Applied Matemathics and Mechanics. North Holland, Amsterdam (1973).

Ambraseys, N. and Hendron, A. "Dynamic behaviour of rock masses." In K. Stagg and O. Zienkiewicz (editors), "Rock Mechanics in Engineering Practice," 203–227. John Wiley and sons, London (1968).

Azevedo, N. M. and Lemos, J. V. "A generalized rigid particle contact model for fracture analysis." *International Journal for Numerical and Analytical Methods in Geomechanics*, 29(3): 269–285 (2005).

Bandis, S. C., Lumdsen, A. C. and Barton, N. "Fundamentals of rock joint deformation." *International Journal of Rock Mechanics and Mining Sciences & Geomechanics Abstracts*, 20(6): 249–268 (1983).

Barton, N. *Rock Quality, Seismic Velocity, Attenuation and Anisotropy.* Taylor and Francis (2007).

Bedford, A. and Drumheller, D. *Introduction to Elastic Wave Propagation.* John Wiley, Chichester (1994).

Belytschko, T. "An overview of semidiscretization and time integration procedures." In T. Belytschko and T. Hughes (editors), "Computational Methods for Transient Analysis," 1–65. North Holland (1983).

Bendat, J. S. and Piersol, A. G. *Random Data - Analysis and Measurement Procedures*, volume 1. John Wiley & Sons, 2 edition (1986).

Bernardo, P. *Environmental Impacts of Blast Excavation of Rocks, with Emphasis on Vibrations (in Portuguese)*. PhD thesis, Lisbon Technical University (2004).

Billaux, D. *Hydrogeology of Fractured Media - Geometry, Connectivity and Hydromechanical Behaviour*. PhD thesis, École Nationale Superieure des Mines de Paris (1990).

Brown, S. R., Kranz, R. L. and Bonner, B. P. "Correlation between the surfaces of natural rock joints." *Geophysical Research Letters*, 13: 1430–1433 (1986).

BSI. *BS 7385: Evaluation and Measurement for Vibration in Buildings*. British Standard Institute (1992).

Cai, J. G. *Effects of Parallel Fractures on Wave Attenuation in Rock*. PhD thesis, Nanyang Technological University (2001).

Cai, M., Kaiser, P. K., Morioka, H., Minami, M., Maejima, T., Tasaka, Y. and Kurose, H. "FLAC/PFC coupled numerical simulation of AE in large-scale underground excavations." *International Journal of Rock Mechanics and Mining Sciences*, 44(4): 550–564 (2007).

Chen, S. G., Cai, J. G., Zhao, J. and Zhou, Y. X. "Discrete element modelling of an underground explosion in a jointed rock mass." *Geotechnical and Geological Engineering*, 18: 59–78 (2000).

Cook, N. "Natural joints in rock: Mechanical, hydraulic and seismic behaviour and properties under normal stress." *International Journal of Rock Mechanics and Mining Science & Geomechanics Abstracts*, 29(3): 198–223 (1992).

Cundall, P. "Numerical experiments on rough joints in shear using a bonded particle model." In F. K. Lehner and J. L. Urai (editors), "Aspects of Tectonic Faulting (Festschrift in Honnour of Georg Mandl)," 1–9. Springer-Verlag, Berlin (2000).

Cundall, P. A. "A computer model for simulating progressive, large-scale movements in blocky rock systems." In "Symposium of the International Society for Rock Meachanics," Nancy (1971).

Cundall, P. A. *UDEC - A Generalized Distinct Element Program for Modelling Jointed Rock*. Report PCAR-1-80. European Research Office, US Army (1980).

Cundall, P. A. "Formulation of a three-dimensional distinct element model - Part I: A scheme to detect and represent contacts in a system composed of many polyhedral blocks." *International Journal of Rock Mechanics and Mining Sciences*, 25: 107–116 (1988).

Cundall, P. A. and Strack, O. D. L. "A discrete numerical model for granular assemblies." *Geotechnique*, 29(1): 47–65 (1979).

DGQ. *NP 2074: Evaluation on the Influence of Vibrations caused by Explosions and Similar Sources (in Portuguese)*. Direcção-Geral da Qualidade (1983).

DIN. *DIN 4150: Structural vibration in buildings*. Deutsches Institut für Normung (1999).

Donzé, F. V. "SDEC – Spherical Discrete Element Method, v. 2.00." Technical report, ISRN Geonum-nst-2001-fr, France (2002).

Donzé, F. V. and Bernasconi, P. "Simulation of blast patters in shaft sinking using discrete element method." *Electronic Journal of Geotechnical Engineering Geology*, 9(B): 22 (2004).

Donzé, F. V., Bouchez, J. and Magnier, S. A. "Modeling fractures in rock blasting." *International Journal of Rock Mechanics and Mining Sciences*, 34(8): 1153–1163 (1997).

Dowding, C. H. *Construction Vibrations*. Prentice Hall International Series in Civil Engineering and Engineering Mechanics. Prentice Hall, 1st edition (1996).

Duffy, J. "A differential stress-strain relation for the hexagonal close-packed array of elastic spheres." In ASME (editor), "Annual Meeting of the American Society of Mechanical Engineering," ASME, New York (1959).

Duvall, W. "Strain-wave shapes in rock near explosions." *Geophysics*, 18(2): 310–323 (1953).

EDP. "Project of the upgrade to the Bemposta dam (in Portuguese)." Technical report, EDP (2007).

Fakhimi, A. and Villegas, T. "Application of dimensional analysis in calibration of a discrete element model for rock deformation and fracture." *Rock Mechanics and Rock Engineering*, 40(2): 193–211 (2007).

Fan, S. C., Jiao, Y. Y. and Zhao, J. "On modelling of incident boundary for wave propagation in jointed rock masses using discrete element method." *Computers and Geotechnics*, 31(1): 57–66 (2004).

Goodman, R. E., Taylor, R. and Breeke, T. "A model for the mechanics of jointed rock." *Journal of Soil Mechanics and Foundations Division ASCE*, 94: 637–659 (1968).

Grasselli, G. "Manuel Rocha Medal Recipient. Shear strength of rock joints based on quantified surface description." *Rock Mechanics and Rock Engineering*, 39(4): 295–314 (2006).

Greenwood, J. and Williamson, J. "Contact of nominally flat surfaces." *Procedings of the Royal Society of London*, 295(1442): 300–319 (1966).

Gutierrez, M. and Barton, N. "Numerical modelling of the hydro-mechanical behavior of single fractures." In "1st North-American Rock Mechanics Symposium," Balkema, Texas, Austin (1994).

Hart, R. D., Cundall, P. A. and Lemos, J. V. "Formulation of a three-dimensional distinct element model - Part II: Mechanical calculations for motion and interaction of a system composed of many polyhedral blocks." *International Journal of Rock Mechanics and Mining Sciences*, 25: 117–125 (1988).

Hazzard, J. F. and Young, R. P. "Numerical investigation of induced cracking and seismic velocity changes in brittle rock." *Geophysical Research Letters*, 31: 4 (2004).

Hentz, S., Donzé, F. V. and Daudeville, L. "Discrete element modelling of concrete submitted to dynamic loading at high strain rates." *Computers & Structures*, 82(29-30): 2509–2524 (2004).

Hildyard, M. W. *Wave interaction with underground openings in fractured rock*. PhD thesis, University of Liverpool (2001).

Hoover, W. G., Ashurst, W. T. and Olness, R. K. "Two-dimensional computer studies of crystal stability and fluid viscosity." *Journal of Chemical Physics*, 60(10): 4043–4047 (1974).

Hopler, R. *Blasters Handbook*. International Society of Explosives Engineers, 17th edition (1998).

Huang, H., Detournay, E. and Bellier, B. "Discrete element modelling of rock cutting." In "37th US Rock Mechanics Symposium - Rock Mechanics for Industry," volume 1, 123–130. Balkema, Vail, Colorado (1999).

Hudson, J. "Wave speeds and attenuation of elastic waves in material containing cracks." *Geophysical Journal of the Royal Astrophysical Society*, 64: 133–150 (1981).

Hudson, J. "A higher order approximation to the wave propagation constants for a cracked solid." *Geophysical Journal of the Royal Astrophysical Society*, 87: 265–274 (1986).

Hudson, J. "Seismic wave propagation through material containing partially saturated cracks." *Geophysical Journal*, 92: 33–37 (1988).

INAG. "http://www.inag.pt (in Portuguese)." (2009).

ISO. *ISO 4866: Mechanical Vibration and Shock - Vibrations in Buildings - Guidelines for the Measurement of Vibrations and Evaluation of their Effects on Buildings*. International Organization for Standardization (1990).

ISO. *ISO 2631: Mechanical Vibration and Shock - Evaluation of Human Exposure to Whole Body Vibration*. International Organization for Standardization (1997).

ISO. *ISO 2041: Vibration and Shock - Vocabulary*. International Organization for Standardization (2009).

ISRM. *ISRM Suggested Method for Determining Shear Strength*. International Society for Rock Mechanics Commission on Standartization of Laboratory and Field Tests (1974).

ISRM. *ISRM Suggested Methods for Quantitative Description of Discontinuities*. International Society for Rock Mechanics Commission on Standartization of Laboratory and Field Tests (1978).

ITA. "Environmental and sustainable development reasons for going underground." Technical report, ITA-AITES (2010).

Itasca. *PFC^{2D} - Two Dimensional Particle Flow Code, Ver. 3.1 User's Manual*. Itasca Consulting Group, Minneapolis (2004).

Itasca. *PFC^{3D} - Three Dimensional Particle Flow Code, Ver. 3.1 User's Manual*. Itasca Consulting Group, Minneapolis (2005).

Itasca. In R. Hart, C. Detournay and P. Cundall (editors), "First Symposium on Continuum and Distinct Element Numerical Modeling in Geo-Engineering," Itasca Consulting Group, Minesota (2008a).

Itasca. *FLAC - Fast Lagrangian Analysis of Continua, Ver. 6.0 User's Manual*. Itasca Consulting Group, Minneapolis (2008b).

Itasca. *FLAC^{3D} - Fast Lagrangian Analysis of Continua in 3 Dimensions, Ver. 4.0 User's Manual*. Itasca Consulting Group, Minneapolis (2010).

Jing, L. "A review of techniques, advances and outstanding issues in numerical modelling for rock mechanics and rock engineering." *International Journal of Rock Mechanics and Mining Sciences*, 40(3): 283–353 (2003).

Johnson, K. L. *Contact Mechanics*. Cambridge University Press (1985).

Johnston, D. H. *The attenuation of seismic waves in dry and saturated rocks*. PhD thesis, Massachusets Institute of Technology (1978).

Jones, J. P. and Whitter, J. S. "Waves at a flexible bonded interface." *Journal of Applied Mechanics*, 40: 905–909 (1967).

Kabeya, K. "Investigation into the peak shear behaviour of rock joints using physical and numerical modeling." In "37th US Rock Mechanics Symposium - Rock Mechanics for Industry," volume 1, 139–446. Balkema, Vail, Colorado (1999).

Karami, A. and Stead, D. "Asperity degradation and damage in the direct shear test: A hybrid FEM/DEM approach." *Rock Mechanics and Rock Engineering*, 41(2): 229–266 (2008).

Kazerani, T. and Zhao, J. "A bonded particle modelling for rock material." In "5th Asian Rock Mechanics Symposium," Tehran, Iran (2008).

Kendall, K. and Tabor, D. "An ultrasonic study of the area of contact between stationary and sliding surfaces." *Procedings of the Royal Society of London*, A 332: 321–340 (1971).

Kerstiëns, C. *A generic UDEC model for rock joint shear tests, including roughness characterization*. Master thesis, Delft University of Technology (1999).

Kiehl, J. R. and Werfling, J. "Measurements and analyses of blasting vibrations." In "ISRM 2003 – Technology Roadmap for Rock Mechanics," South Africa (2003).

Kim, M. K., Kim, S. E., Oh, K. H. and Kim, W. J. "A study on the behavior of rock mass subjected to blasting using modified distinct element method." *International Journal of Rock Mechanics and Mining Sciences*, 34(3-4): 156.e1–156.e14 (1997).

Kim, S., Jeong, W., Jeong, D. and Seok, J. "Numerical simulation of blasting at tunnel contour hole in jointe rock mass." *Tunnelling and Underground Space Technology*, 21(3-4): 306–307 (2006).

King, M. S., Myer, L. R. and Rezowalli, J. "Experimental studies of elastic-wave propagation in a columnar-jointed rock mass." *Geophysical Prospecting*, 34: 1185–1199 (1986).

Kolsky, H. *Stress Waves in Solids*. Monographs on the Physics and Chemistry of the Materials. Clarendon Press, Oxford, 1st edition (1953).

Krajcinovic, D. "Continuum damage mechanics: When and how?" *International Journal of Damage Mechanics,*, 4(3): 217–229 (1995).

Kujundzic, B., Jovanovic, L. and Radosavljevic, Z. "Solution du revêtement d'une galerie en charge par application d' injections a haute pression." In "2nd Congress of the International Society for Rock Mechanics," Belgrade (1970).

Kusumi, H., Matsuoka, T., Ashida, Y. and Tatsumi, S. "Simulation analysis of shear behavior of rock joint by distinct element method." In Konecny (editor), "EUROCK 2005 - Impact of Human Activity on Geological Environment," Taylor and Francis, Brno (2005).

Lamas, L. *Contributions for Understanding the Hydromechanical Behaviour of Pressure Tunnels.* PhD thesis, University of London (1993).

Lemos, J. V. *A Distinct Element Method for Dynamic Analysis of Jointed Rock with Application to Dam Foundation and Fault Motion.* PhD thesis, University of Minnesota (1987).

Lemos, J. V. *Modelling and Failure Analysis in Rock Engineering.* National Laboratory for Civil Engineering, Lisbon, Portugal (2001).

LNEC. "Study of the vibrations induced in the rock mass of the Bemposta dam powerstation by controled blasting (in Portuguese)." Technical report, National Laboratory for Civil Engineering, Lisbon, Portugal (2007).

LNEC. "Geomechanical caractherization works of the rock mass of the Bemposta dam new powerplant (in Portuguese)." Technical report, National Laboratory for Civil Engineering, Lisbon, Portugal (2008).

Lysmer, J. and Kuhlemeyer, A. M. "Finite dynamic model for infinite media." *Journal of the Engineering Mechanics Division of the American Society of Civil Engineers*, 95(4): 859–869 (1969).

Marques, J. C. "Visualization of energy absorbing boundaries in geotechnical problems." In "CMNE/CILAMCE 2007," Oporto, Portugal (2007).

Martin, C. D. *The Strength of Massive Lac du Bonnet Granite around Underground Openings.* PhD thesis, University of Manitoba (1993).

Mata, J., Portela, E. and Dias, J. "A neural network approach for seepage control of Alto Rabagão Dam." In "75th Annual Meeting of the International Commission on Large Dams," San Petersburg (2007).

MathWorks. "Matlab - The Language of Technical Computing." (2009).

Matsuoka, T., Kusumi, H., Ashida, Y. and Watanabe, T. "Simulation of Hopkinson effect by discrete element method." In "ISRM 2003 – Technology Roadmap for Rock Mechanics," South Africa (2003).

Mendes, L. and Campos Costa, A. "LNEC-SPA, Signal Processing and Analysis Tools for Civil Engineers - v 1.0." Technical report, National Laboratory for Civil Engineering, Lisbon, Portugal (2007).

Min, K.-B., Jing., L. and Stephansson, O. "Effect of stress on mechanical and hydraulic rock mass properties – Application of DFN-DEM approach on the data from site investigation at Forsmark, Sweden." (2005).

Mindlin, R. D. "Mechanics of granular media." In "2nd U.S. National Congress of Applied Mechanics," (1954).

Mortazavi, A. and Katsabanis, P. D. "Modelling burden size and strata dip effects on the surface blasting process." *International Journal of Rock Mechanics and Mining Sciences*, 38(4): 481–498 (2001a).

Mortazavi, A. and Katsabanis, P. D. "Modelling of blasthole expansion and explosive gas pressurization in jointed media." *International Journal of Rock Mechanics and Mining Sciences*, 35(4-5) (2001b).

Muralha, J. *Probabilistic Analysis of the mechanical behaviour of Rock Joints (in Portuguese).* PhD thesis, Technical University of Lisbon (1995).

Myer, L. R. "Fractures as collections of cracks." *International Journal of Rock Mechanics and Mining Sciences*, 37(1-2): 231–243 (2000).

Nolte, D. D., Pyrak-Nolte, L. J., Beachy, J. and Ziegler, C. "Transition from the displacement discontinuity limit to the resonant scattering regime for fracture interface waves." *International Journal of Rock Mechanics and Mining Sciences*, 37: 219–230 (2000).

Oreskes, N., Shrader-Frechette, K. and Belitz, K. "Verification, validation and confirmation of numerical models in the earth sciences." *Science*, 263: 641–646 (1994).

Park, E. S., Martin, C. D. and Christiansson, R. "Numerical simulation of the mechanical behavior of discontinuous rock masses." In Itasca (editor), "Numerical Methods in Micromechanics via Particle Methods," Balkema, Kyoto, Japan (2004).

Park, J.-W. and Song, J.-J. "Numerical simulation of direct shear test on rock joint using PFC3D." In "5th Asian Rock Mechanics Symposium," Tehran, Iran (2008).

Patterson, D. W. *Artificial Neural Networks: Theory and Applications*. Prentice Hall (1998).

Persson, P.-A., Holmberg, R. and Lee, J. *Rock Blasting and Explosives Engineering*. CRC Press, 6th edition (2001).

Plesha, M. "Rock joints: theory, constitutive equations." In "Mechanics of Geomaterial Interfaces," Elsevier Science, Netherlands (1995).

Potyondy, D. O. and Cundall, P. A. "A bonded-particle model for rock." *International Journal of Rock Mechanics and Mining Sciences*, 41(8): 1329–1364 (2004).

Potyondy, D. O., Cundall, P. A. and Lee, C. A. "Modelling rock using bonded assemblies of circular particles." In "Rock Mechanics US' 96," (1996).

Pyrak-Nolte, L. and Nolte, D. D. "Frequency dependence of fracture stifness." *Geophysical Research Letters*, 19(3): 4 (1992).

Pyrak-Nolte, L. J. "The seismic response of fractures and the interrelations among fracture properties." *International Journal of Rock Mechanics and Mining Sciences & Geomechanics Abstracts*, 33(8): 787–802 (1996).

Pyrak-Nolte, L. J., Cook, J. M. and Myer, L. R. "Seismic visibility of fractures." In I. W. Farmer (editor), "28th US Symposium on Rock Mechanics," Balkema, Tucson (1987).

Pyrak-Nolte, L. J., Myer, L. R. and Cook, N. G. "Transmission of seismic waves across single natural fractures." *Journal of Geophysical Research*, 95(B6): 22 (1990).

Resende, R., Mata, J., Gomes, J. and Neves, J. "Vibration control of underwater blasting works using artificial neural networks." In "12th International Conference of the IACMAG," Goa, India (2008).

Ribeiro, D. *Dynamic behaviour of bridges under high-speed rail traffic*. PhD thesis, University of Oporto (2004).

Roy, P. P. *Rock Blasting - Effects and Operations*. A.A. Balkema, 1st edition (2005).

Schlangen, E. and Van Mier, J. "Experimental and numerical study of crack propagation in sandstone." In "EUROCK 94 - Rock Mechanics in Petroleum Engineering," 131–138. Balkema, Delft (1994).

Schoenberg, M. "Elastic wave behavior across linear slip interfaces." *Journal Acoustic Society of America*, 68(5): 1516–1521 (1980).

Sena, M. C. R. and Silveira, E. S. S. "An implementation of the Discrete Element Method in a parallel computing environment (in Portuguese)." In "CMNE/CILAMCE," Porto (2007).

Sheriff, R. and Geldart, L. *Exploration Seismololgy*. Cambridge University Press (1995).

Shi, G. H. and Goodman, R. E. "Discontinuous Deformation analysis: A new method for computing stress, strain and sliding of block systems." In Cundall, Sterling and Starfield (editors), "Key questions in Rock Mechanics - 29th US Rock Mechanics Symposium," 381–393. Balkema, Roterdam (1988).

Swan, G. "Determination of stiffness and other joint properties from roughness measurements." *Rock Mechanics and Rock Engineering*, 16: 19–38 (1983).

Tai, Q. and Sadd, M. H. "A discrete element study of the relationship of fabric to wave propagational behaviours in granular materials." *International Journal for Numerical and Analytical Methods in Geomechanics*, 21(5): 295–311 (1997).

Toomey, A. *Particle-based Numerical Modelling of Seismic Wave Propagation in Fractured Rock*. PhD thesis, National University of Ireland (2001).

Tsang, Y. W. and Witherspoon, P. "Hydromechanical behaviour of a deformable rock fracture subject to normal stress." *Journal of Geophysical Research*, 86(B10): 9287–9898 (1981).

USDI. *RI 656: Blasting Vibrations and their Effects on Structures*. United States Department of the Interior (1971).

USDI. *RI 8507: Structure Response and Damage Produced by Ground Vibration from Surface Mine Blasting*. United States Department of the Interior (1980).

Vermeer, P. A. and de Borst, R. "Non-associated plasticity for soils, concrete and rock." *Heron*, 29(3): 1–65 (1992).

VSS. *SN 640 312a: Effect of Vibrations on Constructions*. Union des Professionnels Suisses de la Route (VSS) (1992).

Wang, Z. L., Konietzky, H. and Shen, R. F. "Coupled finite element and discrete element method for underground blast in faulted rock masses." *Soil Dynamics and Earthquake Engineering*, 29(6): 939–945 (2009).

Winkler, K. "Contact stiffness in granular porous materials: Comparison between theory and experiment." *Geophysical Research Letters*, 10(11): 1073–1076 (1983).

Yoon, J. "Application of experimental design and optimization to PFC model calibration in uniaxial compression simulation." *International Journal of Rock Mechanics and Mining Sciences*, 44(6): 871–889 (2007).

Zhao, J. and Cai, J. G. "Transmission of elastic P-waves across single fractures with a nonlinear normal deformational behavior." *Rock Mechanics and Rock Engineering*, 34(1): 3–22 (2001).

Zhao, J., Cai, J. G., Zhao, X. B. and Li, H. B. "Experimental study of ultrasonic wave attenuation across parallel fractures." *Geomechanics and Geoengineering: An International Journal*, 1(2): 87–103 (2006).

Zhu, Z., Mohanty, B. and Xie, H. "Numerical investigation of blasting-induced crack initiation and propagation in rocks." *International Journal of Rock Mechanics and Mining Sciences*, 44(3): 412–424 (2007).

Appendix I

Photographs of the Bemposta Test Site





Figure I.1: Concrete plug at the end of Surface adit seen from the inside.



Figure I.2: Concrete plug at the end of Surface adit seen from the outside.



Figure I.3: Base P1 in the floor of the concrete plug at the end of Surface adit.



Figure I.4: Surface adit photographed from the concrete plug: bases P2 (left), P3 (floor) and P4 (right). Debris from the cave-in are visible on the background.



Figure I.5: Base P2, in the Surface adit.



Figure I.6: Base P3, in the Surface adit. The concrete block is founded on the rock underlying the rubble on the floor of the adit.



Figure I.7: Base P4, in the Surface adit.



Figure I.8: Base P5, in the Surface adit.



Figure I.9: Concrete plug at the beginning of the Outlet adit and base P6 at the wall on the right.



Figure I.10: Detail view of base P6, in the Outlet adit.



Figure I.11: Access adit and bases P7 (wall on the right) and P19 (wall on the left).



Figure I.12: Base P7, in the Access adit.



Figure I.13: Base P19, in the Access adit.

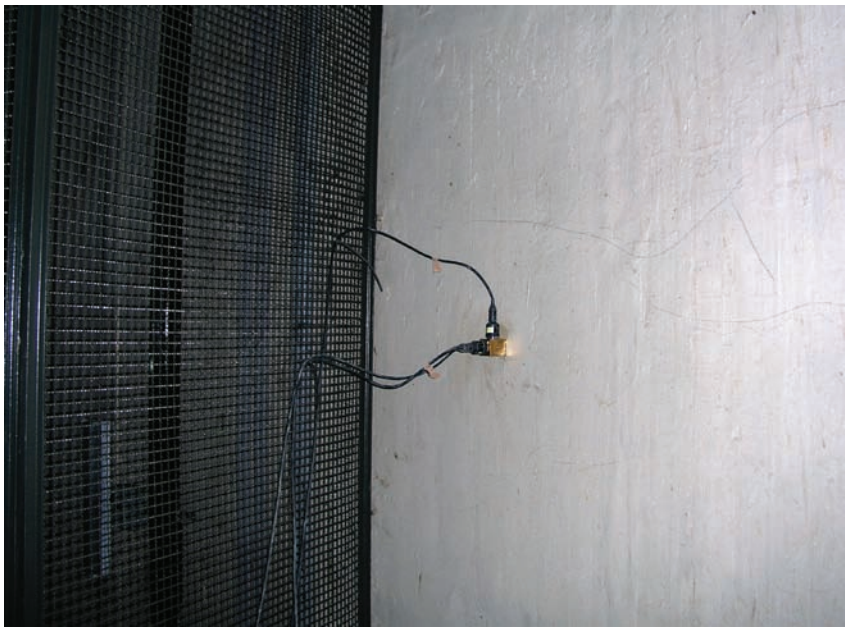


Figure I.14: Base P11, in the elevator and stairs shaft.



Figure I.15: Base P18, in the cable adit.



Figure I.16: Cable adit taking cables from the powerhouse cavern to the shaft. Base P18 was installed in the wall on the left.

Appendix II

Plots of the Bemposta Test Results

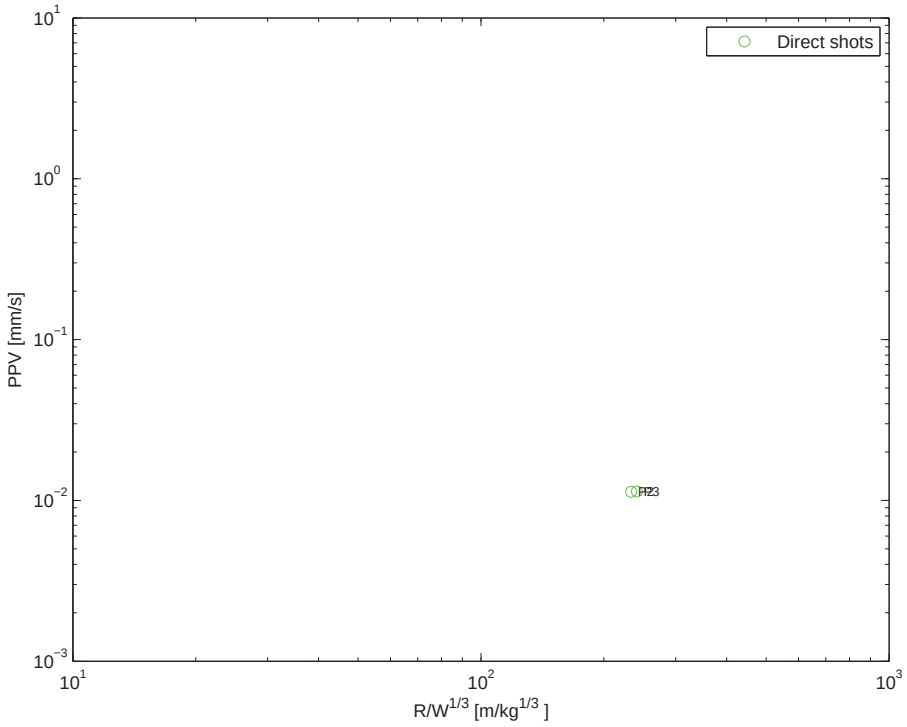


Figure II.1: Plot of peak particle velocity *vs* scalled distance for blast B1.

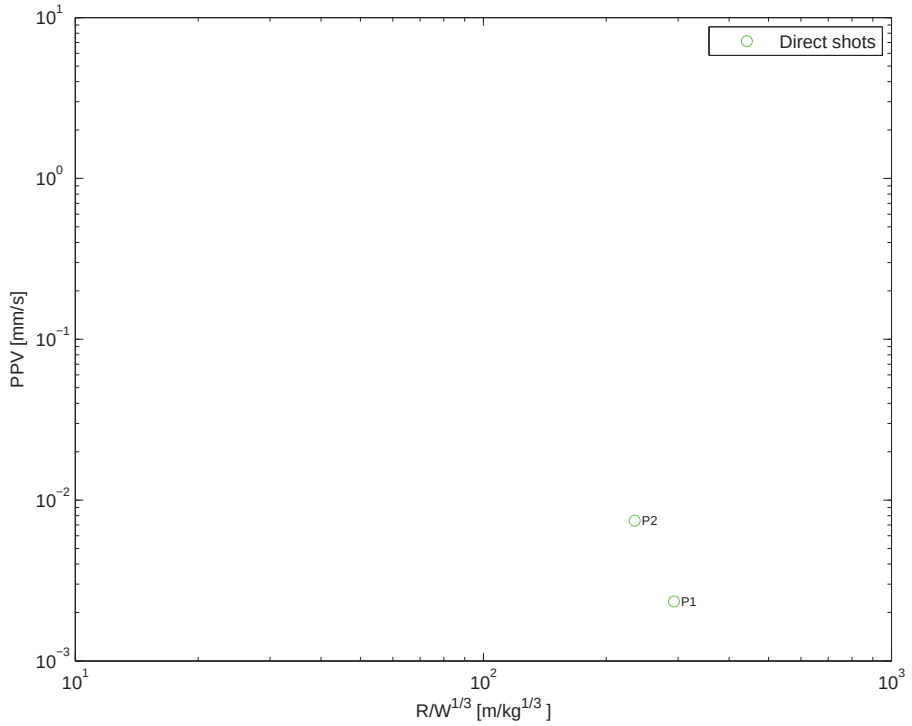


Figure II.2: Plot of peak particle velocity *vs* scalled distance for blast B2.

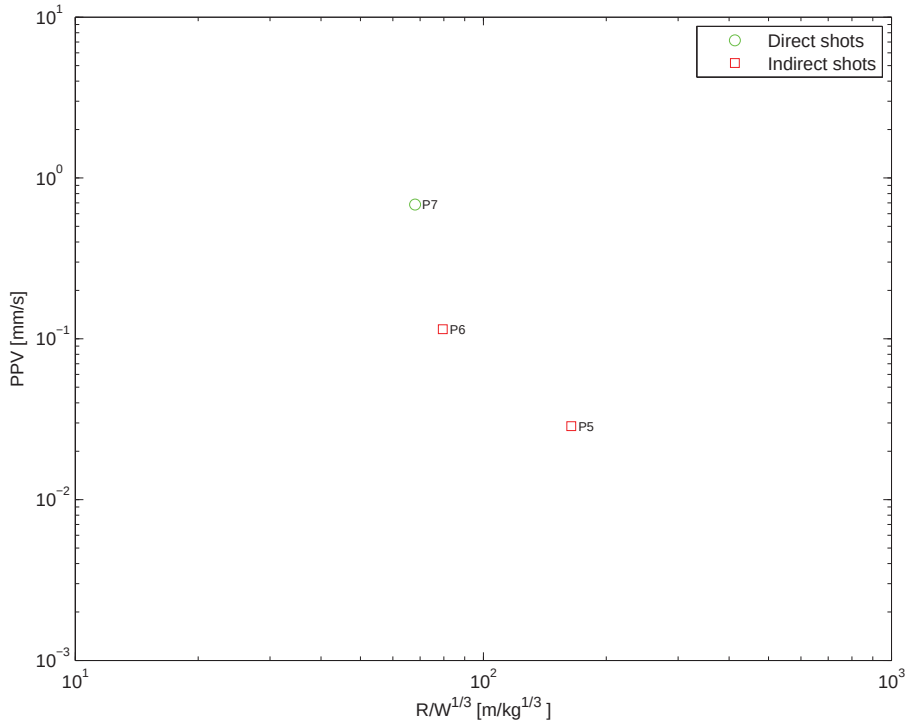


Figure II.3: Plot of peak particle velocity *vs* scalled distance for blast B3.

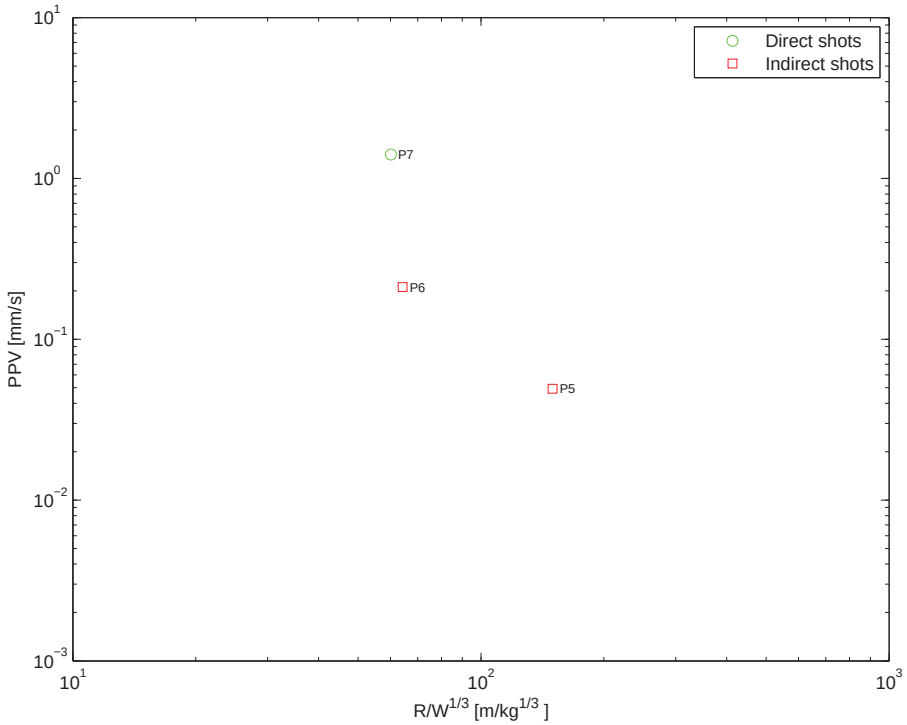


Figure II.4: Plot of peak particle velocity *vs* scalled distance for blast B4.

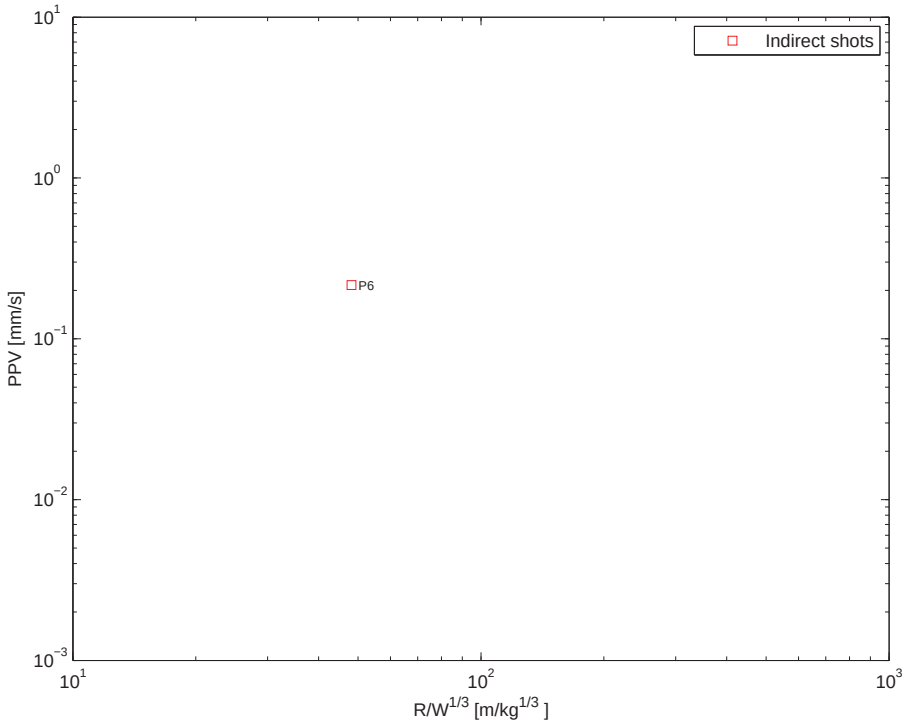


Figure II.5: Plot of peak particle velocity *vs* scalled distance for blast B5.

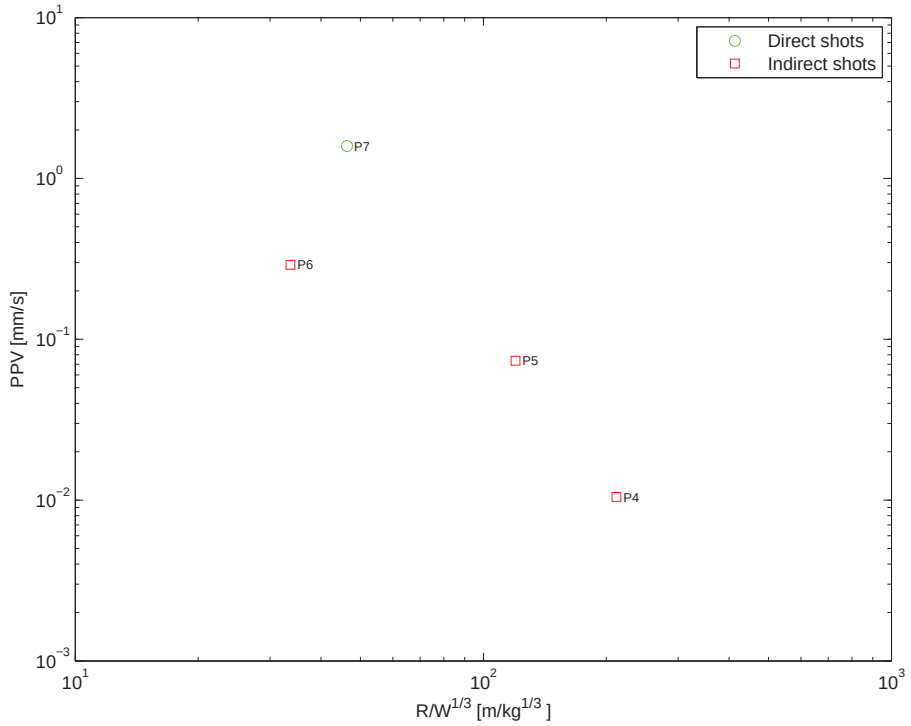


Figure II.6: Plot of peak particle velocity *vs* scalled distance for blast B6.

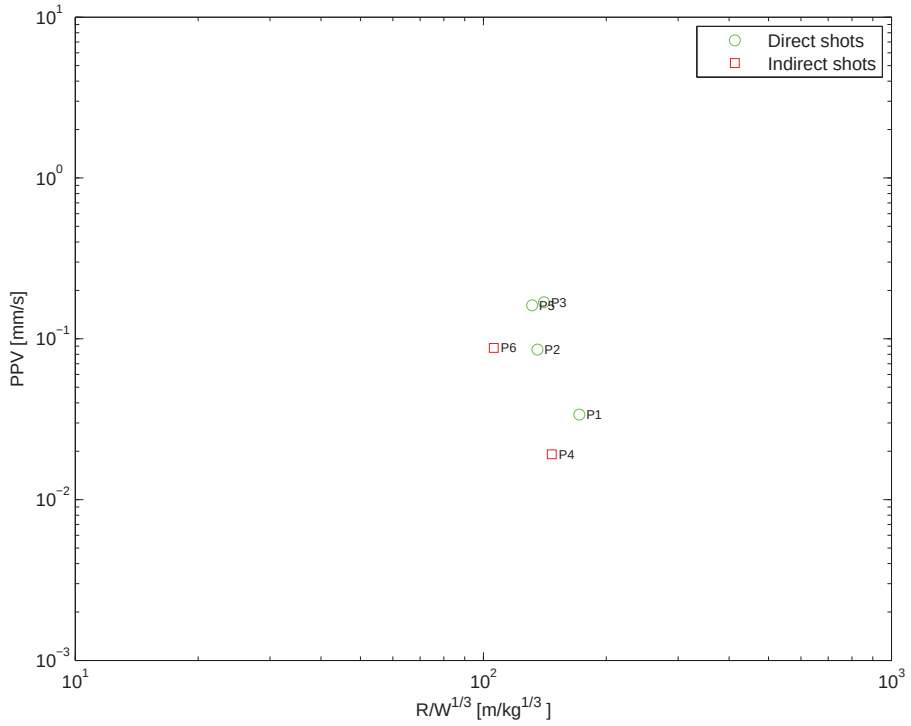


Figure II.7: Plot of peak particle velocity *vs* scalled distance for blast B7.

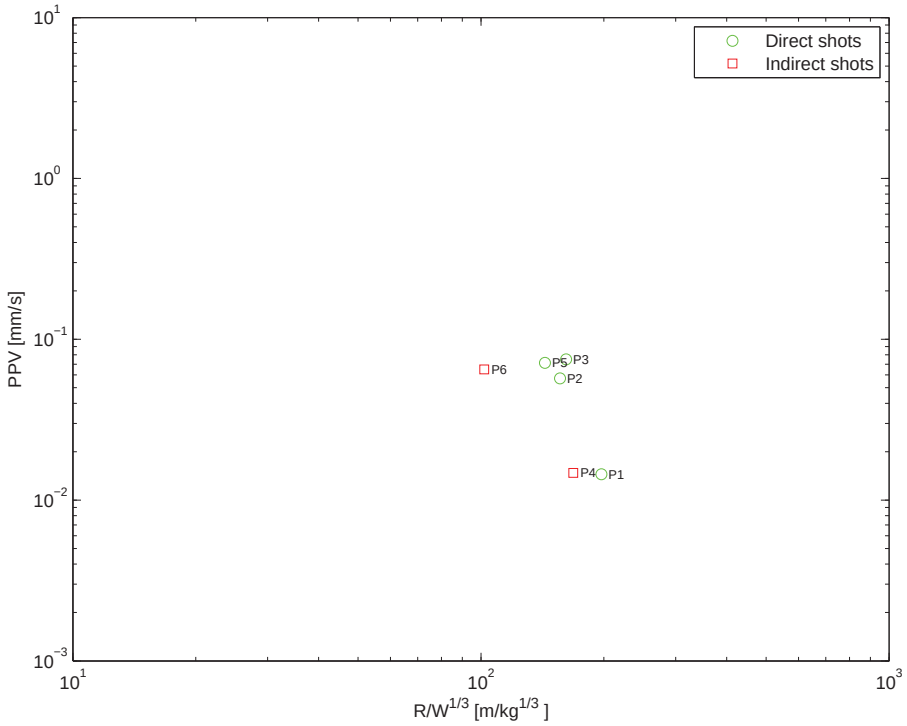


Figure II.8: Plot of peak particle velocity *vs* scalled distance for blast B8.

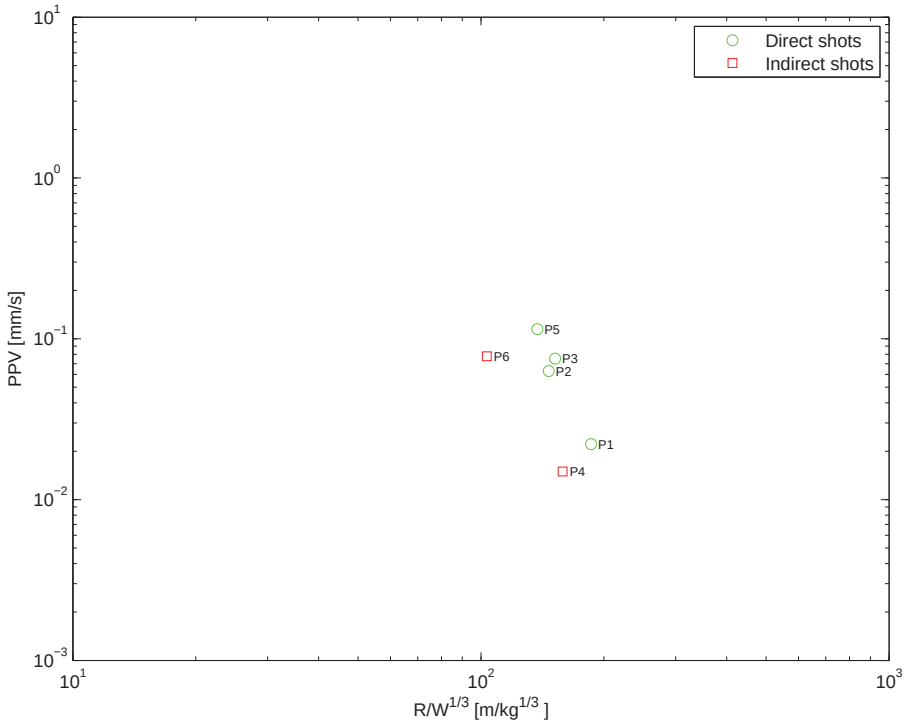


Figure II.9: Plot of peak particle velocity *vs* scalled distance for blast B9.

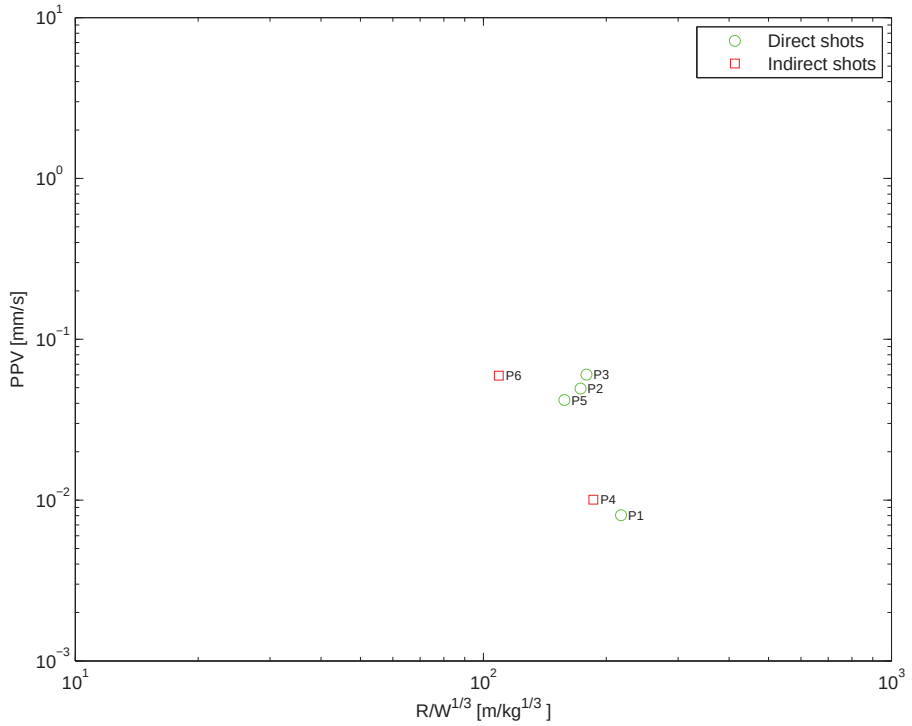


Figure II.10: Plot of peak particle velocity *vs* scalled distance for blast B10.

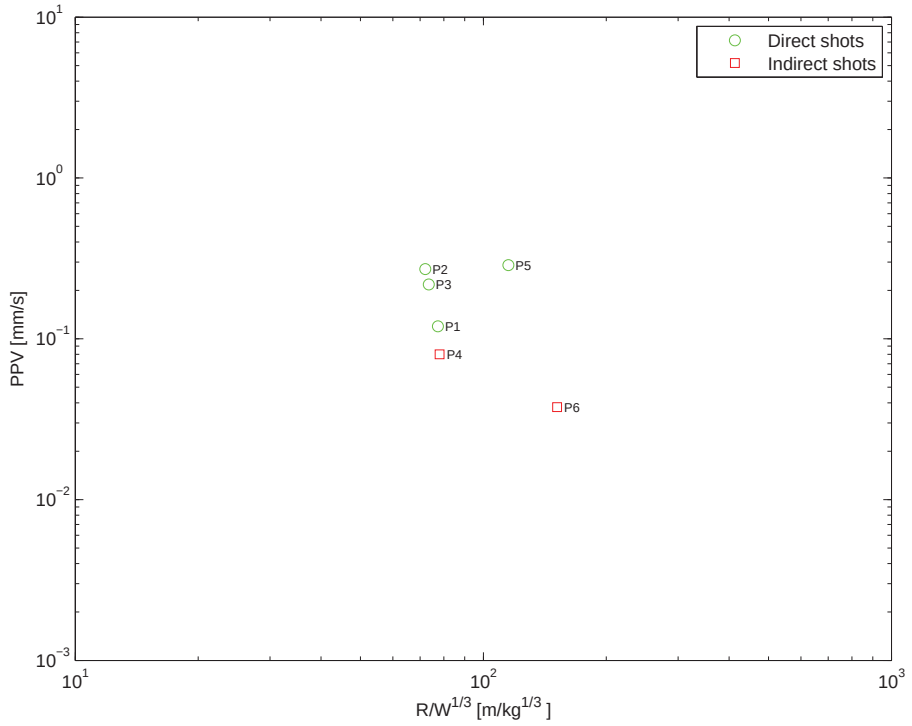


Figure II.11: Plot of peak particle velocity *vs* scalled distance for blast B11.

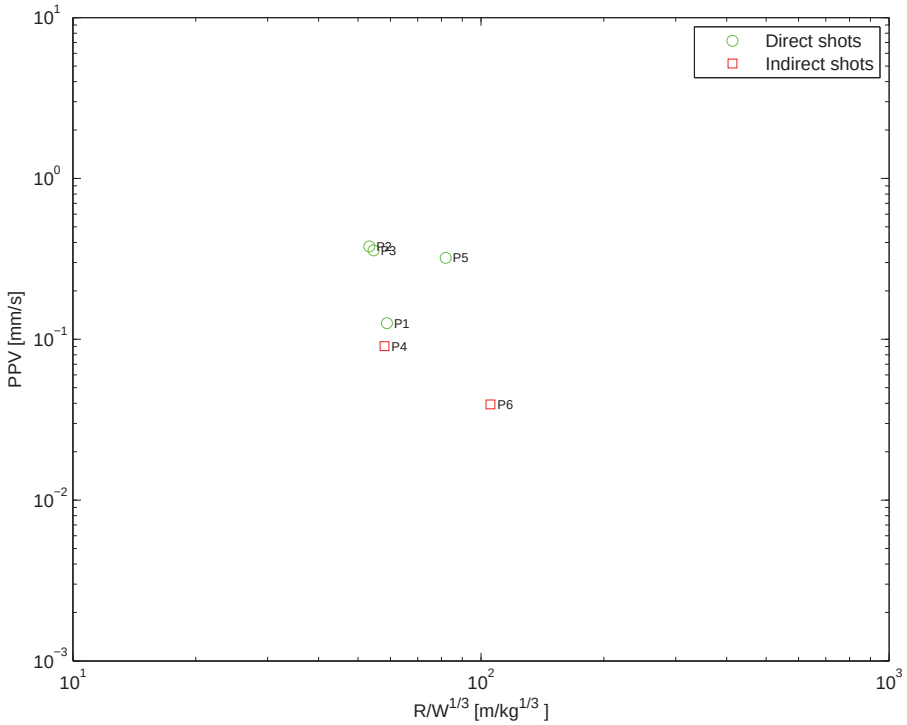


Figure II.12: Plot of peak particle velocity *vs* scalled distance for blast B12.

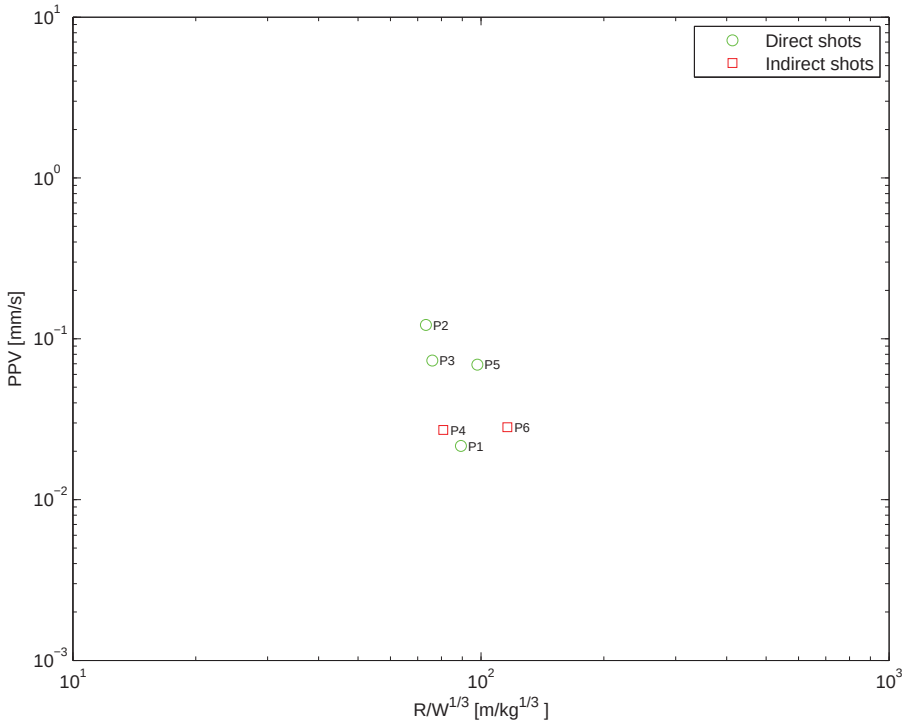


Figure II.13: Plot of peak particle velocity *vs* scalled distance for blast B13.

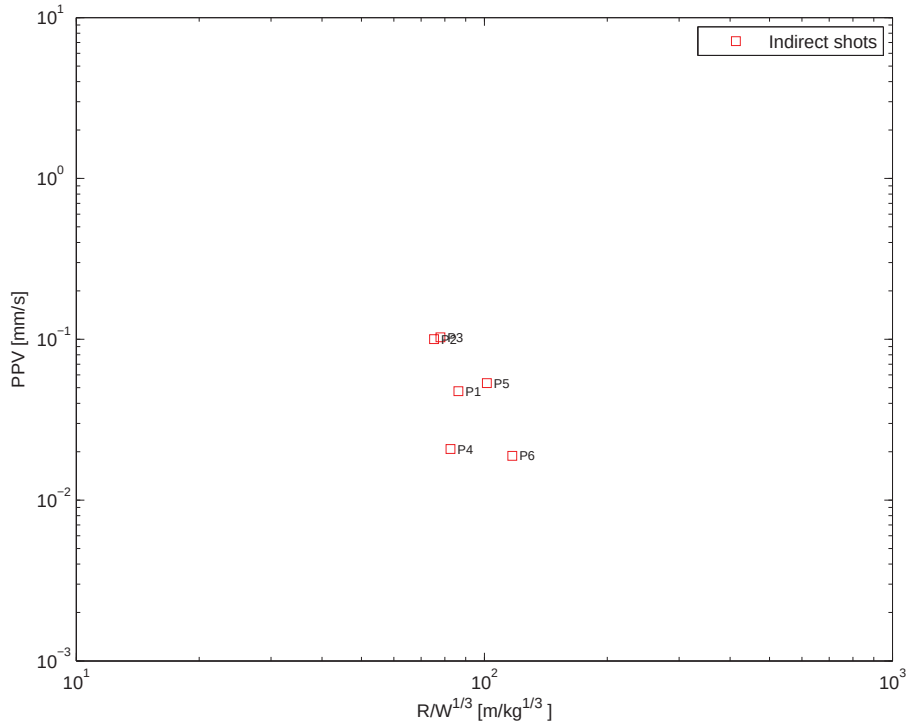


Figure II.14: Plot of peak particle velocity *vs* scalled distance for blast B14.

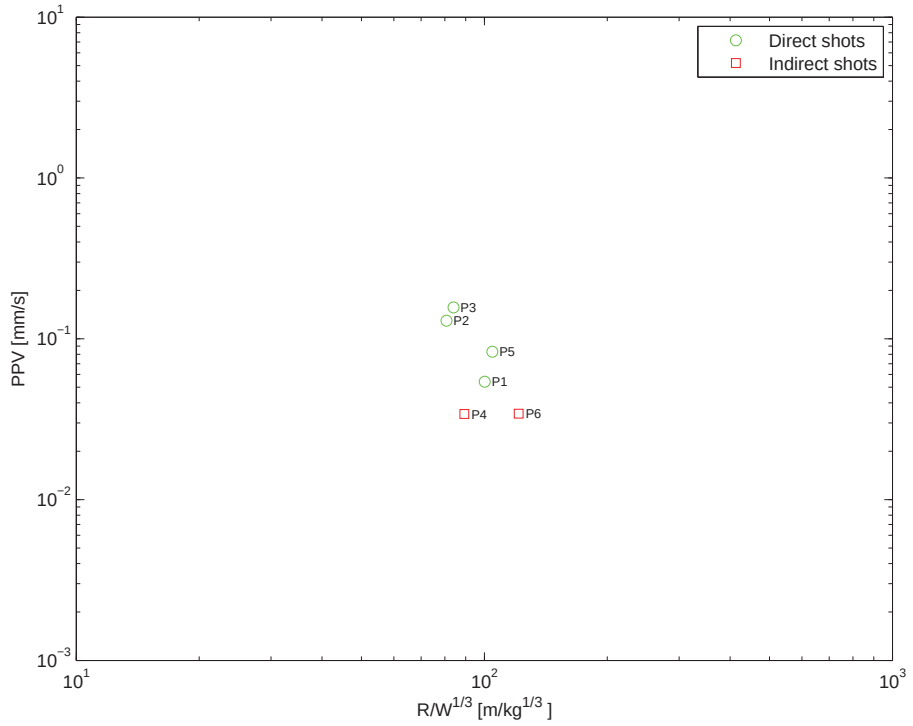


Figure II.15: Plot of peak particle velocity *vs* scalled distance for blast B15.

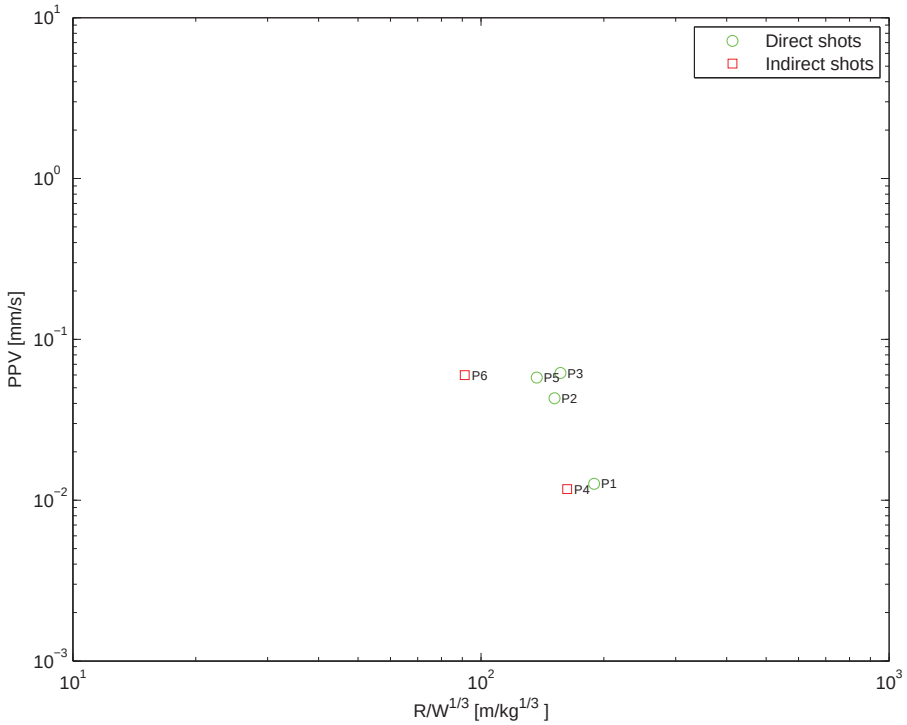


Figure II.16: Plot of peak particle velocity *vs* scalled distance for blast B16.

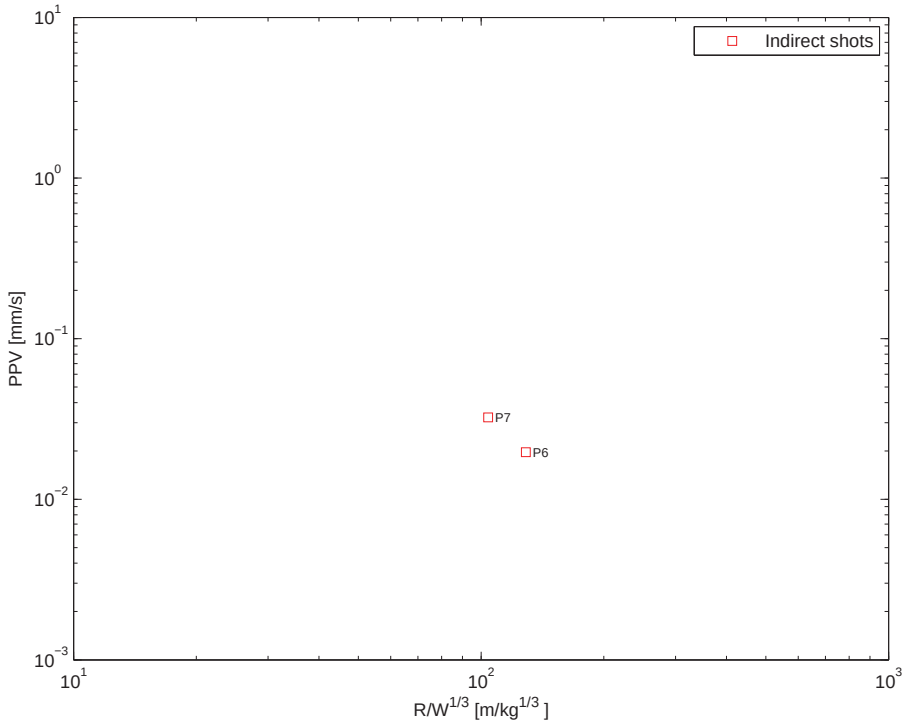


Figure II.17: Plot of peak particle velocity *vs* scalled distance for blast B17.

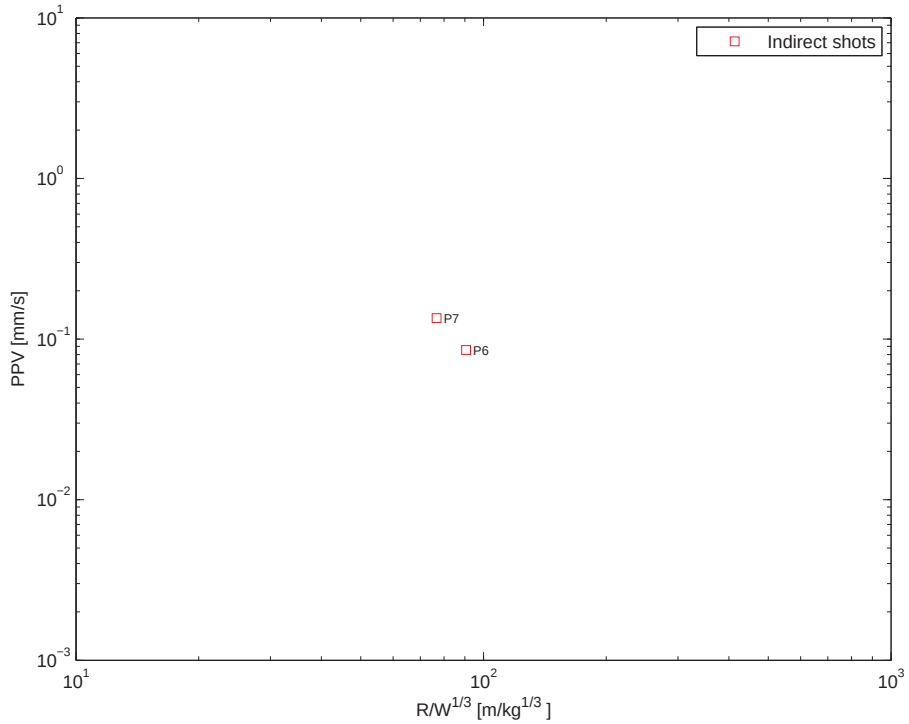


Figure II.18: Plot of peak particle velocity *vs* scalled distance for blast B18.

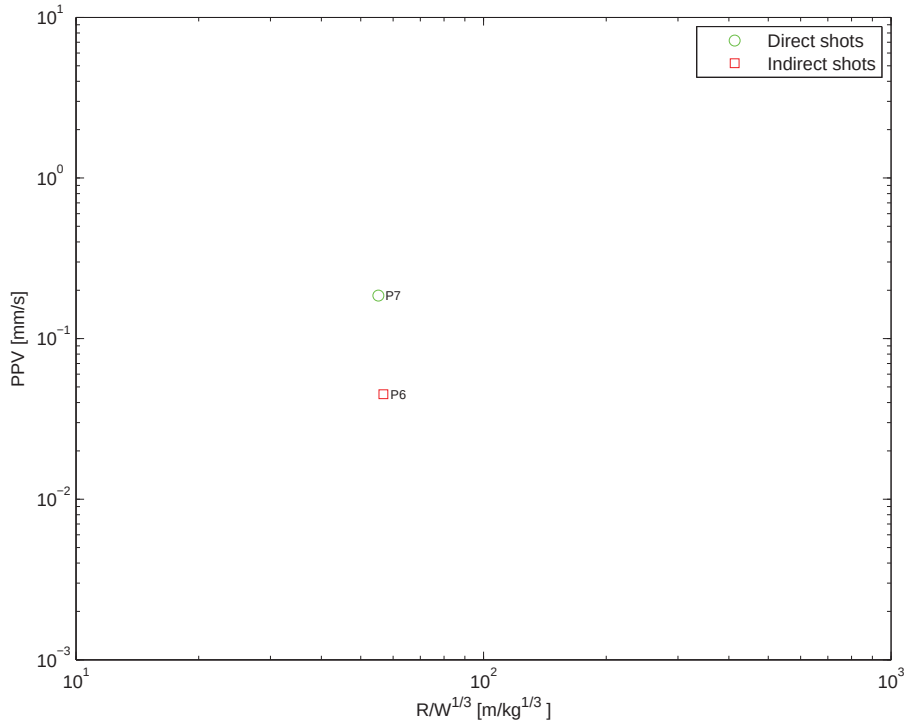


Figure II.19: Plot of peak particle velocity *vs* scalled distance for blast B19.

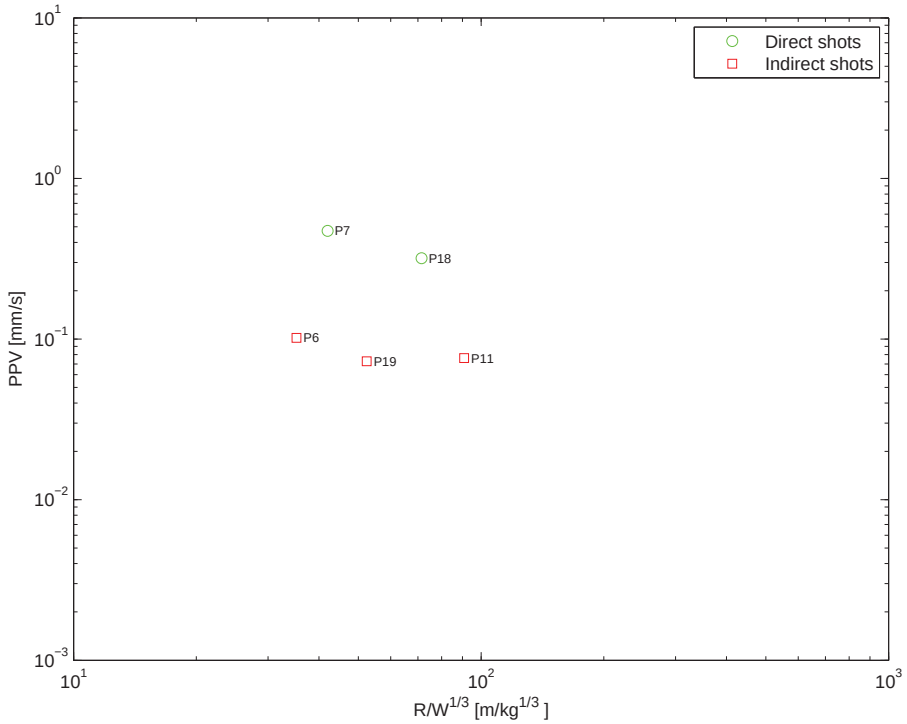


Figure II.20: Plot of peak particle velocity *vs* scalled distance for blast B20.

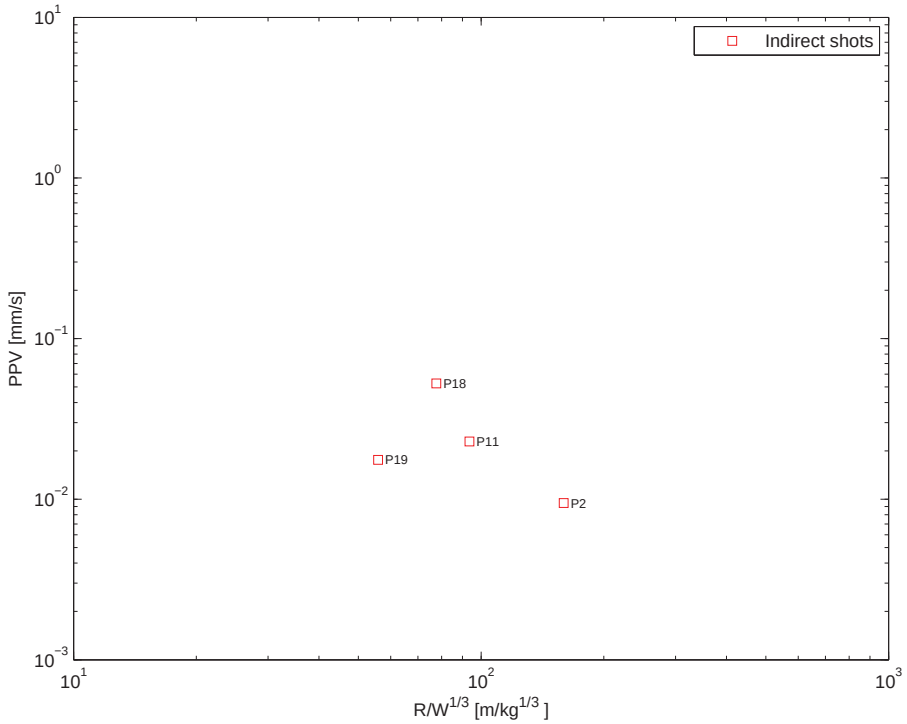


Figure II.21: Plot of peak particle velocity *vs* scalled distance for blast B21.